MULTI-SCALE OBSERVATIONAL STUDY OF SAGITTARIUS B2

Inagural-Dissertation
zur
Erlangung des Doktorgrades
der Mathematisch-Naturwissenschaftlichen Fakultät
der Universität zu Köln
vorgelegt von

Fanyi Meng
aus Heilongjiang, China

12. Dezember 2020

Berichterstatter: Prof. Dr. Peter Schilke
PD Dr. Volker Ossenkopf-Okada
Tag der mündlichen Prüfung: September 2020

Abstract

The giant molecular cloud Sagittarius B2 (SgrB2) is the most massive ($\sim 10^7\,M_\odot$) region with ongoing high-mass star formation in the Galaxy. SgrB2 has a higher density ($> 10^5\,\mathrm{cm}^{-3}$) and dust temperature (∼50–70 K) compared to other star forming regions in the Galactic plane. Additionally, SgrB2 is located at a projected distance of only ∼100 pc to the Galactic center. These features make SgrB2 an excellent case to study high-mass star formation in an extreme, high-pressure environment. Such an environment resembles nearby starburst galaxies. Understanding the structure of the SgrB2 molecular cloud complex is necessary to comprehend the most massive star forming region in our Galaxy, which at the same time provides an unique opportunity to study in detail the nearest counterpart of the extreme environments that dominate star formation in the Universe.

At small scales (0.01–0.1 pc), dense cores appear spread throughout the whole region of SgrB2, embedded within a large scale (∼20 pc) envelope with two main sites of high-mass star formation activity at the center of the cloud: SgrB2(M) and SgrB2(N). In order to characterize the properties of SgrB2 from small to large scales, I started an observational project covering spatial scales from 0.004 pc (1000 au) up to 20 pc (the size of the envelope of SgrB2). At small scales, I studied the physical properties of 308 dense cores distributed throughout the entire SgrB2 cloud. I combined mm wavelength data and cm wavelength data to characterize the properties of dense cores and their associated HII regions. Among the 308 compact dust cores that are identified, 58 are found associated with HII regions, and 49 are associated with outflows. The cores have a mean $m_{\mathrm{H_2}}$ of 150–2500 $M_\odot$, by assuming various dust properties and gas temperatures. Most of the 58 HII regions are ionized by B0 stars. At intermediate scales, I studied the SgrB2(DS) HII region, which is located in the southern part of the envelope. Using VLA data from 4 to 12 GHz, I derived a spectral index between −1.2 and −0.4, suggesting that SgrB2(DS) is a mixture of thermal and non-thermal emission at radio wavelengths. The thermal free-free emission is likely tracing an HII region ionized by an O7 star, while the non-thermal emission can be generated by relativistic electrons created through first-order Fermi acceleration. A model of the Sgr B2(DS) region was developed, which reveals that first-order Fermi acceleration can reproduce the observed flux density and spectral index. At the largest scales, I characterized the physical properties of all the HII regions in the envelope as well as the kinematic structure of the envelope, using newly acquired VLA cm wavelength data and ALMA HC_3N line data. The volume filling factor of ionized gas in the envelope of SgrB2 is $\sim 0.03-0.01$. The HII regions in the envelope are more extended than those in SgrB2(M) and SgrB2(N), suggesting that the HII regions in the envelope may be older than those in the central regions SgrB2(M) and SgrB2(N), and therefore, indicating that high-mass star formation might have started throughout the envelope before than in the central regions. The envelope is also filled with arcs and bubbles, which are traced by HC_3N.

In summary, this study reveals the properties of SgrB2 from the scale of dense dust cores to the large envelope. The dense cores show various evolutionary stages in terms of high-mass star formation activity. The envelope resembles a "swiss cheese" and hosts star forming activities that may have started before those in the central parts of SgrB2.

Additionally, for the first time, a model reveals that synchrotron emission from HII regions can be due to locally produced relativistic electrons accelerated by shocks with moderate velocities.

Zusammenfassung

Die riesige Molekülwolke Sagittarius B2 (SgrB2) ist die massivste ($\sim 10^7\,M_\odot$) Region mit anhaltender Entstehung massereicher Sterne in unserer Galaxie. SgrB2 hat eine höhere Dichte ($> 10^5\,\mathrm{cm}^{-3}$) und Staubtemperatur (∼50–70 K) im Vergleich zu anderen Sternentstehungsgebieten in der galaktischen Ebene. Zudem befindet sich SgrB2 in einer projizierten Entfernung von nur ∼100 pc zum galaktischen Zentrum. Diese Eigenschaften machen SgrB2 zu einem ausgezeichneten Kandidaten für die Untersuchung der Entstehung massereicher Sterne in einer extremen Hochdruckumgebung. Eine solche Umgebung ähnelt der von nahen Starburst-Galaxien. Um die massereichste Sternentstehungsregion in unserer Galaxie zu verstehen, ist es notwendig Strukturen innerhalb des Molekülwolkenkomplexes zu untersuchen. Dies bietet zudem eine einzigartige Gelegenheit, ein Starburst-Galaxien ähnliche Umgebung, welche die Sternentstehung im Universum dominieren, im Detail zu erforschen.

In kleinen Maßstäben (0.01–0.1 pc) sind dichte Kerne über die gesamte Region von SgrB2 verteilt; eingebettet in eine großräumige (∼20 pc) Hülle, die zwei Hauptorte massereicher Sternentstehungsaktivität im Zentrum der Wolke beinhaltet: SgrB2(M) und SgrB2(N). Um die Eigenschaften von SgrB2 von kleinen bis großen Skalen zu charakterisieren, habe ich ein Beobachtungsprojekt begonnen, das räumliche Skalen von 0.004 pc (1000 au) bis 20 pc (die Größe der Hülle von SgrB2) abdeckt. Auf kleinen Skalen untersuchte ich die physikalischen Eigenschaften von 308 dichten Kernen, die über die gesamte SgrB2-Wolke verteilt sind. Ich kombinierte Daten im mm-Wellenlängen- und cm-Wellenlängenbereich, um die Eigenschaften der dichten Kerne und der zugehörigen HII-Regionen zu charakterisieren. Unter den 308 identifizierten kompakten Staubkernen finden sich 58, die mit HII-Regionen assoziiert sind, und 49, die mit 'outflows' assoziiert sind. Die Kerne haben eine mittlere Masse $\mathrm{m}_{\mathrm{H}_2}$ von 150–2500 $M_\odot$, unter der Annahme verschiedener Staubeigenschaften und Gastemperaturen. Die meisten der 58 HII-Regionen sind durch B0-Sterne ionisiert. Auf mittleren Skalen untersuchte ich die SgrB2(DS) HII-Region, die sich im südlichen Teil der Hülle befindet. Mit VLA-Daten von 4 bis 12 GHz leitete ich einen Spektralindex zwischen -1.2 und -0.4 ab, was darauf hindeutet, dass SgrB2(DS) eine Mischung aus thermischer und nicht-thermischer Emission im Radiowellenlängenbereich ist. Die thermisch freie Emission stammt wahrscheinlich von einer HII-Region, die von einem O7-Stern ionisiert wurde. Die nicht-thermische Emission kann durch relativistische Elektronen erzeugt werden, die durch Fermi-Beschleunigung erster Ordnung entstehen. Es wurde ein Modell der Sgr B2(DS)-Region entwickelt, welches zeigt, dass Fermibeschleunigung erster Ordnung die beobachtete Flussdichte und den Spektralindex reproduzieren kann. Auf den größten Skalen charakterisierte ich die physikalischen Eigenschaften aller HII-Regionen in der Hülle sowie die kinematische Struktur der Hülle unter Verwendung neuer VLA-cm-Wellenlängendaten und ALMA HC_3N-Liniendaten. Der Volumenfüllfaktor von ionisiertem Gas in der Hülle von SgrB2 beträgt $\sim 0.03 - 0.01$. Die HII-Regionen in der Hülle sind ausgedehnter als die in SgrB2(M) und SgrB2(N), was darauf zurückzuführen sein kann, dass die HII-Regionen in der Hülle älter sind als die in den zentralen Regionen SgrB2(M) und SgrB2(N). Dies deutet darauf hin, dass die massereiche Sternentstehung in der gesamten Hülle früher begonnen haben könnte als in den zentralen

Regionen. Die Hülle ist auch mit Bögen und Blasen gefüllt, welche in Emission von HC_3N sichtbar sind.

Zusammengefasst: Die Studie beschreibt die Eigenschaften von SgrB2 in den Maßstäben von kleinsten dichten Staubkerne bis hin zur großen Hülle. Die dichten Kerne zeigen verschiedene Entwicklungsstadien hinsichtlich der Aktivität massereicher Sternentstehung. Die Hülle ähnelt einem 'Schweizer Käse' und zeigt Sternentstehungsaktivitäten, die möglicherweise hier früher begonnen haben als im Zentrum von SgrB2. Zudem zeigt ein Modell zum ersten Mal, dass die Synchrotronemission aus HII-Regionen auf lokal erzeugte relativistische Elektronen, die durch Stöße mit moderaten Geschwindigkeiten beschleunigt werden, zurückzuführen sein kann.

Contents

List of Figures

List of Tables

Part I

Introduction

Chapter 1

High-mass Star Formation

High-mass stars ($M > 8\,M_{\odot}$) play a major role in the evolution of galaxies. They synthesize heavy elements, ionize gas, drive shock waves, and change chemical states of the *interstellar medium* (ISM). Due to their relevance, the formation of high-mass stars is one of the most highlighted subject in modern astrophysics. In this chapter, I introduce general properties of the ISM, the regions where stars form, and the formation process of both low-mass and high-mass stars.

1.1 Interstellar medium

Everything between the stars in galaxies is called ISM. The components of the ISM are gas, dust, radiation and magnetic field. The gaseous component of the ISM consists of various phases, from ionized to neutral, from cold ($\sim 10\,\mathrm{K}$) to hot ($> 10^6$ K), and from diffuse ($10^{-2}\,\mathrm{cm}^{-3}$) to dense ($10^6\,\mathrm{cm}^{-3}$). The phases of the gas in the ISM can be categorized as follows (based on Draine, 2011):

HIM: Hot ionized medium, or coronal gas. The HIM has temperature $T \gtrsim 10^{5.5}\,K$, and density[1] $n_{\mathrm{H}} \approx 4 \times 10^{-3}\,\mathrm{cm}^{-3}$ (e.g. Madsen et al., 2006). It is heated by shock waves and cooled through adiabatic expansion and X-ray emission.

WNM: Warm neutral medium, which is mainly HI with $T \approx 5000\,\mathrm{K}$ and $n_{\mathrm{H}} \approx 0.6\,\mathrm{cm}^{-3}$ (e.g. Kanekar et al., 2003).

CNM: Cold neutral medium, atomic gas (mainly HI) that has $T \approx 100\,\mathrm{K}$ and $n_{\mathrm{H}} \approx 30\,\mathrm{cm}^{-3}$ (e.g. Wolfire et al., 2003).

Diffuse molecular gas: Mainly H_2 that has $T \approx 50\,\mathrm{K}$ and $n_{\mathrm{H}} \approx 100\,\mathrm{cm}^{-3}$ (e.g. Ando et al., 2019). Compare to CNM, the lower temperature and higher density enhances the abundance of H_2.

Dense molecular gas: Mainly H_2. Usually, the temperature of dense molecular gas ranges from 10 to $\gtrsim 50$ K and the density (n_{H}) ranges from 10^3 to $\gtrsim 10^6\,\mathrm{cm}^{-3}$. Dense molecular gas is usually coupled with dust, which makes it visually dark (visual extinction $A_{\mathrm{V}} \gtrsim 3\,\mathrm{mag}$). Molecular clouds contain most of the dense molecular gas and constitute the sites where star formation takes place.

[1]The density is defined as H nucleon density, i.e. the number of H nucleons in unit volume.

HII: Ionized gas, mainly protons and electrons. The temperature of HII regions ranges from $\sim 5\times10^3$ to $\sim 10^4$ K. The density ($n_{\rm H}$) of HII gas can range from ~ 1 to $10^4\,{\rm cm^{-3}}$. HII regions are usually ionized by nearby O-type stars, which can emit Lyman continuum photons (with energy above 13.6 eV).

The pressure, which is $p = n_{\rm H}T$, of HIM, WNM, CNM and diffuse H_2 are all $\sim 3000\,{\rm K\,cm^{-3}}$. Dense molecular gas and HII gas can have pressure even higher than $\sim 10^8\,{\rm K\,cm^{-3}}$. Based on the information mentioned above, phases of ISM on the T–n diagram is shown in Fig. 1.1. SgrB2, which is one of the most massive star forming regions in our Galaxy and the main target of study of this thesis, is also plotted in Fig. 1.1. The temperature and density of the molecular and ionized contents of SgrB2 are based on previous observational studies (e.g. Schmiedeke et al., 2016; Sánchez-Monge et al., 2017; Schwörer et al., 2019) and this work (see Part III).

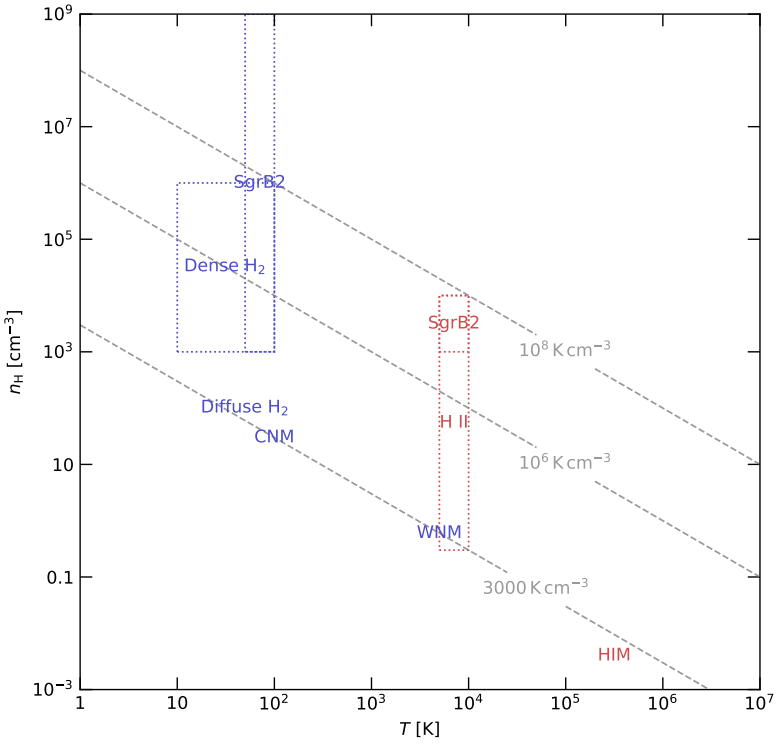

Figure 1.1 Temperature, density and pressure of different phases of ISM. The phases with names in blue are neutral, while the phases with names in red are ionized. Gray dashed lines indicate iso-pressure lines. 'SgrB2' in blue represents the molecular component of SgrB2, while 'SgrB2' in red represents the ionized gas in SgrB2. The physical parameters of SgrB2 is based on previous observational studies on SgrB2 (Schmiedeke et al., 2016; Sánchez-Monge et al., 2017; Schwörer et al., 2019) and this work.

The mass of the Milky Way within a radius of 60 kpc is $4.6\times10^{11}\,M_\odot$, to which baryonic matter contributes $9.5\times10^{10}\,M_\odot$ with a gas fraction of 13%, i.e., $1.2\times10^{10}\,M_\odot$ (Kalberla et al., 2007). This total gas mass is divided in HI mass, accounting for about $8\times10^9\,M_\odot$, WIM mass, accounting for $2\times10^9\,M_\odot$, and molecular mass corresponding to about $2.5\times10^9\,M_\odot$ (Kalberla & Kerp, 2009).

Table 1.1 Properties of clouds, clumps, and cores

	Mass $M_\odot$	Size pc	Mean density cm^{-3}	T_g K
Clouds	10^3–10^4	2–15	50–500	≈ 10
Clumps	50–500	0.3–3	10^3–10^4	10–20
Cores	0.5–5	0.03–0.2	10^4–10^5	8–12

Note: Values are from (Bergin & Tafalla, 2007).

In the ISM, I pay special attention to the two high pressure phases, dense molecular gas and HII gas. In Section 1.4 I introduce HII regions. Here I briefly summarize the properties of the dense molecular gas. Due to the dust component that couples with gas, dense molecular gas is dark in the visible light wavelengths. Therefore, these regions are also called 'dark clouds'. Due to the efficient cooling through rotational emission of CO, dense molecular regions are also cold, see Fig. 1.1. Such cold dark clouds are the birthplaces of stars. Dense molecular gas displays a hierarchical spatial structure. Conventionally, the largest entities of dense molecular gas are called 'clouds', medium sized structures are called 'clumps' and the smallest structures are usually referred to as 'cores'. The basic properties of these three kind of structures are summarized in Table 1.1.

1.2 Low-mass star formation

Compared to high-mass stars, the formation process of low-mass stars ($M < 8M_\odot$) is relatively well understood. The formation process of a low-mass star can be described as five stages (based on Shu et al., 1987; Kauffmann, 2007):

1. Clouds fragment into clumps, within which cores from. When the magnetic field and turbulence are not strong enough to support the cloud against self-gravity, material in the clouds collapse and form cores. The typical lifetime of the dense cores is $\sim 10^6$ yr. These cores are usually cold, with temperatures of 10–20 K, which makes most their radiation occur in the sub-mm and FIR regimes (i.e., their spectral energy distribution, or SED, peaks at these wavelengths).

2. The core collapses inside-out and forms a protostar embedded in an envelope of dust and gas. The SED is still black body, with an effective temperature (T_eff) less than 70 K. This stage lasts for $< 3 \times 10^4$ yr.

3. Surrounding the protostar there is a circumstellar disk. The mass initially contained in the cloud collapses or is transported from the envelope around the protostar down onto the disk, and finally it is accreted to the protostar through the disk. The effective temperature is approximately $70 - 650$ K. This stage lasts for $\sim 2 \times 10^5$ yr. Bipolar outflows perpendicular to the disk plane carry angular momentum away from the system. The SED of this stage shows an excess at infrared (mid and near-IR) wavelengths.

4. The accretion stops. The star enters the pre-main-sequence phase and becomes a classical T Tauri star, which undergoes gravitational contraction. There is still a disk

surrounding the star. The system has $T_{\rm eff} \sim 650 - 2880$ K. This stage lasts for $\sim 1 \times 10^6$ yr.

5. The star still has gravitational contraction, but the disk is either very weak or absent. The system has $T_{\rm eff} \gtrsim 3000$ K. This stage lasts for $\sim 1 \times 10^6$ yr.

1.3 High-mass star formation

According to the initial stellar mass function (IMF, Kroupa, 2001), low-mass stars constitute most of the stellar mass in galaxies. However, high-mass stars ($M > 8 M_\odot$) dominate the luminosity of these galaxies. This is due to the fact that the luminosity of stars strongly depends on the stellar mass, $L \propto M^{>2.8}$ (Eker et al., 2018). For instance, a $10\,M_\odot$ star has $L \sim 10^4\,L_\odot$. Apart from the thermal emission of the stars themselves, high mass stars are the major energy input into the ISM via various feedback mechanisms, such as stellar winds, outflows, and ionization. The death of high-mass stars, which is in form of supernova explosions, also shapes the physical and chemical structure of the galaxies (see e.g. Bolatto et al., 2013).

The formation process of high-mass stars can be summarized as four phases (based on Zinnecker & Yorke, 2007; Tan et al., 2014):

Compression: The forming sites of high-mass stars are *infrared dark clouds* (IRDCs). IRDCs, as suggested by their name, are optically thick at the wavelengths of $\sim 1 - 10\,\mu$m. The gravo-turbulent fragmentation of IRDCs leads to the formation of starless cores ($\sim 100\,M_\odot$) or starless clumps ($\sim 1000\,M_\odot$). Such gravitationally compressed cores and clumps are the initial sites of high-mass star formation.

Collapse: If the gravity forces in the cores are stronger than the supporting forces from thermal pressure, turbulence, magnetic field, and rotation, the cores will collapse. The collapse results in the formation of optically thick, pressure supported protostellar objects.

Accretion: Due to the adiabatic heating, the core gains enough pressure to overcome gravity. The collapse phase stops. The core gains mass through accretion. Simultaneously, the hydrogen burning starts in the newly formed star.

Disruption: The newly born high-mass stars disrupt the cloud where they formed from via feedback processes such as winds, outflows, expansion of HII regions, and eventually supernova explosions.

High-mass star formation is not a scaled-up version of low-mass star formation. The differences between low-mass star formation and high-mass star formation can be summarized as follows:

The stars that are more massive than B3 stars are hot enough to emit UV photons. UV photons with energy > 11.2 eV can dissociate molecular hydrogen in the cloud and photons with energy > 13.6 eV can ionize hydrogen atoms to create HII regions. However, low-mass stars cannot generate HII regions. Details of the HII region ionized by high-mass stars are presented in Section 1.4.

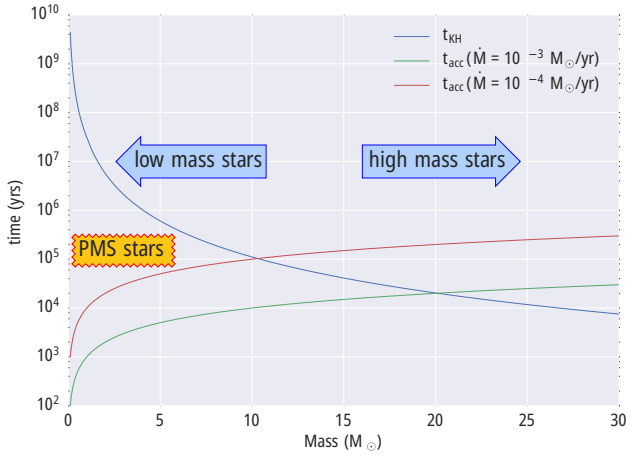

Figure 1.2 Kelvin-Helmholtz timescale (blue) against free-fall timescale for various stellar masses. The free-fall time of two mass accretion rates, $10^{-3}\,M_\odot$/yr and $10^{-4}\,M_\odot$/yr are plotted in green and red, respectively. This plot is adopted from (Schilke, 2015).

The Kelvin-Helmholtz timescale ($t_{\rm KH}$) describes the time of the prestellar contraction. Since contraction of the protostar is a process of transforming the gravitational energy to radiation, $t_{\rm KH}$ can be written as the ratio between gravitational energy and luminosity:

$$t_{\rm KH} = \frac{GM^2}{RL}, \tag{1.1}$$

where G is the gravitational constant. M, R, and L are the mass, radius, and luminosity of the protostar. Another relevant time scale is the free-fall timescale ($t_{\rm ff}$), which represents the typical time that the accretion takes:

$$t_{\rm ff} = \left(\frac{3\pi}{32G\rho}\right)^{1/2}, \tag{1.2}$$

where ρ is the density of the envelope that the protostar accrete material from, which affects the mass accretion rate. In Fig. 1.2, the relationship of $t_{\rm KH}$ and $t_{\rm ff}$ is plotted, for two mass accretion rates $10^{-3}\,M_\odot$/yr and $10^{-4}\,M_\odot$/yr, respectively. For low-mass star formation, the $t_{\rm KH} > t_{\rm ff}$. Therefore, after the accretion finishes, the central star can quietly contract under gravity. Such a star is a pre-main-sequence (PMS) star. However, high-mass stars have $t_{\rm KH} < t_{\rm ff}$. Therefore, the high-mass stars skip the PMS star phase, and are directly born on the main sequence. High-mass stars have their nuclear fusion started while still accreting matter.

Because of the active feedbacks that high-mass star formation accompanied with, high-mass star formation can trigger new star forming activities. Such chain-triggering process can result in starbursts. While the low-mass stars are less influential on their environment.

The accretion phase of high-mass star formation faces one critical problem: if the accretion is homogeneous and only thermally supported, the accretion will be stopped by radiation from the central star when the stellar mass reaches $\sim 5\,M_\odot$. The radiation from the central star has a direct impact on the dust, which in turn also affects the gas due to the

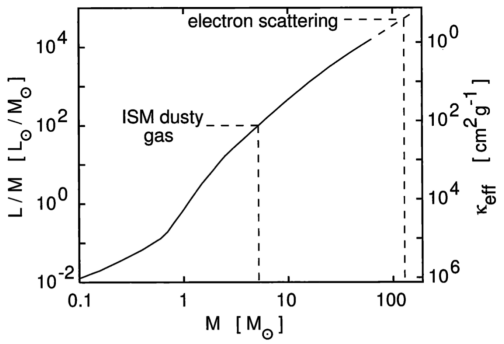

Figure 1.3 Luminosity to mass ratio (left), and critical effective opacity (right) of main sequence stars. Two mass upper limits, $\sim 5\,M_\odot$ (dust coupled with gas in ISM) and $130\,M_\odot$ (pure electron scattering) are marked. Credit: (Yorke, 2004).

well coupling between dust and gas. The critical effective opacity $\kappa_{\rm eff}$, which is the maximum effective opacity of the accretable material, is plotted against stellar mass in Fig. 1.3. Since in the accretion phase, the central high-mass star is embedded in optically thick dust, $\kappa_{\rm eff}$ has a lower limit, which translate into an upper limit of the stellar mass, $\sim 5\,M_\odot$.

Such an upper limit of $\sim 5\,M_\odot$ for the mass of a star contradicts the observations. Several attempts have been made to adjust the accretion model and explain the existence of high-mass stars. One model is called '*monolithic collapse*' (McKee & Tan, 2003), which means that the cores are supported not only by thermal pressure, but also by turbulence. Thus, more material can be accumulated, because the cores can have a mass above the *Jeans mass* via extra support against gravity, and therefore can cause higher accretion rates. Noteworthy, the extra mass does not come with too-much extra luminosity (compared to the standard luminosity-mass relationship of stars), therefore the accretion can breakthrough the $\sim 5\,M_\odot$ upper limit. Another model is called '*competitive accretion*' (Bonnell et al., 2001). In this model, the stars form in a cluster and accrete through Bondi-Hoyle accretion. The accretion rate is determined by the gravity potential of the cluster. Thus, the stars closer to the center of the cluster can accrete faster and consequently become more massive. Two key differences between these two models are: 1) The monolithic collapse requires the initial density distribution to be peaked (density profile $n \propto r^{-1.5}$), while the competitive accretion model starts from a more homogeneous density distribution. 2) Since the monolithic collapse model assumes that the cores are individually accreting material, and the accretion rate is directly related to the core mass, the mass of the stars is closely related to the mass of the cores. On the other hans, the stars formed in the competitive accretion model will have masses that depend on their trajectories in the cloud.

Although various models of high-mass star formation have been proposed proposed, the presence of an envelope hinders the direct observational study of the high-mass star formation process itself. Thus, observing the by-products of high mass star formation is usually the strategy that observational astrophysics take.

Different signposts of high-mass star formation exist and have been used to determine, among other things, the lifetimes of the process of formation of these stars. Among these signposts, methanol (CH_3OH) and hydroxil (OH) masers allow us to identify the exact location of the high-mass protostars. This is because these masers need intense far-IR

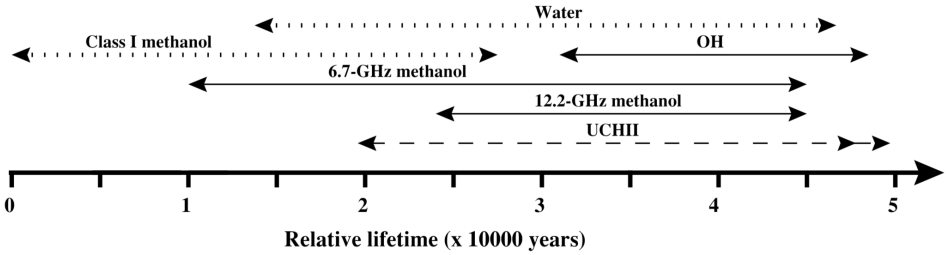

Figure 1.4 Evolutionary of masers and UCHII regions that are associated with high-mass star formation. The double arrow of UCHII suggests that its presence will last beyond the end of this plot. Credit: (Breen et al., 2010)

Table 1.2 Physical properties of HII regions.

	Size pc	Density cm^{-3}	Emission Measure $pc\,cm^{-6}$	Ionized Mass $M_\odot$
Hypercompact	$\lesssim 0.03$	$\gtrsim 10^6$	$\gtrsim 10^{10}$	$\sim 10^{-3}$
Ultracompact	$\lesssim 0.1$	$\gtrsim 10^4$	$\gtrsim 10^7$	$\sim 10^{-2}$
Compact	$\lesssim 0.5$	$\gtrsim 5 \times 10^3$	$\gtrsim 10^7$	~ 1
Classical	~ 10	$\sim$100	$\sim 10^2$	$\sim 10^5$
Giant	~ 100	~ 30	$\sim 5 \times 10^5$	$10^3 - 10^6$
Supergiant	> 100	~ 10	$\sim 10^5$	$10^6 - 10^8$

Note: Adapted from (Kurtz, 2005).

sources in their vicinity to be radiatively pumped. Similar to low-mass star formation, outflows are also used to identify and study high-mass star formation. One difference between the outflows of low-mass and high-mass star formation is that the former one is usually more collimated. Another signpost of high-mass star formation are the so-called hot molecular cores, which are heated by the high-mass stars inside them, are warm and chemically rich. Finally, HII regions, which is probably the most characteristic tracer of high-mass star formation, are also frequently observed. Since HII regions are one of the main type of sources studied in this thesis, I discuss in more detail the properties of HII regions in Sect. 1.4. It is worth to note that masers, outflows, and HII regions trace different evolutionary stages of the formation of high-mass stars. In Fig. 1.4, the evolutionary scheme of various masers associated with high-mass star formation is plotted (adapted from Breen et al., 2010). The life time of outflows is of the same order of magnitude as $t_{\rm ff}$ (Beuther et al., 2002).

1.4 HII regions

When high-mass stars are formed, the Lyman continuum photons from the newly born star ionize the dense gas and dust surrounding them, generating a hypercompact HII region (HCHII) or ultracompact HII region (UCHII). As the names suggests, HII regions are conventionally categorized by their sizes and densities. The physical properties of six types of HII regions are listed in Table 1.2.

The size of the HII region is called the Strømgren radius ($R_{\rm S}$), which is determined by the balance of ionization and recombination in the HII region. $R_{\rm S}$ can be expressed as:

$$R_{\rm S} = \left(\frac{3\dot{N}_{\rm Ly}}{4\pi\alpha_{\rm H} n_{\rm e}^2} \right)^{1/3}, \tag{1.3}$$

where $\dot{N}_{\rm Ly}$ is the flux of Lyman continuum photons from the central stars, $\alpha_{\rm H}$ is the recombination coefficient for atomic hydrogen, and $n_{\rm e}$ is the volume density of electron (also regarded as the density of protons, approximately). Assuming that the electron temperature $T_{\rm e} = 10^4\,{\rm K}$, then $\alpha_{\rm H} \sim 2 \times 10^{-13}\,{\rm cm^{-3}\,s^{-1}}$. Thus,

$$R_{\rm S} \approx 1.7\,{\rm pc} \left(\frac{\dot{N}_{\rm Ly}}{10^{50}\,{\rm s^{-1}}} \right)^{1/3} \left(\frac{n_{\rm e}}{10^3\,{\rm cm^{-3}}} \right)^{-2/3}. \tag{1.4}$$

The corresponding mass of the HII region is:

$$M \approx 600\,M_\odot \left(\frac{\dot{N}_{\rm Ly}}{10^{50}\,{\rm s^{-1}}} \right) \left(\frac{n_{\rm e}}{10^3\,{\rm cm^{-3}}} \right)^{-1}. \tag{1.5}$$

The HII region expands because of its pressure, and the expansion speed is approximately the sound speed in it, which is ~ 12 km s^{-1} , for $T_{\rm e} = 10^4\,{\rm K}$. Thus, the typical time scale of the expansion is:

$$t_{\rm expand} \approx 1.7 \times 10^5\,{\rm yrs} \left(\frac{\dot{N}_{\rm Ly}}{10^{50}\,{\rm s^{-1}}} \right)^{1/3} \left(\frac{n_{\rm e}}{10^3\,{\rm cm^{-3}}} \right)^{-2/3}. \tag{1.6}$$

The emission from HII regions is mainly free-free continuum and RRLs, which are both introduced in Section A.2.

1.5 The Central Molecular Zone

The *Central Molecular Zone* (CMZ) is the inner $\sim 500\,{\rm pc}$ region of the Milky Way (see e.g. Morris & Serabyn, 1996; Bally et al., 2010; Kruijssen et al., 2014, 2015; Henshaw et al., 2016; Ginsburg et al., 2018). The CMZ, which contains $2 - 6 \times 10^7\,{\rm M_\odot}$ molecular gas, has a gas density higher by ~ 2 orders of magnitude than the typical density in the disk of the Galaxy (see e.g. Longmore et al., 2013). The gas temperature in the CMZ can be $> 100\,{\rm K}$, higher than the usual temperatures (10–30 K) in the molecular gas of the galactic disk. These high temperature and high density makes the CMZ an environment that resembles high-z galaxies (Kruijssen & Longmore, 2013). The CMZ has a star-to-gas ratio ~ 10 times higher than our solar neighborhood or clouds and cores in the Perseus star-forming region, but within the same order of magnitude as high-z galaxies (Longmore et al., 2013, see Fig. 1.5).

Despite the extreme-like properties of the CMZ listed above, it is deficient in star formation activity when compared to the disk of the Galaxy (Kauffmann et al., 2017a,b). As shown in Fig. 1.6, the star formation rate of the CMZ is lower by approximately one order of magnitude compared to the interpolated value between the Milky Way clouds and other galaxies.

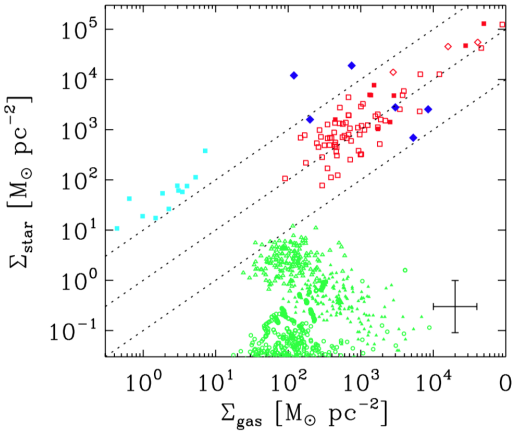

Figure 1.5 Variation of the stellar surface density $\Sigma_{\rm star}$ and $\Sigma_{\rm gas}$. Blue spots are CMZ, red spots are high-z galaxies, and the green spots are the clouds in the solar neighborhood and the Perseus Cloud. Credit: (Longmore et al., 2013).

Apart from the distinct physical properties, one of the most interesting features of the CMZ is its gas streams. Four coherent gas streams have been recently identified (e.g. Kruijssen et al., 2015; Henshaw et al., 2016), as shown in Figure 1.7. These gas streams surround the Galactic Center, with a distance of ∼150 pc to the Galactic Center. The velocity span is $\sim$ 200 km s^{-1} . Most of the relevant molecular clouds (such as SgrB2) and young stellar clusters (such as Arches and Quintuplet, see Kruijssen et al., 2015) in the CMZ are located along this streams, suggesting that they have an important role on the evolution of molecular clouds in the CMZ and the star formation process itself.

1.6 The Sagittarius B2 star forming region

Sagittarius B2 (hereafter SgrB2) is the most massive ($\sim 10^7$ $M_\odot$, see e.g., Goldsmith et al. 1990) region with ongoing high-mass star formation in the Galaxy, and has a higher density ($> 10^5$ cm^{-3}) and dust temperature (∼50–70 K) compared to other star forming regions in the Galactic plane (see e.g., Ginsburg et al., 2016; Schmiedeke et al., 2016; Sánchez-Monge et al., 2017). Sgr B2 is located at a distance of 8.34 ± 0.16 kpc, at only 100 pc in projection from the Galactic center (Reid et al., 2014)[2].

In the central ∼ 2 pc, there are the two well-known hot cores Sgr B2(N) and Sgr B2(M) (see e.g., Schmiedeke et al., 2016; Sánchez-Monge et al., 2017), which contain at least 70 high-mass stars with spectral types from O5 to B0 (see e.g., Gaume et al., 1995; De Pree et al., 1998, 2014). A recent study (Schwörer et al., 2019) shows that the structure of the gaseous and dust content of Sgr B2(N) is a central hub with converging filaments. Sgr B2(M) is found to have its mass distributed in several fragments. The H_2 volume density of dense cores of SgrB2(N) and (M) is $10^5 - 10^7$ $M_\odot$ pc^{-3}, i.e., one or two orders of magnitude higher than the stellar densities of super star clusters (Sánchez-Monge et al., 2017). Surrounding the two hot cores, there is a larger envelope with a radius of 20 pc that contains more than

[2] A new distance to the Galactic center has been measured to be 8.127 ± 0.031 kpc (Gravity Collaboration et al., 2018). For consistency with the paper published within the same series of studies of Sgr B2, we use the distance reported by Reid et al. (2014).

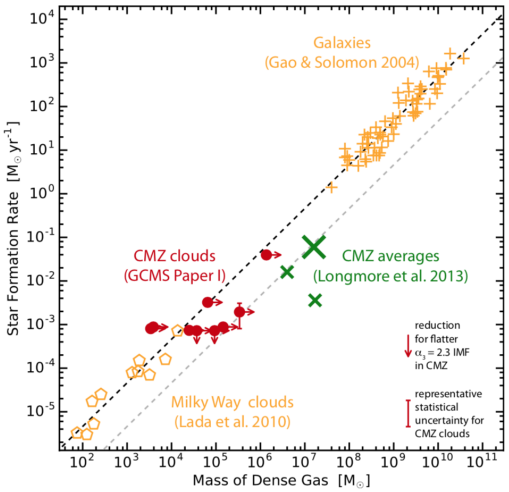

Figure 1.6 Observed star formation rates vs. the mass of dense gas residing at visual extinctions $A_\mathrm{V} > 7\,\mathrm{mag}$. Credit: (Kauffmann et al., 2017a).

99% of the total mass of Sgr B2 (Schmiedeke et al., 2016). The envelope has lower density $n_\mathrm{H} = 10^3\,\mathrm{cm}^{-3}$ and lower gas temperature $T \sim 50\,\mathrm{K}$ compared to the two central hot cores of SgrB2. A sketch of the envelope and the central hot cores is shown in Figure 1.8.

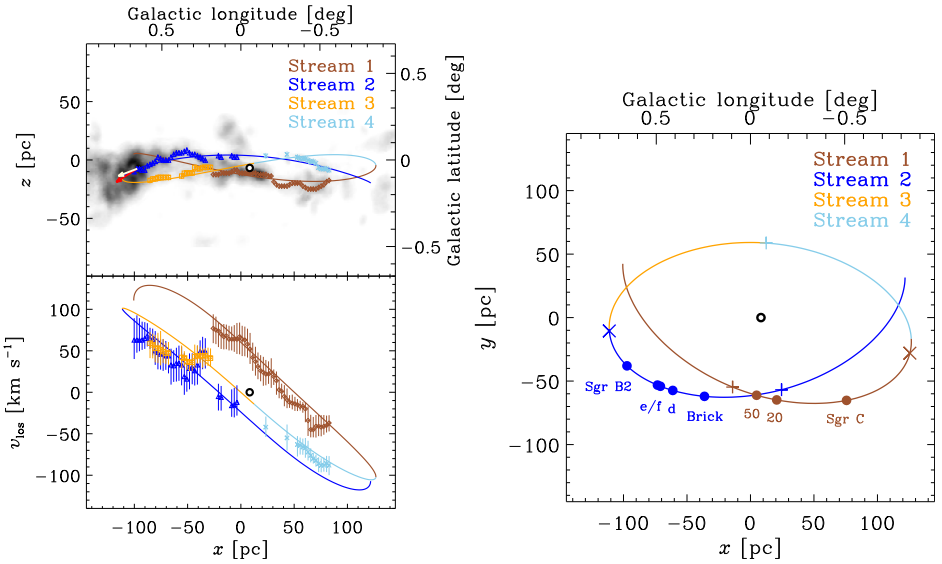

Figure 1.7 The four gas streams in CMZ, from Kruijssen et al. (2015). *Left Upper*: Integrated-intensity map of $NH_3(1, 1)$ emission near galactic center overlaid by modeled streams. *Left Lower*: Four streams in position-velocity plot. *Right*: Top-down view of the model of the streams.

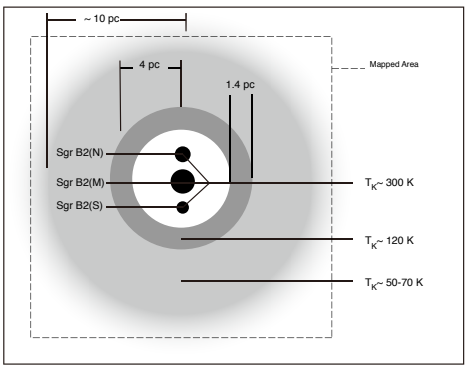

Figure 1.8 Sketch showing the structures of Sgr B2 star forming region, adopted from (Goicoechea et al., 2004).

Chapter 2

About this work

SgrB2 has been the target of many observational campaigns, most of these observations have focused on the two hot cores Sgr B2(N) and (M) (e.g. de Pree et al., 1993, 1995, 1996; De Pree et al., 1998, 2014; Qin et al., 2008, 2011; Belloche et al., 2013), and recently some attention has been paid to the large scale envelope. Single-dish telescopes have been used to map a large area around SgrB2 (e.g. de Vicente et al., 1997, 2000; Molinari et al., 2011; Jones et al., 2011), achieving only coarse (20–40″) angular resolution. Martín-Pintado et al. (1999) used the VLA to map an area of $3' \times 3'$ in the ammonia inversion lines (3,3) and (4,4), with good angular resolution (∼3″). Although covering only a small portion of the inner envelope, they find an interesting dense gas structure dominated by rings, arcs and filaments. The rings have sizes of 1–3 pc, thicknesses of 0.2–0.4 pc, contain warm gas (∼40–70 K), and some of them have expansion velocities of ∼6–10 km s^{-1}. The authors suggest that expanding bubbles, which produce these ammonia hot shells, are triggering new high-mass star formation in the envelope. Recent observations, with ALMA at 3 mm revealed more than 271 high-mass protostellar cores distributed throughout the envelope (Ginsburg et al., 2018). These observations suggest that SgrB2 would resemble a "swiss cheese" with large holes dominating the large-scale structure and dense cores spread all over the envelope.

Several questions still need to be answered:

- What are the physical properties of the 271 cores identified by Ginsburg et al. (2018)? Are they starless or do already show signposts of star formation activity such as UCHII regions or outflows?
- Jones et al. (2008) found that the southern part of the envelope of SgrB2 has possible non-thermal emission. Is this non-thermal emission real? What is its physical origin? Can it be related to the high-mass star formation activity in the envelope?
- Is the large scale (∼ 20 pc) envelope of SgrB2 filled with ionized gas? If so, what is the filling factor of ionized gas at large scales? Are the expanding bubbles and arcs revealed by Martín-Pintado et al. (1999) also present all over the envelope?

In order to answer these questions, I started a multi-frequency observational study on SgrB2, covering spatial scales from 0.1″(0.004 pc or 1000 au) up to 20 pc (the size of the envelope). A summary of the observational data used in this thesis is plotted in Fig. 2.1. Among all the data, I led the observation of VLA in C and X bands (4–12 GHz), with configurations A, BnC and D. These datasets cover spatial scales from 0.2″to ∼ 15′and contains

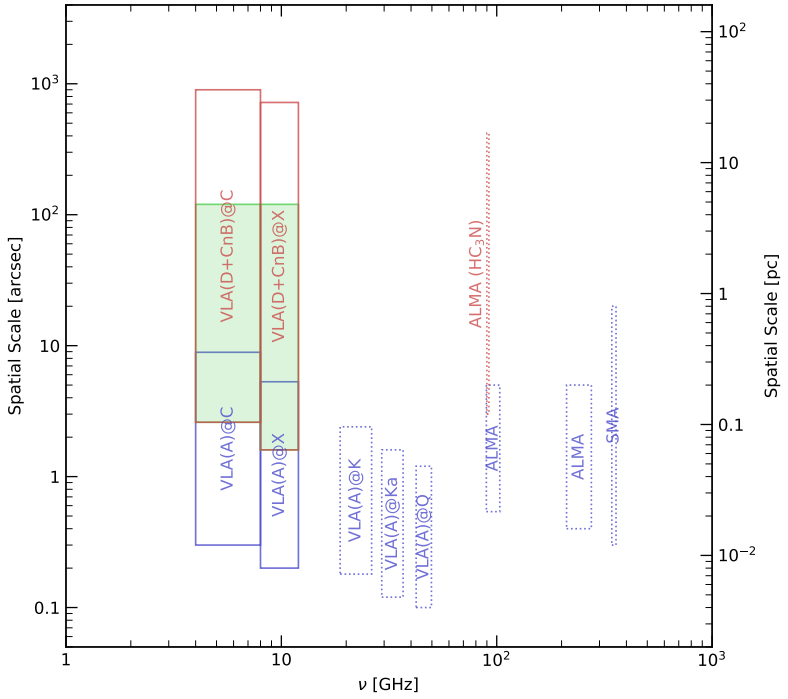

Figure 2.1 Frequency and spatial scales covered by the data used in this thesis. The data used for studying small scales (Chapter 5) are in blue. The data used for studying medium scales (Chapter 6) are marked as green shade. The data used for studying large scales (Chapter 7) are in red. The lower edge of each box marks the resolution. The upper edges stands for largest scale that the data are sensitive to for blue boxes. For red boxes, the upper edges stands for the mapped scale. The upper edge of the green shade corresponds to the tough size of SgrB2(DS). The observations that I led are marked with solid boxes.

continuum and spectral line (RRLs). The high angular resolution observations of VLA in K, Ka, and Q bands (PI. Adam Ginsburg) with configuration A, which I participated, gives me the continuum data that has resolution of $\sim 0.1''$and covers $20 - 50$ GHz. Additionally, the high angular resolution (resolution$\lesssim 0.5''$) data from ALMA (see Sánchez-Monge et al., 2017) and SMA (see Qin et al., 2011) at mm wavelengths are also used, with frequencies ranging from 100 to 300 GHz. Molecular line (HC_3N (10–9)) data, observed with ALMA (PI. Adam Ginsburg) is also used.

The thesis consists four parts. Along with this introduction part, the remaining parts are:

Part II I describe the data reduction processes, including a brief introduction to interferometers (Chapter 3), and the techniques to process the interferometric data (Chapter 4).

Part III I present my multi-scale study on SgrB2, divided in three scale ranges::

Small Scale: With high angular resolution data (resolution as good as 4×10^{-2} pc, marked in blue in Figure 2.1), I study the physical properties of 308 dense cores distributed throughout the entire SgrB2 (Chapter 5)

Medium Scale: I focus on an $\sim 2'$region called SgrB2(DS). With the VLA data (marked as green shade in Figure 2.1), I study the non-thermal emission from SgrB2(DS) (Chapter 6).

Large Scale: With the VLA data, both of continuum and RRL, together with the ALMA data of HC_3N line (marked in red in Figure 2.1), I study the large scale (up to the whole cloud, $20'$) properties of SgrB2 (Chapter 7).

Part IV I summarize the main findings of this thesis and discuss possible future paths to continue exploring and understanding the high-mass star-forming complex SgrB2.

Part II

Data Reduction

Chapter 3

Interferometers

In this part, I discuss the main observing technique that was used in this research: radio interferometry. In the current chapter, I briefly review the theory of interferometry, based on references by Condon & Ransom (2016); Wilson et al. (2009), and then I introduce the Very Large Array (VLA) as an example of interferometer.

3.1 A brief introduction to interferometry

3.1.1 Comparison between interferometers and single-dish telescopes

Before introducing the interferometers, I consider the field pattern (distribution of the response to a signal) of a single dish antenna. If an electric field $g(u, v)$ illuminates a two-dimensional aperture, the response, or the electric field pattern of the aperture, $f(l, m)$, is the Fourier transform of $g(u, v)$:

$$f(l,m) \propto \int_{-\infty}^{\infty}\int_{-\infty}^{\infty} g(u,v)e^{-i2\pi(lu+mv)}du\ dv. \tag{3.1}$$

Where $u = x/\lambda$ and $v = y/\lambda$, and λ is the wavelength of the signal. Coordinates on the aperture are (x, y), while the angular coordinates of the field pattern are (l, m).

Compared to interferometers, some of the limitations of single dish antennas are as follows:

- The resolution, i.e. the beam size, is limited by the diffraction limit of the interaction between electromagnetic wave and an aperture. For a single dish, the two-dimensional integration in Eq. 3.1 is zero outside of the effective area of the dish. Thus, $f(l, m)$ is the Fourier transform of a $g(u, v)$ which is only finite within an area of $\pi D^2/4$, assuming a round dish with a diameter of D. Then the resolution is $\sim \lambda/D$, where λ is the wavelength. For a single dish, D is constrained by engineering obstacles. For example, due to gravity, the geometry of the dish will deviates dramatically from parabolic at some position angle when D is too large. In contrast, the interferometers can have a $g(u, v)$ distributed in a much larger area than $\pi D^2/4$, where D is the diameter of the individual antenna of the interferometric array. In other words, the size of a single antenna is decoupled from the (u, v) coordinates, which means that the resolution can be improved without the necessity of building gigantic antennas.

- For a single dish, the sensitivity is $\sigma \propto A_e^{-1}$, where A_e is the effective collecting area. On the other hand, for an interferometer with N antennas, the sensitivity is $\sigma \propto [N(N-1)]^{-1/2} A_e^{-1}$, where A_e is the effective collecting area of each individual antenna in the array. Apparently, for an interferometer with $N \gg 2$, the sensitivity is better than the single dish telescope with a similar dish size by a factor of $\sim N$.

- The pointing accuracy of a single dish is limited by mechanical and environmental factors. For example, deformation of the dish under gravity or due to heat, wind, and intrinsic mechanical flaws can all affect the pointing accuracy of the single dish telescope. However, pointing accuracy is usually required to be as good as approximately 10% of the beam size. In contrast, the pointing accuracy of interferometers does not depend strongly on the pointing accuracy of the single dish, but mainly on atmospheric factors. Although the correction of the atmospheric factors needs calibration, but most of the efforts and time is after the observation, which saves time of the telescope and also has a higher "ceiling" of the achievable pointing accuracy.

- Besides single point observations, mapping is usually used, like in this research. For a single dish telescope, even if it is equipped with multi-beam receiver, continuous mechanical movement of the dish is still needed to scan over an area in the sky for most of the cases. However, the dishes of an interferometer do not need such a mechanical movements. Considering that the Earth is rotating and the observing is not instantaneous, the dishes in interferometer still need to move to track the source, but such movements is usually much slower than the scanning movements of the single dishes and therefore is usually not the bottleneck of the observing efficiency. Of course, if the desired mapping area is larger than the beam size of a single antenna in an interferometer, moving of the telescopes are also needed.

- The fluctuations of the receiver gain, which appear as direct current components, and the large scale emission on the sky, can be filtered out automatically by the interferometer. The later aspect is not necessarily an advantage of the interferometer compared to single dish telescopes, but it is helpful for the observations that focus on a small-scale structures, like parts of this research.

The comparison between interferometer and single dish is of course not a one-sided game. Single dishes are more efficient in observations of time variable sources (e.g. pulsars) and large scale structures. In this thesis, I focus on the time-independent properties of the star forming complex SgrB2 and I am at studying detailed structures in the region. Thus, interferometers, which can provide a much better resolution in the details, are adopted.

3.1.2 Interferometry

Consider a simple interferometer of two antennas, 1 and 2, separated by a vector $\vec{b}$, as illustrated in Fig. 3.1. Here $\vec{b}$ and sometimes $|\vec{b}|$ is called as "baseline". The signal received by the two antennas comes from a distant point source in the direction $\hat{s}$ with an electromagnetic wave defined by an amplitude V and a frequency ω. The light-travel delay between the two telescopes is $|\vec{b}| \cos\theta$, which causes a time delay τ_g between telescopes 1 and 2, that can be written as $\tau_g = |\vec{b}| \cos\theta / c$.

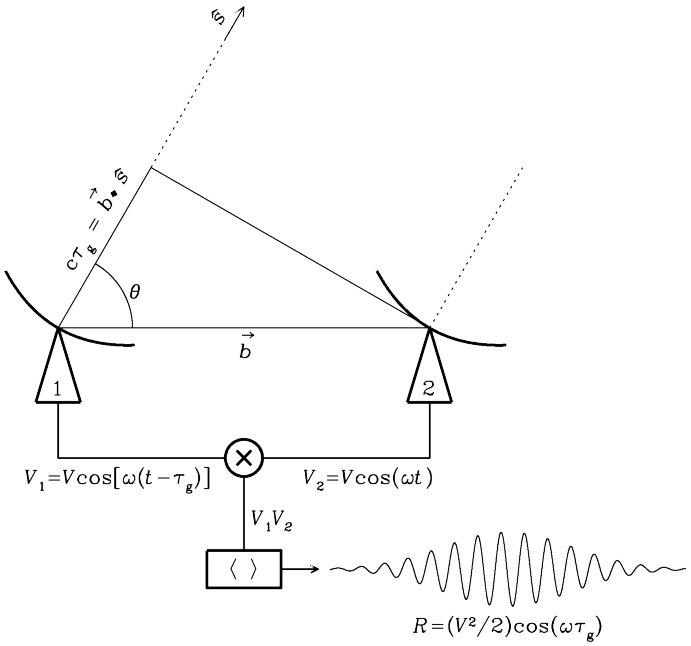

Figure 3.1 Diagram of two-element interferometry (credit: Condon & Ransom, 2016). Signal from a distant point source is on direction $\hat{s}$ with electric amplitude of V and frequency of ω. Baseline is $\vec{b}$. Light-travel delay between the two telescopes is $|\vec{b}|\cos\theta$, which causes a phase difference between telescope 1 and 2, $\tau_g = |\vec{b}|\cos\theta/c$. After the multiplying of the two-way signals ($\otimes$) and time averaging ($\langle\ \rangle$), the response of the system is a fringe $R = (V^2/2)\cos(\omega\tau_g)$.

The two signals received by the antennas 1 and 2 can be described by $V_1 = V\cos[\omega(t-\tau_g)]$ and $V_2 = V\cos(\omega t)$, respectively. These two signals go through a correlator, which go a multiplies (combines) and applies a time average of these two signals. The multiplication V_1V_2 results in two sinusoidal components: $\cos(2\omega t - \omega\tau_g)$ and $\cos(\omega\tau_g)$. Time averaging eliminates the first cosine, which is time-dependent. Thus, the response of this two-element interferometer is:

$$R = \left(\frac{V^2}{2}\right)\cos(\omega\tau_g). \tag{3.2}$$

The amplitude is proportional to V^2, which is proportional to the flux density of the point source, S. The point source can move relative to the interferometer, e.g. due to the rotation of the Earth, i.e. θ (see Figure 3.2) is not a constant but a variable. In this situation, R can be considered a function of θ. The "fringes" of $R(\theta)$ are shown in Fig. 3.2, for two-, three- and four-element interferometers, respectively. One can notice that the fringes are not simply sinusoidal functions but multiplied by a power pattern, which is the power patter of the individual antenna, named as *primary beam*. The primary beam depends on the single antenna. If all the antennas are identical, then the primary beam is independent from the number and locations of the antennas in an interferometer.

For a N-element interferometer, there are $N(N-1)$ "antenna pairs". The response of each antenna pair forms a fringe. The frequencies of these fringes depend on the projected baseline ($|\vec{b}|\cos(\theta)$) of each antenna pair. For a point source, the overlapping of these $N(N-1)$ responses add up to form a function as depicted in the lowest panel in Fig. 3.2.

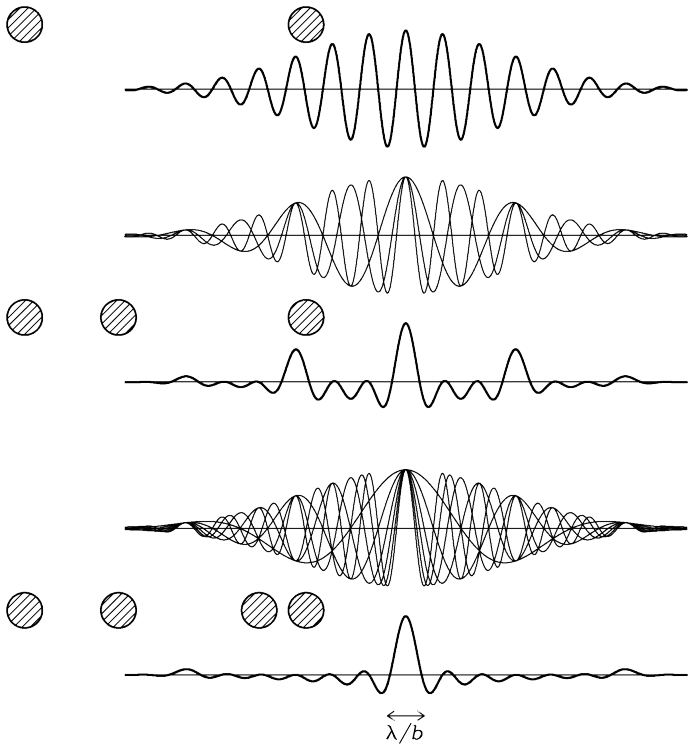

Figure 3.2 Fringes from interferometers with 2, 3, and 4 dishes when observing a point source (credit: Condon & Ransom, 2016). The fringes stands for the function of telescope response R as a function of the position, θ, of the source.

The image of the point source consists of a main peak, with a width of $\sim \lambda/|\vec{b}|$, and several small waves spread all over the primary beam. The main peak is called *synthesized beam*, depends only on the projected baseline and the wavelength, and is independent from the properties of the individual antennas. Due to the existence of the small waves, such an images is called *dirty image*. It is possible to minimize the dirtiness (small waves) in the image by increasing the number of antennas N, as shown in Fig. 3.2. Another method uses the motion of the observing site relative to the source, which is usually due to the rotation of the Earth.

Besides the response expressed in Eq. 3.2 that is in the form of cosine function, R can be in sine form when a delay is added to one of the telescopes in the "antenna pairs". Then Eq. 3.2 can be extended to the complex domain with the combination of the cosine and sine parts. If the source is not a point source but has a finite spatial extension defined by the function $I_\nu(l, m)$, the response of the telescope is a complex *visibility*:

$$V(u, v) = \iint \frac{I_\nu(l, m)}{\sqrt{1 - l^2 - m^2}} e^{-i2\pi(ul+vm)} \, dl \, dm, \tag{3.3}$$

where (l, m) are the coordinates on the sky and (u, v) are the components of the baseline vector. The geometric relationship of the coordinates (l, m) and (u, v) is illustrated in Fig. 3.3. Here we ignore the coordinate w by assuming $w = 0$.

The visibility $V(u, v)$ is the raw data recorded by an interferometer. This is a complex and discrete measurement. The discreteness of the visibility is due to the fact that the antennas cannot cover the entire uv plane continuously. In another word, the interferome-

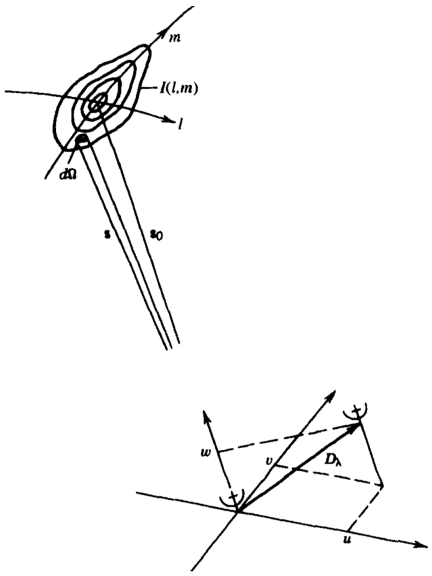

Figure 3.3 Geometric relationship of (l, m) and (u, v, w). (l, m) are the coordinates on the sky and (u, v) are the components of the baseline vector D_λ. (credit: Thompson et al., 2017, editted.).

ter observation is a sampling of the Fourier transformation of $I_\nu(l, m)$ with discrete (u, v) points. According to Fourier transform, it is obvious that the smallest scale that an interferometer is sensitive to is determined by its longest baseline, while the largest scale that an interferometer is sensitive to is determined by its shortest baseline.

Finally, $I(l, m)$ can be chromatic, which means that the receivers of interferometers can observe a broad frequency range, and in practical terms, spectral lines. The primary beam, which is also called *pointing*, is limited in size. So for large objects extending more than the size of a pointing, the *mosaic* mode can be used.

3.2 VLA: an example of interferometer

The Very Large Array (VLA) is an interferometer working in the meter-centimeter wavelength regime, or in frequencies, from 0.058 GHz (4 m) to 50 GHz (7 mm). The VLA consists of 27 antennas, each has a diameter of 25 m, and it has four configurations, i.e. the position pattern of the 27 dishes can change from the most extended configuration (called A array), to the most compact (called D array). The VLA is the main telescope used in this thesis, and it is the most powerful interferometer in this frequency regime (till 2020). Thus, we use VLA as a representative example of interferometers in this section.

The spatial distribution (configuration) of antennas of the VLA is in a "Y" shape. An example of the configuration "BnC" (a mixture of the configurations B and C) is illustrated in Fig. 3.4. In Fig. 3.5, I plot the *uv* coverage of this configuration at certain frequency ranges of the C and X bands. As a comparison, the *uv* coverage of D- and A- configurations are also plotted as colored blocks.

In order to cover a large portion of the sky, one needs multiple pointings in a mode that is called "mosaic". Two examples of mosaics are shown in Figure 3.6. In this thesis, mosaic

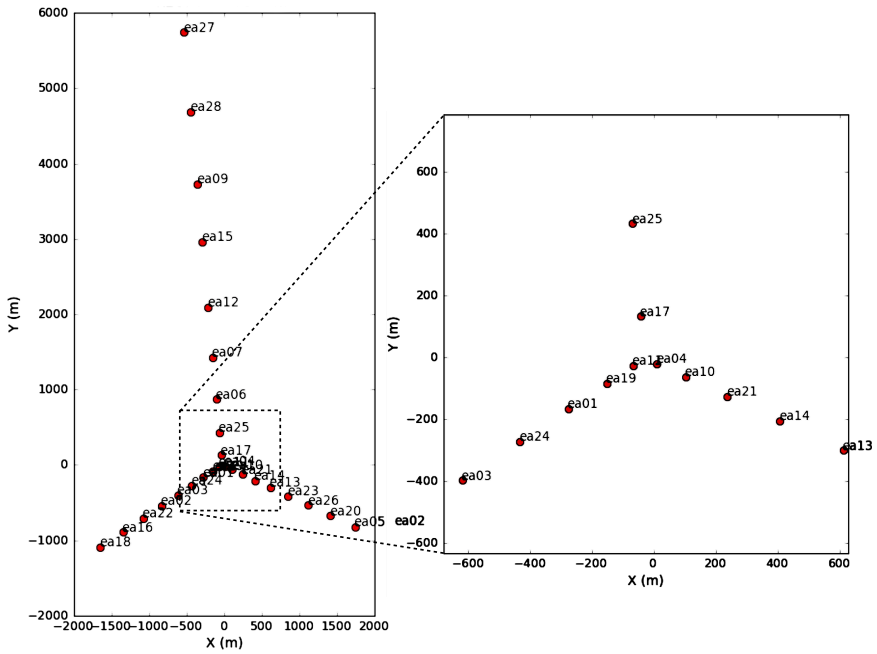

Figure 3.4 Distribution of antennas of VLA in BnC configuration, which is recorded in the measurement set of project 16a-195. A zoomed-in of the central part is plotted.

mode is used to cover the entire $20' \times 20'$region of SgrB2. Due to that the primary beam size is affected by frequency, the pointing size is different between C and X band, which are $7.5'$and $4.5'$, respectively. Therefore I used two different mosaic setups for them. For details, see Fig. 3.6.

Table 3.1 Spectral windows of VLA projects

Band	SpwID[a]	Line[b]	#Chans[c]	Ch0[d]	ChanWid[e]	TotBW[f]	CtrFreq[g]
				MHz	kHz	MHz	MHz
C	0	–	64	4832.000	2000.000	128.0	4895.0000
C	1	–	64	4960.000	2000.000	128.0	5023.0000
C	2	Cont.	128	4006.000	1000.000	128.0	4069.5000
C	3	Cont.	128	4134.000	1000.000	128.0	4197.5000
C	4	Cont.	128	4262.000	1000.000	128.0	4325.5000
C	5	Cont.	128	4390.000	1000.000	128.0	4453.5000
C	6	Cont.	128	4518.000	1000.000	128.0	4581.5000
C	7	Cont.	128	4646.000	1000.000	128.0	4709.5000
C	8	Cont.	128	4774.000	1000.000	128.0	4837.5000
C	9	Cont.	128	4902.000	1000.000	128.0	4965.5000
C	10	Cont.	128	5030.000	1000.000	128.0	5093.5000
C	11	Cont.	128	5158.000	1000.000	128.0	5221.5000
C	12	Cont.	128	5286.000	1000.000	128.0	5349.5000
C	13	Cont.	128	5414.000	1000.000	128.0	5477.5000
C	14	Cont.	128	5542.000	1000.000	128.0	5605.5000
C	15	Cont.	128	5670.000	1000.000	128.0	5733.5000
C	16	Cont.	128	5798.000	1000.000	128.0	5861.5000

Table 3.1 Spectral windows of VLA projects (*continued*)

Band	SpwID[a]	Line[b]	#Chans[c]	Ch0[d]	ChanWid[e]	TotBW[f]	CtrFreq[g]
				MHz	kHz	MHz	MHz
C	17	Cont.	128	5926.000	1000.000	128.0	5989.5000
C	18	Cont.	128	5946.000	1000.000	128.0	6009.5000
C	19	Cont.	128	6074.000	1000.000	128.0	6137.5000
C	20	Cont.	128	6202.000	1000.000	128.0	6265.5000
C	21	Cont.	128	6330.000	1000.000	128.0	6393.5000
C	22	Cont.	128	6458.000	1000.000	128.0	6521.5000
C	23	Cont.	128	6586.000	1000.000	128.0	6649.5000
C	24	Cont.	128	6714.000	1000.000	128.0	6777.5000
C	25	Cont.	128	6842.000	1000.000	128.0	6905.5000
C	26	Cont.	128	6970.000	1000.000	128.0	7033.5000
C	27	Cont.	128	7098.000	1000.000	128.0	7161.5000
C	28	Cont.	128	7226.000	1000.000	128.0	7289.5000
C	29	Cont.	128	7354.000	1000.000	128.0	7417.5000
C	30	Cont.	128	7482.000	1000.000	128.0	7545.5000
C	31	Cont.	128	7610.000	1000.000	128.0	7673.5000
C	32	Cont.	128	7738.000	1000.000	128.0	7801.5000
C	33	Cont.	128	7866.000	1000.000	128.0	7929.5000
C	34	H115α	256	4264.735	31.250	8.0	4268.7192
C	35	H114α	256	4376.000	31.250	8.0	4379.9844
C	36	H113α	256	4494.405	31.250	8.0	4498.3889
C	37	H112α	256	4615.431	31.250	8.0	4619.4156
C	38	OH	512	4748.137	7.812	4.0	4750.1329
C	39	H_2CO	512	4825.128	15.625	8.0	4829.1203
C	40	H_2CO	512	4950.214	15.625	8.0	4954.2065
C	41	CH_3OH	512	5002.770	7.812	4.0	5004.7656
C	42	OH	1024	6030.429	7.812	8.0	6034.4248
C	43	H100α	256	6475.661	31.250	8.0	6479.6457
C	44	CH_3OH	1024	6664.000	7.812	8.0	6667.9961
C	45	H99α	256	6673.005	31.250	8.0	6676.9889
C	46	H98α	256	6878.447	31.250	8.0	6882.4313
C	47	H97α	256	7090.000	31.250	8.0	7093.9844
X	0	–	64	8332.000	2000.000	128.0	8395.0000
X	1	–	64	8460.000	2000.000	128.0	8523.0000
X	2	Cont.	128	8006.000	1000.000	128.0	8069.5000
X	3	Cont.	128	8134.000	1000.000	128.0	8197.5000
X	4	Cont.	128	8262.000	1000.000	128.0	8325.5000
X	5	Cont.	128	8390.000	1000.000	128.0	8453.5000
X	6	Cont.	128	8518.000	1000.000	128.0	8581.5000
X	7	Cont.	128	8646.000	1000.000	128.0	8709.5000
X	8	Cont.	128	8774.000	1000.000	128.0	8837.5000
X	9	Cont.	128	8902.000	1000.000	128.0	8965.5000
X	10	Cont.	128	9030.000	1000.000	128.0	9093.5000
X	11	Cont.	128	9158.000	1000.000	128.0	9221.5000
X	12	Cont.	128	9286.000	1000.000	128.0	9349.5000
X	13	Cont.	128	9414.000	1000.000	128.0	9477.5000
X	14	Cont.	128	9542.000	1000.000	128.0	9605.5000

Table 3.1 Spectral windows of VLA projects (*continued*)

Band	SpwID[a]	Line[b]	#Chans[c]	Ch0[d]	ChanWid[e]	TotBW[f]	CtrFreq[g]
				MHz	kHz	MHz	MHz
X	15	Cont.	128	9670.000	1000.000	128.0	9733.5000
X	16	Cont.	128	9798.000	1000.000	128.0	9861.5000
X	17	Cont.	128	9926.000	1000.000	128.0	9989.5000
X	18	Cont.	128	9946.000	1000.000	128.0	10009.5000
X	19	Cont.	128	10074.000	1000.000	128.0	10137.5000
X	20	Cont.	128	10202.000	1000.000	128.0	10265.5000
X	21	Cont.	128	10330.000	1000.000	128.0	10393.5000
X	22	Cont.	128	10458.000	1000.000	128.0	10521.5000
X	23	Cont.	128	10586.000	1000.000	128.0	10649.5000
X	24	Cont.	128	10714.000	1000.000	128.0	10777.5000
X	25	Cont.	128	10842.000	1000.000	128.0	10905.5000
X	26	Cont.	128	10970.000	1000.000	128.0	11033.5000
X	27	Cont.	128	11098.000	1000.000	128.0	11161.5000
X	28	Cont.	128	11226.000	1000.000	128.0	11289.5000
X	29	Cont.	128	11354.000	1000.000	128.0	11417.5000
X	30	Cont.	128	11482.000	1000.000	128.0	11545.5000
X	31	Cont.	128	11610.000	1000.000	128.0	11673.5000
X	32	Cont.	128	11738.000	1000.000	128.0	11801.5000
X	33	Cont.	128	11866.000	1000.000	128.0	11929.5000
X	34	H92α	512	8302.539	31.250	16.0	8310.5235
X	35	H91α	512	8578.014	31.250	16.0	8585.9981
X	36	H90α	512	8865.807	31.250	16.0	8873.7914
X	37	HC_3N	1536	9089.113	10.417	16.0	9097.1074
X	38	H89α	512	9166.599	31.250	16.0	9174.5833
X	39	H88α	256	9480.709	62.500	16.0	9488.6780
X	40	H87α	256	9810.228	62.500	16.0	9818.1967
X	41	H86α	256	10154.715	62.500	16.0	10162.6838
X	42	HDO	1024	10269.113	15.625	16.0	10277.1051
X	43	H85α	256	10515.505	62.500	16.0	10523.4740
X	44	H84α	256	10893.579	62.500	16.0	10901.5473
X	45	H83α	256	11289.980	62.500	16.0	11297.9486

[a] ID of spectral windows, can be used in CASA to select `spw`.
[b] The spectral line that this spectral window is assigned to include. Continuum is abbreviated as 'Cont.', which stands for the spectral window assigned for continuum observations.
[c] Number of channels in this spectral window.
[d] Frequency of the starting channel of this spectral window.
[e] Width of the channels in this spectral window.
[f] Total bandwidth (in frequency) of this spectral window.
[g] Frequency of the central channel of this spectral window.

Regarding the frequency coverage and the spectral setup, the VLA can do both continuum and spectral line observations, with or without polarization. Here I take the observational projects of this thesis as an example. The observation in X band, from 8 to 12 GHz, consists of 32 continuum spectral windows. In Table 3.1, the setup of the spectral windows

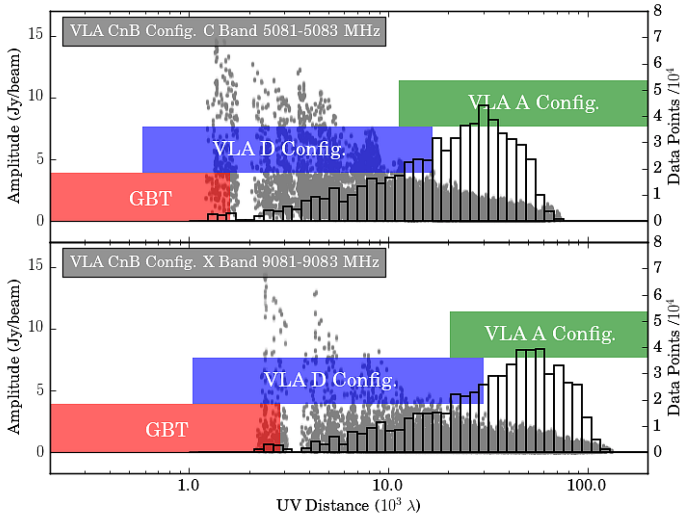

Figure 3.5 Histogram of *uv* coverage of VLA. The scatters are the amplitude-*uv* distribution of BnC configuration, while the histogram is the sampling frequency at different *uv* distance. The colored blocks are the *uv* coverage of GBT, VLA D- and A- configuration.

used in our VLA projects is listed. The three projects share the same setup. The spectral setup includes spectral windows for both continuum and spectral line observations. The polarization setup includes RR and LL mode only, without RL or LR mode. Conventionally, spectral line observations require narrower channel widths, which is equivalent to higher spectral resolution. In our setup, spectral windows like `spw44` in C band have channel width as narrow as 7.812 KHz. Considering that the central frequency of `spw44` in C band is 6.7 GHz, such a channel width results in a velocity resolution of ~ 0.1 km s^{-1}, which is sufficient to resolve the targeted spectral line of the 6.7 GHz CH_3OH maser transition. Regarding the observations of the data used in this thesis, see Section 5.1, 6.1, and for more details.

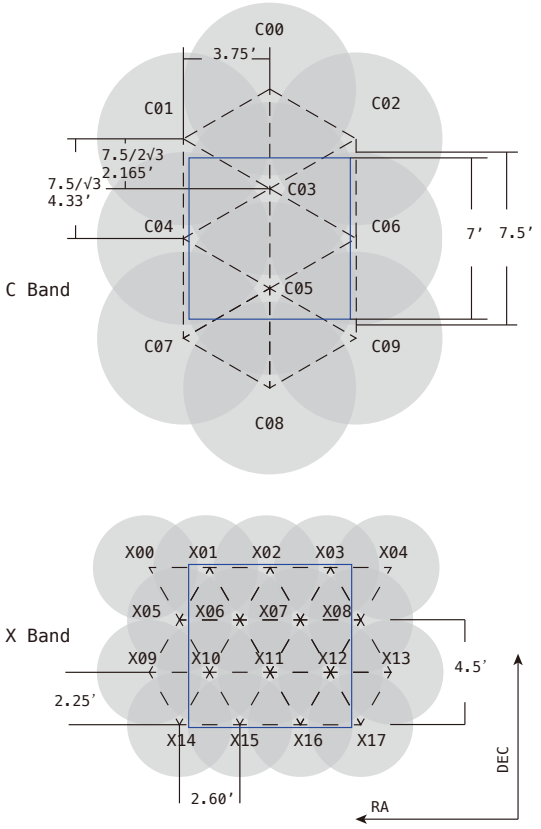

Figure 3.6 Mosaic pattern used in this study, for C and X band respectively. Pointings' name are marked. The mosaic pattern is according to the recommendation of the VLA proposal guide. Central square is the $7' \times 7'$ area that covers the center of SgrB2.

Chapter 4

Calibration, Imaging and Self-calibration

In this chapter, I explain the processing of the data used in this thesis. The data in this chapter were obtained in the VLA projects 16A-095, 16B-031, and 17B-063. This chapter is partially based on the CASA guides[1]. The software used for data processing is CASA (McMullin et al., 2007), version 4.5, 4.7, and 5.1.

The focus of this chapter is that how to recover $I_\nu(l, m)$ from $V(u, v)$, where $I_\nu(l, m)$ and $V(u, v)$ are the Fourier transform of each other, see Eq. 3.3. The three major stages are calibration (Sect. 4.1), imaging (Sect. 4.2), and self-calibration (Sect. 4.3). Alongside with the continuum data processing, stacking of RRLs are also introduced in this chapter (Sect. 4.4).

4.1 Calibration

In reality, interferometers cannot measure $V(u, v, f)$ in Eq. 3.3 perfectly[2], but is only capable to measure a $V'(u, v, f)$ instead. Following the CASA guides, I call V' the *observed visibility* while V the *true visibility*. Since during the observations, not only our target (SgrB2 in this study), but also calibrators (3C286 and J1820_2528 in this study) are observed. For the calibrators, we know the true visibility and the observed visibility simultaneously. Thus one can derive the relationship between V' and V from the calibrator and then use such a relationship to correct V' of the target to get V of the target.

The measure contributions to the difference between V' and V are from the atmosphere and the instruments, which can be written as (based on the CASA guides):

$$V'_{i,j}(u, v, f) = b_{i,j}[B_i(f, t)B^*_j(f, t)]g_i(t)g_j(t)V_{i,j}(u, v, f)e^{i[\theta_i(t)-\theta_j(t)]}. \tag{4.1}$$

The subscriptions i, j represent two different antennas in an array. A pair of antennas determines one data point, V or V'. The only factor that depends on both of the antennas is the *baseline term* $b_{i,j}$, which is caused by the position shift of the antenna relative to where it should be. Here 'where it should be' can be regarded as the positions of antennas that can

[1] `https://casaguides.nrao.edu`

[2] Eq. 3.3 is for the monochromatic emission. Here one more parameter, frequency (f), is added in V since I consider a multi-frequency observation here.

form the baseline with which the calibrators were observed as 'models' (not the observations of the calibrators in this study, but usually done by the observatories). In principle, since V and V' depend on three parameters, (u, v, f). Thus, usually, the factors should also have these three parameters. However, the frequency dependent part of the factors is separated to form the *compleX bandpass*, $B_i(f, t)$. The compleX bandpass depends on individual antennas. To correct it, the bandpass calibrator (3C286 in this study) should have a known SED. Also, one can notice that $B_i(f, t)$ is time-dependent, since the atmosphere and the instruments are time variable. When $B_i(f, t)$ is separated, the left over part of the factors are frequency independent, which is the *complex gain*. The complex gain has two parts, amplitude $g_i(t)$ and phase $\theta_i(t)$. Similar to $B_i(f, t)$, $g_i(t)$ and $\theta_i(t)$ depend on individual antennas and are time-dependent. The necessity of separating the amplitude and phase is partially due to that they need different calibrators. The amplitude calibrator (3C286 in this study, the same one as the bandpass calibrator) should be bright and has well defined flux at the observational frequency. The phase calibrator (J1820_2528 in this study) should be close enough to the target (SgrB2), due to that the atmosphere's contribution to the complex gain is not isotropic and rapidly variable. Thus shorter angular distance from the calibrator to the target, as well as a shorter time interval between the observation of the calibrator and the target, mean that the atmosphere conditions of obtaining the V' of the calibrator and the target is more similar, which will result in a better calibration.

The process of calibration is to compare the $V'_{i,j}(u, v, f)$ of the calibrators with the corresponding models to derive the so-called *calibration table* of the factors described in the last paragraph. A calibration table can be regarded as a set of solutions of each factor. Since the factors are mutually connected to each other, iterations are needed in the actual calibration processes. The calibration tables in last iteration is taken into account in the next iteration to improve the accuracy of the calibration tables of other factors. A flow chart showing the calibration processes is shown in Fig. 4.1.

4.2 Imaging

As discussed in Sect. 3.1, the nearest distance between two telescopes in an array are usually larger than the diameter of the telescope, which means that the *uv* sampling cannot cover the vicinity around the zero point. Zero *uv*-distance corresponds to the large scale signal which determines the absolute total flux of the image. In principle, the sum of the visibility taken from most of the interferometers is 0. By imaging, one can try to fit the visibility to recover the actual flux. Similar to the vicinity around the zero *uv*-distance, the space between the discrete *uv* sampling points can be filled by imaging as well.

Two widely-adopted algorithms for imaging are Maximum Entropy Method (MEM) and CLEAN (Högbom, 1974). In this study CLEAN is used. Therefore in this section I explain the imaging processes with CLEAN as an example. The software used here is CASA (version 4.5, 4.7.2 and 5.4). Two major functions of CLEAN in CASA are `clean` and `tclean`. In this section, I will focus on the effects of parameters in these functions instead of giving an detailed instruction on the technical details of `clean` and `tclean`. Due to that CLEAN is widely used for imaging, the imaging process is be also called 'clean' or 'cleaning' in this thesis. In this chapter, the capitalized term, e.g. CLEAN mean the algorithm, while the terms in mono-space fonts, e.g. `tclean`, means a implementation of an algorithm, or a

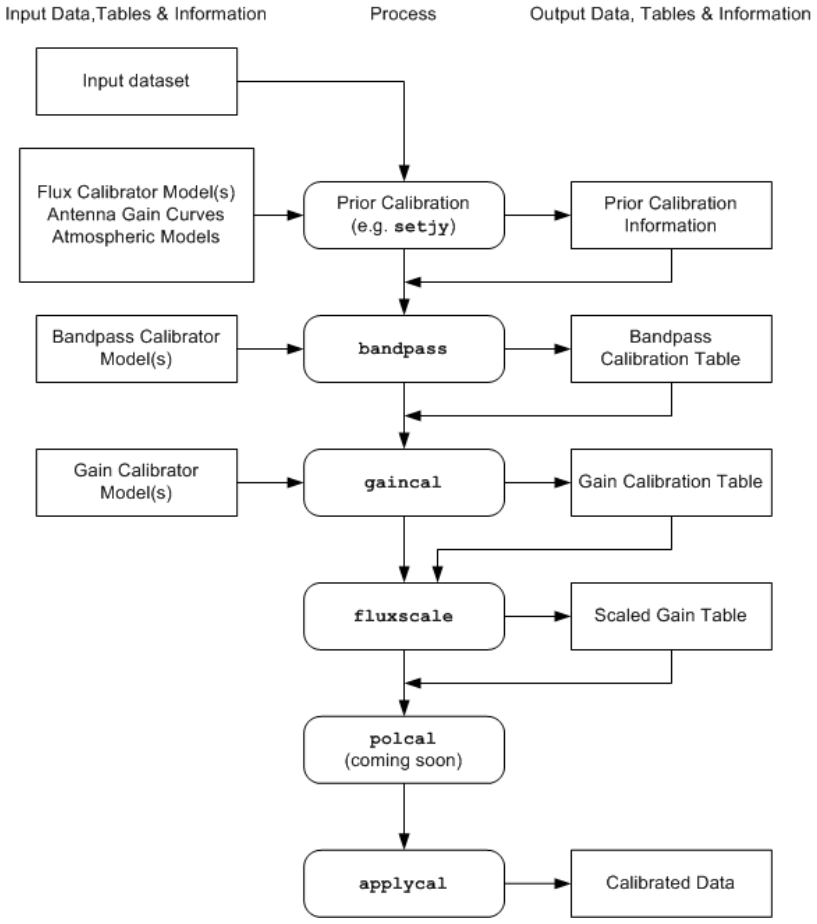

Figure 4.1 The calibration flow chart. Credit: `https://casa.nrao.edu/casadocs/`

function in a certain software package. Also any part of a piece of code in CASA are in mono-space fonts, e.g. `niter`.

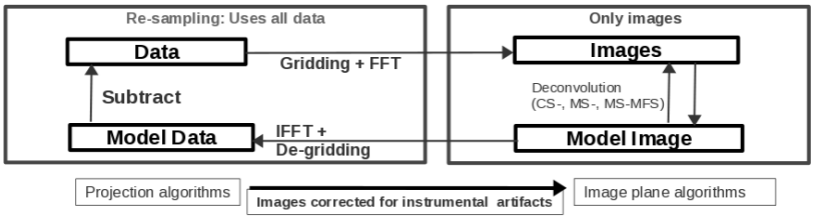

Figure 4.2 The chart of the CLEAN algorithm. Credit: `https://casaguides.nrao.edu/`

The algorithm CLEAN treat the sky as an ensemble of point sources, or δ functions. The Fourier transform of a δ function is a uniform function $V(u, v) \equiv V_0$. If such a uniform V is sampled by the interferometer, the resulting function will be the spatial distribution of the telescopes. For VLA, $V(u_i, v_i)$ will be 28 points distributed in a 'Y' shape at a certain time. Considering the rotation of the Earth, during a finite period of time, the $V(u_i, v_i)$ will be like the trajectory of the rotation of such 28 points. During the deconvolution, $V(u_i, v_i)$ will be reversely Fourier transformed and become the *point spread function*, or PSF. Thus

the gaps between the sampling points, or the gaps between the antennas on the ground, result in that each of the point on the image, which is generated by Fourier transform of the visibility, is convolved with such a PSF. The CLEAN algorithm, apart from doing a reverse Fourier transformation to get an image from the visibility, tries to remove the PSF components that is convolved with the real signal. As shown in Fig. 4.2, a CLEAN algorithm consists five steps:

1. Griding the visibility data into 2-D or 3-D array. Weights are given to different *uv* distances. Then perform an FFT (Fast Fourier Transform), to get a *dirty image*. The dirty image can be regarded as a convolution of the real image that we aim to get with the PSF. The pixel size and number of pixels of the dirty image are determined by the griding process of the visibility, since FFT performs between two arrays with the same shape.

2. Perform correlation of the PSF and the dirty image from step 1 to find the brightest point and then subtract the convolution of the point with PSF from the image[3]. Also, add the point to an image called 'model image'. This step can be repeatedly executed. Each loop of this step is called a *minor circle*.

3. Perform an FFT on the model image, and de-grid the FFT result to match the original visibility. The model is regarded as the 'real' signal here. This step is to tell how much portion of each $V'(u_i, v_i)$ is real, marked as $M(u_i, v_i)$.

4. Subtracting the model visibility from the original visibility, to get a new visibility, which is called the *residual image*. Then repeat the steps above. The loop of steps 1–4 is called *major circle*.

5. Finally, due to some stop criteria, usually the number of iterations or the noise level, the major circle stops. The model image is convolved with a beam, which can be set or fitted from the PSF, and then added to the residual image, to get the final *cleaned image*.

The steps above is called the *Cotton-Schwab* cleaning algorithm and can be selected in CASA function `clean` by setting `imagermode='csclean'`. The five steps above only depicts a simplified picture of how CLEAN algorithm works in general. However, in actual imaging processes, complications are involved. In the following subsections, I will talk about the functions of several selected parameters of `clean` with examples from the data processing of the VLA data used in this research. By dosing this, apart from explaining the details of CLEAN algorithm and the `clean` function of CASA, I also show the technical background of the data that I use in Part III.

4.2.1 Number of iterations and loop gain

In the CLEAN algorithm, number of iterations is one of the major factors that determines the 'depth' of the imaging. Here 'depth' is a qualitative description of much of the PSF contribution, which is also called 'artifacts', in the image is removed. The less artifacts

[3]Actually, in CASA, not the entire flux but only a portion of the flux of the point was convolved to the PSF and taken to the model image. The portion is determined by the parameter `gain` in CASA

are in the image, the deeper the clean is. The number of iterations can be controlled by setting an upper limit in CASA or setting stopping criteria, e.g. noise level the residual image reaches. In Fig. 4.4, panel (a) and (b), two case with different number of iterations (as `niter` in CASA) are shown. These two plots correspond to the same visibility. In the imaging process, except for `niter`, all the other parameters are the same. It is obvious that the image after 5×10^4 iterations of CLEAN has overall less artifacts and higher dynamic range than the one after 10^4 iterations.

Although that usually more iterations result in higher image quality. If CLEAN runs too deep, e.g. too many number of iterations are conducted, artifacts will be taken into the model image in minor circles, which is called *over-clean*. This usually happens when imaging data with high dynamic range. For the bright spots, the resulting PSF has positive and negative parts. The absolute value of those negative parts can be significantly higher than the rest part of the image. Then the subtraction of the PSF of the bright spot from the residual image can introduce artificial positive spots into it which are the brightest parts in the next major circle. These brightest parts will taken into model image and call additional artifacts. In Fig. 4.4, panel (c) and (d), two case are shown. When cleaned with 5×10^4 iterations, the over-clean effect does not appear or is not obvious. However, if the clean go deeper to 10^5 iterations, while other parameters are kept unchanged, over-clean occurs and more artifacts are included in the image.

Loop gain is also a factor that affects the quality of imaging. The factor `gain` in CASA controls the portion of the brightest point that taken from the residual image to the model image. Similar to the effects of number of iterations, larger loop gain makes clean go deeper and therefore improve the image quality, until the over-clean occurs. As shown in Fig. 4.5, panel (a) and (b), when the number of iteration is not too large, increasing the loop gain from 0.1 to 0.5 makes the imaging go deeper and results in image that has higher dynamic range. While for a deeper clean, see Fig. 4.5, panel (c) and (d), increasing loop gain from 0.05 to 0.1 makes the over-clean more severe. One can notice that the four images shown in Fig. 4.5 resemble the images in Fig. 4.4. This is due to the similarity of the effects that `niter` and `gain` have in most of the cases.

4.2.2 Weighting

During CLEAN, one needs to balance between sensitivity and resolution by assigning weighting to different uv distance. When griding the visibility into cells, weighting, denoted as w, is multiplied to the data, then the visibility data are 'put' into the uv-grids. The visibility before this griding process has already a weighting for each data point, which I call it 'the original weighting', denoted as w_0.

The parameter `weighting` of `tclean` controls the weighting scheme in CASA. There are three weighting schemes to select from, *natural*, *uniform*, and *briggs*. The natural weighting keeps the original weighting in the visibility, simply $w = w_0$. Since the inner part of VLA array has a higher density of antennas, more data are accumulated in the uv cells in the short uv distance part. Thus the natural weighting naturally results in a lower resolution. Sensitivity resulted from the natural weighting is the highest among the three weighting schemes. On the contrast, uniform weighting takes the accumulation of visibility data in each uv cell into account. The original weighting of all the visibility data that accumulate in one uv cell are added up, denoted as $w_{\rm cell}$. Then the uniform weighting assigned for each

visibility data point is $w_0/w_{\rm cell}$. Thus, the effect that VLA array has more antenna in the short *uv* distance part is compensated. Uniform weighting gives higher resolution but lower sensitivity. Briggs weighting is between natural and uniform weighting. One parameter for briggs weighting is `robust`. With `robust=-2`, briggs is close to uniform weighting while with `robust=2`, briggs is close to natural weighting. In this study, `robust` between 0 and 0.5 is widely used, which is a trade-off between sensitivity and resolution. In Fig. 4.6, examples of these three weightings are shown. It is worth to notice here that the CLEAN goes to different depth in the three plots in Fig. 4.6 which means that the sensitivities of these three plot should not be compared with each other. These plots are just for showing 1) the difference of resolution among these three weighting schemes, which is also revealed by there beam sizes, and 2) the difference of how the large scale structures are recovered. The image with uniform weighting has highest resolution while loses large scale emission.

4.2.3 *uv* coverage

For certain scientific goals, e.g. investigating SED in this study, one need to select a *uv* range within the entire *uv* coverage of the visibility. The parameter `uvrange` in `tclean` can select a certain *uv* range from the visibility to be used for CLEAN. Fig. 4.7 shows the images cleaned with different `uvrange`. Fig. 4.8 shows the *uv* coverage of the VLA data on SgrB2 used in this study, from configurations D and CnB combined, from 4 to 8 GHz (C band). The whole `uvrange`, in panel (a), use the entire *uv* coverage. While the images in panel (b), (c), and, (d), are cleaned with `uvrange` of 1 kλ–100 kλ, 5 kλ–60 kλ, and 20 kλ–40 kλ, respectively. It is obvious that wider *uv* coverage results in less artifacts. Additionally, the narrow *uv* coverage prevents the image from recovering the flux on certain spatial scales. For example, the flux from SgrB2(DS) is nearly filtered out in panel (d) of Fig. 4.7 while in panel (a) and (b) are better recovered.

4.2.4 Deconvolver

The parameter `deconvolver` determines the minor cycle algorithm in `tclean`. In this section, I introduce `hogbom`, `clark`, `multiscale`, and `mtmfs`. There are more deconvolvers to select, which are beyond the coverage of this thesis.

The modes of PSF are defined by selection between `hogbom` (Högbom, 1974) and `clark` (Clark, 1980). The entire PSF is used in the minor cycle when `hogbom` is selected, while a patch of the PSF is adopted when `clark` is used. As shown in Fig. 4.9, the image cleaned with the `hogbom` mode has lower level of artifacts and therefore has higher dynamic range, while the image cleaned with `clark` PSF mode are more severely affected by artifacts. On the other hand, since the `clark` mode involves less pixels in the correlation algorithm between PSF and the residual image in minor cycles, it accelerates the CLEAN processes, which is crucial when imaging huge datasets.

In the ordinary CLEAN algorithm, the sky is assumed to be an ensemble of point sources, which may not fit well for imaging extend sources. By setting `multiscale` as the deconvolver, `tclean` regards the emission from the targets as an overlap of emission on different scales. For more details about such a multi-scale mode, see Cornwell (2008). When `multiscale` is set as the deconvolver, parameters `scales` and `smallscalebias` can be set. The integers in the `scales` are multiplied by the beam size to be used as the scales in the imaging process.

The parameter `smallscalebias` determines how much weight is given to small scales. If `smallscalebias=1` then large scale is weighted to zero while `smallscalebias`< 0.2 weights all the scales nearly equally (see CASA guides). From my tests on different `scales` and `smallscalebias`, and compared with non-multi-scale mode, the differences of the produced images are nearly negligible, see Fig 4.10.

When imaging visibility of continuum signal which covers a wide frequency range, the SED of the continuum emission needs to be taken into account. Thus I use multi-term multi frequency synthesis (MTMFS) as deconvolver, in which mode, `tclean` average the visibility data with polynomial weightings when they are accumulated into the *uv* grids. The MTMFS mode is implemented by selecting devonvoler as `mtmfs`, and `nterms` can be selected. The parameter `nterms` defines the order of polynomial (`nterms`= order + 1), which can be treated as a Taylor expansion of the real SED at a certain frequency. In this study, we used `nterms=2`, which corresponds to a power-law SED. The zero-order image, which is the flux at the central frequency of the band, is named as `tt0`, while the spectral index is `tt1`. Examples of the `tt0` and `tt1` images are shown in Fig. 4.11. It is worth to notice that the `tt1` image in Fig. 4.11 deviated significantly from the spectral index map shown in Fig. 6.4. In C band, the *uv* coverage, in the unit of wavelength, changes by an order of two from 4 to 8 GHz. Thus the visibilities at different frequencies withing this 4 GHz wide band are actually sensitive to different spatial scales. Therefore here the `tt1` map might not be able to represent the spectral index map.

4.3 Self-calibration

Self-calibration is a method to improve the image quality by using the model of the source to calibrate the complex gains of the interferometer. The calibrators that used during the observations cannot be observed simultaneously with the target (SgrB2 in this study). Thus the during the time interval between the observations on the calibrators and the science targets, the conditions of the atmosphere and the instrument may vary. However, if the target itself is used as calibrator, the calibration is real-time.

Here I show one procedure of self-calibration as an example. Imaging the visibility. CLEAN run shallowly here, with `threshold=20mJy`, i.e. ten times larger than the final RMS I want to archive. The shallowness here ensure that only real signals from the brightest parts of the image, in my case SgrB2(M) and SgrB2(N) are taken into the model image, and avoid the interference of the artifacts. Then the model images are Fourier transformed into a column called *model column* in the measurement set. Generate a phase-calibration table. The table is generated by setting `solint='int'` and `calmod='p'`, which stands for that the solution interval is the integration period, which is 2 s in our observation setup, and only phase are solved. Then apply the phase-calibration table to the image. Such a phase-only self calibration were performed repetitively, each time with a deeper clean. Images before and after self-calibration are plotted in Fig. 4.12. The clean parameters for these two images are the same. We can see that the image after the self calibration apparently has less artifacts.

Although I only introduce the self calibration on phase, similar procedures with amplitude and bandpass can be also applied. Additionally, `solint` does not necessarily set to `int` but a longer time interval.

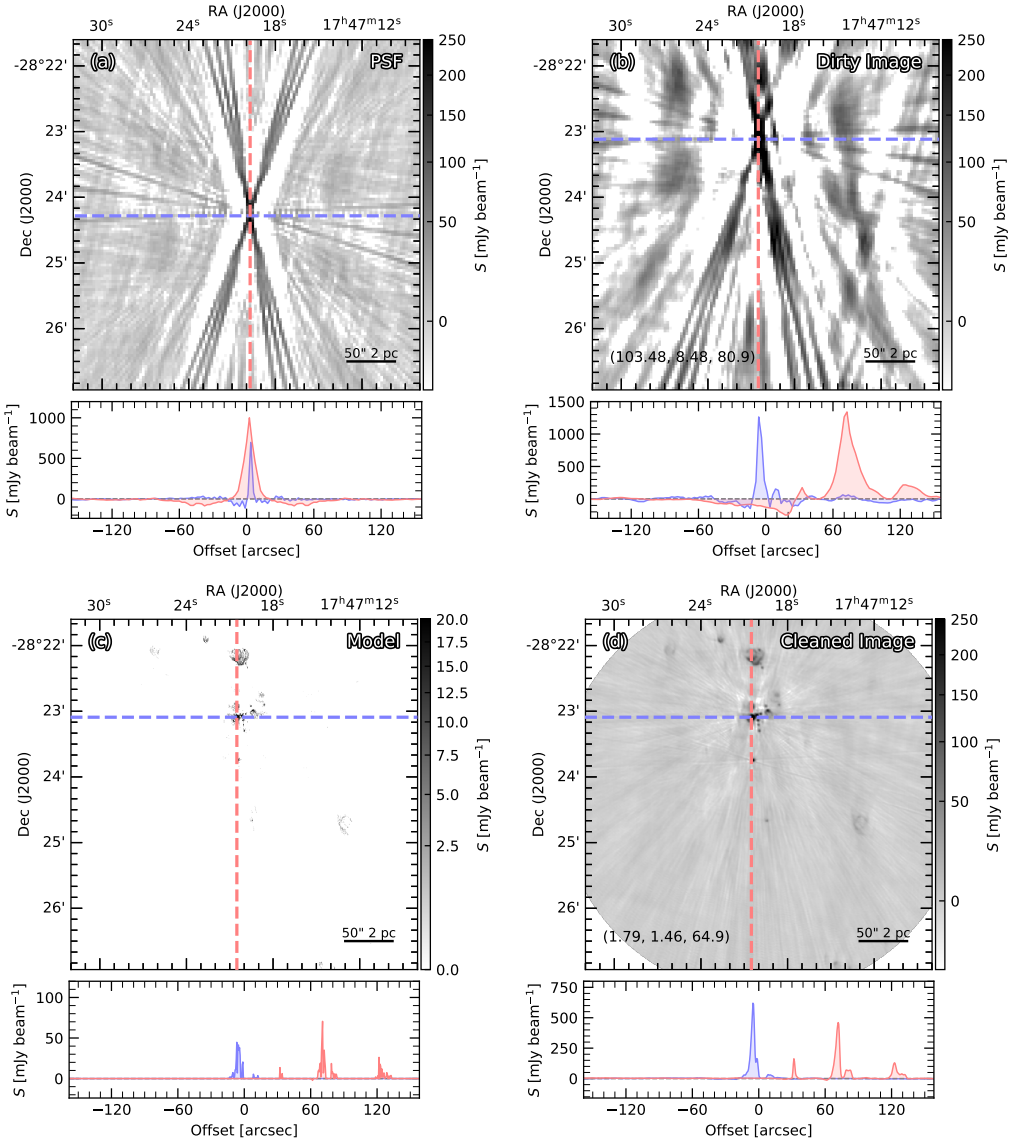

Figure 4.3 Example of the functions and images used in the CLEAN algorithm. *Panel (a):* the PSF. The visibility is the 'X11' pointing of the 16a195 VLA project (X band, CnB configuration). Image size is 128 × 128 pixels and each cell has a size of 2.5″×2.5″. *Panel (b):* The dirty image, which is obtained as a image of a `niter=0` clean process. The griding and cell size are the same as the PSF. *Panel (c):* The model image of the X11, from the same data as in panel (a) and (b). Cleaned with 5718 iterations, with a loop gain of 0.1. *Panel (d):* The resulting cleaned image, produced in the same CLEAN process as panel (c). Each image has two profile cuts. The absolution values in each image should not be directly compared with each other, due to the different physical meaning they have or different beam sizes they have. Panel (b) and (d) have meaningful beam sizes, which are marked on the lower left corner of their images, in the format of. The CASA version used for panel (a) and (b) is `4.5.2-REL (r36115)`, and for panel (c) and (d) is `5.1.1-5`.

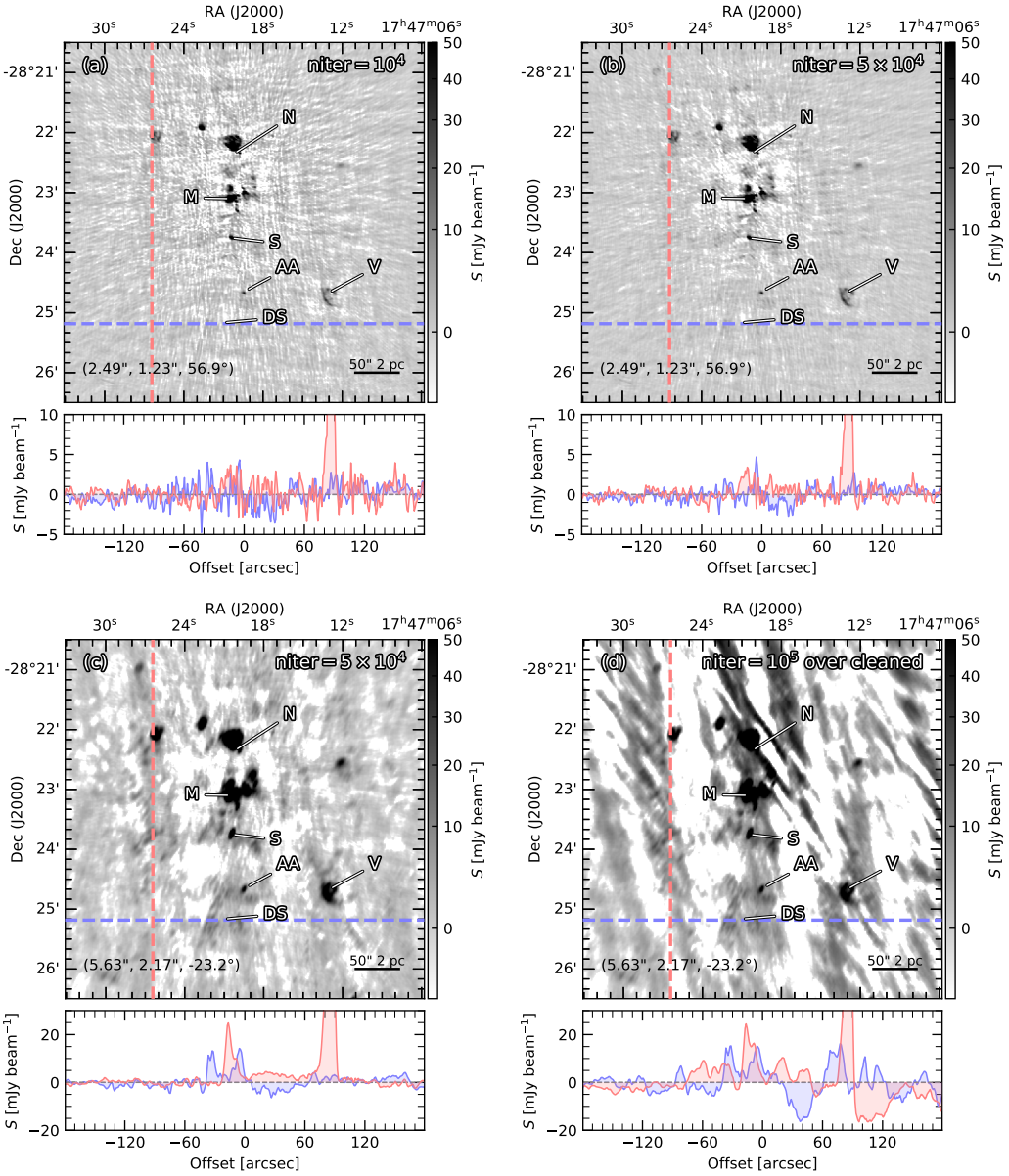

Figure 4.4 Example of the cleaned images with different `niter`. The number of iterations are marked on the upper right corner of each panel. Except for `niter`, `clean` has the same parameters between (a) and (b), and between (c) and (d). However, between (a) and (c), or (b) and (d), the parameters are different in `clean`. Each image has two profile cuts, in blue and red. The offset of each profile increase from left to right and from bottom to top. Beam sizes are marked on the lower left corner of each panel, in format $(\theta_{\rm maj}, \theta_{\rm min}, {\rm PA})$. The data is from 16a195 VLA project (X band, CnB configuration) of SgrB2. The CASA version is `4.5.2-REL (r36115)`.

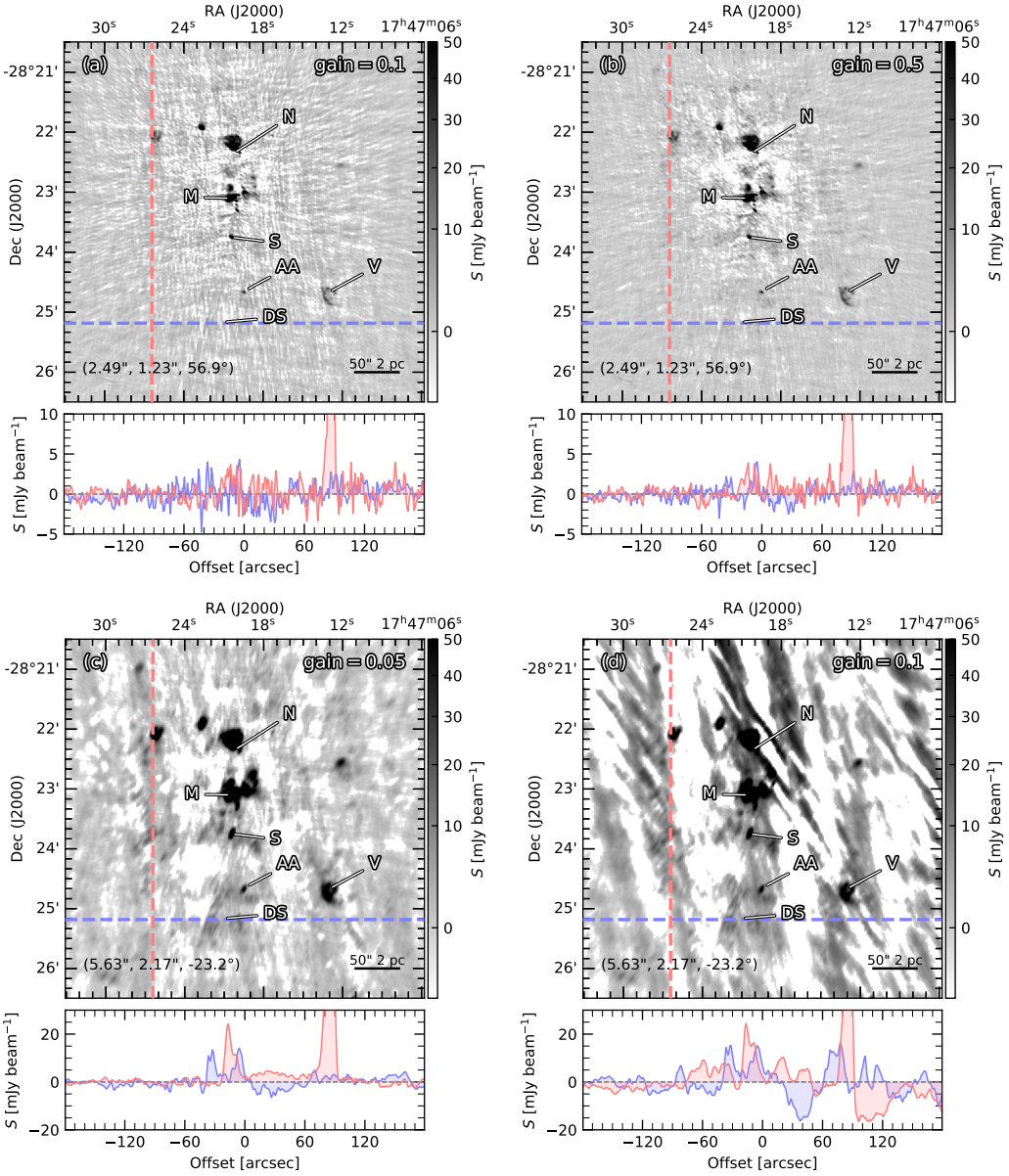

Figure 4.5 Images generated with different `gain`. Panel (a) and (b) is from `clean` with the same parameters in CASA except `gain`, which is marked on the upper right corner of each panel. Same for panel (c) and (d). Each image has two profile cuts, in blue and red. The offset of each profile increase from left to right and from bottom to top. Beam sizes are marked on the lower left corner of each panel, in format $(\theta_{\rm maj}, \theta_{\rm min}, {\rm PA})$. The data is from 16a195 VLA project (X band, CnB configuration) of SgrB2. The CASA version is `4.5.2-REL (r36115)`.

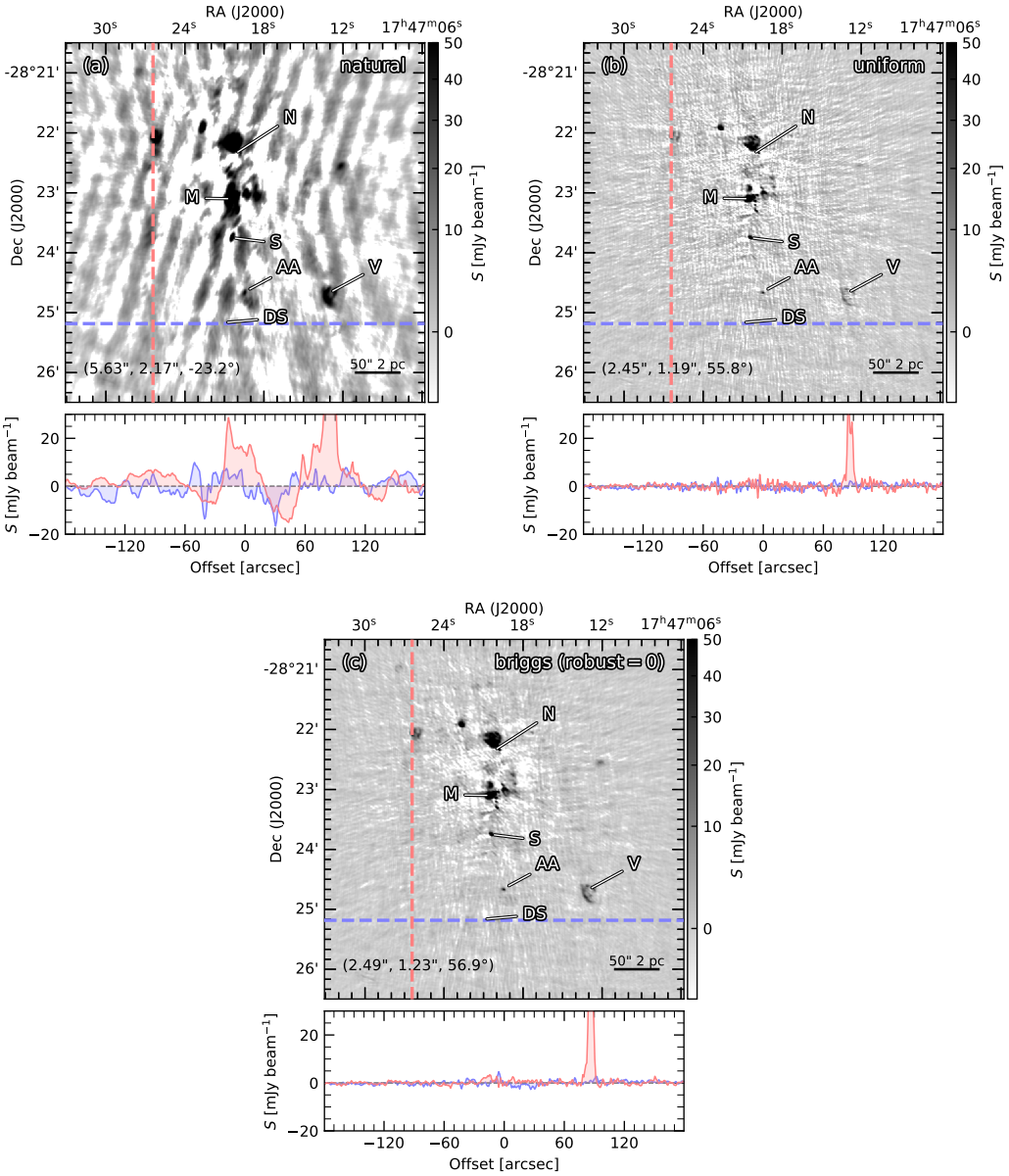

Figure 4.6 Images generated with `natural`, `uniform`, and `briggs` (`robust=0`) weightings. The weighting parameters are marked on the upper right corner of each panel. Parameters other than weighting in `clean` are the same for all the three plots. Each image has two profile cuts, in blue and red. The offset of each profile increase from left to right and from bottom to top. Beam sizes are marked on the lower left corner of each panel, in format $(\theta_{\rm maj}, \theta_{\rm min}, {\rm PA})$. The data is from 16a195 VLA project (X band, CnB configuration) of SgrB2. The CASA version is `4.5.2-REL (r36115)`.

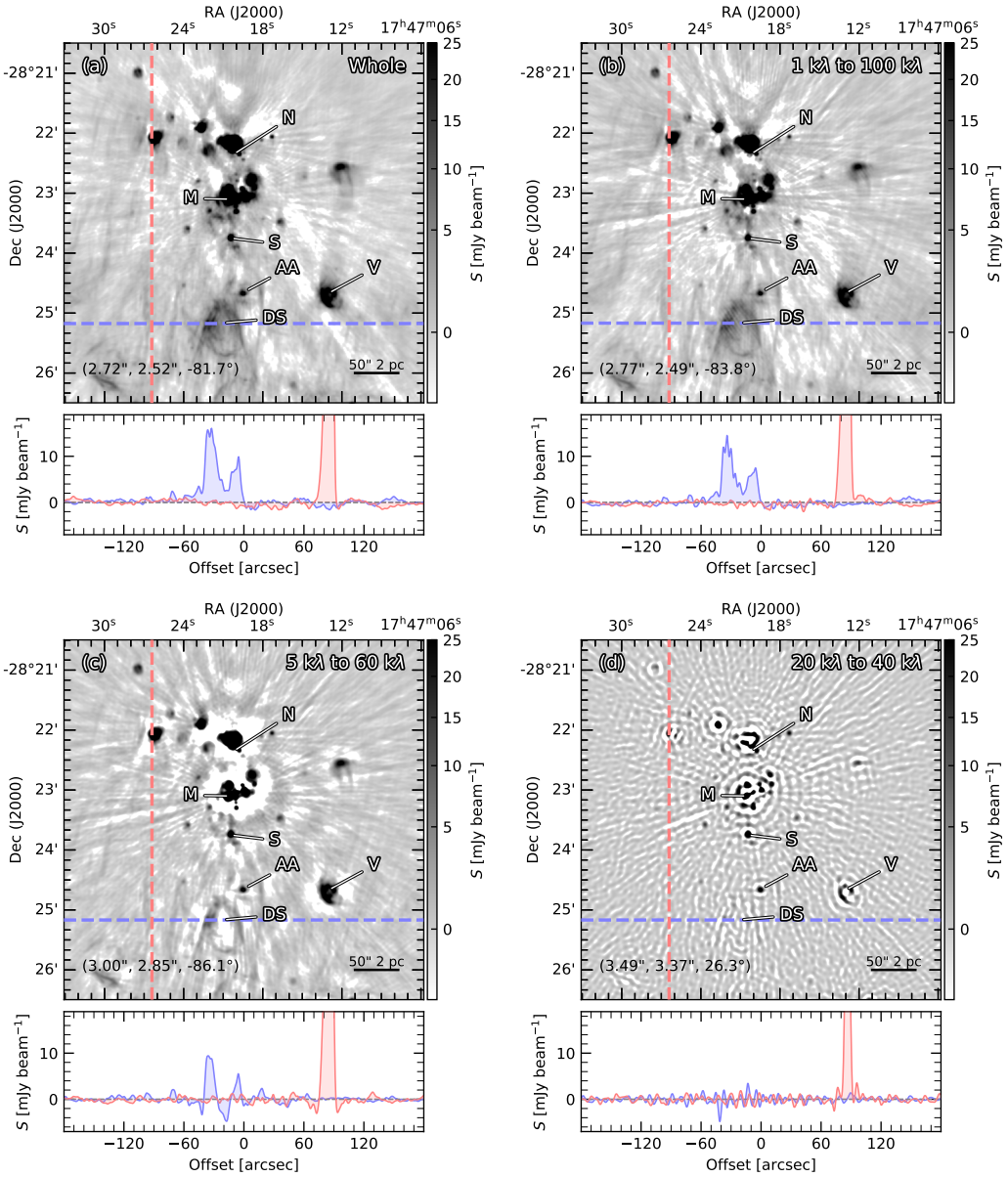

Figure 4.7 Images with different *uv* range. The selected *uv* range are marked on the upper right corner of each panel. Parameters other than `uvrange` in `tclean` are the same for all the plots. Each image has two profile cuts, in blue and red. The offset of each profile increase from left to right and from bottom to top. Beam sizes are marked on the lower left corner of each panel, in format $(\theta_{\rm maj}, \theta_{\rm min}, {\rm PA})$. The data is from VLA observations towards SgrB2 (C band (4–8 GHz), CnB and D configurations combined) of SgrB2. The CASA version is `4.7.2-REL (r39762)`.

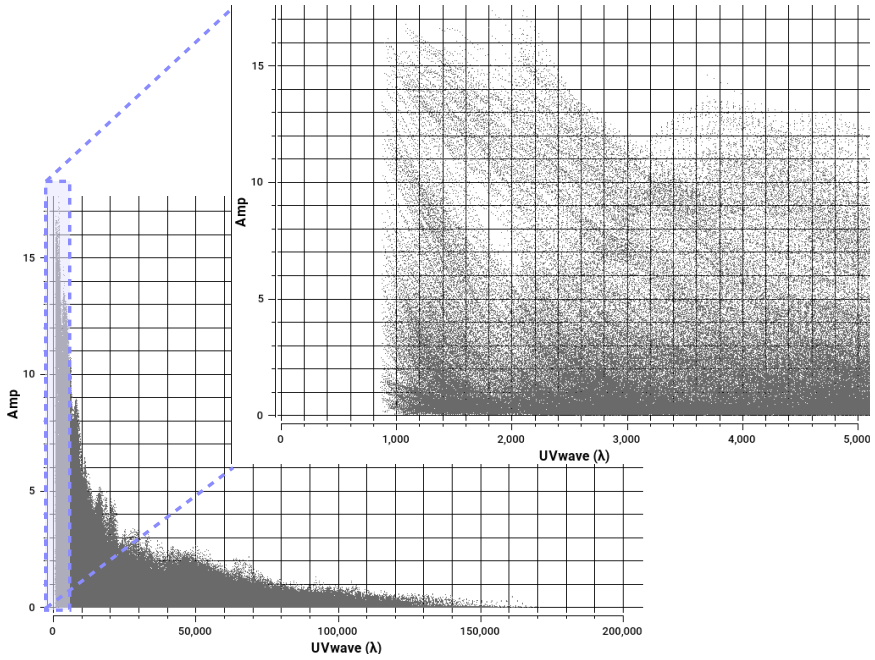

Figure 4.8 Amplitude against *uv* coverage of VLA data used in this study, from the combination of D array and CnB array, C band (4–8 GHz). A zoom-in of the shorter *uv* distance part is shown.

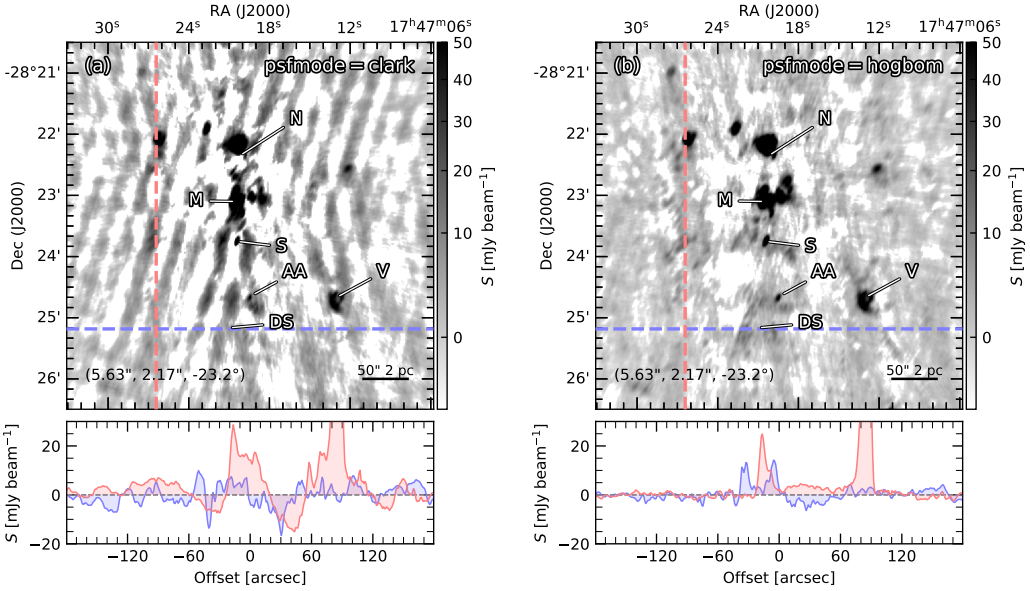

Figure 4.9 Images generated with different `psfmode`. The psf modes are marked on the upper right corner of each panel. Each image has two profile cuts, in blue and red. The offset of each profile increase from left to right and from bottom to top. Beam sizes are marked on the lower left corner of each panel, in format $(\theta_{\rm maj}, \theta_{\rm min}, {\rm PA})$. The data is from 16a195 VLA project (X band, CnB configuration) of SgrB2. The CASA version is `4.5.2-REL (r36115)`.

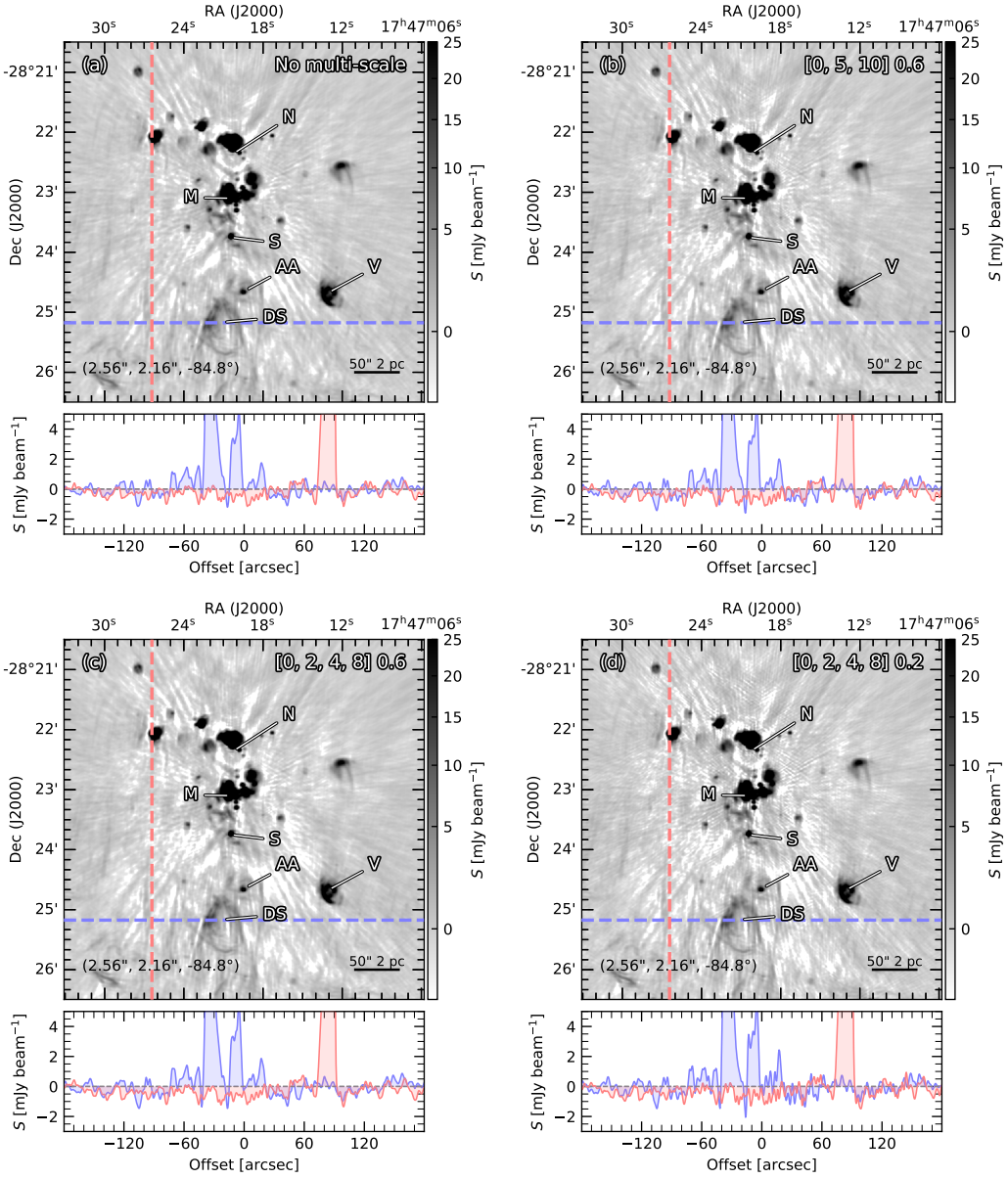

Figure 4.10 Effects of multi-scale as the devonvolver. Images cleaned without multi-scale is shown in panel (a), while that cleaned with multi-scales are shown in panel (b), (c), and (d). Parameters other than `multi-scale` in `tclean` are the same for all the plots. The scales and small scale biases are marked on the upper right corner of each plot. Each image has two profile cuts, in blue and red. The offset of each profile increase from left to right and from bottom to top. Beam sizes are marked on the lower left corner of each panel, in format $(\theta_{\rm maj}, \theta_{\rm min}, {\rm PA})$. The data is from VLA observations towards SgrB2 C band (4–8 GHz), CnB configuration of SgrB2. The CASA version is `4.7.2-REL (r39762)`.

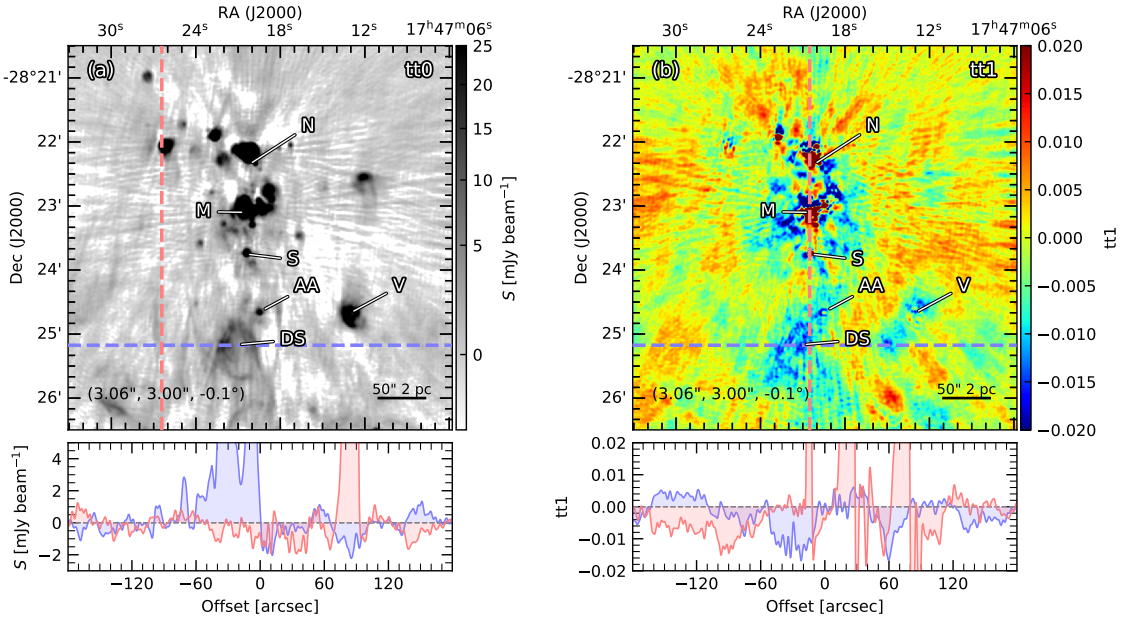

Figure 4.11 Images of `tt0` and `tt1` from the MTMFS mode of CLEAN, plotted in panel (a) and (b) respectively. Each image has two profile cuts, in blue and red. The offset of each profile increase from left to right and from bottom to top. Beam sizes are marked on the lower left corner of each panel, in format $(\theta_{\rm maj}, \theta_{\rm min}, {\rm PA})$. The data is from 16a195 VLA project (C band, CnB configuration) of SgrB2. The CASA version is `5.1.1-5` .

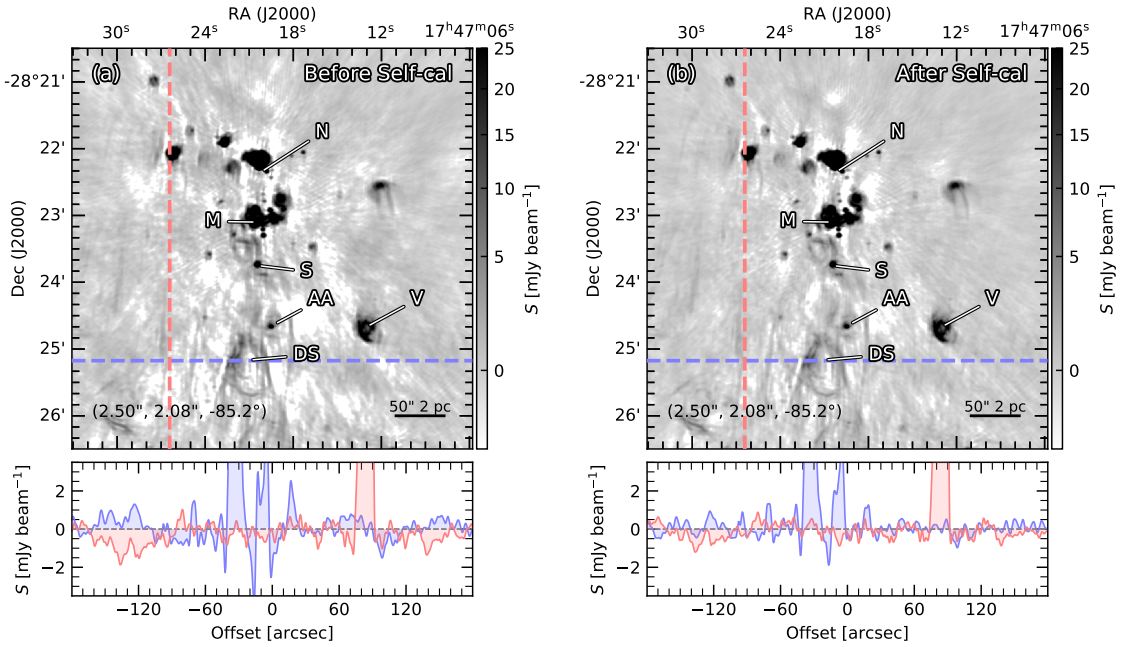

Figure 4.12 Images before and after self calibration, in panel (a) and (b), respectively. Each image has two profile cuts, in blue and red. The offset of each profile increase from left to right and from bottom to top. Beam sizes are marked on the lower left corner of each panel, in format $(\theta_{\rm maj}, \theta_{\rm min}, {\rm PA})$. The data is from VLA observations towards SgrB2 C band (4–8 GHz), CnB configuration of SgrB2. The CASA version is `4.7.2-REL (r39762)`.

4.4 Stacking RRLs

Spectral lines are included in our observations. Among the spectral line in the datasets used in this study, most of them are hydrogen RRLs, from H83α to H115α. Due to the similar excitation conditions of these centimeter RRLs, I stack them to form two lines to increase the SNR and make a deeper clean possible.

The conventional method of stacking RRLs is that the RRLs are firstly cleaned and them the images of them are stacked. I call this method 'image stack'. Due to the narrow frequency coverage of a single RRL, them clean process is usually much shallower compared to the continuum. To utilize the full 4 GHz frequency coverages of C and X bands in this study, I use an alternative way to stack the RRLs. The steps are as follows:

1. Resample the visibilities of the N RRLs into the same spectral structure. All the spectral windows containing RRLs are resampled to have a channel width of 2.5 km s^{-1} and have the same starting channel of -60 km s^{-1} . The total channel number of channels of each RRL is denoted as M. The m-th channel of H$n\alpha$ is denoted as $v_m(n)$.

2. Split the same velocity channel $v_m(n)$ from each spectral window. For N RRLs that each has M velocity channels, I get $N \cdot M$ measurement sets. Then I combine all the N visibilities of the same velocity into one measurement set, to get v_m(all), where 'all' means that the measurement set contains information from all the N RRLs. Thus, I have M measurement sets, each covers a frequency range as wide as $\sim$4 GHz.

3. Clean the M measurement sets as continuum. Then I get M continuum images, which are channels maps of the stacked RRL. All the techniques described in Sect. 4.2 can be used here.

4. Smooth all the M channel images into the same resolution and assemble them to form a datacube, which is the stacked RRL image.

I call this method as 'visibility stack'. The advantage of this method compared to image stack is that each of channel image are cleaned with a much wider frequency coverage, therefore, wider uv coverage. Thus the clean can go deeper and higher dynamic range is archived. In this study, the eight RRLs in C band, from H97α to H100α and from H112α to H115α are stack with 'visibility stack' to form one RRL. While the ten RRLs in X band, from H83α to H92α are stacked into one RRL with 'visibility stack'. A diagram describing the visibility stack of the RRLs in this study is shown in Fig. 4.13. For comparison, I also use performed 'image stack' on the same RRLs. The comparison between the outcomes of these two methods are shown in Fig. 4.14. Obviously, the visibility stack method gives much less artifacts.

When adopting the visibility stacking method, each channel are cleaned with a $\sim$4 GHz frequency coverage, and the gaps are fitted in the clean process. However, the image stack only use discrete narrow spectral windows in this $\sim$4 GHz range. Thus the actual uv range that covered by these two methods do not only determines the depth of cleaning but also the intensity of the stacked RRLs, due to the fact that the RRLs can have varying intensity in different spatial scales. Such a difference can be seen in Fig. 4.14.

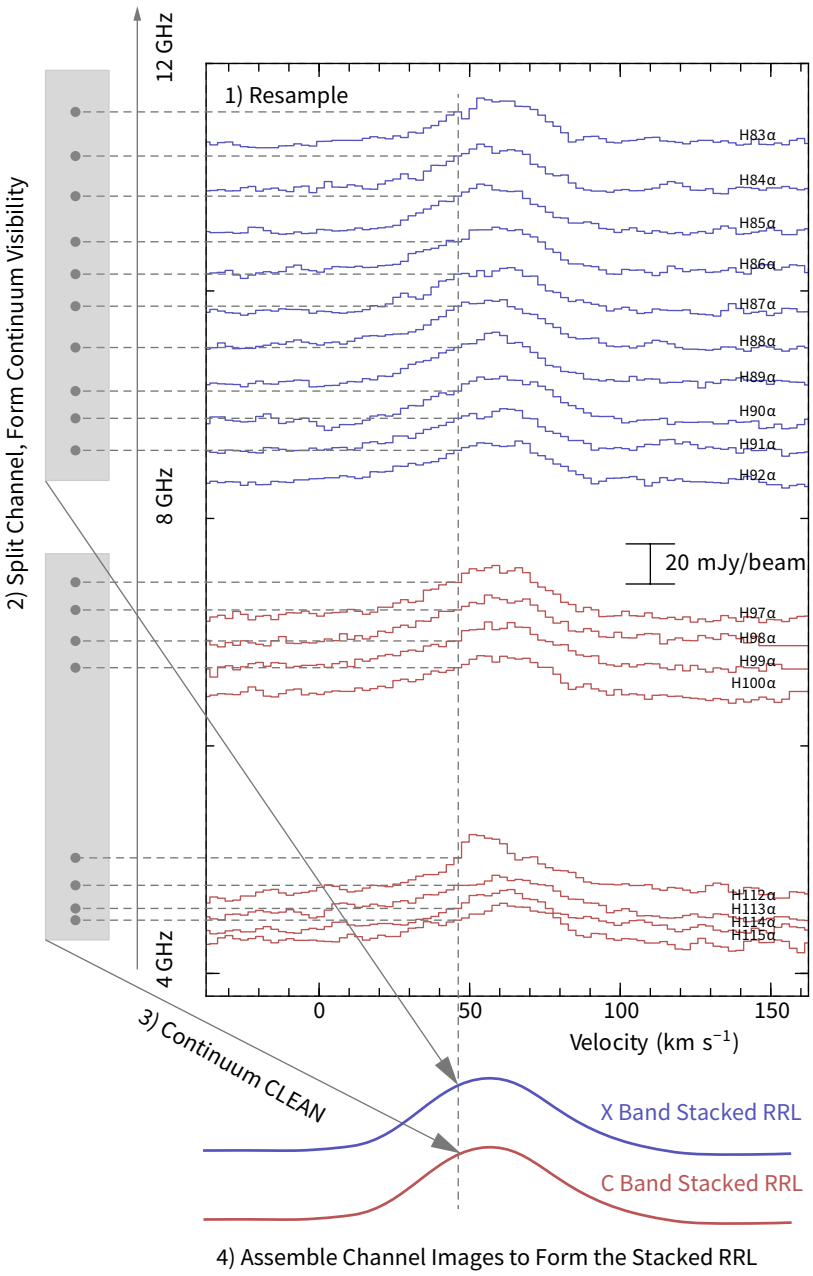

Figure 4.13 Demonstration of visibility stack, using the data from the CnB array of VLA on SgrB2. The RRLs are taken at the center of SgrB2(M), X band RRLs in blue and C band RRLs in red.

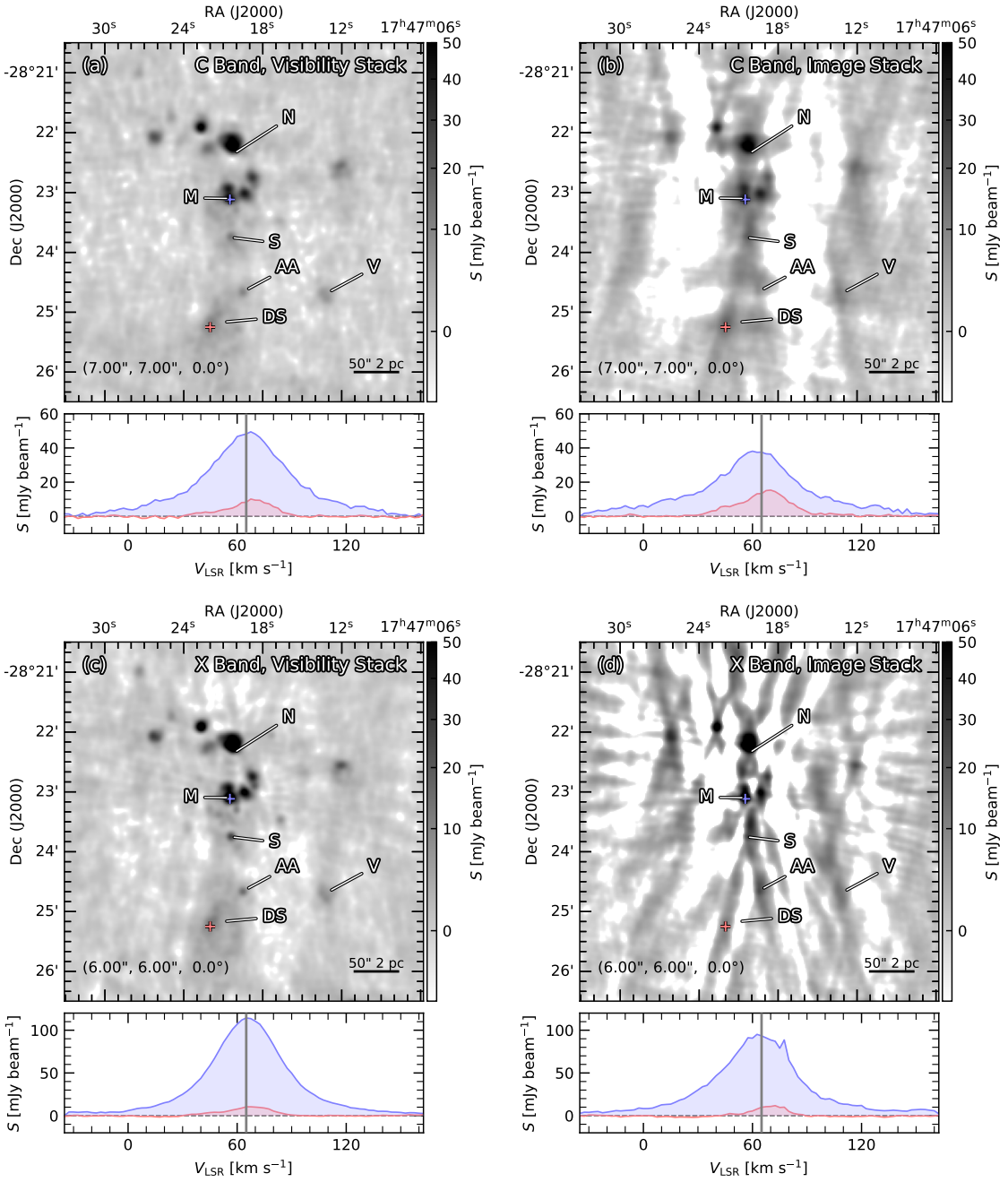

Figure 4.14 Comparison between visibility stack and image stack of RRLs. Panel (a) and (c) are from visibility stack while (b) and (d) are from image stack. Panel (a) and (b) are images of the C band RRLs while (c) and (d) are images of the X band RRLs. The spectra of stacked RRL are shown below each image. The position where the spectra are taken are marked with the color that match the plotted spectra in each image. Beam sizes are marked on the lower left corner of each panel, in format $(\theta_{\rm maj}, \theta_{\rm min}, {\rm PA})$. The data are from D and CnB configurations of VLA. The CASA version is 4.7.2-REL (r39762).

Part III

Sagittarius B2

Chapter 5

Small Scale: Compact Cores

The most prominent feature of SgrB2 in small scales (0.01 pc–0.1 pc) is the presence of dense dust cores. Using 1 mm data (ALMA), Sánchez-Monge et al. (2017) studied the physical and chemical properties of 20 and 27 cores in SgrB2(N) and SgrB2(M), respectively. Ginsburg et al. (2018) identified 217 dense dust cores in 3 mm wavelength, and investigated their dust properties. In this chapter, I combine mm wavelength data (ALMA and SMA), which traces the dust component, and the cm wavelength data (VLA), which traces the ionized component, to characterize the properties of dense cores and their associated UCHII regions throughout the whole SgrB2 region. Such a multi-frequency study allows me to better understand the physical properties and evolutionary stages of these dense cores in SgrB2. In Sect. 5.1 I describe the observations. Section 5.2 shows the results. In Sect. 5.3 I analyze the results. In Sect. 5.4 I summarize this chapter.

5.1 Observation and data reduction

In this research, I include the continuum data from eight frequency bands, ranging from 4 to 343 GHz. Data from three interferometers: VLA, ALMA, and SMA, are adopted. See Table 5.1 for an overview of the data at the eight bands.

Table 5.1 Data Overview

Num	Telescope (bands)	ν_0[a] GHz	$\Delta\nu$[b] GHz	Beam size[c] ($''$, $''$)	P.A. $^\circ$
1	VLA C	6.0	4.0	(0.62, 0.28)	7.27
2	VLA X	10.0	4.0	(0.36, 0.15)	3.12
3	VLA K	22.5	7.5	(0.18, 0.08)	−10.02
4	VLA Ka	33.0	7.6	(0.12, 0.05)	7.52
5	VLA Q	45.9	7.5	(0.10, 0.04)	−21.19
6	ALMA 3mm	96.4	13.8	(0.54, 0.46)	68.31
7	ALMA 1mm	243.0	1.9	(0.40, 0.40)	0.0
8	SMA	344.2	4.0	(0.40, 0.24)	16.39

[a] Central frequency of the band.

[b] Band width.

[c] FWHM along the major and minor axes of a 2D Gaussian beam.

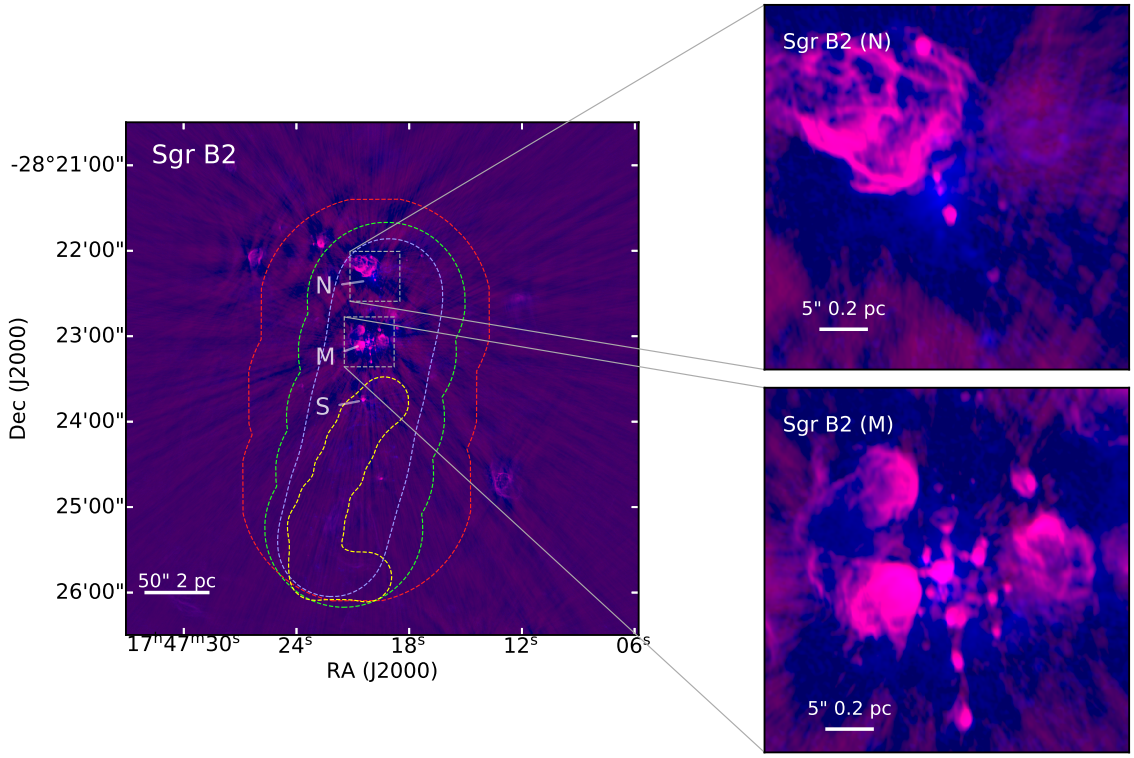

Figure 5.1 The region covered by the VLA C- and X-Band and ALMA 3 mm. Red dashed contour: The region covered by VLA K-Band. Green dashed contour: The region covered by VLA Ka-Band. Blue dashed contour: The region covered by VLA Q-Band. Gray dashed rectangles: The regions covered by ALMA 1 mm and SMA. Yellow 'L'-shaped region: The region covered by the SiO image. Pseudo-color background: Red is the VLA C-Band intensity map, which has a synthesized beam of $0.62'' \times 0.28''$, PA is 7.27 degree. Blue is the ALMA 3 mm map, which has a synthesized beam of $0.54'' \times 0.46''$, PA is 68.31 degree.

The spatial coverage of the images at the eight frequency bands is not always the same. In this study, we use the area covered by the mosaic of ALMA 96 GHz data, which is approximately $6' \times 6'$. The intrinsic spatial coverage of the VLA 6 GHz and 10 GHz observations is larger than the $6' \times 6'$ area, but only the central $6' \times 6'$ area coincident with the ALMA 96 GHz data is taken into account in the following analysis. The observations at the other five frequency bands cover smaller areas, as marked in Figure 5.1.

In total, the considered VLA observations cover the frequency range from 4 GHz to 46 GHz, in the C, X, K, Ka, and Q bands. The C (4–8 GHz) and X (8–12 GHz) band data are observed from October 1 to 12, 2016 (project 16B-031, PI: F. Meng) in the most extended A configuration. For both bands, we used 64 spectral windows with a bandwidth of 128 MHz each. Mosaic mode was used, with 10 and 18 pointings for each band, respectively. The primary beam of each pointing is $7.5'$ and $4.5'$ respectively. Quasar 3C286 was used as the flux and bandpass calibrator, the SED of which is $S_\nu = 5.059 \pm 0.021$ Jy$\times (S/8.435\ \mathrm{GHz})^{-0.46}$ from 0.5 to 50 GHz (Perley & Butler, 2013). Quasar J1820-2528 was used as the phase calibrator. The details of the data reduction is described in Chapter 4.

The K (19–26 GHz), Ka (29–37 GHz), and Q (42–50 GHz) band data are observed from

March 5 to April 18, 2018 (project 18A-229, PI: A. Ginsburg) in A configuration. For K band, we used 45 spectral windows with a bandwidth of 128 MHz each. For Ka band, we used 49 spectral windows with a bandwidth of 128 MHz each. For Q band, we used 50 spectral windows with a bandwidth of 128 MHz each. Mosaic mode was used, with 3, 5, and 7 pointings for the K, Ka, and Q bands, respectively. The primary beam of each pointing is 2.0′, 1.4′, and 1.0′for the K, Ka, and Q bands, respectively. Quasar 3C286 was used as the flux and bandpass calibrator. Quasar J1744-3116 was used as the phase calibrator.

For the millimeter bands, I used the 3 mm (96 GHz) data of the ALMA project 2013.1.00269.S (PI: A. Ginsburg), and the 1 mm (243 GHz) data of the ALMA project 2013.1.00332.S (PI: P. Schilke). The details of the observations of both projects can be found in Ginsburg et al. (2018) and Sánchez-Monge et al. (2017), respectively. The observational details of the SMA data at 343 GHz are also introduced in the latter reference, although the original publication of the data can be found in Qin et al. (2011).

5.2 Results

I identified 308 compact cores in SgrB2. See Table B.1 for the core positions, types, and associated objects. In this section, I present the procedure and criteria of the core identification, as well as the photometric methods used to determine the flux of the cores at the different frequency bands.

5.2.1 Core identification

Due to the hierarchical structure of SgrB2, I applied `Dendrograms` (Rosolowsky et al., 2008) to identify the local maxim on background emission. The "leaves" identified by `Dendrograms` are regarded as cores. Since the 6 and 96 GHz images cover the whole region (see Figure 5.1) and have the best sensitivity, I performed the core identification on them. For the `Dendrograms` analysis, because of the different spatial resolution and sensitivity of the 6 and 96 GHz images, I used different sets of parameters. Parameter `min_value`, which means that any structure below `min_value` will be ignored, is set to 0.2 mJy/beam and 0.1 mJy/beam for 6 and 96 GHz images, respectively. Parameter `min_delta`, which is the minimum height required for a structure to be retained, are set to 0.4 and 0.5 mJy/beam for the 6 and 96 GHz images, respectively. Parameter `min_npix`, which is the minimum number of pixels that a structure should contain in order to remain an independent structure, is set to 64 for both images. I use the coordinates of the core center and the fitted core size, which are the major axis, minor axis and position angle of 2D Gausssian, returned by `Dendrograms` as input to the next step.

Out of all the leaves identified by `Dendrogram`, I selected only those for which the major axis is shorter than two times the beam size (0.65″, see below), to which the images are smoothed in the next step. By doing this, our sample includes only compact cores, and allows us to exclude the most extended structures. This restriction to the size of the cores results in an upper limit to the core size of ~ 0.05 pc ($\sim 10^4$ au).

It is worth to note that the core identification was applied to the 6 GHz and 96 GHz images at their original angular resolution (see Table 5.1) to make sure that neighboring cores can be well resolved and identified. After the core identification, and with the aim of comparing the cores across different frequencies, I smoothed the images of all the eight

bands to a uniform resolution of 0.65″, which corresponds to the largest circle that can contain all the beams of the eight bands.

Initially, I identified 208 cores. In addition, I performed a cross-check between the cores identified following the method described above and the cores reported by Ginsburg et al. (2018). Since the dataset at 96 GHz used by these two studies is the same and the core-identification criteria are similar. Out of the 208 cores, 171 are also identified by Ginsburg et al. (2018). This means that among the 271 cores identified by Ginsburg et al. (2018), 100 are not identified with the method described above. Such a difference in core identification between these two studies can be caused by the fact that `Dendrogram` is more sensitive to a core individually located on a bright background, but it is less sensitive to cores that are located in a crowded region. To make my sample as complete as possible, I use the union set of the 208 cores identified by myself and the cores identified by Ginsburg et al. (2018). In total, 308 cores are included in this study.

The 308 cores are divided in two types (see Table B.1). Type I cores include the cores identified at both 96 GHz and 6 GHz, while Type II are the cores only detected at 96 GHz. There is no core identified only at 6 GHz. Since the location of the emission peak of a core can change at different frequencies, I determine the peaks within one beam area (0.65″×0.65″) between two different frequencies as the same core. Among all the 308 cores, 58 are identified as Type I. The positions of Type I and Type II cores are shown in Figure 5.2.

5.2.2 Photometry

Photometry methods on the core flux depends on if the core is resolved or not. In this study, I applied two methods to obtain the flux of the cores.

- Assuming that the cores are ideally unresolved, i.e. core size much smaller than the beam size, then the peak flux density of a core can be directly treated as the flux of the core. What I need to do is just replacing the unit mJy/beam with mJy. The flux acquired with such a method is denoted as $S_{\rm p}$.

- Assuming that the cores have Gaussian radial intensity profiles, I perform the photometry in a circle centered at the core center with radius 0.83″ (hereafter photometry-circle). Since the images are smoothed to a resolution of 0.65″, 0.83″ corresponds to the 3σ of the Gaussian beam. The flux acquired with such a method is denoted as $S_{3\sigma}$. Ideally, if a core is unresolved, $S_{3\sigma} \approx S_{\rm p}$, since the integration of a 2D Gaussian within the 3σ radius includes 99.4% of all the emitted flux. If a core is resolved, i.e. has a radius $r_{\rm core} > 0$, then $S_{3\sigma} > S_{\rm p}$.

Since all the 308 cores are detected at 96 GHz band, I used $S_{3\sigma}$ and $S_{\rm p}$ at 96 GHz to test if the cores are unresolved. The flux $S_{3\sigma}$ and $S_{\rm p}$ of all the 308 co3es are listed in Table B.1 and plotted in Figure 5.3. Most of the cores have $S_{3\sigma} \approx 2S_{\rm p}$, see Figure 5.3. Thus, most of the cores are not ideally unresolved.

To quantify that to what degree the cores are resolved, I modeled $S_{3\sigma}/S_{\rm p}$ for different core sizes. The cores are assumed to have homogeneous flux density within the circle of radius $r_{\rm core}$, while has zero flux density outside $r_{\rm core}$. The images of such synthetic cores are smoothed to the resolution of this study, 0.65″×0.65″, and the two photometry methods

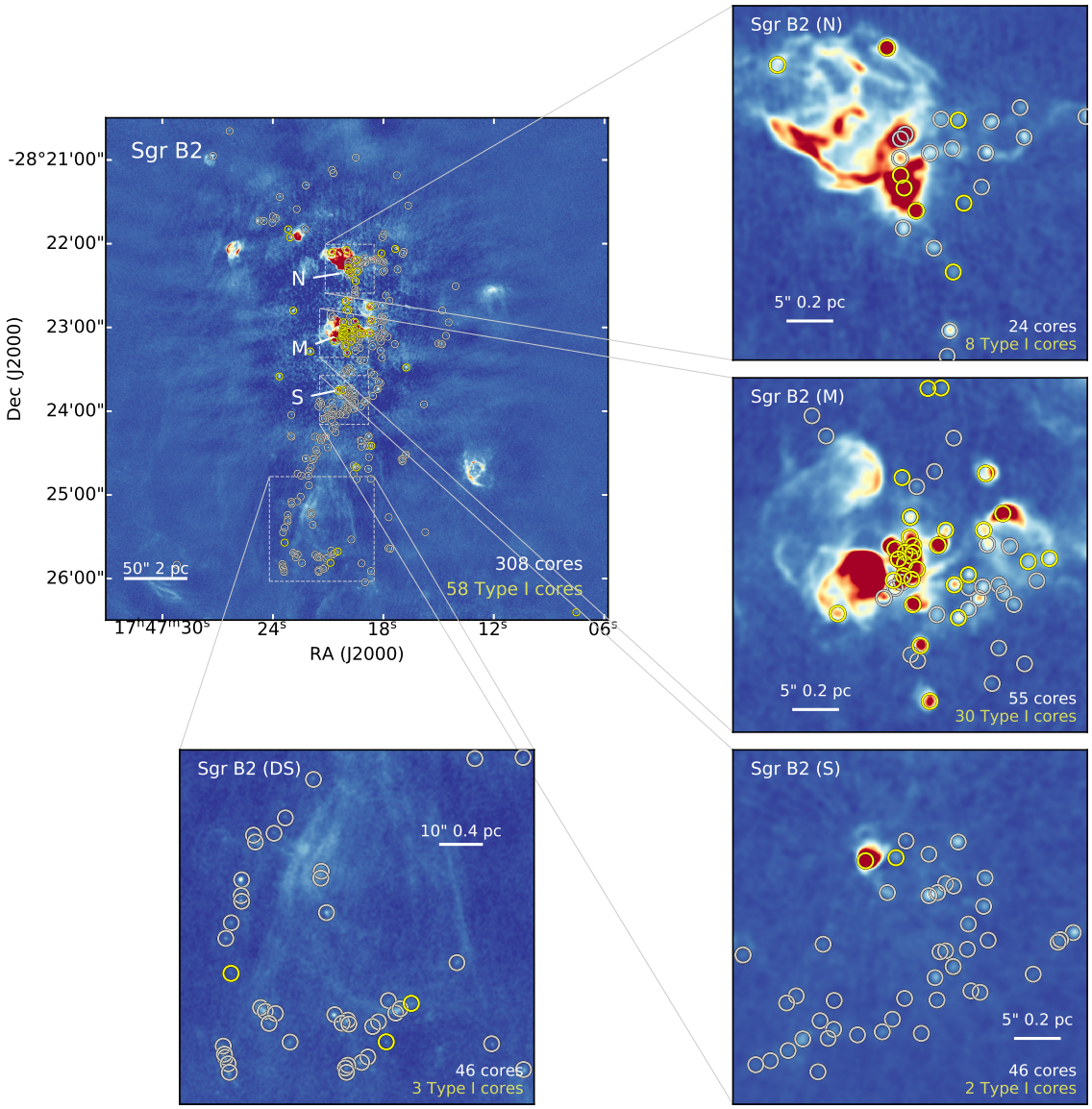

Figure 5.2 The spatial distribution of all the cores. Type I cores are marked as yellow circles while Type II cores are marked with gray circles. The background image is the 96 GHz intensity map. Core counting of the entire SgrB2 and SgrB2 (N), (M), (S), and (DS) are written on the lower right corner of each subplot. The sizes of the circles are set to make the core positions visible, which is irrelevant to the actual sizes of the cores.

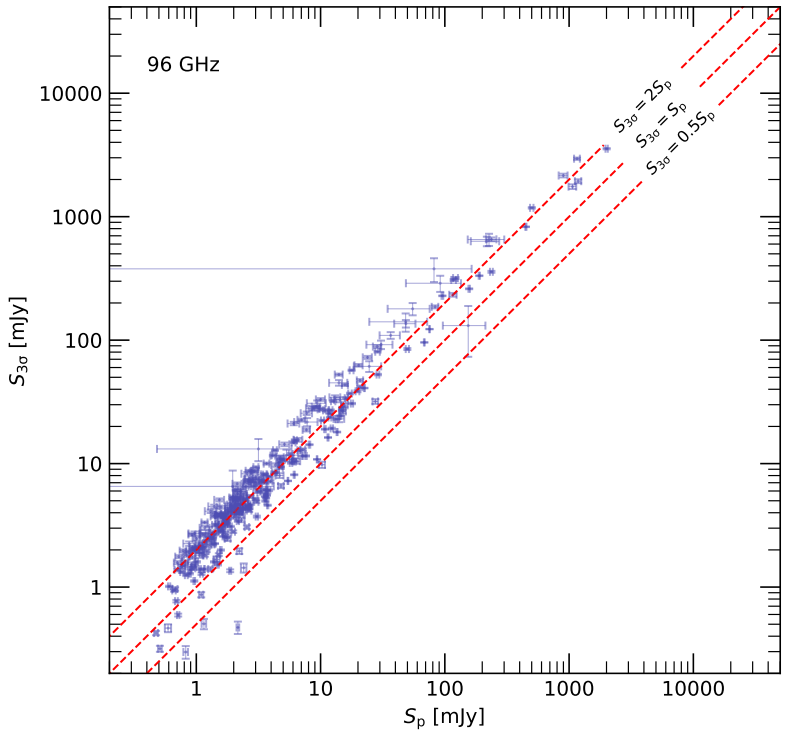

Figure 5.3 Correlation between $S_{3\sigma}$ and $S_{\rm p}$ at 96 GHz for all the 308 co3es. Dashed lines mark where $S_{3\sigma} = 2S_{\rm p}$, $S_{3\sigma} = S_{\rm p}$ and $S_{3\sigma} = 0.5S_{\rm p}$ respectively.

applied. The relation between $S_{3\sigma}/S_{\rm p}$ and $r_{\rm core}$ is shown in Figure 5.4. Since that $S_{3\sigma}/S_{\rm p}$ sensitively depends on $r_{\rm core}$ up to 1.3″, it can be used to derive $r_{\rm core}$, for $r_{\rm core} \lesssim 1.3''$.

Following the results presented in Figure 5.4, I estimate the core radius, $r_{\rm core}$, from the flux ratio, $S_{3\sigma}/S_{\rm p}$, at 96 GHz. Out of the 308 cores, 14 have $S_{3\sigma}/S_{\rm p} < 1$, which are excluded from the statistics. For the remaining 294 cores, the mean $r_{\rm core}$ is 0.55″. Most of the cores have $r_{\rm core}$ between 0.35″– 0.75″. Although the $S_{3\sigma}/S_{\rm p}$ ratio can help to estimate the core radius, the $r_{\rm core}$ of a certain core can be over- or under-estimated due to the artifacts. For instance, due to the artifacts in the images, if the cores are located in the positive hills (negative bowls) of the artifacts, both of $S_{3\sigma}$ and $S_{\rm p}$ will be over-estimated (under-estimated) by adding (subtracting) a common 'background', which will alter $S_{3\sigma}/S_{\rm p}$. Therefore, I do not use $r_{\rm core}$ of each core in the following analysis, but take the mean $r_{\rm core}$, 0.55″ as the radius of all the cores.

Since most of the cores are not ideally unresolved, i.e. $r_{\rm core} \ll 0.65''$. At 96 GHz, I took $S_{3\sigma}$ as the flux (S_{96}) of each core that has $S_{3\sigma}/S_{\rm p} \geq 1$. For the 14 cores that have $S_{3\sigma}/S_{\rm p} < 1$, I took $S_{\rm p}$ as their flux (S_{96}). For other bands, similarly, $S_\nu = \max(S_{3\sigma}, S_{\rm p})$. For S_ν of all the eight bands, see Table 5.2.

The uncertainty of flux of each core was obtained with the following procedure. The RMS of flux within an annulus around the photometry-circle, denoted as $\rm RMS_{Annu}$, was calculated. The annulus has a inner radius of 0.83″and a outer radius of 1.66″. Then the un-

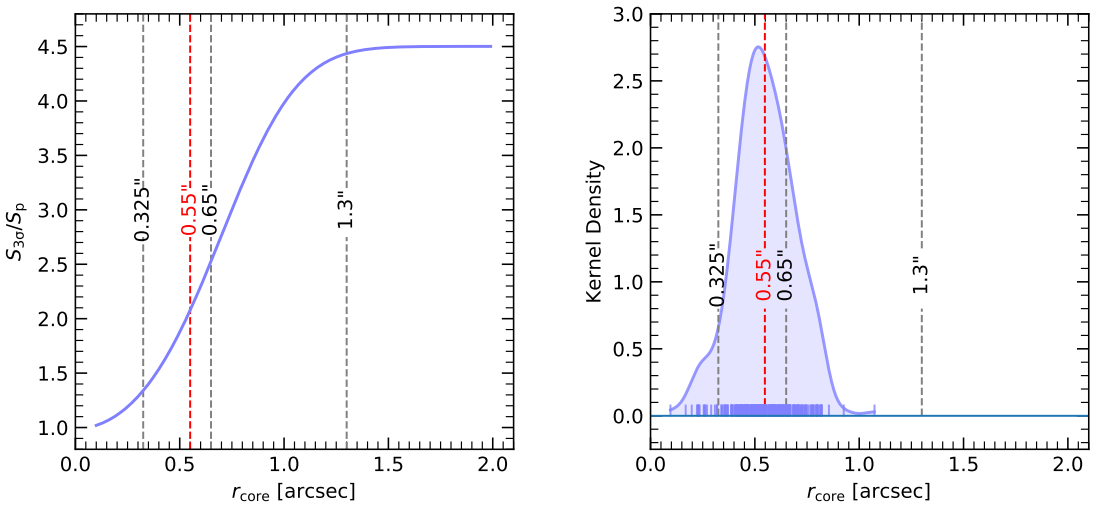

Figure 5.4 *Left panel:* Relation between $S_{3\sigma}/S_{\rm p}$ and $r_{\rm core}$, for a beam of $0.65''\times0.65''$. *Right panel:* The estimated $r_{\rm core}$ of the cores. In both panels, 1/2-beam, 1-beam, 2-beam radius, and the mean of the estimated core size ($0.55''$) are marked.

certainty of flux of each core can be derived as $\delta S_\nu = 3\sqrt{N_{\rm Circ}}{\rm RMS}_{\rm Annu}/N_{\rm Beam}$, where $N_{\rm circ}$ is number of pixels in the photometry circle, and $N_{\rm Beam}$ is the number of pixels in a beam (see Section A.1 for the details of photometry). In bands other than 6 GHz and 96 GHz, most of the images are affected by artifacts that can affect the determination of the flux. I manually selected the cores that are spatially adjacent to artifact patterns and discarded the flux determined with the photometric analysis described above. Instead, I used the uncertainty of the flux to derive an upper limit of the flux: $S_\nu < 10\sqrt{N_{\rm Circ}}{\rm RMS}_{\rm Annu}/N_{\rm Beam}$. It is worth to note that such an upper limit is also severely affected by artifacts, therefore, they are not used to constrain the parameters of the SED (fitting, see next sections), but just as a guidance on the upper limit of the flux at different frequencies. The uncertainty and upper limits of Type I cores in all the eight bands are listed in Table 5.2.

In Figure 5.5, I present the distribution of fluxes at 96 GHz (S_{96}) for all cores. The mean value of S_{96} is 72.1 mJy, while for Type I cores it is 214.9 mJy and for Type II cores it is 16.9 mJy. The Type I cores are systematically brighter at 96 GHz and have a wider flux distribution than the 250 Type II cores.

Table 5.2 Flux of Type I cores

ID	S_6 mJy	S_{10} mJy	S_{22} mJy	S_{33} mJy	S_{46} mJy	S_{96} mJy	S_{274} mJy	S_{343} mJy
1	0.9 ± 0.4	<2.0	<13	–	–	6.1 ± 0.2	–	–
2	11.4 ± 0.6	10.8 ± 0.9	<8.5	–	–	25.5 ± 0.7	–	–
3	8.7 ± 0.6	14.8 ± 0.8	<7.0	<3.7	<6.0	19.3 ± 0.8	–	–
4	77.5 ± 1.6	58.4 ± 2.0	<10.0	<10	<16	228.5 ± 4.5	<92	<206
5	21.5 ± 1.2	<4.0	<5.2	<5.9	<9.0	52.6 ± 3.1	<28	<123
6	6.8 ± 0.1	<1.6	<5.6	<3.1	<5.8	10.8 ± 0.2	–	–
7	4.2 ± 0.3	<3.4	<5.5	<5.7	<8.5	22.6 ± 1.5	121.6 ± 8.9	<115
8	14.1 ± 0.9	20.3 ± 1.4	<11	26.7 ± 3.8	69.9 ± 5.8	655 ± 69	5427 ± 572	11885 ± 1142

Table 5.2 Flux of Type I cores (*continued*)

ID	S_6 mJy	S_{10} mJy	S_{22} mJy	S_{33} mJy	S_{46} mJy	S_{96} mJy	S_{274} mJy	S_{343} mJy
9	3.9 ± 1.3	8.0 ± 2.1	< 9.1	< 10	52.6 ± 6.7	1179 ± 48	9956 ± 446	18998 ± 986
10	1.3 ± 0.3	< 2.2	< 7.1	< 6.6	< 5.4	8.5 ± 0.5	< 74	< 130
11	45.3 ± 1.0	33.9 ± 1.7	44.0 ± 3.6	32.5 ± 2.7	37.1 ± 2.7	233 ± 24	585 ± 208	430 ± 348
12	1.2 ± 0.7	< 3.4	< 5.3	< 5.4	< 5.6	10.8 ± 0.6	19 ± 21	500 ± 31
13	5.8 ± 0.2	< 3.5	< 12	< 6.8	53.1 ± 2.5	95.9 ± 1.6	–	–
14	20.3 ± 1.7	< 5.0	< 4.6	< 5.2	< 6.1	28.9 ± 2.2	–	–
15	1.0 ± 0.4	< 3.7	< 5.0	< 7.6	< 12	7.2 ± 0.4	–	–
16	0.9 ± 0.7	< 4.6	< 4.8	< 4.4	< 13	7.1 ± 0.5	–	–
17	5.7 ± 0.4	< 1.4	< 5.6	< 8.5	–	8.7 ± 0.4	–	–
18	25.9 ± 0.8	18.0 ± 0.7	< 3.9	< 4.3	< 7.8	57.0 ± 1.9	–	–
19	28.0 ± 2.0	34.5 ± 2.7	< 10	< 13	< 12	80.6 ± 3.6	212 ± 18	< 104
20	0.7 ± 0.8	< 3.5	< 11	< 18	< 18	9.7 ± 1.0	< 31	332 ± 24
21	10.0 ± 0.6	< 10	< 21	< 30	< 24	41.9 ± 2.8	< 75	38 ± 40
22	68.7 ± 6.3	46.9 ± 3.0	21.7 ± 8.2	-0.7 ± 6.1	51.0 ± 8.1	186 ± 15	259 ± 24	< 36
23	20.4 ± 4.5	13.9 ± 5.4	< 22	< 26	< 41	61 ± 18	< 60	< 120
24	37.5 ± 2.8	< 6.8	< 19	< 13	< 10	72.5 ± 6.0	< 53	162 ± 28
25	20.6 ± 5.2	< 18	< 76	< 43	< 128	141 ± 71	< 600	< 1418
26	60.2 ± 2.1	82.1 ± 3.4	45.8 ± 7.5	34.9 ± 7.9	201.3 ± 5.8	332.4 ± 6.6	117 ± 20	382 ± 47
27	47.6 ± 7.3	< 21	< 80	< 55	< 274	632 ± 168	< 1350	< 2992
28	13.1 ± 1.8	9.0 ± 4.6	38.7 ± 7.1	57.2 ± 8.5	217.2 ± 10.0	358 ± 19	239 ± 55	770 ± 66
29	120.8 ± 5.9	< 23	< 53	< 49	< 399	2154 ± 222	< 1361	< 2889
30	10.0 ± 0.6	< 3.4	< 9.4	< 7.3	< 8.4	29.7 ± 2.8	–	–
31	127.8 ± 5.3	< 22	< 61	< 53	< 351	2949 ± 186	< 1111	< 2339
32	86.0 ± 7.1	40.1 ± 7.5	299 ± 22	121 ± 18	785 ± 124	1751 ± 228	4644 ± 436	10546 ± 930
33	7.9 ± 0.7	5.5 ± 1.1	< 10	< 11	< 8.4	43.4 ± 2.6	192 ± 14	463 ± 33
34	9.5 ± 0.8	< 3.6	< 8.9	< 14	< 11	33.1 ± 2.5	70.6 ± 9.6	< 61
35	91.8 ± 7.0	< 21	< 81	< 61	< 215	3550 ± 129	< 1123	< 2376
36	36.8 ± 7.6	57.2 ± 7.0	12 ± 24	20 ± 20	856 ± 112	1938 ± 209	5132 ± 453	10622 ± 956
37	12.6 ± 6.7	< 25	< 61	< 48	< 430	378 ± 247	< 1674	< 3495
38	9.9 ± 1.1	< 12	< 12	< 11	< 15	26.4 ± 2.8	< 91	< 88
39	14.6 ± 5.3	< 24	< 45	< 61	< 405	653 ± 222	< 1345	< 2744
40	6.0 ± 2.6	< 15	< 24	< 43	< 213	289 ± 130	< 950	< 1965
41	11.7 ± 6.9	< 21	< 30	< 49	< 94	179 ± 61	< 549	< 1059
42	18.0 ± 0.5	< 10	< 16	< 12	< 17	52.6 ± 2.2	< 93	< 70
43	50.5 ± 2.7	37.7 ± 5.3	< 24	< 27	142.1 ± 5.8	260.5 ± 6.5	< 85	< 187
44	30.8 ± 2.5	< 5.3	< 21	< 13	< 9.7	88.7 ± 6.6	< 33	< 46
45	7.7 ± 0.5	10.3 ± 1.2	< 8.2	< 10	< 16	38.5 ± 2.1	< 58	< 83
46	36.2 ± 0.8	19.2 ± 3.4	19.7 ± 2.7	27.6 ± 5.1	53.6 ± 4.4	122.8 ± 1.4	< 69	< 65
47	6.0 ± 0.4	1.7 ± 0.5	< 4.4	< 7.6	< 10	9.4 ± 0.4	–	–
48	42.2 ± 1.4	36.8 ± 2.5	< 11	< 10	< 12	84.7 ± 4.5	70 ± 13	< 81
49	4.8 ± 0.5	< 2.8	< 2.7	< 8.3	–	5.7 ± 0.5	–	–
50	7.8 ± 0.6	2.9 ± 0.3	< 4.8	< 10	–	7.3 ± 0.5	–	–
51	4.2 ± 1.7	< 4.4	< 12	< 16	< 9.6	11.7 ± 3.8	–	–
52	95.4 ± 5.8	87.6 ± 4.0	129 ± 11	60.1 ± 8.2	405.3 ± 4.7	828 ± 15	–	–
53	0.81 ± 0.06	< 1.9	< 3.1	< 2.5	< 2.8	24.3 ± 0.7	–	–
54	27.0 ± 1.0	< 2.4	< 3.7	< 2.3	< 2.4	37.0 ± 1.7	–	–
55	1.87 ± 0.05	< 0.7	< 0.9	< 0.09	< 0.7	0.51 ± 0.05	–	–
56	2.1 ± 0.2	< 0.6	< 1.3	< 0.1	< 0.7	2.7 ± 0.2	–	–
57	0.29 ± 0.03	< 0.7	< 1.4	< 0.07	< 1.0	0.77 ± 0.05	–	–
58	0.15 ± 0.02	< 0.3	–	–	–	2.7 ± 0.1	–	–

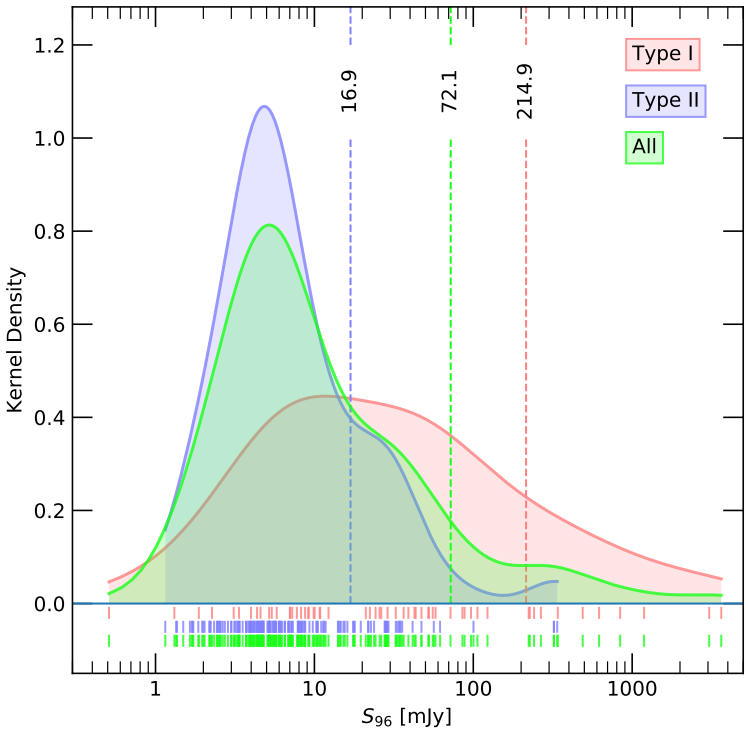

Figure 5.5 The KDE of the flux at 96 GHz of Type I (Pink), Type II (Blue), and all the cores (Green). Mean values of flux are marked with corresponding colors.

5.3 Analysis

5.3.1 Modeling the SED

Free-free emission from ionized gas is mainly traced by cm wavelength emissions (e.g. the 6 GHz emission), while the dust emission is mainly traced by mm wavelength emissions (e.g. the 96 GHz emission). The SEDs of the cores can be modeled as superpositions of free-free emission and dust emission. In this section, I solve the free-free emission intensity and the dust mass of each of the type I core from the 6 GHz and 96 GHz flux. The detailed SEDs of all the type I cores are shown in Figure C.1.

The optically thin free-free emission from an HII region can be expressed as a power-law SED (see e.g. Wilson et al., 2009):

$$S_{\mathrm{ff}\nu} = S_{\mathrm{ff6}} \left(\frac{\nu}{6\ \mathrm{GHz}} \right)^{-0.1} \tag{5.1}$$

where S_{ff6} is the free-free flux at 6 GHz. From S_{ff6}, I estimate the mass of the HII regions with S_{ff6}, which can be expressed as:

$$\left(\frac{M_{\mathrm{HII}}}{M_\odot} \right) = 3.15 \times 10^{-12} \left(\frac{S_\nu}{\mathrm{Jy}} \right)^{0.5} \left(\frac{\nu}{\mathrm{GHz}} \right)^{0.5} \left(\frac{T_\mathrm{e}}{\mathrm{K}} \right)^{0.175} \left(\frac{D}{\mathrm{pc}} \right)^{2.5} \left(\frac{\theta_\mathrm{S}}{\mathrm{arcsec}} \right)^{1.5}, \tag{5.2}$$

where T_e is the electron temperature, D is the distance to the source, and θ_S is the angular size of the source. I assume that the free-free emission is from HII regions with a radius of $0.5''$and an electron temperature of 10^4 K. Then the mass of the HII region can be expressed as:

$$\left(\frac{M_{\rm HII}}{M_\odot}\right) = 0.09 \left(\frac{S_\nu}{\rm Jy}\right)^{0.5}. \tag{5.3}$$

Alongside with $M_{\rm HII}$, the flux of Lyman continuum photons ($\dot{N}_{\rm Ly}$) from each core can be calculated following Eq. A.29. Assuming that $T_e = 10^4$ K, Eq. A.29 is reduced to:

$$\frac{\dot{N}_{\rm Ly}}{\rm s^{-1}} = 7.405 \times 10^{48} \frac{S_{\rm ff6}}{\rm Jy}. \tag{5.4}$$

The dust emission SED can be modeled as a gray-body, see Equation A.33. I assume that

$$\kappa_0 \left(\frac{\nu}{\nu_0}\right)^\beta N_{\rm d} \ll 1 \tag{5.5}$$

then Equation A.33 can be approximated to

$$S_\nu = \frac{2h\nu^3}{c^2} \frac{1}{e^{\frac{h\nu}{k_{\rm B}T_{\rm d}}} - 1} \kappa_0 \left(\frac{\nu}{\nu_0}\right)^\beta N_{\rm d} \frac{A}{D^2}. \tag{5.6}$$

where $N_{\rm d}A$ is simply the mass of dust within one core, $M_{\rm d}$. I assume a gas-to-dust ratio of 100, then the dust flux and gas mass $M_{\rm H_2}$ have a relationship:

$$S_\nu = \frac{2h\nu^3}{c^2} \frac{1}{e^{\frac{h\nu}{k_{\rm B}T_{\rm d}}} - 1} \kappa_0 \left(\frac{\nu}{\nu_0}\right)^\beta \frac{M_{\rm H_2}}{100} D^{-2}. \tag{5.7}$$

For the models of dust opacity $\kappa_0 \left(\frac{\nu}{\nu_0}\right)^\beta$, I take "mrn8" and "thin8" from Table A.1, which stands for agglomerated naked and thin-ice-mantle-covered dust grains in density of 10^8 cm^{-3} (see Ossenkopf & Henning, 1994), respectively. Also, I assume two cases in which dust temperature $T_{\rm d}$ is 50 and 100 K, following Sánchez-Monge et al. (2017). Thus, I solve the superposition of Equation 5.1 and Equation 5.7 by inserting S_6 and S_{96}.

Table 5.3 Physical parameters of Type I cores

	mrn8					thin8				
		$T_{\rm d}=50$ K		$T_{\rm d}=100$ K			$T_{\rm d}=50$ K		$T_{\rm d}=100$ K	
ID	$S_{\rm ff6}$ mJy	$M_{\rm HII}$ $M_\odot$	$M_{\rm H_2}$ $M_\odot$	$M_{\rm HII}$ $M_\odot$	$M_{\rm H_2}$ $M_\odot$	$S_{\rm ff6}$ mJy	$M_{\rm HII}$ $M_\odot$	$M_{\rm H_2}$ $M_\odot$	$M_{\rm HII}$ $M_\odot$	$M_{\rm H_2}$ $M_\odot$
1	0.9	0.09	5.0	0.09	2.4	0.9	0.09	39.8	0.09	19.4
2	11.4	0.30	15.6	0.30	7.6	11.4	0.30	123.9	0.30	60.5
3	8.7	0.27	11.7	0.27	5.7	8.7	0.27	93.0	0.27	45.4
4	77.5	0.79	156.3	0.79	76.4	77.5	0.79	1245.1	0.79	608.2
5	21.5	0.42	33.4	0.42	16.3	21.5	0.42	266.2	0.42	130.0
6	6.8	0.23	5.2	0.23	2.6	6.8	0.23	41.6	0.23	20.3
7	4.2	0.18	17.9	0.18	8.8	4.2	0.18	142.8	0.18	69.7
8	13.9	0.34	593.6	0.34	290.0	14.0	0.34	4728.4	0.34	2309.7
9	3.6	0.17	1082.7	0.17	528.9	3.8	0.18	8624.3	0.18	4212.8
10	1.3	0.10	6.9	0.10	3.4	1.3	0.10	55.0	0.10	26.9

Table 5.3 Physical parameters of Type I cores (*continued*)

	mrn8					thin8				
		$T_{\rm d}=50$ K		$T_{\rm d}=100$ K			$T_{\rm d}=50$ K		$T_{\rm d}=100$ K	
ID	$S_{\rm ff6}$ mJy	$M_{\rm HII}$ $M_\odot$	$M_{\rm H_2}$ $M_\odot$	$M_{\rm HII}$ $M_\odot$	$M_{\rm H_2}$ $M_\odot$	$S_{\rm ff6}$ mJy	$M_{\rm HII}$ $M_\odot$	$M_{\rm H_2}$ $M_\odot$	$M_{\rm HII}$ $M_\odot$	$M_{\rm H_2}$ $M_\odot$
11	45.3	0.61	182.9	0.61	89.3	45.3	0.61	1456.9	0.61	711.7
12	1.2	0.10	9.1	0.10	4.4	1.2	0.10	72.4	0.10	35.4
13	5.7	0.22	84.2	0.22	41.1	5.7	0.22	671.0	0.22	327.8
14	20.3	0.41	12.4	0.41	6.1	20.3	0.41	99.0	0.41	48.4
15	1.0	0.09	5.9	0.09	2.9	1.0	0.09	46.8	0.09	22.8
16	0.9	0.09	5.8	0.09	2.9	0.9	0.09	46.5	0.09	22.7
17	5.7	0.21	4.1	0.21	2.0	5.7	0.21	32.4	0.21	15.8
18	25.9	0.46	34.4	0.46	16.8	25.9	0.46	274.3	0.46	134.0
19	28.0	0.48	54.6	0.48	26.7	28.0	0.48	435.2	0.48	212.6
20	0.7	0.07	8.5	0.07	4.1	0.7	0.07	67.6	0.07	33.0
21	9.9	0.28	31.6	0.28	15.4	10.0	0.28	251.7	0.28	123.0
22	68.7	0.75	123.4	0.75	60.3	68.7	0.75	982.7	0.75	480.0
23	20.3	0.41	42.2	0.41	20.6	20.4	0.41	336.5	0.41	164.4
24	37.5	0.55	40.6	0.55	19.8	37.5	0.55	323.1	0.55	157.8
25	20.6	0.41	115.1	0.41	56.2	20.6	0.41	917.1	0.41	448.0
26	60.1	0.70	264.1	0.70	129.0	60.2	0.70	2103.5	0.70	1027.5
27	47.5	0.62	548.8	0.62	268.1	47.6	0.62	4371.8	0.62	2135.5
28	13.1	0.33	320.0	0.33	156.3	13.1	0.33	2549.3	0.33	1245.3
29	120.3	0.99	1899.1	0.99	927.7	120.7	0.99	15127.4	0.99	7389.4
30	10.0	0.28	20.3	0.28	9.9	10.0	0.28	161.9	0.28	79.1
31	127.1	1.01	2625.8	1.01	1282.6	127.6	1.02	20915.3	1.02	10216.7
32	85.6	0.83	1552.0	0.83	758.1	85.9	0.83	12362.4	0.83	6038.8
33	7.9	0.25	34.5	0.25	16.8	7.9	0.25	274.6	0.25	134.2
34	9.5	0.28	23.8	0.28	11.6	9.5	0.28	189.8	0.28	92.7
35	91.0	0.86	3204.7	0.86	1565.4	91.7	0.86	25526.3	0.86	12469.0
36	36.4	0.54	1758.9	0.54	859.2	36.7	0.55	14010.6	0.55	6843.9
37	12.5	0.32	339.1	0.32	165.7	12.6	0.32	2701.4	0.32	1319.6
38	9.9	0.28	17.5	0.28	8.5	9.9	0.28	139.0	0.28	67.9
39	14.4	0.34	590.9	0.34	288.6	14.6	0.34	4706.4	0.34	2299.0
40	6.0	0.22	261.8	0.22	127.9	6.0	0.22	2085.6	0.22	1018.8
41	11.6	0.31	156.9	0.31	76.7	11.7	0.31	1250.0	0.31	610.6
42	18.0	0.38	35.9	0.38	17.5	18.0	0.38	285.6	0.38	139.5
43	50.4	0.64	204.7	0.64	100.0	50.4	0.64	1630.2	0.64	796.3
44	30.8	0.50	60.1	0.50	29.4	30.8	0.50	479.1	0.50	234.0
45	7.7	0.25	30.1	0.25	14.7	7.7	0.25	239.8	0.25	117.1
46	36.2	0.54	87.8	0.54	42.9	36.2	0.54	699.2	0.54	341.5
47	6.0	0.22	4.4	0.22	2.2	6.0	0.22	35.1	0.22	17.1
48	42.2	0.58	48.5	0.58	23.7	42.2	0.58	386.7	0.58	188.9
49	4.8	0.20	1.9	0.20	1.0	4.8	0.20	15.5	0.20	7.6
50	7.8	0.25	1.3	0.25	0.6	7.8	0.25	10.5	0.25	5.1
51	4.2	0.18	7.9	0.18	3.8	4.2	0.18	62.6	0.18	30.6
52	95.2	0.88	695.7	0.88	339.9	95.4	0.88	5541.9	0.88	2707.1
53	0.8	0.08	21.8	0.08	10.7	0.8	0.08	174.0	0.08	85.0
54	27.0	0.47	15.2	0.47	7.4	27.0	0.47	120.9	0.47	59.0
55	–	–	–	–	–	–	–	–	–	–
56	2.1	0.13	1.0	0.13	0.5	2.1	0.13	7.8	0.13	3.8
57	0.3	0.05	0.5	0.05	0.2	0.3	0.05	4.0	0.05	2.0
58	0.1	0.03	2.3	0.03	1.1	0.1	0.03	18.7	0.03	9.1

In Table 5.3 I list the values of $S_{\rm ff6}$, $M_{\rm HII}$, and $M_{\rm H_2}$ of each core. As shown in Table 5.3, although varying $T_{\rm d}$ and dust opacity models give distinct values of $M_{\rm H_2}$, $S_{\rm ff6}$ remains nearly unchanged. This is due to the contribution of dust emission at 6 GHz is negligible.

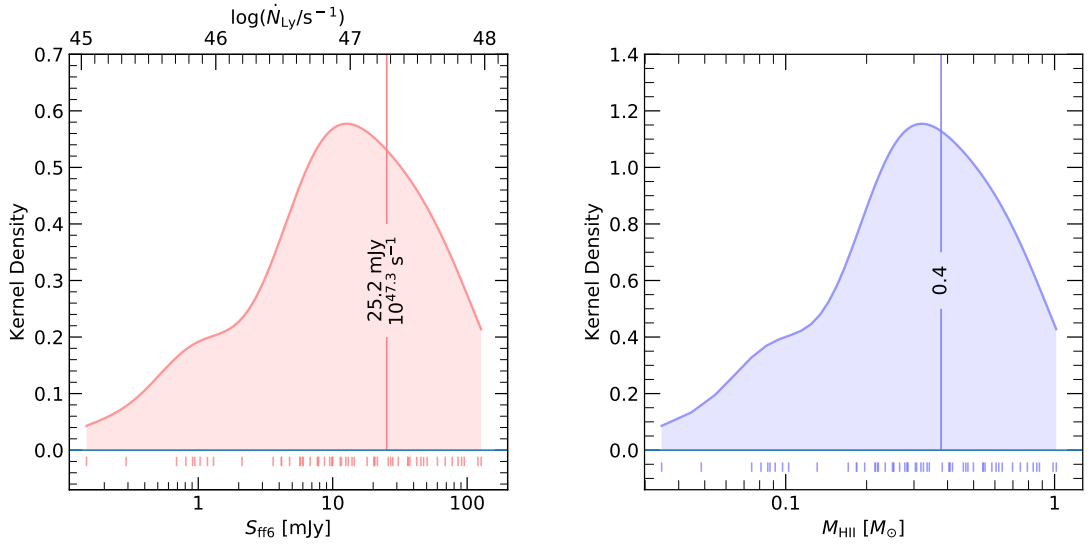

Figure 5.6 *Left panel:*Probability distribution of $S_{\rm ff6}$ and Lyman photon flux for all the type I cores. Due to that $S_{\rm ff6}$ of the four cases in Table 5.3 of each core are very similar to each other, here only the distribution of the case "thin8" and $T_{\rm d} = 100$ K is shown. The average value of $S_{\rm ff6}$ is marked. The upper axis shows the corresponding Lyman photon flux. *Right panel:* Probability distribution of $M_{\rm HII}$ and Lyman photon flux for all the type I cores, for similar reasons like the distribution of $S_{\rm ff6}$ only the case "thin8" and $T_{\rm d} = 100$ K is shown. The average value of $M_{\rm HII}$ is marked.

In Figure 5.6, I show the probability density distribution of $S_{\rm ff6}$, $\dot{N}_{\rm Ly}$, $M_{\rm HII}$. For $S_{\rm ff6}$, I use the case "thin8" and $T_{\rm d} = 100$ K to represent all the four cases. The average value of $S_{\rm ff6}$ of all the type I cores is 25.2 mJy, which correspond to $\dot{N}_{\rm Ly} = 10^{47.3}$ s^{-1}. Such a flux of Lyman continuum photons corresponds to a B0 star (see Panagia, 1973). The average value of the derived $M_{\rm HII}$ of all the type I cores is 0.4 $M_\odot$.

The distribution of $M_{\rm H_2}$ and the ratio between $M_{\rm HII}$ and $M_{\rm H_2}$ are shown in Figure 5.7. For $M_{\rm H_2}$, the KDE of all the four cases in Table 5.3 are plotted. The gaseous mass of the cores with dust opacity model 'thin8' are in general larger by a factor of 8 than the mass derived with dust opacity model 'mrn8'. With the same dust opacity model, $M_{\rm H_2}$ is proportional to $T_{\rm d}$. The average $M_{\rm H_2}$ is 150, 307, 1196, and 2448 $M_\odot$ under the four cases (for the four cases, see Figure 5.6). The ratio between mass of HII region and the gaseous mass of the core is $10^{-3.1}$, $10^{-2.8}$, $10^{-2.2}$, and $10^{-1.9}$ for the four cases.

The relationship between $S_{\rm ff6}$ (and the corresponding $\dot{N}_{\rm Ly}$) and $M_{\rm H_2}$ of type I cores, for the cases of "mrn8" and "thin8", and $T_{\rm d}$ is 50 and 100 K, is plotted in Figure 5.8, the averaged value of $S_{\rm ff6}$ with $T_{\rm d} = 50$ and 100 K is regarded as data while half of the difference between these two cases are treated as error. For both of the cases, I approximately get $S_{\rm ff6} \propto M_{\rm H_2}^{0.4}$.

Additionally, the relationship between $M_{\rm HII}$ and $M_{\rm H_2}$ are plotted, see Figure 5.9. The averaged value and the difference between two opacity models are treated as the same as in

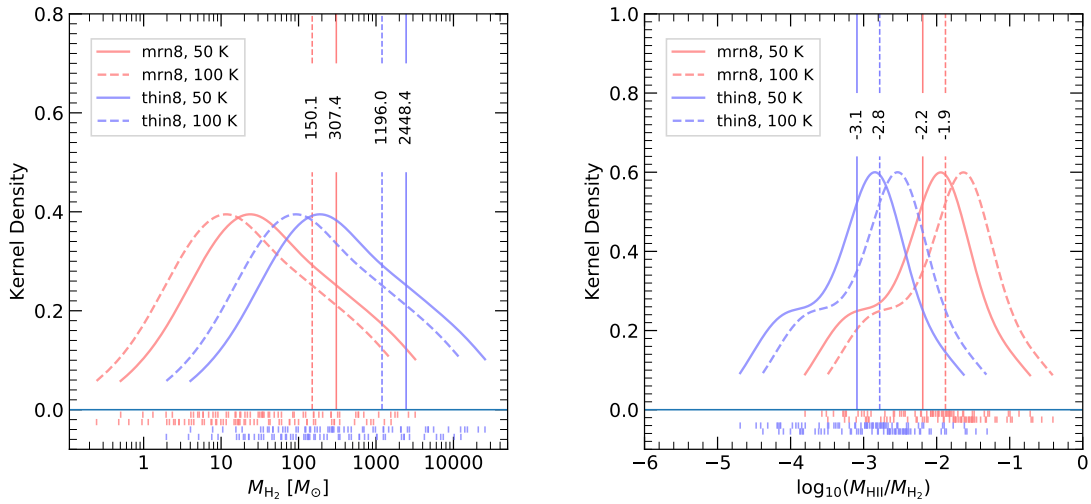

Figure 5.7 *Left panel:*Probability distribution of M_{H_2} for all the type I cores. Two dust opacity models "mrn8" and "thin8" are combined with two T_d, 50 and 100 K, and therefore four distributions are shown. The averaged M_{H_2} of each distribution is shown. *Right panel:* Probability distribution of M_{HII}/M_{H_2} for all the type I cores. Same as the left panel, four distributions are shown. The averaged M_{H_2} of each distribution is shown.

Figure 5.8. As expected, since $M_{II} \propto S_{ff6}^{1/2}$, I get $M_{II} \propto M_{H_2}^{0.21}$.

5.3.2 Associated objects

I searched for possible associations of other objects and sources with the 308 cores identified in the SgrB2 region. For this, I used additional observations of masers, X-ray sources and outflows, and searched for counterparts in a circle of radius 0.83″ around each core. In the following, I present the association of the compact cores with other features and objects.

Masers and X-ray sources

In total, 24 cores are found associated with masers[1], and 3 cores are found associated with X-ray emission (X-ray source cataloag: Takagi et al., 2002; Muno et al., 2006). Among all the 24 cores that are associated with maser, 62.5%(15) are type I cores, which is higher than the percentage (19%) of type I cores in the entire sample.

The 6 GHz methanol (CH_3OH) masers occur only when associated with massive young stars (Caswell et al., 2010). I found 9 cores associated with 6 GHz methanol masers, among which 5 are type II cores. The 4.8 GHz formaldehyde (H_2CO) masers are pumped by continuum emission from a nearby HII region (Mehringer et al., 1994). Among the five formaldehyde masers detected by Whiteoak & Gardner (1983) and four formaldehyde masers detected by Mehringer et al. (1994), which are named alphabetically from A to I, six are found associated with ten cores in our catalog, with D, G, and H leftover. Additionally,

[1] The masers are: OH maser (Braz & Epchtein, 1983; Lindqvist et al., 1992; Argon et al., 2000; Caswell, 2004), 6 GHz CH_3OH maser (Caswell et al., 2010), and 4.8 GHz H_2CO maser (Mehringer et al., 1994).

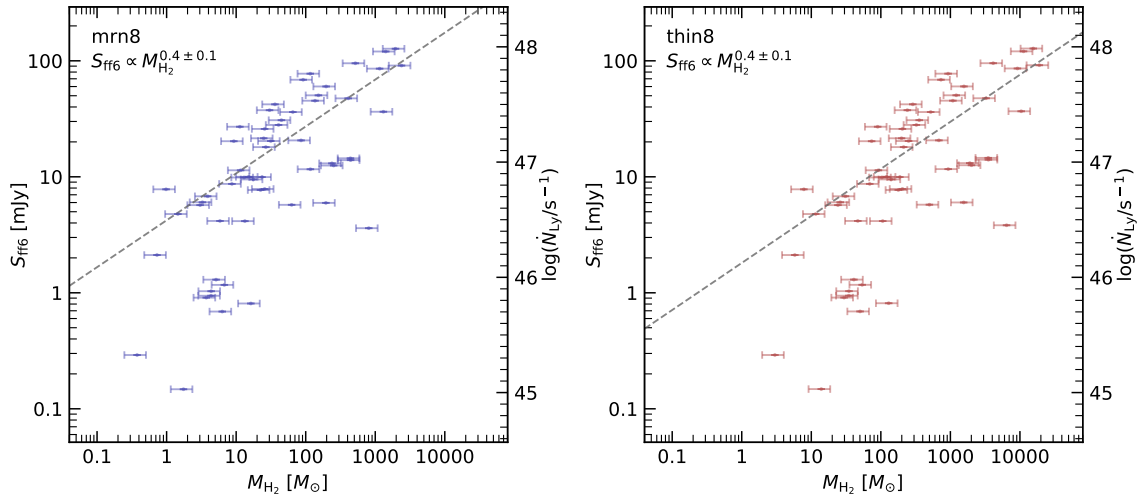

Figure 5.8 Relation between $S_{\rm ff6}$ and $M_{\rm H_2}$ of type I cores (left axis). Relation between Lyman photon flux and $M_{\rm H_2}$ of type I cores (right axis). for for case "mrn8" and "thin8" in left and right panel respectively. Averaged value with $T_{\rm d}$ = 50 and 100 K is regarded as data while half of the difference between these two cases are treated as error.

OH masers (Braz & Epchtein, 1983; Lindqvist et al., 1992; Argon et al., 2000; Caswell, 2004) are also identified to be associated with eleven cores.

It is worth to notice that three cores are found to be associated with X-ray source. Among the three cores, two are in the center of SgrB2(M), while one (core #55) is in SgrB2(DS), and associated with 2MASS J17472335-2825340 (Muno et al., 2006). Very likely, core #55 is an extragalactic source instead of really in SgrB2, which will be further discussed in the following sections.

Outflows

Outflows can be traced by SiO emission (e.g. Schilke et al., 1997). In this section, I investigated the spatial correlation of the outflows traced by the SiO (5–4) and the cores.

The SiO (5–4) emission was observed with ALMA (Project 18A-229, P.I. A. Ginsburg). For the details of the observation and data reduction, see Ginsburg et. al. (in prep.). The resolution is $0.35'' \times 0.24''$, with P.A. of $-80°$. The spectral resolution is 1.35 km s^{-1}. The typical RMS of the image is 0.9 mJy/beam. The observation covers SgrB2(S) and the eastern part of SgrB2(DS), see Figure. 5.1.

The peak intensity map of SiO (5–4) is shown in Figure 5.10. Due to the artifacts around SgrB2(S), I only analyze the part of the image with declination < -28:24:00. Masked out all the pixels below 3×0.9 mJy/beam, I get also the moment 1 map of SiO (5–4), see Figure 5.11. Most of the outflows traced by the SiO emission have velocity difference between two lobes of ~ 10 km s^{-1} . Also, most of the outflows are associated with cores. Among all the 120 cores covered by the SiO image, 49 are identified as associated with outflows, see Table B.1. It is worth to mention that for the cores that are in the vicinity of

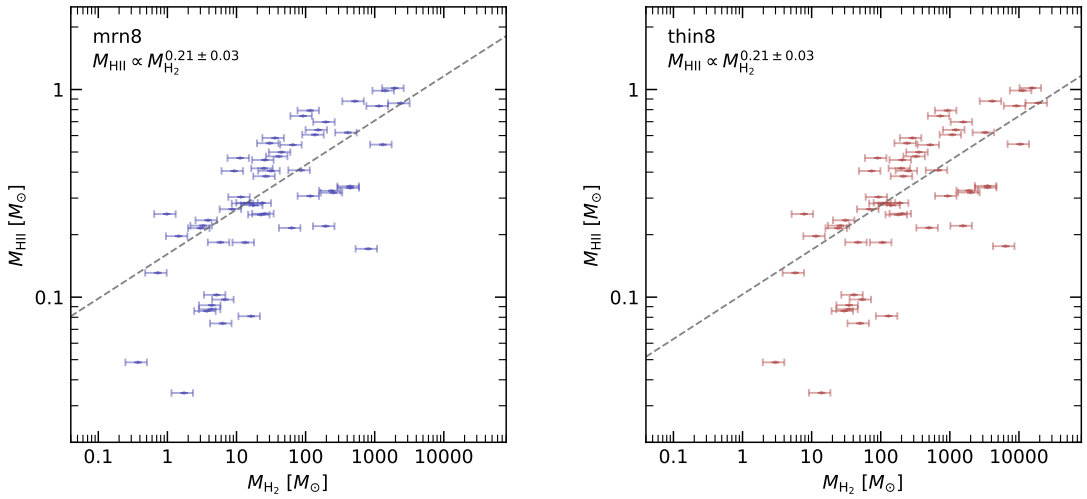

Figure 5.9 Relation between $M_{\rm HII}$ and $M_{\rm H_2}$ of type I cores, for for case "mrn8" and "thin8" in left and right panel respectively. Averaged value with $T_{\rm d} = 50$ and 100 K is regarded as data while half of the difference between these two cases are treated as error.

SgrB2(DS), the artifact impede the identification of the real outflows, so it is also unknown if the cores are associated with outflows there. Considering this, almost all the cores that are in the east lobe of the SgrB2(DS) region are associated with outflows.

5.3.3 Evolutionary stages

The associated objects of the dust cores are the hints of evolutionary stages in star formation activity. In Table 5.4, I summarize the number of associated objects of the dust cores in the subregions, SgrB2(N), SgrB2(M), SgrB2(S), SgrB2(DS), and the rest part of envelope, of SgrB2.

The Type I cores are associated with HII regions, since the emission at 6 GHz traces free-free emission. Among all the 58 Type I cores, 8 are in SgrB2(N), 30 are in SgrB2(M),

Table 5.4 Associated objects of the dust cores.

Region	N	M	S	DS	Rest[a]	Total
Dust core	24	55	46	46	137	308
HII region	8	30	2	3	15	58
CH_3OH Maser	2	2	0	0	5	9
H_2CO Maser	2	2	0	0	2	6
OH Maser	2	3	1	0	5	11
Outflow	_[b]	_[b]	_[b]	31	18[b]	49[b]

a: Rest of the envelope.
b: Not fully covered by the SiO map.

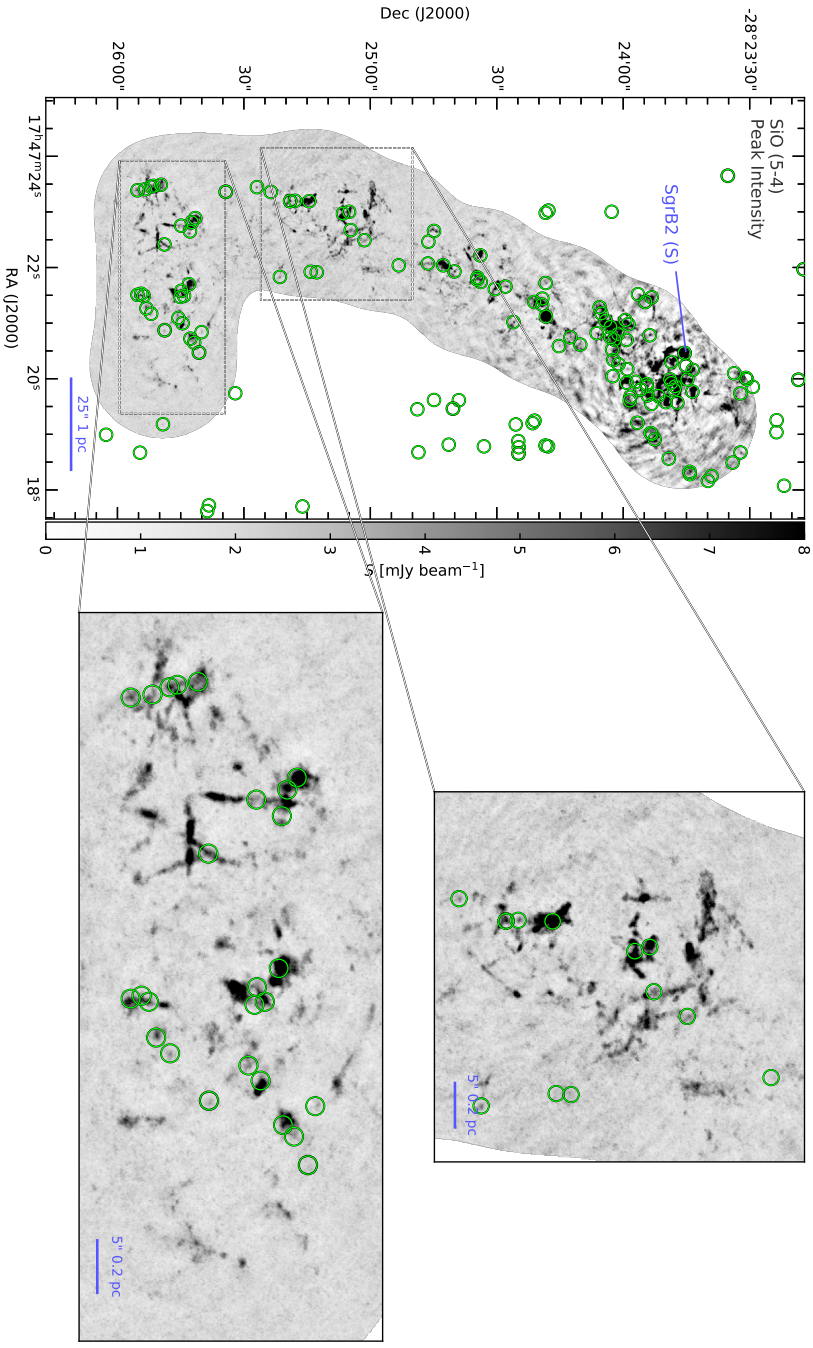

Figure 5.10 Peak intensity map of SiO (5-4) line. The zoomed in plots are the regions in SgrB2(DS) that with abundant outflows. The resolution of the image is $0.35'' \times 0.24''$, with P.A. of $-80°$. The identified cores are marked as green circles, whose size is irrelevant to the size of the cores.

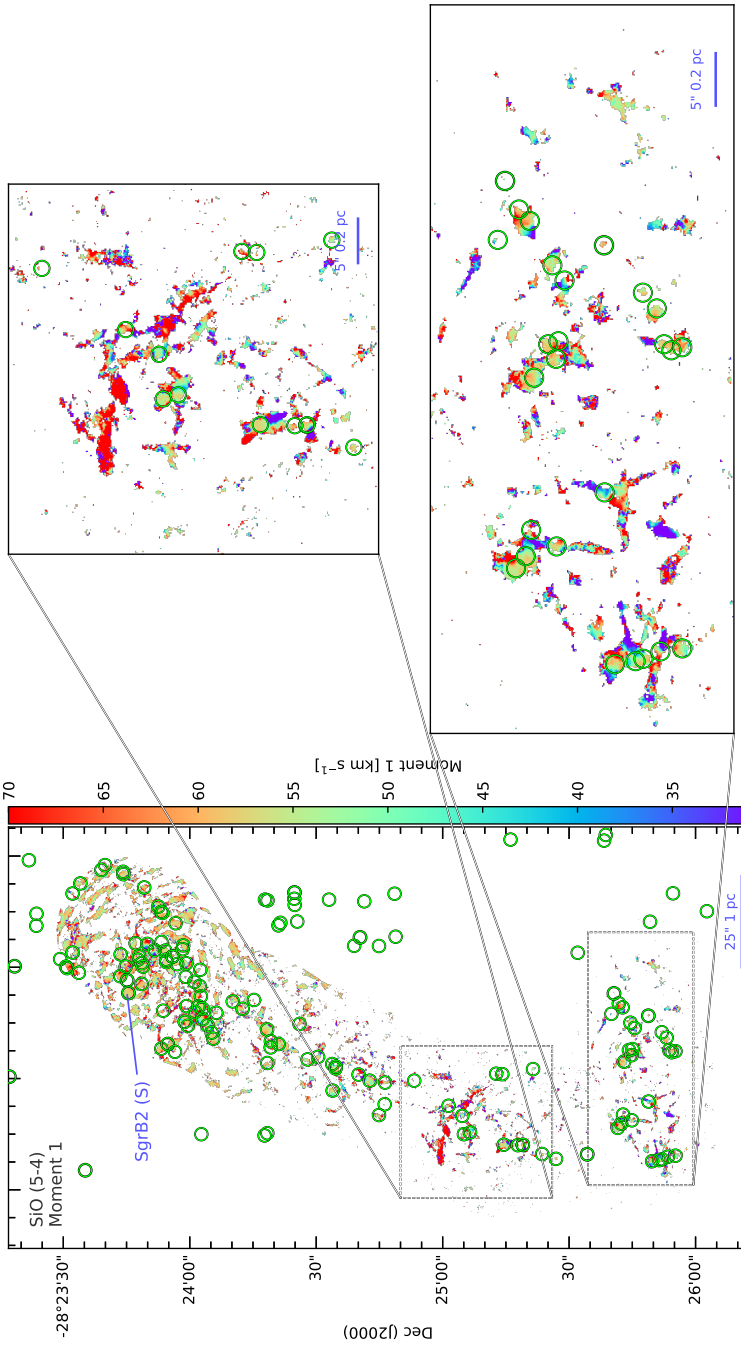

Figure 5.11 Moment 1 map of SiO (5-4) line. The zoomed in plots are the regions in SgrB2(DS) that with abundant outflows. The resolution of the image is $0.35'' \times 0.24''$, with P.A. of $-80°$. The identified cores are marked as green circles, whose size is irrelevant to the size of the cores.

2 are in SgrB2(S), 3 are in SgrB2(DS) and 15 in the rest of the envelope. Hence, the percentage of the dust cores that are associated with HII region are 33%, 55%, 4%, and 7% for SgrB2(N), SgrB2(M), SgrB2(S), and SgrB2(DS), respectively. While for the rest part of the envelope, the percentage is 11%. For the dust cores, being associated with HII region is a sign of being more evolved (see e.g. Breen et al., 2010). Therefore, the cores in SgrB2(M) are the most evolved compare to the cores in other regions, while the cores in SgrB2(S) and SgrB2(DS) are less evolved. The evolutionary stages of the cores in SgrB2(N) are between that of SgrB2(M) and SgrB2(DS) or SgrB2(S).

The CH_3OH-, H_2CO-, and OH-masers trace the star forming activities. In Table 5.4, the number of masers that are associated with the dust cores that are in each region are listed. The cores in both of SgrB2(M) and SgrB2(N) are associated with two CH_3OH maser and two H_2CO. The cores in SgrB2(DS) has no associated masers. Such a lack of associated masers also suggested that the cores in SgrB2(DS) are less evolved than that in SgrB2(N) and SgrB2(M).

The collimated outflows are the footprints of the very early stages of star formation activity (see e.g. Beuther et al., 2002). Unfortunately, the image area of SiO, which traces the outflows, covers only SgrB2(DS) and its vicinity[2]. Among all the cores in SgrB2(DS), 2/3 are associated with outflows. Such a high fraction confirms that the cores in SgrB2(DS) is at their very early evolutionary stages.

5.4 Summary

In this chapter, with the data from eight frequency bands, from cm wavelength to mm wavelength, I have characterized the properties of the dense cores and their associated HII regions throughout the whole SgrB2 region. Additionally, I searched for other star formation tracers associated with these dense cores. My main results are:

- From data at 96 GHz, 308 dust cores are identified, out of which 58 cores are found associated with HII regions and named Type I cores. The dust cores that have no associated HII regions are named Type II cores. The mean value of flux density at 96 GHz for Type I cores is 214.9 mJy and for Type II cores is 16.9 mJy.

- The SEDs of Type I cores have been modeled. Type I cores have a mean m_{H_2} of 150–2500 $M_\odot$ for gas temperatures 50–100 K. Most of the 58 HII regions have a Lyman continuum photon flux between $10^{46} - 10^{48}\,s^{-1}$, which corresponds to stellar spectral types around B0 and O9.

- Evolutionary stages of the cores in SgrB2(N), SgrB2(M), SgrB2(S), and SgrB2(DS) are analyzed. Among the cores in SgrB2(N) and SgrB2(M), 33% and 55% are associated with HII regions, respectively. While for the 46 cores in SgrB2(S) and the 46 cores in SgrB2(DS), this percentage is 4% and 7%, respectively. Out of the 46 cores in SgrB2(DS), 31 are associated with outflows, which are traced by SiO emission. Therefore, I conclude that the cores in SgrB2(M) are more evolved, followed by the cores in SgrB2(N). The cores in SgrB2(S) and SgrB2(DS) are less evolved and are at their very early stages.

[2]For the reason why I treat it as not covering SgrB2(S), see Section 5.3.2.

Chapter 6

Medium Scale: Deep South

In previous chapter I studied the properties of dense cores in SgrB2. A remarkable feature is the presence of about 60 dense cores in the southern region, following an arc-shape distribution. This group of cores is spatially coincident with the arc-shaped feature detected in NH_3 by Martín-Pintado et al. (1999), which is referred to as Deep South (hereafter DS) by Ginsburg et al. (2018). At the position of Sgr B2(DS), Mehringer et al. (1993) report the detection of radio continuum and radio recombination line (RRL) emission (see also LaRosa et al., 2000; Law et al., 2008a). Such continuum emission at radio wavelengths along with RRLs is usually related to thermal ionized gas from HII regions (e.g., Kurtz, 2002, 2005). However, along with the thermal emission detected in previous studies, non-thermal emission, has also been found in Sgr B2 due to relativistic electrons (LaRosa et al., 2005; Hollis et al., 2007; Protheroe et al., 2008; Jones et al., 2011). Yusef-Zadeh et al. (2007a, 2013, 2016) studied the presence of non-thermal emission in the Galactic Center region including Sgr B2. Particularly, observations at 255 MHz, 327 MHz, and 1.4 GHz (Yusef-Zadeh et al., 2007b) revealed non-thermal emission in Sgr B2(M). The thermal and non-thermal contribution to the radio continuum emission can be distinguished by their spectral energy distribution (hereafter SED). The SEDs of both thermal and non-thermal emission can be described by power-laws $S_\nu \propto \nu^\alpha$, where α is the so-called spectral index, which varies from -0.1 to $+2$ for thermal emission (see e.g., Sánchez-Monge et al., 2013) and becomes significantly negative for non-thermal emission (e.g., $\alpha = -0.8$, see Platania et al., 1998).

In this chapter, I present Very Large Array (VLA) observations of Sgr B2(DS) in the frequency regime 4–12 GHz, with configurations BnC and D. Thus, this study focuses on spatial scales from 0.1–5 pc. In Sect. 6.1 I describe the observations as well as the data reduction process. Section 6.2 shows the results, and the study of the spectral index. In Sect. 4 I aim at decomposing the thermal and non-thermal components dominating the emission at radio wavelengths, while in Sect. 5 I discuss on the origin of the non-thermal emission. Finally, I summarize this chapter in Sect. 6.

6.1 Observations and data reduction

We used the VLA in its CnB and D configurations to observe the entire Sgr B2 complex in the frequency bands C (4–8 GHz) and X (8–12 GHz). The observations with the CnB configuration were conducted on May 3 and 5, 2016 (project 16A-195). On February 22

and 23, 2017, the D configuration was employed for the observations (project 17B-063). The continuum emission was observed by combining a total of 64 spectral windows with a bandwidth of 128 MHz each. Alongside the continuum observations, high-resolution spectral windows were used for line observations. Eighteen RRLs in the frequency range from 4 to 12 GHz were observed with a spectral resolution between 31.25 and 62.5 kHz (1–2 km s^{-1}). In Table 6.1, we list the rest frequencies of the 18 RRLs. We used the mosaic mode to cover the whole extent of Sgr B2 ($\sim 20' \times 20'$). A total of 10 and 18 pointings, with primary beam sizes of $7.5'$ and $4.5'$ for the C and X bands, respectively, were used. The quasar 3C286 was used as a flux and bandpass calibrator. The SED of 3C286 from 0.5 to 50 GHz was measured by Perley & Butler (2013), with a flux of 5.059 ± 0.021 Jy at 8.435 GHz and a spectral index of -0.46. The quasar J1820-2528, the flux of which is 1.3 Jy in the C and X bands, was used as phase calibrator. The calibration was done using the standard VLA pipelines provided by the NRAO[1].

Calibration and imaging were done in Common Astronomy Software Applications (CASA) 4.7.2 (McMullin et al., 2007). The calibrated measurement sets of the CnB and D array data were concatenated to improve the *uv* sampling. Self-calibration was performed to reduce imaging artifacts and improve the final sensitivity of the image. Three loops of phase-only self-calibration were conducted, with solution time intervals of two seconds, equal to the integration time of the observations. The self-calibrated measurement sets were used for imaging. All the pointings of the mosaic in each band were primary beam corrected and the mosaic was imaged using the CASA task `tclean`. With a robust factor of 0.5, the images of the C and X bands have synthesized beams of $2.7'' \times 2.5''$, with a position angle (PA) of -82° and $1.8'' \times 1.5''$(PA $= 76^\circ$), respectively. The PA is defined positive north to east. Under such resolutions, the root mean square (RMS) noise of the C and X band images are 0.4 mJy/beam and 0.2 mJy/beam respectively. This RMS noise is limited by dynamic range effects due to the bright emission in the region. We achieve a dynamic range of about 4000 and 2000 for the X- and C-band images, respectively. To investigate the SED over the whole 4–12 GHz range, the measurement sets of the C and X bands were divided into 12 frequency ranges. Thus, 12 images from 4 to 12 GHz were obtained. The *uv* coverage was restricted to 0.6–50 kλ for each frequency range to ensure that every image is sensitive to same spatial scales. The 12 images are convolved to a final circular Gaussian beam of $4''$. In addition to the continuum emission, we also imaged the 18 RRLs. In order to increase the signal-to-noise ratio, we stacked the neighboring RRLs to produce a final set of four stacked RRLs (see Table 6.1 for details). All the RRL images were resampled to a common spectral resolution of 2.5 km s^{-1}. Finally, and with the aim of compensating for the low sensitivity (3 mJy/beam per 2.5-km/s channel), the images of the four stacked RRLs are smoothed to a resolution of $8''$, resulting in a final sensitivity of 1 mJy/beam per 2.5-km/s channel.

[1] The National Radio Astronomy Observatory is a facility of the National Science Foundation operated under cooperative agreement by Associated Universities, Inc.

Table 6.1 Observed and stacked RRLs

RRL	ν_0 (MHz)	Stacked (ν)[a]	RRL	ν_0 (MHz)	Stacked (ν)[a]
H115α	4268.14		H100α	6478.76	
H114α	4380.95	RRL 4.4 GHz	H99α	6676.08	RRL 6.8 GHz
H113α	4497.78		H98α	6881.49	
H112α	4618.79		H97α	7095.41	
H92α	8309.38		H87α	9816.86	
H91α	8584.82		H86α	10161.30	
H90α	8872.57	RRL 8.9 GHz	H85α	10522.04	RRL 10.5 GHz
H89α	9173.32		H84α	10900.06	
H88α	9487.82		H83α	11296.41	

[a] The frequencies of the stacked RRLs are labels corresponding to the average frequency of the stacked lines. These values do not correspond to actual transition frequencies, and are only used in the excitation analysis of Sect. 6.3.2.

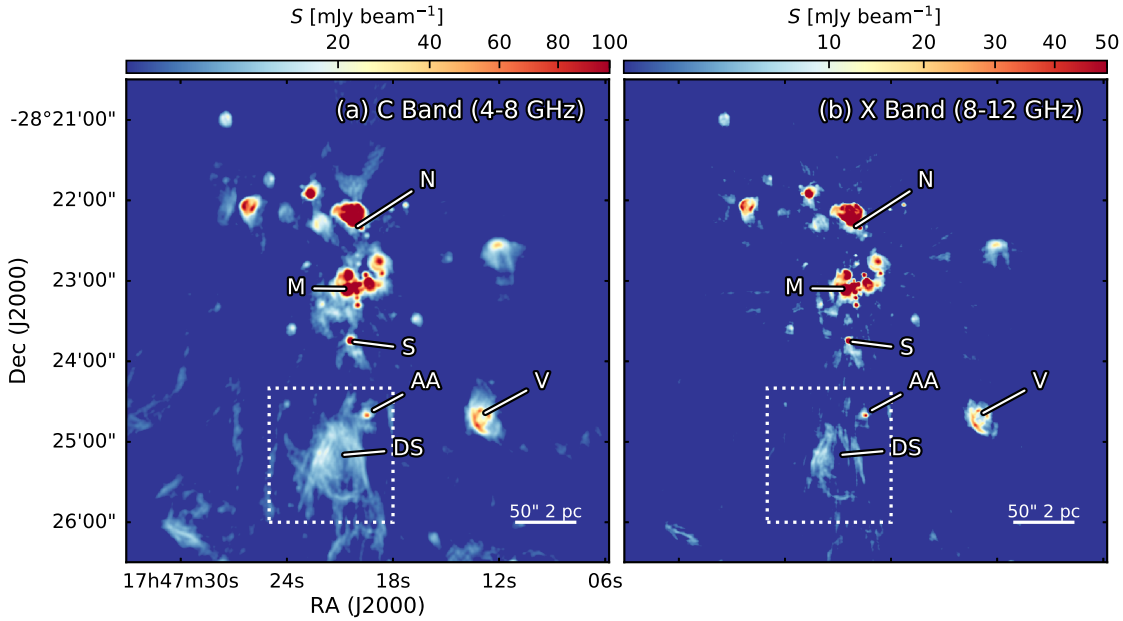

Figure 6.1 Continuum images of Sgr B2 in C (panel a) and X (panel b) bands. Relevant regions are marked with their names (see Mehringer et al., 1993). The dashed boxes mark the region of DS. The synthesized beam of the C and X images are 2.7″×2.5″and 1.82″×1.53″, respectively

6.2 Results

In this section I discuss the distribution of the radio continuum emission in the Sgr B2 region, characterize the spectral index, and study the RRL emission. We pay special attention to the Sgr B2(DS) region.

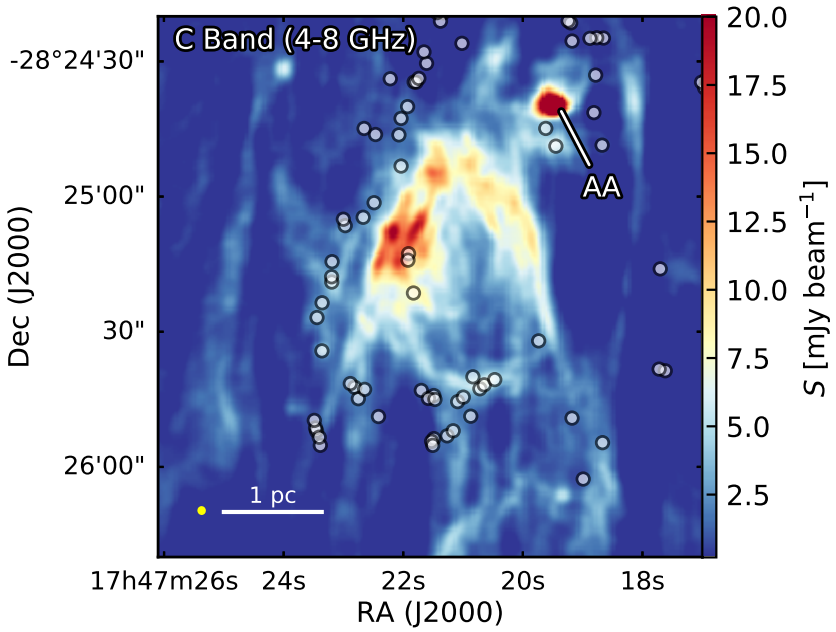

Figure 6.2 C band (4–8 GHz) continuum emission map of Sgr B2(DS). The circles mark the positions of the high-mass protostellar cores identified by Ginsburg et al. (2018). The synthesized beam is shown as a yellow ellipse at the bottom left corner.

6.2.1 Ionized gas in Sgr B2(DS)

The images of the Sgr B2 region in the C and X bands are shown in Fig. 6.1. Some relevant objects such as the regions Sgr B2(N), (M) and (S) are indicated, as well as source V and the HII region AA (see Mehringer et al., 1993). The DS region is the main focus of this chapter. It appears as a bubble-like structure with an outer-diameter of ∼1.5 pc. The thickness of the bubble edge is ∼0.3 pc, with the eastern part being stronger than the western region of the bubble, in both X and C-band images. Filaments and arcs are found along the edge of the bubble, while the emission towards the center is just at the RMS noise level.

The radio continuum emission in DS is spatially connected to the high-mass dust cores revealed by previous ALMA observations at millimeter wavelengths (Ginsburg et al., 2018). As shown in Fig. 6.2, more than 60 dust cores are located at the outskirts of the bubble-like structure, with a larger population of dense cores to the east.

6.2.2 Spectral index analysis

The C and X band data, from 4 to 12 GHz, are divided into 12 tomographic maps and convolved to a common angular resolution of 4″. To ensure that each of the 12 channel maps is sensitive to similar spatial scales, I have set the *uv* limit to the common range 0.6–50 kλ. In Fig. 6.3, I show the portion of the map corresponding to Sgr B2(DS). The intensity decreases significantly from 4 GHz to 12 GHz. I analyzed the SED of the radio emission in DS by fitting a power law to the 12 tomographic maps. I define the variation of flux with frequency as $S_\nu \propto \nu^\alpha$, where S_ν denotes the flux density, ν stands for frequency, and α is the spectral index. The power-law fitting is conducted pixel by pixel for the whole map. For each pixel, the spectral index is fit only if the emission in all the 12 tomographic

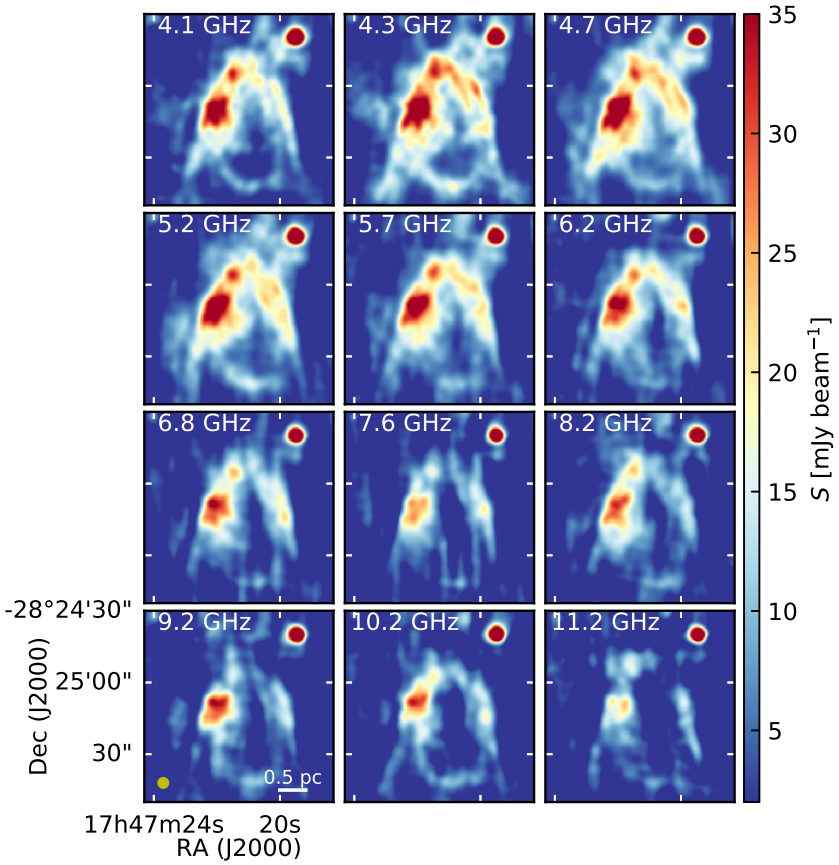

Figure 6.3 Channel maps of the Sgr B2(DS) region. All the 12 maps have been produced considering the same *uv* range limited to 0.6–50 kλ, and have been convolved to a circular beam of 4″. The synthesized beam is shown as a yellow circle in the bottom left panel.

maps is above 3σ, otherwise the pixel is masked. To avoid effects of possible artifacts, the fitting minimizes a loss function $r(z) = \sqrt{1 + z/0.01} - 1$, where z is the square of the difference between the fit power-law function and the observed intensity in the 12 frequency ranges. The uncertainty of α is obtained from the corresponding diagonal element of the covariance matrix of the fitting.

The fit spectral index map of the whole Sgr B2 region, as well as the map of uncertainty of α are shown in Fig. 6.4. The hot cores N, M, as well as other sources in the whole Sgr B2 region, except DS, show spectral indices between -0.01 and 2, which are consistent with thermal emission from HII regions. The central parts in N and M have spectral index values greater than 1, which indicates that the emission is optically thick. At the edges of these hot cores we determine flatter SEDs (e.g., $\alpha = -0.1$), suggesting that the centimeter emission at the edges of these HII regions becomes optically thin.

In contrast to most regions in Sgr B2, the major part of DS shows negative spectral index values (see also Fig. 6.5). I have highlighted the SED of six selected positions in the DS region and shown them in Fig. 6.5. Source AA is included as reference for the spectral index, since it is a known HII region with optically thin free-free emission (Mehringer et al., 1993). As displayed in Fig. 6.5, source AA has $\alpha = 0.01 \pm 0.06$, consistent with optically

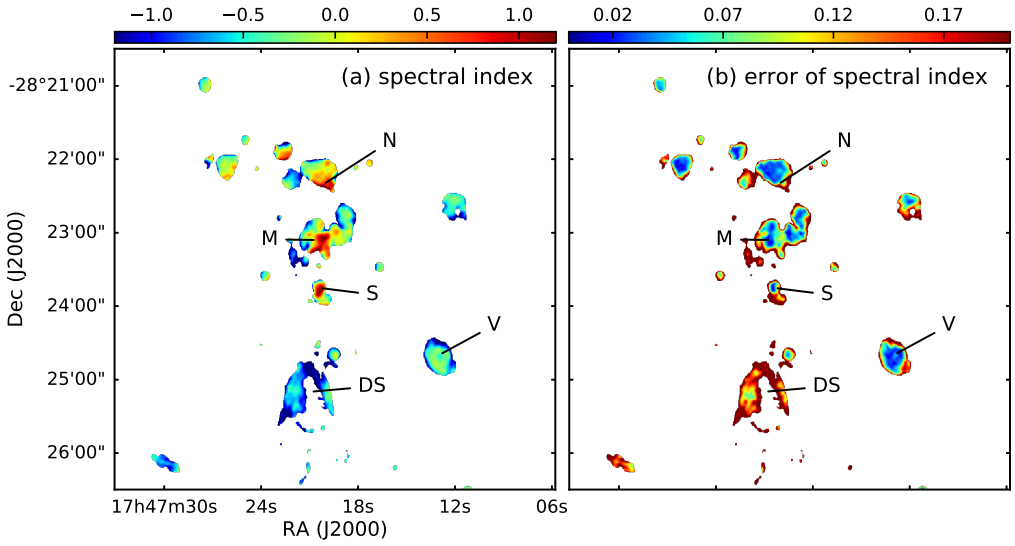

Figure 6.4 The spectral index (α, panel a) and its uncertainty, (panel b) throughout the whole Sgr B2 region. The regions marked in both panels correspond to those regions also labeled in Fig. 6.1. See Sect. 6.2.2 for details in the calculation of the spectral index.

thin free-free emission. The other five spots have negative spectral indices, ranging from -0.4 to -1.2. Such values indicate the existence of non-thermal emission in DS. As shown in the map, the distribution of the non-thermal emission extends to more than 1 pc and forms arc structures.

6.2.3 Radio recombination line emission

In addition to the continuum emission, we also observed RRLs in the whole Sgr B2 region. Due to the low sensitivity of these maps, I have smoothed the images to $8''$. At this resolution it is still capable to resolve the structure of the DS region. On the smoothed maps, Gaussian fitting was conducted and peak intensity, centroid velocity, line width and integrated intensity were obtained for all the four stacked RRLs (see Fig. 6.6).

The integrated intensity maps of the four RRLs show distinct spatial distribution. At 4.4 GHz, the emission appears relatively diffuse, while at 6.8 GHz, different clumpy structures are visible. At 8.9 GHz the northern part of DS is brighter, while at 10.5 GHz, the southern part of DS has more emission. Such a variation is inconsistent with a simple thermal RRL scenario but suggests the presence of other excitation mechanisms, which will be discussed in Sect. 6.3.2. The velocity maps of the four RRLs are in agreement for the four images. The eastern lobe of the bubble shows a velocity gradient ranging from velocities about 70 km s^{-1} in the center down to 55 km s^{-1} in the outer edge. As shown in the line width maps, the RRLs are typically broad, with values above 30 km s^{-1}, significantly exceeding the thermal broadening of RRLs in HII regions with electron temperatures $T_e = 10^4$ K ($\Delta v \approx 20$ km s^{-1}). Notably, the line width at the eastern edge of the bubble reaches more than 40 km s^{-1}. The velocity difference between the eastern edge of DS and the center, together with the increase of line width at the eastern edge, suggests a possible

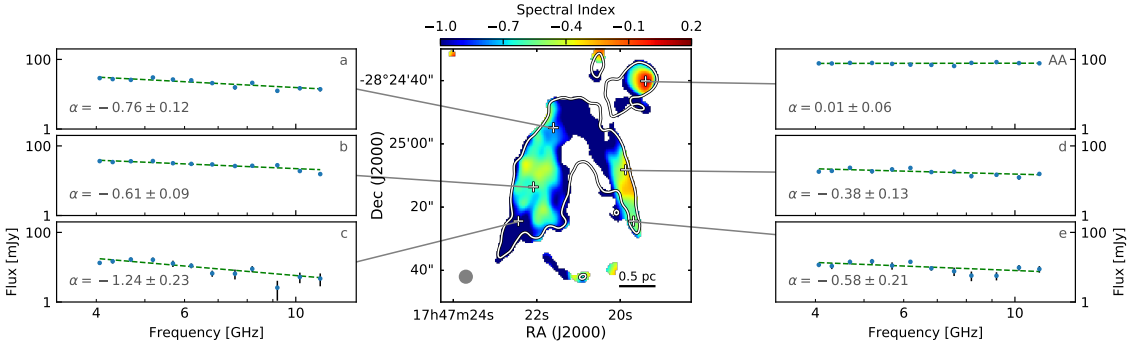

Figure 6.5 The spectral index of DS. Six spots are taken as examples to show the fitting of SED and the fit spectral index (α). The contours are where the flux density at 4 GHz is 10 mJy/beam. The angular resolution is $4''\times4''$, and the beam is shown in the lower left corner.

interaction between the expanding HII region and its surrounding material.

6.3 Thermal and non-thermal components in Sgr B2(DS)

The power-law fitting of the continuum emission in Sgr B2(DS) results in a spectral index α that varies from -1.2 to -0.1. The observed range of values of α implies that the centimeter continuum emission in DS is a mixture of thermal and non-thermal contributions. In this section, I dissect the thermal and non-thermal components in the continuum emission and also analyze the properties of the RRL emission.

6.3.1 Disentangling the thermal and non-thermal components

In the following I present two different approaches to disentangle the contributions of the thermal and non-thermal emission in order to better characterize their origin in Sect. 6.4. The two methods are extrapolating high-frequency emission and fitting the SED with fixed spectral indices.

Extrapolating high-frequency emission

Thermal emission at radio wavelengths is characterized by a relation in which the intensity increases with or is independent of the frequency. On the contrary, the non-thermal emission is characterized by the intensity decreasing with frequency. This suggests that the emission at higher frequencies (corresponding to 11.2 GHz in our dataset) is likely to be dominated by the thermal component, while the emission at lower frequencies (corresponding to 4 GHz) is dominated by the non-thermal component. In the first approach, I assume that the emission at the highest frequency in our data is dominated by pure thermal (free-free) emission.

The total flux of DS at 11.2 GHz is 0.5 Jy within a diameter of $\sim36''$, corresponding to a brightness temperature of 14 K. For a typical HII region temperature of 5×10^3–10^4 K, the optical depth τ ranges from 1.4×10^{-3} to 2.8×10^{-3}. Therefore, the free-free emission of DS is optically thin. I use the typical spectral index $\alpha=-0.1$ of optically thin free-free emission to extrapolate the 11.2 GHz flux density to 4 GHz. The extrapolated thermal component is

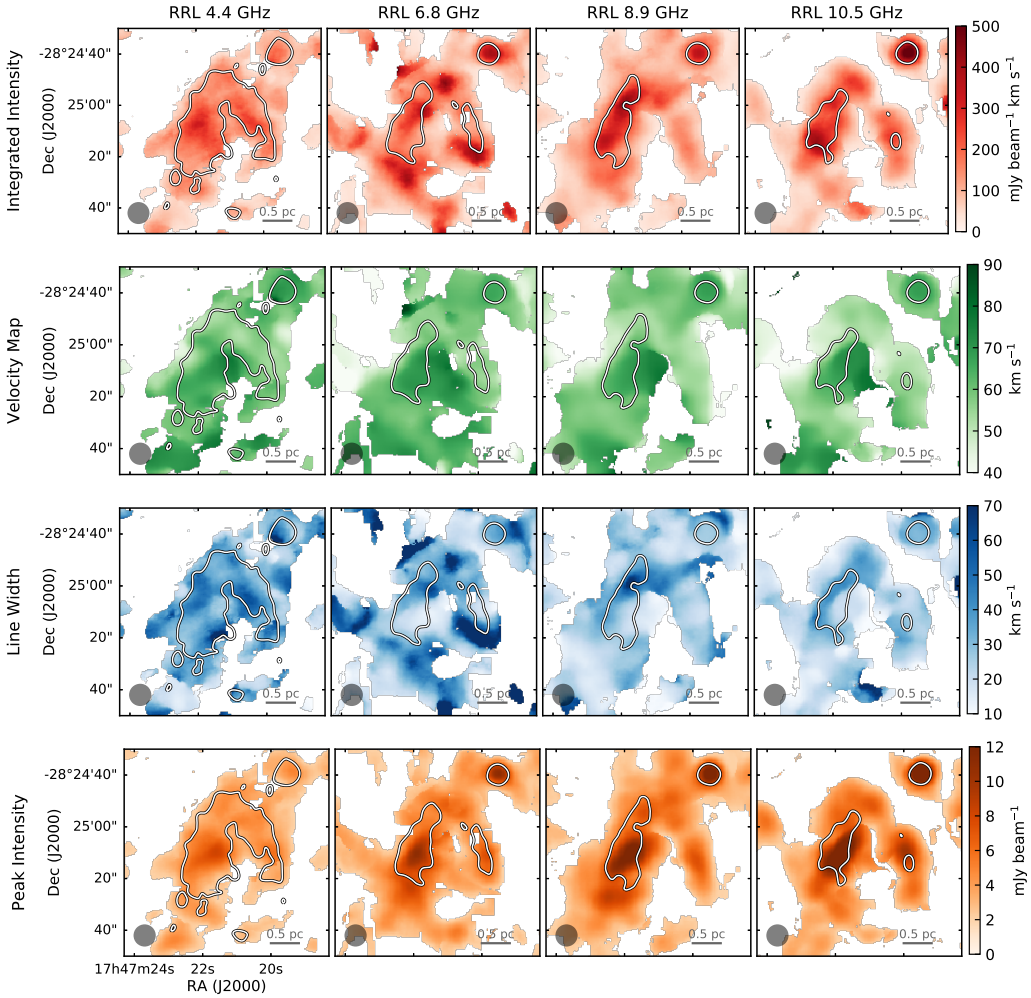

Figure 6.6 Maps of the fit parameters of RRLs in DS. From top to bottom the four rows show the integrated intensity, centroid velocity, line width, and peak intensity. The RRLs are fit with a Gaussian function. The synthesized beam (8 arcsec) is shown at the lower left corner of each panel. Continuum emission at respective frequencies (4.4, 6.8, 8.9 and 10.5 GHz) are overlaid as contours.

subtracted from the observed flux density at 4 GHz to get a pure non-thermal component. In Fig. 6.7 I show the derived thermal and non-thermal components at 4 GHz. The non-thermal emission appears more widespread, while the thermal component appears concentrated in different clumps located along the edge of the bubble. As expected, the HII region AA has strong thermal emission, while at 4 GHz, the contribution from the non-thermal component drops below the RMS level. Only in the southeastern region, connecting source AA with the bubble-like structure of DS, I find some presence of a possible contribution of non-thermal emission.

The total observed flux at 4 GHz (within the circle highlighted in Fig. 6.7) is ∼1.5 Jy, for which I determine that ∼60% has a non-thermal origin. Since I have assumed that the emission at 11.2 GHz is purely thermal, the contribution of thermal emission at 4 GHz is most likely overestimated and therefore, the non-thermal contribution may be underestimated.

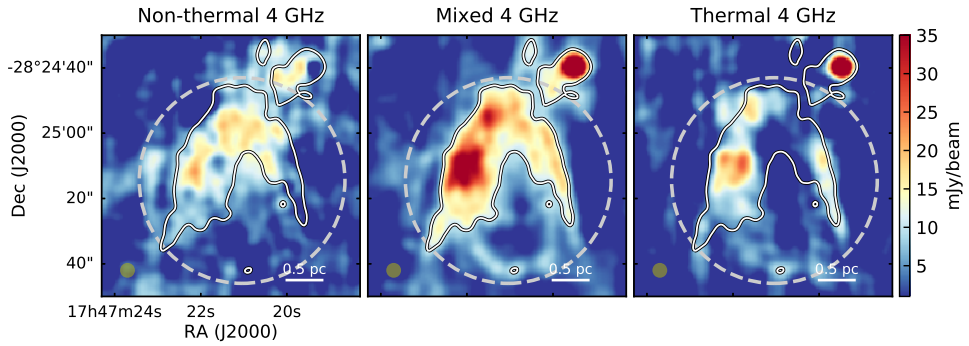

Figure 6.7 Spatial distribution of synchrotron (or non-thermal, left panel), mixed (central panel, corresponding to observed image) and free-free (or thermal, right panel) components of DS at 4 GHz as derived from method described in Sect. 6.3.1. The thermal emission map is extrapolated from 12 GHz assuming that at this frequency the emission is originated by a thermal component with a spectral index $\alpha = -0.1$. The non-thermal emission is obtained by subtracting the extrapolated thermal emission from the mixed emission. The contours are the same as in Fig. 6.5. All panels have a circular beam of $4''$ (shown in the bottom left corner of each panel). The dashed circles indicate the region in which we calculate the flux density of DS (see Sect. 6.3.1).

Fitting the SED with fixed spectral indices

In a second approach, I aim at simultaneously determining the contribution of thermal and non-thermal emission. For this, I fit the SED covering the whole range from 4 to 12 GHz with two power-law functions describing each component. For the thermal component, the power-law is $S_{\rm th}(\nu) \propto \nu^{-0.1}$, assuming that the emission is optically thin free-free. For the non-thermal component, I use $S_{\rm nt}(\nu) \propto \nu^{-0.7}$ (see Hollis et al., 2003; Protheroe et al., 2008; Jones et al., 2011). I fit the observed SED with a linear superposition of these two power-law functions and get the contribution of each component at different frequencies.

As shown in Fig. 6.8, at 4 GHz, the spatial distribution of the non-thermal component is more widespread compared to the thermal component which is mainly concentrated in the central part of the eastern lobe. This is consistent with the spatial distribution of the two components shown in Sect. 6.3.1. The HII region AA appears to have pure thermal emission in the center, with a possible contribution of non-thermal emission in the outskirts. The presence of non-thermal emission in the outskirts of HII regions have been found in a handful of objects (e.g., Garay et al., 1996; Mücke et al., 2002; Veena et al., 2016, 2019).

From the simultaneous fit of a thermal and non-thermal components, I determine that 90% of the total emission at 4 GHz has a non-thermal origin in Sgr B2(DS). The difference of the relative contribution of thermal and non-thermal components derived from the two methods (see Sect. 6.3.1) can be due to either the assumption of the thermal dominance at 11.2 GHz considered in the model presented in the previous section, or the fixed values of α for the thermal and non-thermal components used in this method. Overall, the results of both methods are in agreement and confirm the presence of extended non-thermal emission in Sgr B2(DS). Further observations at higher and lower frequencies may help to better

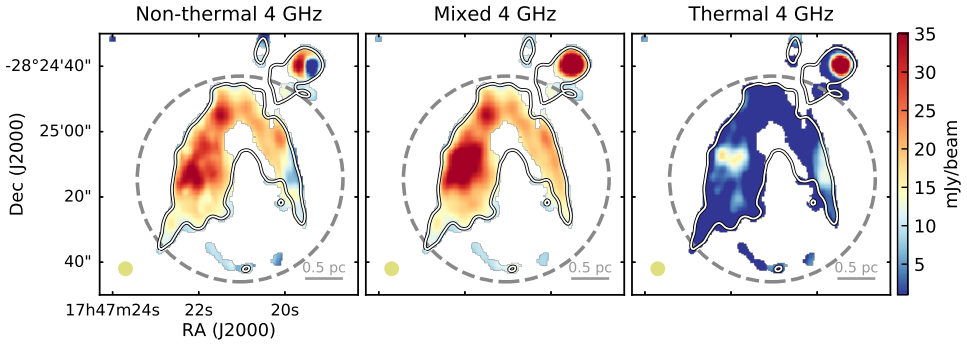

Figure 6.8 Spatial distribution of the synchrotron (left panel), mixed (central panel) and free-free (right panel) components of DS at 4 GHz. All the three images are obtained after fitting the observed SED with the sum of two power-law functions: $S_{\rm th}(\nu) \propto \nu^{-0.1}$ and $S_{\rm nt}(\nu) \propto \nu^{-0.7}$ for the thermal and non-thermal components, respectively (see details in Sect. 6.3.1). The contours are the same as in Fig. 6.5. All panels have a circular beam of $4''$ (shown in the bottom left corner of each panel). The dashed circles indicate the region in which we calculated the flux density of DS (see Sect. 6.3.1).

constrain the properties and distribution of the thermal and non-thermal components in this region.

6.3.2 Stimulated RRLs

As discussed in Sect. 6.2.3, the RRLs integrated intensity distribution varies significantly among the four stacked frequencies. From Fig. 6.6, one can see that the peak intensity of RRLs at the center of the eastern lobe increases monotonically with frequency, which suggests that the RRLs at this part of DS are excited under local thermodynamic equilibrium (LTE) conditions, since under LTE the peak intensity of RRLs obey $S_\nu \propto \nu$. However, at the edge of DS, as shown in Fig. 6.9, the peak intensities of the RRLs exhibit anti-correlation with frequency at 6.8, 8.9, and 10.5 GHz, which suggests that the RRLs in these regions are probably under non-LTE conditions.

I also find that the RRLs are likely excited under non-LTE conditions when comparing their emission with the continuum brightness. Under LTE, the integrated intensity of RRLs relates to optically thin free-free emission as

$$\frac{S_{\rm L}}{S_{\rm C}} \left(\frac{\Delta v}{\rm km\ s^{-1}} \right) = 6.985 \times 10^3 \left(\frac{\nu}{\rm GHz} \right)^{1.1} \left(\frac{T_{\rm e}}{\rm K} \right)^{-1.15}, \tag{6.1}$$

where $S_{\rm L}$ and $S_{\rm C}$ are the peak flux of RRL and flux of free-free continuum, respectively, and $T_{\rm e}$ is the electron temperature. Adopting $T_{\rm e} = 8000$ K (see Mehringer et al., 1993), I derive the corresponding free-free continuum level of the four stacked RRLs (RRL-derived free-free emission, hereafter RFE). The comparison between the RFE and the continuum emission at the four frequencies is shown in Fig. 6.10. The observed continuum emission is supposed to be a mixture of free-free and synchrotron emission, which should have a higher intensity than the RFE maps. However, the RFE exceeds the observed continuum by a

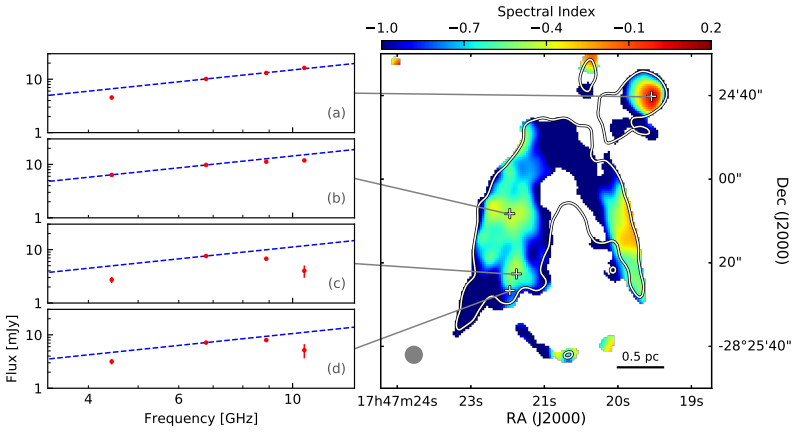

Figure 6.9 *Right:* Spectral index map of the Sgr B2(DS) as shown in the central panel of Fig. 6.5. The map of the uncertainty of spectral index is as shown in the right panel of Fig. 6.4. *Left:* Peak intensities of the four stacked RRLs (see Table 6.1) at four selected positions. Position (a) corresponds to the well-known HII region AA, while the other positions have been selected to probe regions with negative spectral indices. The dashed line in each panels marks the scenario for LTE under which the flux is proportional to the frequency.

factor of ∼2 at the low frequency end. One possible origin of this excess is that the RRLs are not under LTE conditions but stimulated.

To characterize the stimulation of RRLs, I introduce the RRL peak ratio η. According to theoretical models, the peak intensity of stimulated RRLs and frequency are anti-correlated at high frequencies (Shaver, 1978). Therefore, I consider the RRLs at 8.9 and 10.5 GHz and define

$$\eta = 0.85 \frac{S_{10.5\ \mathrm{GHz}}}{S_{8.9\ \mathrm{GHz}}}, \tag{6.2}$$

where $S_{10.5\ \mathrm{GHz}}$ and $S_{8.9\ \mathrm{GHz}}$ are the RRL peak intensities, respectively, while the normalization factor $0.85 = 8.9/10.5$ result in $\eta = 1$ when LTE conditions hold. When the RRLs are stimulated, $\eta < 1$. In Fig. 6.11 I show the η map of DS. From the plot, one can see that in the central and western part of DS, $\eta \approx 1$, which indicates that the emission is under LTE. At the eastern edge of DS, I find $\eta < 1$, which suggests the presence of stimulated emission. Notably, source AA displays $\eta = 1$, meaning that its emission is under LTE, which is consistent with the scenario that source AA is an HII region with only thermal emission.

I quantify the correlation between non-thermal emission and the stimulation of RRLs, by plotting η against α pixel by pixel (see Fig. 6.12). A total of 63% of the pixels in DS have $\alpha < -0.1$, meaning associated with non-thermal emission. Among these non-thermal pixels, 86% (53% of all the pixels in DS) have $\eta < 1$, i.e., the RRLs are stimulated under non-LTE conditions. Out of all the pixels, 58% have $\eta < 1$. The vast majority (92%) are associated with non-thermal emission. Therefore, most of the area in DS associated with non-thermal emission is also associated with stimulated RRLs, and similarly, almost all the parts associated with stimulated RRLs show non-thermal emission. The correlation between α and η seen in Fig. 6.12 is consistent with the scenario that RRLs can be stimulated by non-thermal emission (Shaver, 1978).

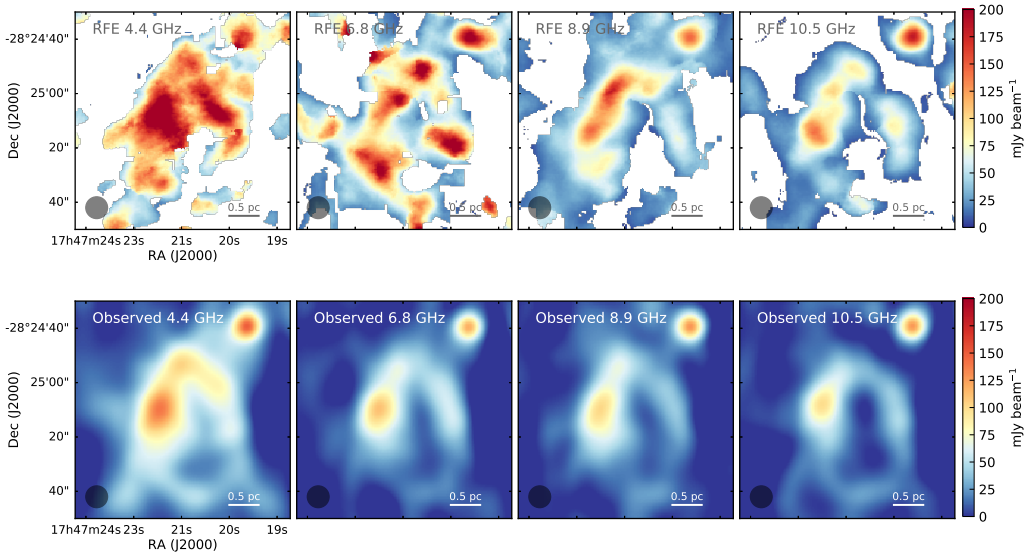

Figure 6.10 *Top panels*: Free-free continuum maps of the Sgr B2(DS) region derived from the four staked RRLs (RFE as described in Sect. 6.3.2, following Eq. 6.1) at 4.4, 6.8, 8.9, and 10.5 GHz.. *Bottom panel*: Observed continuum emission at 4.4, 6.8, 8.9 and 10.5 GHz. For comparison, the observed continuum maps are also smoothed to 8″, the beam is shown as the shaded circle in the lower left of each plot.

6.4 Origin of thermal and non-thermal emission

I have found that the DS region, located within the envelope of Sgr B2, shows a mix of thermal free-free and non-thermal synchrotron continuum emission at radio wavelengths. This kind of radio continuum emission may have different origins: HII regions, supernova remnants (SNRs), planetary nebulae (PNe) or extragalactic radio sources. Although the most probable origin is the HII region, I have explored the other three scenarios. I searched the XMM-Newton catalog for X-ray sources in the region, and found no source associated with DS in the 0.5–12 keV continuum bands (Ponti et al., 2015). The lack of bright X-ray emission suggests that I can exclude a scenario in which DS is a SNR. In a different scenario, PNe can emit in the radio regime, however, their typical size ranges from 0.03 to 0.1 pc, i.e., significantly smaller than the radius of DS (0.5 pc). Additionally, the age of PNe is expected to be between 10^7 and 10^{10} yr (e.g., Bressan et al., 1993), much longer than the age of Sgr B2 (estimated to be about 0.74 Myr, see Kruijssen et al., 2015). Also, I estimate the total mass of the ionized gas in DS to be $\sim$ 500 $M_\odot$, which is much larger than the mass of a typical low-mass star that can generate a PN. Therefore, I exclude the possibility that DS is a PN. The minimum detectable flux density of our images is $\sim$0.2 mJy, which can be used to estimate the expectable number of extragalactic radio sources. In the entire area of Sgr B2 ($7' \times 7'$), the expected number of extragalactic radio sources is $\sim$1, while in the $1' \times 1'$area of DS, the number is $\sim$0.03 (see Condon et al., 1998; Anglada et al., 1998). Additionally, the spatial extension of DS ($\sim 1'$) is significantly larger than the typical size of extragalactic radio sources (see Condon et al., 1998). Therefore, the possibility that DS is an extragalactic radio source is excluded. Thus, the only remaining scenario is DS being an HII region. In this section, I discuss the properties of the central star and the possible

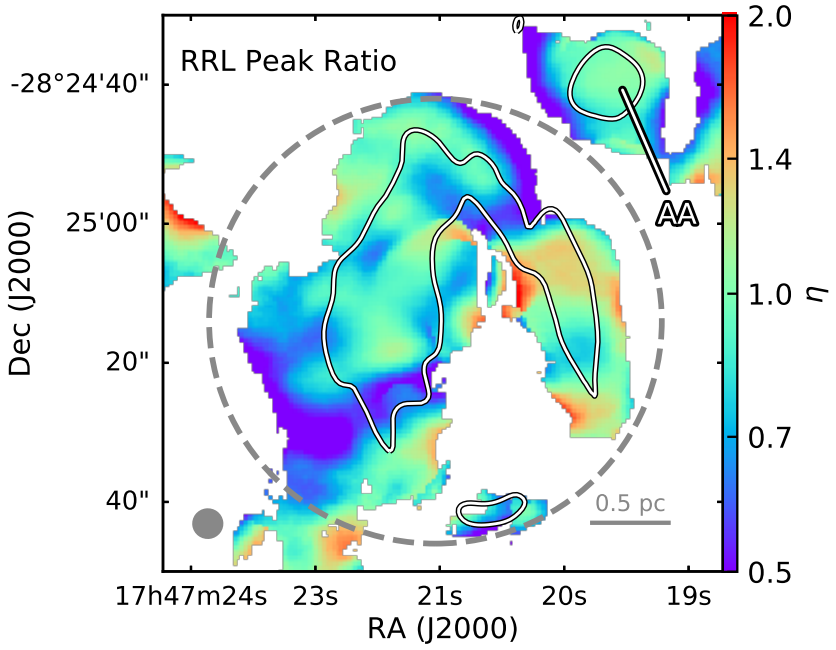

Figure 6.11 Map of η (see Sect. 6.3.2) in DS. The X band continuum emission is overlaid as contours. The synthesized beam, corresponding to $8''$, is plotted as a dark circle at the lower left corner. The dashed circle indicates the area in which pixels are taken into account for Fig. 6.12.

mechanisms that can produce the observed non-thermal emission.

6.4.1 Ionization by a central star

According to Eq. A.29, the flux of Lyman continuum photons from DS can be calculated. The total flux of the free-free emission in DS is 0.5 Jy at 11.2 GHz, assuming that the continuum emission at this frequency is pure thermal. For a typical HII region, the electron temperature ranges from 5000 to 10000 K (Zuckerman et al., 1967). Taking $D = 8.34$ kpc for Sgr B2, I obtain a flux of Lyman continuum photons of 4–6 $\times 10^{48}$ s^{-1}. Such a Lyman continuum flux corresponds to an O7 ZAMS star (see Table II of Panagia, 1973). I have searched the *Spitzer* infrared images (e.g., Ramírez et al., 2008) for a possible infrared counterpart of the star ionizing the HII region in DS, but found no clear candidate. Also the young stellar object catalog of (Yusef-Zadeh et al., 2009) does not show any infrared source in the center of DS. One possible reason for the lack of a detected infrared source in DS is the high extinction. Assuming a column density of molecular hydrogen of 10^{24} cm^{-2} in DS (Schmiedeke et al., 2016; Ginsburg et al., 2018), the extinction at 5 μm is $\sim$ 20, based on the grain model by Li & Draine (2001). For an O7 star at a distance of 8.34 kpc, this extinction result in an apparent magnitude $\sim$ 30, which is non-detectable in current infrared images.

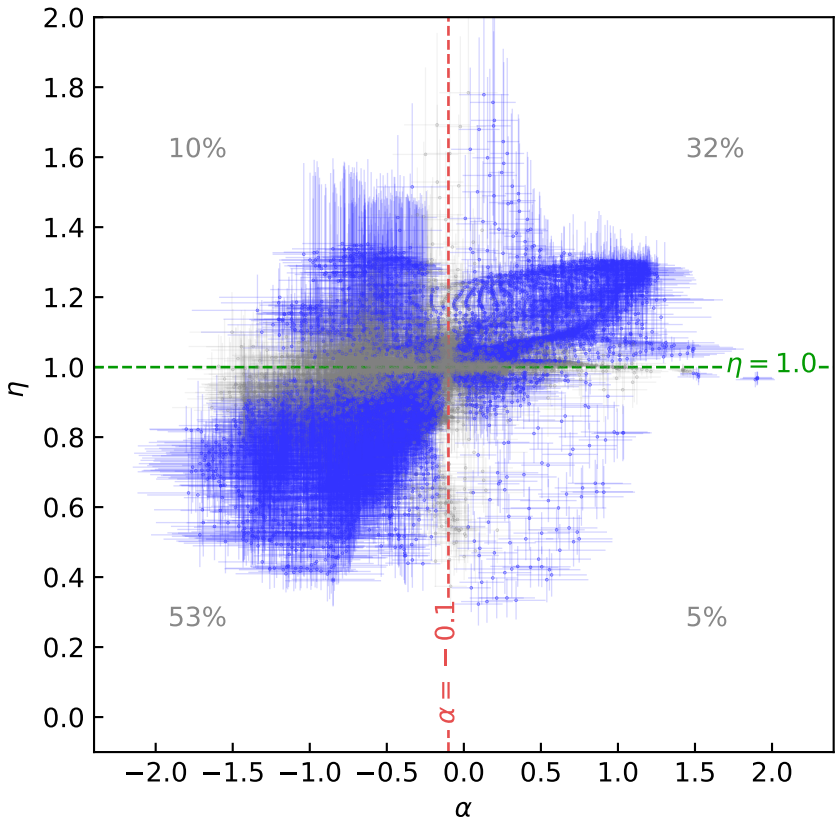

Figure 6.12 Plot of η against spectral index (α). Only the pixels that are in the area marked by the dashed circle in Fig. 6.11 are taken into account, thus the influence of source AA is excluded. The criterion of non-thermal emission, $\alpha = -0.1$, is shown with a vertical dashed line, while the criterion of stimulated RRL emission, $\eta = 1$, is shown as a horizontal dashed line. These two orthogonal lines divide the whole α–η space into four quadrants. For each quadrant, the number of pixels within it as a percentage of the number of all the pixels is written. The points with error bars crossing the $\alpha = -0.1$ or $\eta = 1$ lines are colored gray and neglected in the statistics.

6.4.2 Non-thermal emission origin

The interaction between cosmic-ray nuclei and the interstellar medium produces secondary electrons (and positrons). These secondary electrons can be a source of synchrotron emission like the one detected in Sgr B2(DS). Protheroe et al. (2008) analyze diffusion models and indicate that for secondary electrons to radiate synchrotron emission at GHz frequencies in ∼1 mG magnetic field, cosmic-ray particles should have multi-GeV energies, whereas such cosmic-ray particles cannot penetrate into the cloud due to the high gas density in Sgr B2 (see, e.g., Padovani et al., 2009, 2013). Thus, the penetration of cosmic rays from outside (e.g., from the nearby Galactic center) is excluded as a possible origin to the non-thermal emission observed in Sgr B2(DS).

However, the presence of synchrotron emission is the fingerprint of relativistic electrons. Padovani et al. (2015, 2016) showed that particle acceleration can take place at a shock location in protostars according to the first-order Fermi acceleration mechanism (also known as

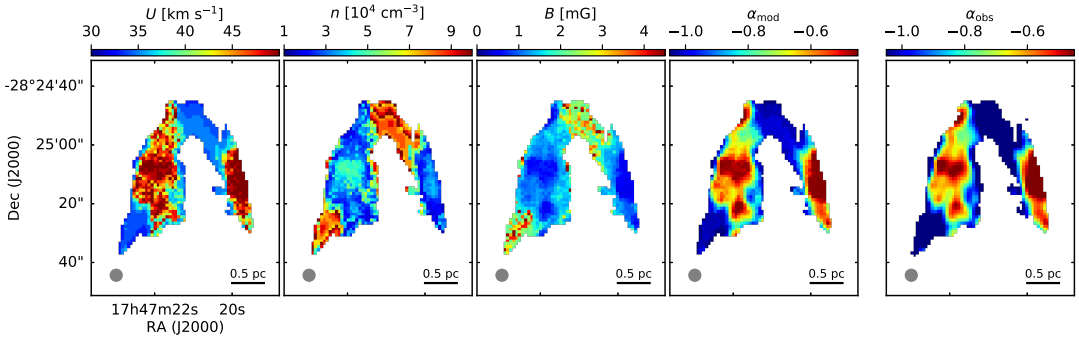

Figure 6.13 Maps of shock velocity (U), volume density (n), and magnetic field strength (B) of DS that reproduce the observed flux density maps at the 12 frequencies (see Fig. 6.3) by the First-order Fermi acceleration model through a χ^2 test using the model described in Padovani et al. (2019). The model also generates the modeled spectral index ($\alpha_{\rm mod}$) map which is consistent with the observed $\alpha_{\rm obs}$ map.

diffusive shock acceleration). In fact, local thermal particles are accelerated up to relativistic energies while crossing back and forth a shock surface thanks to magnetic fluctuations around the shock itself.

In a companion paper, (Padovani et al., 2019), including me, present an extension to this theory applied to HII regions. We demonstrate that electrons can be efficiently accelerated under the hypothesis that the flow velocity in the reference frame of an expanding HII region hitting denser material is sufficiently high (> 35 km s^{-1}) to switch on particle acceleration. The main parameters of the model are the magnetic field strength, the the flow velocity in the shock reference frame (hereafter velocity), the temperature, the volume density, and the ionization fraction. Assuming a complete ionized medium and a temperature of 8000 K (see Sect. 6.3.2), we studied the parameter space volume density-magnetic field strength and computed the emerging shock-accelerated electron flux for a shock radius of 0.36 pc, which is the average distance between the center of DS and the inner surface of the synchrotron emitting region. This electron flux is used to compute the synchrotron emissivity and then the flux density between 4 and 12 GHz for a beam of 4″and an average emitting region size[2] of 0.85 pc. We performed a χ^2 test to find the values of the velocity (U), density (n), and magnetic field strength (B) that best reproduce the observations. For the flux densities we obtain an average accuracy of about 20% assuming $33 \lesssim U \lesssim 50$ km s^{-1}, $10^4 \lesssim n/{\rm cm}^{-3} \lesssim 9 \times 10^4$, and $0.3 \lesssim B/{\rm mG} \lesssim 4$. From the model, we derive maps of the velocity, magnetic field strength and density in the Sgr B2(DS) region (see Fig. 6.13). The magnetic field strength is found to be in the range 0.5–2 mG as reported by Crutcher et al. (1996). The model also gives an α map of DS, which is in agreement with the observed α map (Fig. 6.5). It is interesting to notice that the velocity is lower where the density is higher. One reason might be that the flow is moving faster towards the east-west direction, which is the direction of minimum resistance. In contrast, the velocity is lower toward the northern direction where the density is higher. Although the RRL line width cannot be directly used to determine the shock speed, we note that it is significantly larger than

[2]The average size, L, of a shell-shaped emitting region with inner and outer radii, $R_{\rm in}$ and $R_{\rm out}$, respectively, is $L = (\pi/2)R_{\rm out}(1 - R_{\rm in}^2/R_{\rm out}^2)$. For DS we assume $R_{\rm in} = 0.36$ pc and $R_{\rm out} = 0.72$ pc.

the typical expansion velocity of an HII region (10 km s^{-1} Draine, 2011), which points to an additional mechanism of acceleration. One possible origin of the high velocity is the presence of a stellar wind driven by the O7 star that likely ionizes the HII region (see e.g., Veena et al., 2016; Pereira et al., 2016; Kiminki et al., 2017). We note that velocities of about 35 km s^{-1} are in agreement with what is obtained by simulations of HII regions of O and B stars driving strong stellar winds (Steggles et al., 2017).

It is important to remark that the flux densities (from which the spectral index is derived) estimated by our model are based on the assumption that all the parameters (magnetic field strength, velocity, temperature, density, and ionization fraction) are constant along the line of sight. For a proper modeling, one should account for the spatial variations of these quantities. However, the fact that model results are already fairly comparable with observations is an indication that shock-accelerated electrons may represent the key to explain the synchrotron emission in Sgr B2(DS). Previous studies (e.g., Yusef-Zadeh et al., 2007a,b, 2013, 2016) indicate that cosmic-ray induced non-thermal emission is common in the Galactic center region. On large scales, where the density is not as high as in the envelope of SgrB2, cosmic rays may play a dominant role in the production of relativistic electrons, while in extremely dense regions (and smaller scales, like Sgr B2(DS)) HII region shocks may be a dominant source of non-thermal emission.

6.5 Summary

I have observed the giant molecular cloud Sgr B2 with the VLA in its D and CnB configurations. I obtained continuum and RRL maps in the frequency range 4–12 GHz, covering a spatial extent of about $20' \times 20'$, with a beam size of $4''$. I have focused our study on the Sgr B2(DS) region, located in the southern area of the Sgr B2 envelope. My main results are:

- Sgr B2(DS) is bright at radio wavelengths, with intensities in the range 10–50 mJy/beam, within the observed 4 to 12 GHz frequency range. At $4''$ resolution, DS appears as bubble-like HII region with a diameter of about 1.5 pc, powered by an O7 star, and surrounded by dense gas and a series of dense cores distributed in an arc structure around it.

- I find that the total flux of DS decreases from 1.9 Jy at 4 GHz down to 0.5 Jy at 12 GHz. Spectral analysis shows that the spectral index of DS varies from -0.4 to -1.2, suggesting the presence of non-thermal emission, in addition to the thermal emission of the HII region. I decompose the thermal and non-thermal components in DS, and find that the thermal emission is clumpy and concentrated in the eastern lobe of the bubble-like structure, while the non-thermal emission appears widespread over the whole region.

- The emission of RRLs in DS show a central velocity varying from 70 km s^{-1} in the center to 55 km s^{-1} in the outer edge. The line widths of the RRLs range from 30 to 40 km s^{-1}. From the RRLs integrated intensity, we derive the corresponding thermal continuum emission, which exceeds the observed continuum by a factor of about 2 at the low frequency end. In addition, the RRLs intensity does not follow the $S_\nu \propto \nu$ relation expected for RRLs under LTE conditions, but drops at high

frequencies likely due to non-LTE effects. I find a correlation between the presence of non-thermal emission (i.e., negative spectral indices) and those regions where RRLs are excited under non-LTE conditions. This suggests that RRLs in Sgr B2(DS) are possibly stimulated by synchrotron emission.

- Collaborated with Padovani et al. (2019), we modeled the observed synchrotron emission, and found that relativistic electrons can be produced via first-order Fermi acceleration, which is triggered by the interaction between the expanding HII region and the denser surrounding material. The model, which is presented in a companion paper of Padovani et al. (2019), reproduces the observed flux density and spectral index. From the model, we derive maps of the flow velocity in the shock reference frame, magnetic field strength and density in the Sgr B2(DS) region. Velocities are found to be between 35 and 50 km s^{-1} as found in simulations of cometary HII regions of O and B stars driving strong stellar winds. The magnetic field strength is found to be in the range 0.3–4 mG as reported by Crutcher et al. (1996) and the density in the range of $1 - 9 \times 10^4$ cm^{-3}.

Chapter 7

Large Scale: The Envelope

The large scale structure of SgrB2 is mainly the envelope in which the two main hot cores SgrB2(N) and SgrB2(M) are embedded. Martín-Pintado et al. (1999) studied the dense gas in the envelope with high-resolution observations (beam size: $3''$), but covering an area of only $3'\times3'$. Jones et al. (2012) observed multiple molecular lines in the envelope of SgrB2 with Mopra telescope, which covers $5'\times5'$ of the envelope but only has a resolution of $\sim 40''$. Apart from the molecular gas, the ionized gas in the envelope has been observed with telescopes such as the VLA and GBT, but the resulting dataset were either limited in resolution (e.g. Law et al., 2008b) or in sensitivity (e.g. LaRosa et al., 2000) compared to the VLA data used in this thesis. In this chapter, using the novel VLA cm wavelength data and the ALMA HC_3N line data, I characterize the physical properties of the HII regions in the envelope as well as the kinematic structure of the envelope that traced by RRLs and dense molecular line. In Sect. 5.1 I describe the observations. Section 5.2 shows the results. In Sect. 5.3 I analyze the results. In Sect. 5.4 I summarize this chapter.

7.1 Observation and data reduction

Three datasets are used for this chapter. Details of the observation and data reduction of these three datasets are described in the following.

VLA continuum: The observations are as described in Section 6.1. Since the spectral index is not the main focus of this chapter, I utilize the full *uv* coverage of the C and X band data. The angular resolution of the datasets are $(2.72'', 2.52'', -81.7^\circ)$ and $(1.82'', 1.53'', -76.0^\circ)$, respectively[1]. Due to artifacts in the images, I do not use $n\times$RMS as the sensitivity in this chapter. However, the sensitivity is determined based on the level of artifacts (see the intensity profiles shown in Fig. 7.1 and Fig. 7.2). I estimate the sensitivities to be 1.5 mJy/beam and 1.0 mJy/beam for the C and X band images, respectively. Although the original images cover a large area (see Fig. 3.6), but considering the low SNR at the edge of the images, I use the central $\sim 12' \times 12'$ area for both bands in this chapter. The spectral coverage is 4–8 GHz and 8–12 GHz for the C and X band, respectively.

RRLs: The observation of RRLs are described in Section 6.1. Utilizing the 'visibility stack' method, which is described in Section 4.4, the eight RRLs in C band and ten

[1]Resolution in format $(\theta_{\rm maj}, \theta_{\rm min}, {\rm PA})$.

RRLs in X band are stacked to form two datacubes, namely 'RRLC' and 'RRLX'. The resolution of RRLC and RRLX are 7″and 4″respectively, which is the resolution that the RRL images were smoothed to during stacking. The spectral resolution of RRLC and RRLX are both 2.5 km s^{-1} . The velocity coverage of RRLC and RRLX are both from −35 km s^{-1} to 165 km s^{-1} . Due to its better image quality and higher resolution compared to RRLC, I focus on RRLX in this chapter. The RMS per channel of RRLX is ∼ 0.5 mJy/beam. The spatial coverage is the same as that of the continuum images of the VLA. The frequency coverage and *uv* coverage of RRLX, although discretely sampled compared to the continuum images, is regarded as the same as that of the continuum image in X band.

HC_3N: The details of the observation of the HC_3N(10-9) datacube, which has been observed with ALMA, is described by Ginsburg et al. (2018). The velocity coverage of the dataset is from −200 km s^{-1} to 200 km s^{-1}, with a velocity resolution of 2 km s^{-1} . The rest frequency of HC_3N(10-9) is 90.9790230 GHz (according to CDMS, see Müller et al., 2001). Due to the lack of large scale emission in the datacube, which is probably caused by the lack of short *uv* distance coverage, and, consequently, the presence of negative bowls in the image, I do not estimate the RMS of this dataset. The spatial coverage of the HC_3N image is ∼ 7′ × 7′, with a resolution of (3.46″, 1.95″, 72.5°). Although the continuum subtraction has already been conducted on the cube (see Ginsburg et al., 2018), I apply a median subtraction on the cube again to better remove the continuum component. The median is calculated from −200 km s^{-1} to −150 km s^{-1}, where the spectra are line-free.

The observation of VLA continuum and RRLs was lead by me, as described in Section 6.1. The ALMA observations of HC_3N was led by Ginsburg. The data reduction of VLA continuum and RRLs are done by myself. Ginsburg did the date reduction of the HC_3N data, and allows me to process and conduct further analysis on the FITS file.

7.2 Results

This chapter focuses on two major components in the envelope of SgrB2, HII regions and molecular gas. The VLA continuum and RRL data allow us to study the distribution, kinematics, and physical properties of the HII region (ionized gas). The HC_3N (10–9) emission observed with ALMA traces dense molecular gas in the envelope. In this section, I present results on both components.

7.2.1 Ionized gas

The continuum emission in the centimeter bands traces mainly the free-free thermal emission from HII regions. Although as shown in Chapter 6, SgrB2 (DS) is also partially associated with synchrotron emission, the other regions of the envelope of SgrB2 seem to be dominated by thermal emission. The intensity maps of the entire envelope of SgrB2 and zoom-in maps are presented in Fig. 7.1 and Fig. 7.2, for the C and X bands respectively.

The peak intensity map of RRLX is shown in Fig. 7.4 while a zoom-in is displayed in Fig. 7.5. The detection threshold is set to be 1.0 mJy/beam. I fit RRLX with Gaussian profiles and produce maps of the fitted parameters – integrated intensity, central velocity

and line width. The integrated intensity map is shown in Fig. 7.6. At the center of (N) and (M), the integrated intensity of RRLX reaches 3.1 Jy/beam and 4.2 Jy/beam respectively. The central velocity of RRLX in the entire SgrB2 ranges from 40 to 90 km s^{-1} , see Fig. 7.7. The line width of RRLX is from 20 to 45 km s^{-1} in SgrB2, see Fig. 7.8.

Mehringer et al. (1993) detected and characterized fourteen HII regions in the envelope of SgrB2. In this chapter, these fourteen HII regions are named as 'M93#', where '#' is the ID used by Mehringer et al. (1993). I have identified eight new HII regions that are named as 'IG#', where 'IG' stands for 'ionized gas' while the '#' is the minutes and seconds of the declination of the HII region. In total, I have identified 22 radio continuum sources in the envelope of SgrB2. In Table 7.1, I list their observational parameters. Column 'R', which stands for radius of the core, is the radius of the minimum circle that can include all the valid pixels of the HII regions. Here 'valid pixels' means the pixels that have flux density above the noise level. The 22 HII regions have R ranging from 1.8″to 30″. HII region IG2715 has the largest spatial extension, which may result in the underestimation of its real flux density due to filtering effect of the interferometric observations. Columns $S_{\rm C}$ and $S_{\rm X}$ of Table 7.1 list the flux density within the circle with radius R (for the photometry method used, see Eq. A.12). The uncertainty of the flux densities are derived as $\sigma\sqrt{N}$, where σ is the typical noise level, which is 1.5 and 1.0 mJy/beam for C and X band, respectively, and N is the number of valid pixels that are used in the photometric analysis. The spectral index, derived from $S_{\rm C}$ and $S_{\rm X}$, is denoted as α. The here-listed α, compared to the pixel-by-pixel spectral index shown in the map of Fig. 6.4, reflects the overall (average) spectral index of the whole HII region. Most of the HII regions have α between -0.1 and 0.1, which suggests that they are mainly associated with optically thin free-free emission. The two largest HII regions, IG2608 and IG2715 have negative α, which is probably due to different interferometric spatial filtering in both bands. Since the C band image recovers larger scales compared to the X band image, if a HII region has a significant portion of large scale flux density, its total flux will be more severely underestimated in the X band than in the C band, which may cause the measured α to be smaller than the real value.

The observed parameters of RRLX are also listed in Table 7.1. The integrated intensity is calculated similarly as the photometry done for $S_{\rm C}$ and $S_{\rm X}$. While the central velocity ('Velo') and line width ('FWHM') are average values from the valid pixels. The 'error' for Velo and FWHM are the standard deviations of the corresponding quantities, calculated from all the valid pixels of the HII regions. The velocity of the HII regions ranges from ~ 50 km s^{-1} to 84 km s^{-1} (IG2608). The line width ranges from ~ 20 km s^{-1} to 55 km s^{-1} . These velocities are consistent with ionized gas at temperatures of 10^4 K, and that the excess in the line width for some regions (e.g. M92C) may be due to internal dynamics (e.g., expansion, or further multiplicity not resolved in our data).

Table 7.1 Observed parameters of HII regions in the envelope of SgrB2

Region	RA[a]	Dec[b]	R arcsec	$S_{\rm C}$ mJy	$S_{\rm X}$ mJy	α	Int[c] mJy km s^{-1}	Velo[d] km s^{-1}	FWHM [e] km s^{-1}
IG2207	18.11	22:07.2	2.0	8.8 ± 0.3	12.0 ± 0.5	0.6 ± 0.1	21.2 ± 1.5	74 ± 15	55 ± 41
IG2210	24.12	22:09.1	6.0	42.2 ± 0.9	35.7 ± 1.2	-0.3 ± 0.1	85.3 ± 3.2	59.8 ± 4.2	16.4 ± 2.0
IG2243	14.89	22:43.3	3.1	10.2 ± 0.5	15.4 ± 0.8	0.8 ± 0.2	39.7 ± 2.0	67.1 ± 7.1	18.6 ± 2.4
IG2431	20.46	24:29.7	3.5	19.0 ± 0.6	17.2 ± 0.9	-0.2 ± 0.2	133.3 ± 2.6	59.1 ± 4.9	33.6 ± 6.0

continued

Table 7.1 Observed parameters of HII regions in the envelope of SgrB2

Region	RA[a]	Dec[b]	R arcsec	S_C mJy	S_X mJy	α	Int[c] mJy km s^{-1}	Velo[d] km s^{-1}	FWHM [e] km s^{-1}
IG2432	24.00	24:31.9	2.2	6.5 ± 0.3	5.7 ± 0.5	-0.3 ± 0.3	27.3 ± 1.5	55.3 ± 8.0	26.2 ± 4.0
IG2608	29.85	26:10.0	16	228.3 ± 2.0	115.7 ± 2.3	-1.33[f]± 0.06	765.9 ± 6.6	84 ± 15	31 ± 12
IG2611	15.69	26:12.5	5.0	26.1 ± 0.7	19.6 ± 1.0	-0.6 ± 0.2	41.2 ± 2.8	64.0 ± 6.3	19.5 ± 5.4
IG2715	33.94	27:02.8	30	233.0 ± 2.6	9.6 ± 0.8	-6.2[f]± 0.2	4569 ± 21	70.5 ± 8.0	28 ± 13
M92A	11.22	26:32.0	5.0	189.3 ± 0.9	176.6 ± 1.3	-0.14 ± 0.02	761.5 ± 3.7	59.5 ± 3.6	31.3 ± 3.6
M92B	13.63	26:54.2	5.0	366.0 ± 0.9	352.1 ± 1.4	-0.08 ± 0.01	1313.3 ± 3.7	56.1 ± 3.9	39.6 ± 5.5
M92C	14.63	26:52.4	5.0	831.1 ± 0.9	861.6 ± 1.4	0.071 ± 0.005	2447.1 ± 3.7	53.2 ± 4.1	43.8 ± 5.3
M92D	15.35	26:45.2	5.0	126.6 ± 0.8	132.7 ± 1.3	0.09 ± 0.03	554.8 ± 3.7	61.7 ± 8.4	40 ± 24
M93BB	22.13	22:17.6	6.5	258.5 ± 1.1	200.3 ± 1.8	-0.50 ± 0.03	942.6 ± 4.8	64.8 ± 4.1	22.7 ± 2.1
M93L	22.64	21:54.5	5.5	1093.7 ± 0.9	1225.0 ± 1.5	0.222 ± 0.004	4755.3 ± 4.1	75.3 ± 4.1	30.4 ± 4.9
M93O	22.89	22:48.2	2.3	12.4 ± 0.3	12.0 ± 0.5	-0.1 ± 0.1	47.5 ± 1.5	80 ± 12	29.9 ± 5.7
M93P	23.69	23:35.4	2.4	20.4 ± 0.3	23.1 ± 0.6	0.24 ± 0.08	44.6 ± 1.5	80 ± 11	21.5 ± 3.5
M93Q	24.86	21:44.5	1.8	11.6 ± 0.3	11.9 ± 0.4	0.1 ± 0.1	37.7 ± 1.1	66 ± 12	20.6 ± 4.1
M93R	26.11	22:05.0	6.9	885.7 ± 1.1	865.1 ± 1.8	-0.046 ± 0.007	2910.2 ± 4.8	58.1 ± 3.1	32.5 ± 5.0
M93T	27.44	21:00.3	4.3	84.8 ± 0.7	85.5 ± 1.1	0.02 ± 0.04	342.9 ± 2.9	57 ± 12	44 ± 10
M93U	12.13	22:36.6	6.3	234.9 ± 1.0	221.1 ± 1.7	-0.12 ± 0.02	969.3 ± 4.4	66.5 ± 3.6	26.5 ± 2.9
M93W	16.70	23:28.9	5.0	61.5 ± 0.8	58.4 ± 1.2	-0.10 ± 0.06	150.3 ± 3.3	67.6 ± 4.5	17.0 ± 2.8
M93X	17.31	22:03.8	2.3	26.2 ± 0.3	32.2 ± 0.5	0.40 ± 0.06	66.3 ± 1.5	58.9 ± 8.4	25.1 ± 4.5

[a] RA '17:47:SS.SS' is denotes as 'SS.SS'.
[b] Dec '-28:MM:SS.S' is denotes as 'MM:SS.S'.
[c] Integrated intensity of RRLX.
[d] Central velocity of RRLX.
[e] Line width (FWHM) of RRLX.
[f] Affected by different sensitivity and *uv* coverages.

In the following, I investigate the probability distribution function (PDF) of the flux density S in the C and X bands over the entire mapped region. The probability density of S, denoted as $p(S)$, is defined as

$$p(S)\,\Delta S = \frac{N(S)}{N}, \tag{7.1}$$

where $N(S)$ is the number of pixels with flux density between S and $S + \Delta S$, and N is the total number of 'valid pixels', i.e., pixels with $S > 0.01$ mJy/beam. The PDF of both bands is shown in Fig. 7.9. For fluxes in the range 1.5–300 and 1.0–150 mJy/beam, for C and X band respectively, $p(S)$ displays a power law relationship, with indices -1.77 ± 0.02 and -1.73 ± 0.02 respectively. As a comparison, the PDF of a molecular cloud under self-gravity also follows power-law (e.g. Klessen, 2000), with a power-law index between -1.5 and -2 for free-fall collapsing clouds (Schneider et al., 2015). For a more detailed study, I have also determined the PDF for three different regions: SgrB2(N), (M) and (DS). The PDFs are shown in Figs. 7.10, 7.11, and 7.12. For each region, subregions are selected to derive the PDFs. The overall trend shows that the central denser subregions have shallower PDFs. The power-law indices of SgrB2(N) and (M) range from -1.3 to -0.8, while (DS) has indices ~ -3. It is worth to notice that the spacial filtering effect introduced by the interferometers may affect the indices (see e.g. Ossenkopf-Okada et al., 2016). The results presented above and the discussion on the PDFs in Section 7.3.1 are based on the assumption that the biases on the PDF caused by the incomplete sampling in our data is not severe.

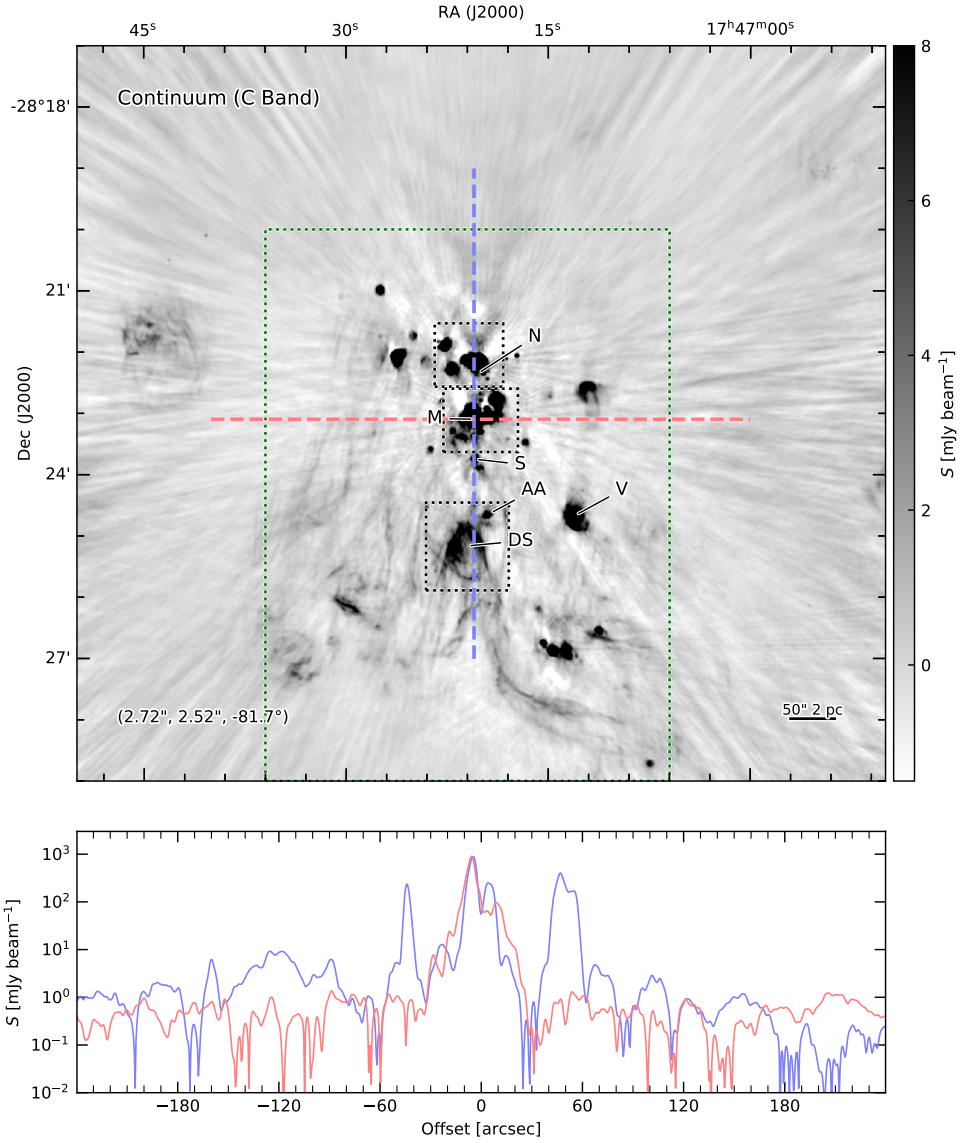

Figure 7.1 *Upper Panel:* Image of the entire SgrB2 envelope in C band. Beam pattern is marked in format $(\theta_{\rm maj}, \theta_{\rm min}, {\rm PA})$. *Lower Panel:* Two profile cuts, which marked in blue and red in the upper panel. To show the negative artifacts in the log-scale plot, the profiles are the absolute value of the intensity profile. The offset of each profile increase from left to right and from bottom to top. The dotted box marks the plot region of Fig. 7.3.

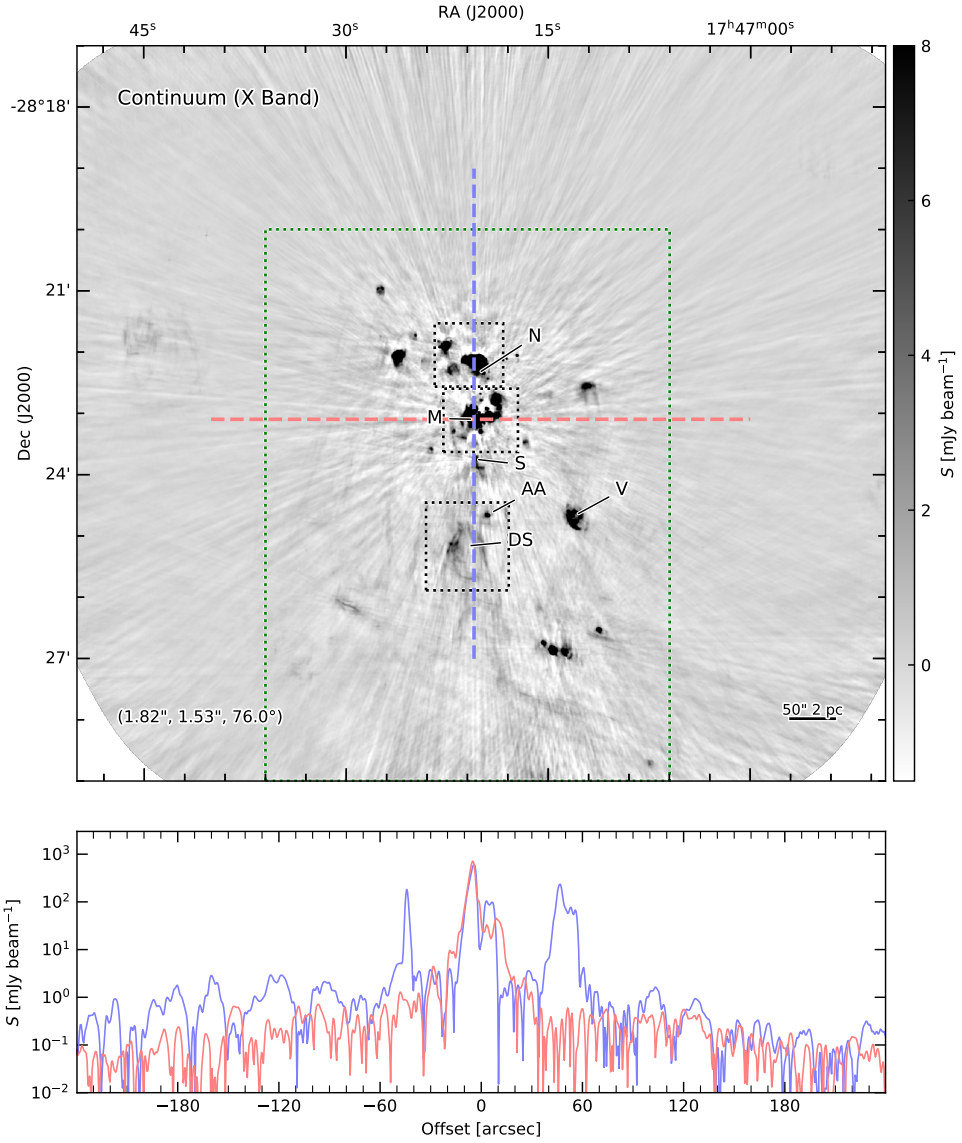

Figure 7.2 *Upper Panel:* Image of the entire SgrB2 envelope in X band. Beam pattern is marked in format $(\theta_{\rm maj}, \theta_{\rm min}, {\rm PA})$. *Lower Panel:* Two profile cuts, which marked in blue and red in the upper panel. To show the negative artifacts in the log-scale plot, the profiles are the absolute value of the intensity profile. The offset of each profile increase from left to right and from bottom to top. The dotted box marks the plot region of Fig. 7.3.

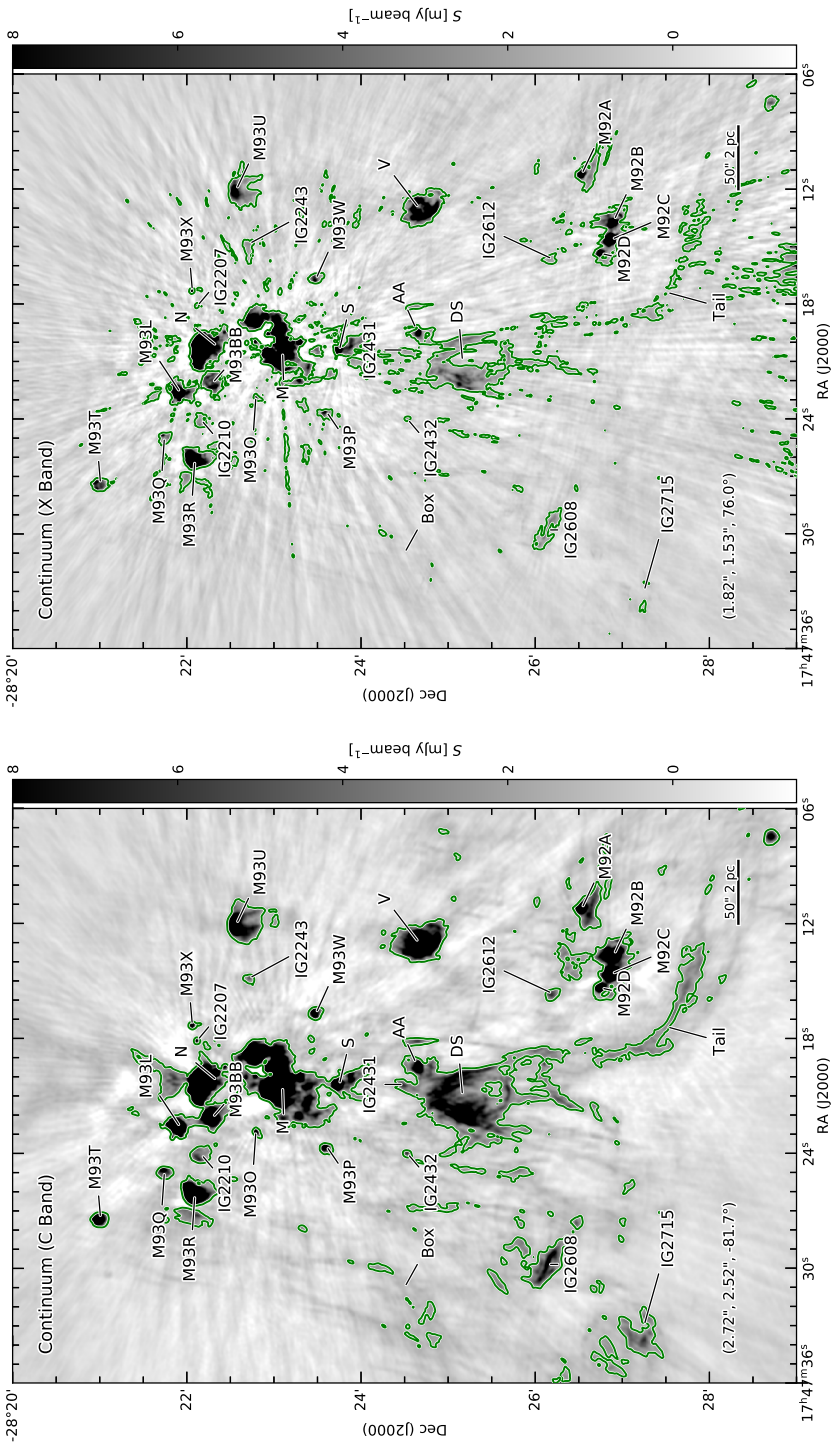

Figure 7.3 HII regions in Sgr B2 envelope. Back ground are the C (*left panel*) and X (*right panel*) bands VLA images. HII regions are marked.

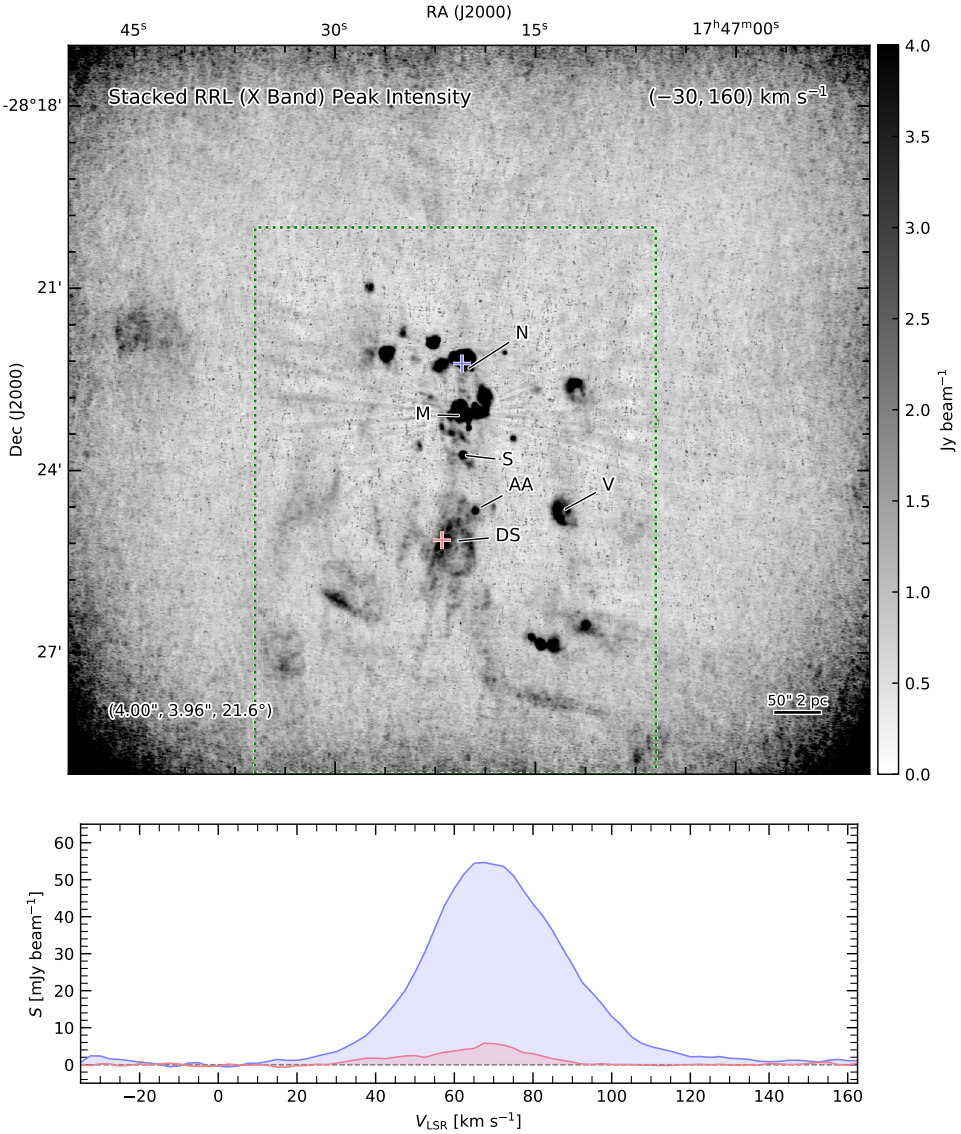

Figure 7.4 *Upper Panel:* Image of the peak intensity of RRL in X band. Beam pattern is marked in format $(\theta_{\rm maj}, \theta_{\rm min}, {\rm PA})$. *Lower Panel:* Two RRL spectra, which marked as blue and red '+' in the upper panel. The dotted box marks the plot region of Fig. 7.5.

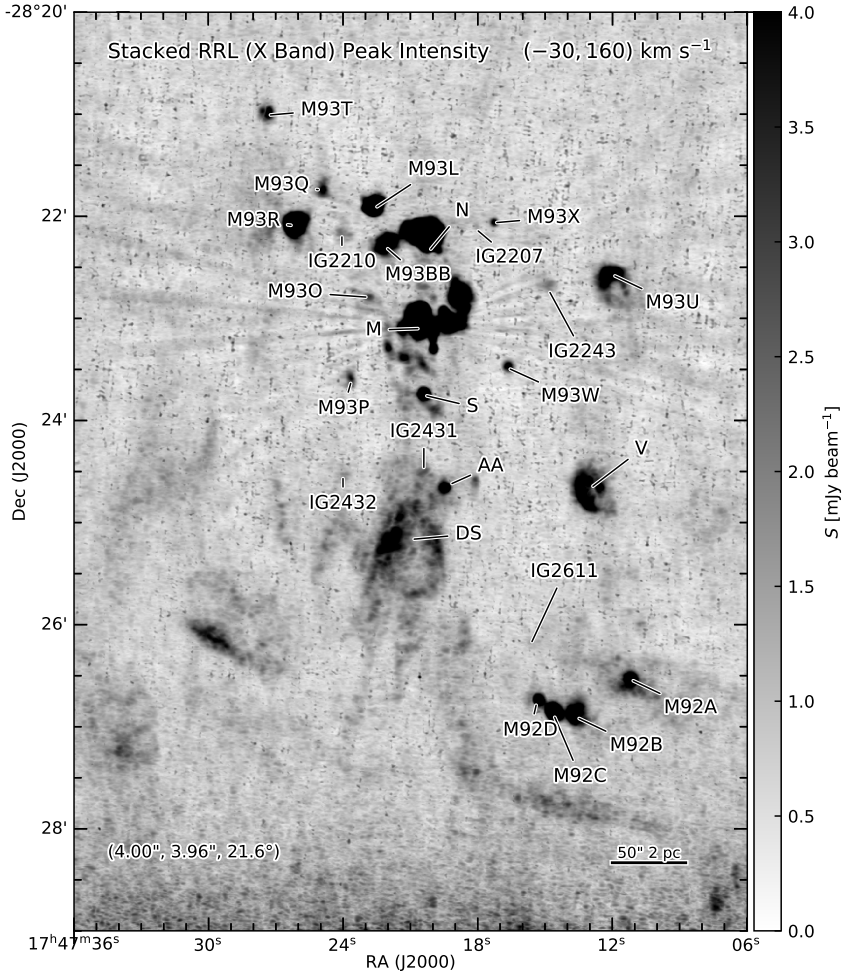

Figure 7.5 HII regions in Sgr B2 envelope. Back ground is the X band RRL peak intensity map, same as in Fig 7.4. HII regions are marked.

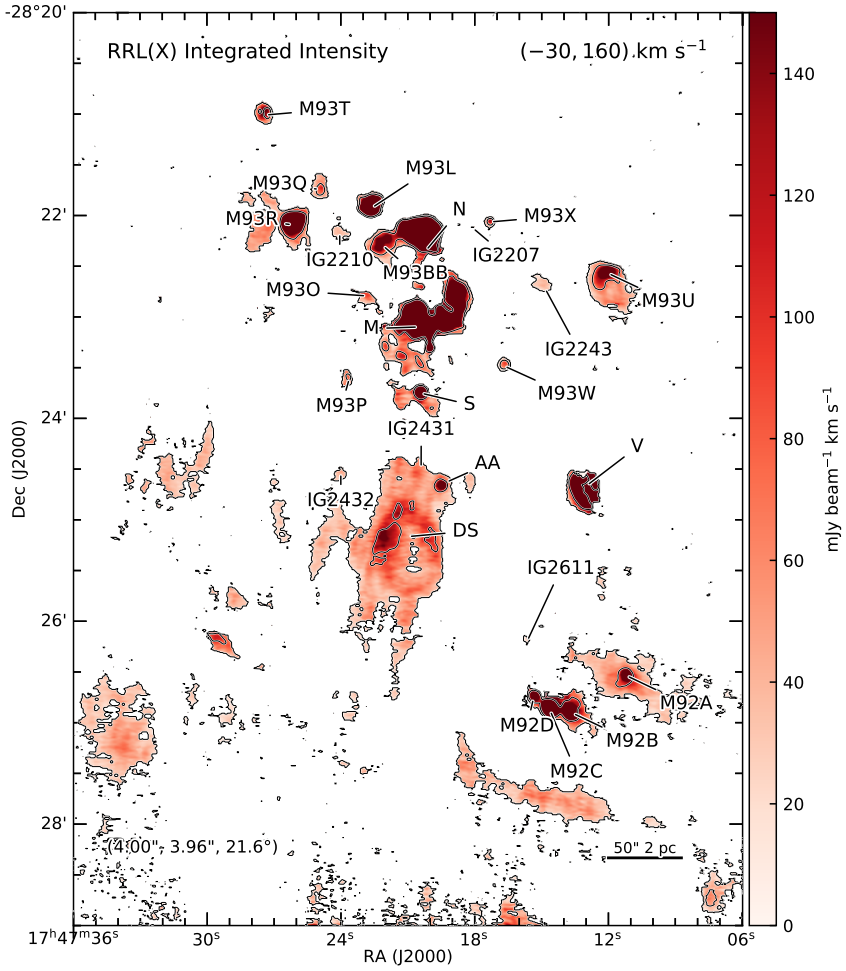

Figure 7.6 Integrated intensity map of X band RRL. Beam pattern is marked in format $(\theta_{\rm maj}, \theta_{\rm min}, {\rm PA})$. HII regions are marked. Contours are the 1.0 mJy/beam level of peak intensity.

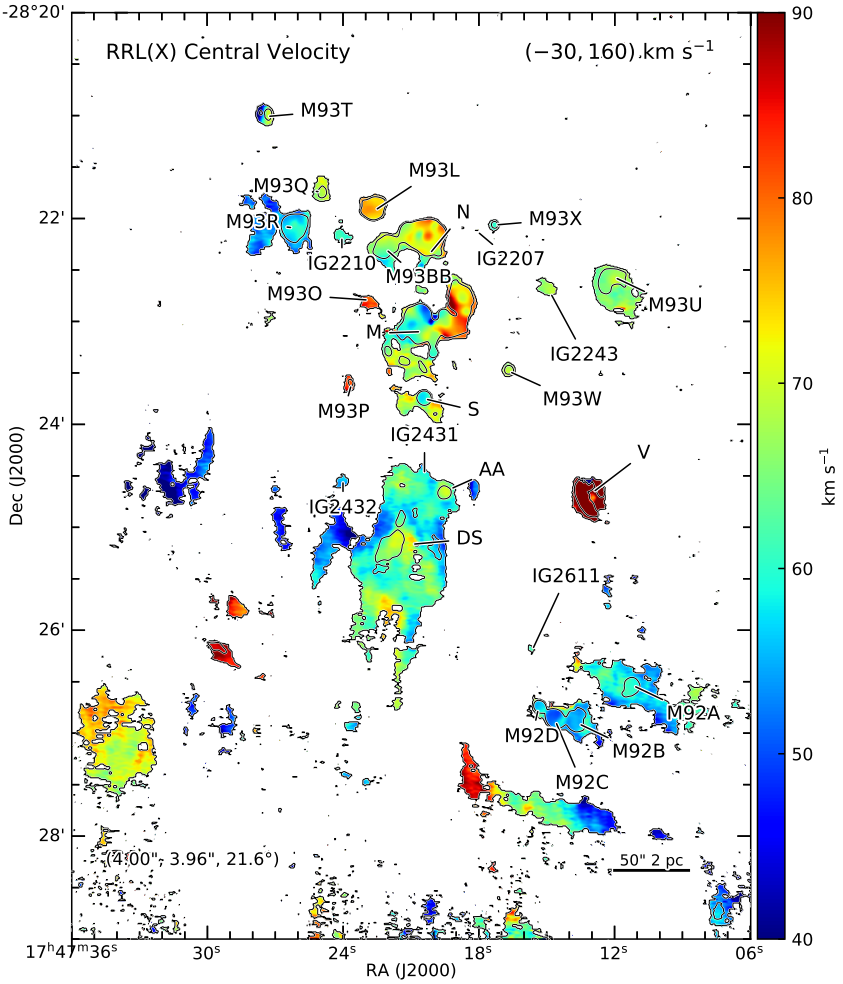

Figure 7.7 Velocity map of X band RRL. Beam pattern is marked in format $(\theta_{\rm maj}, \theta_{\rm min}, {\rm PA})$. HII regions are marked. Contours are the 1.0 mJy/beam level of peak intensity.

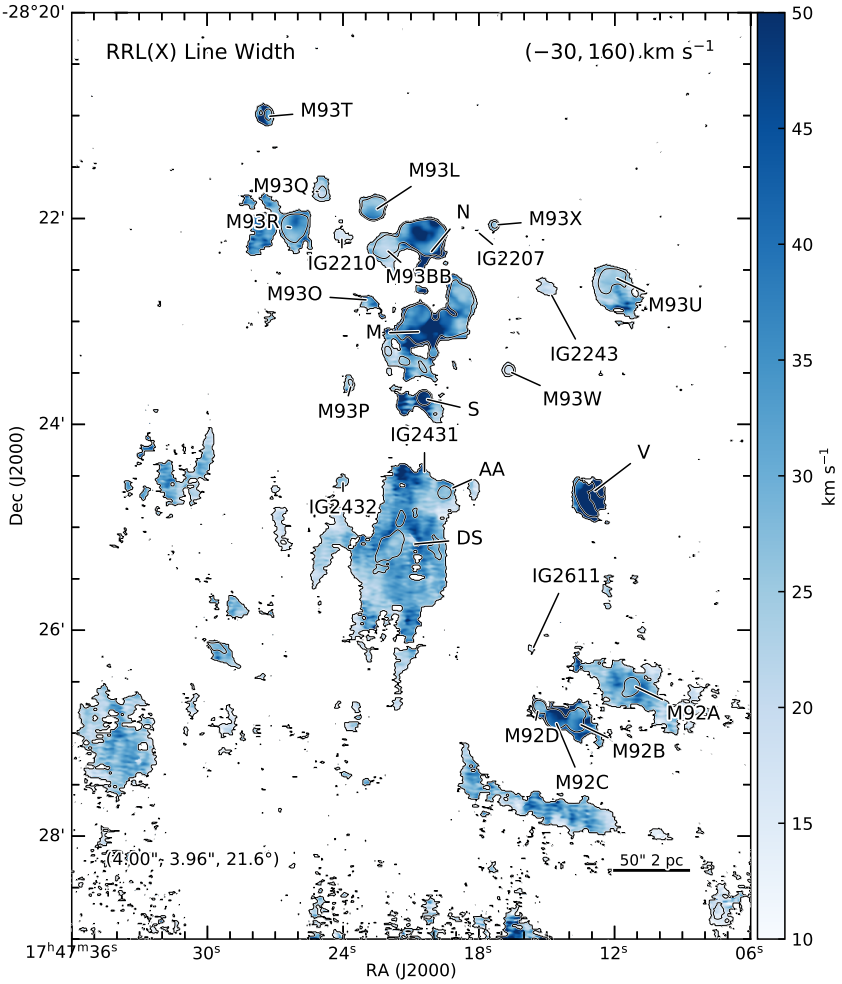

Figure 7.8 Line width map of X band RRL. Beam pattern is marked in format $(\theta_{\rm maj}, \theta_{\rm min}, {\rm PA})$. HII regions are marked. Contours are the 1.0 mJy/beam level of peak intensity.

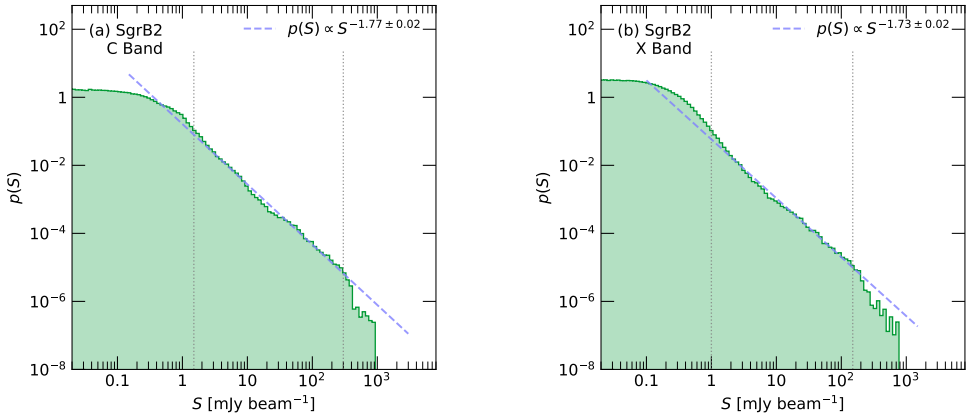

Figure 7.9 PDF of C and X band continuum intensity of the entire SgrB2 region, in panel (a) and (b) respectively. The plower-law fitting are marked as blue dashed lines. The intensity ranges that are taken into account in the power-law fitting are marked with gray dotted lines. The fitting results are written on the upper right corner of each panel.

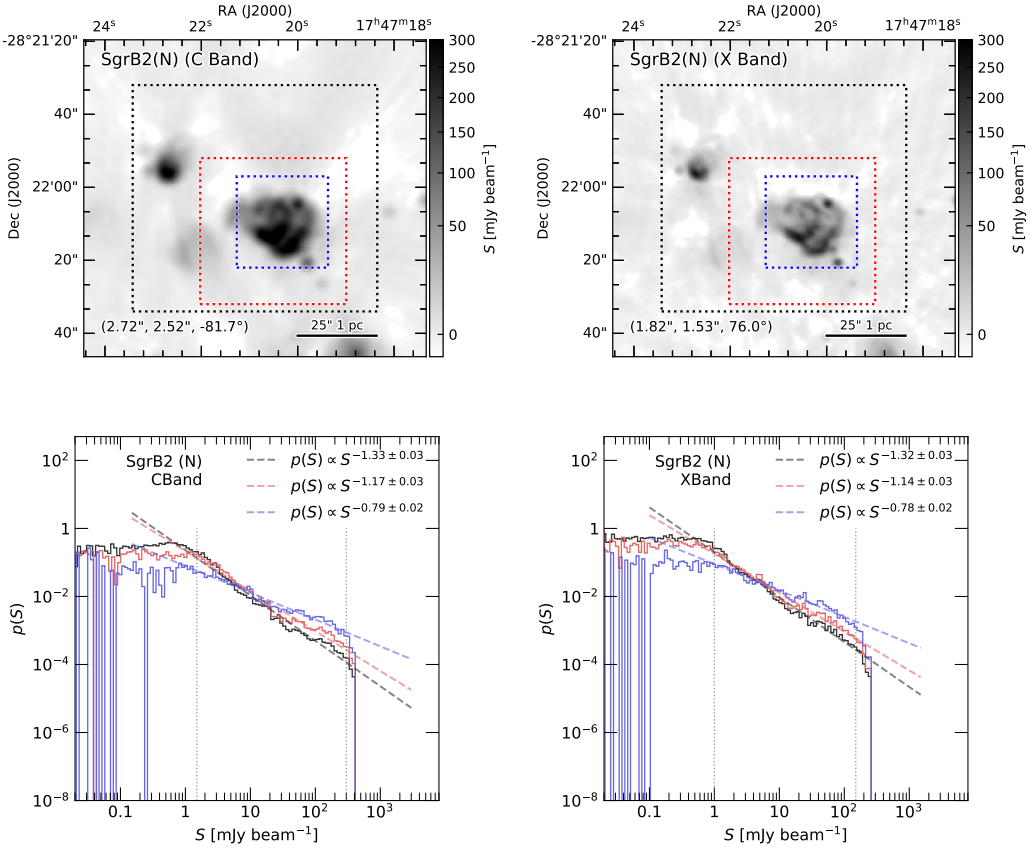

Figure 7.10 PDF of C and X band continuum intensity of SgrB2(N). The plower-law fitting are marked as dashed lines. The regions that are taken into account in the calculation of PDF are marked with corresponding colors. The intensity ranges that are taken into account in the power-law fitting are marked with gray dotted lines. The fitting results are written on the upper right corner of each panel.

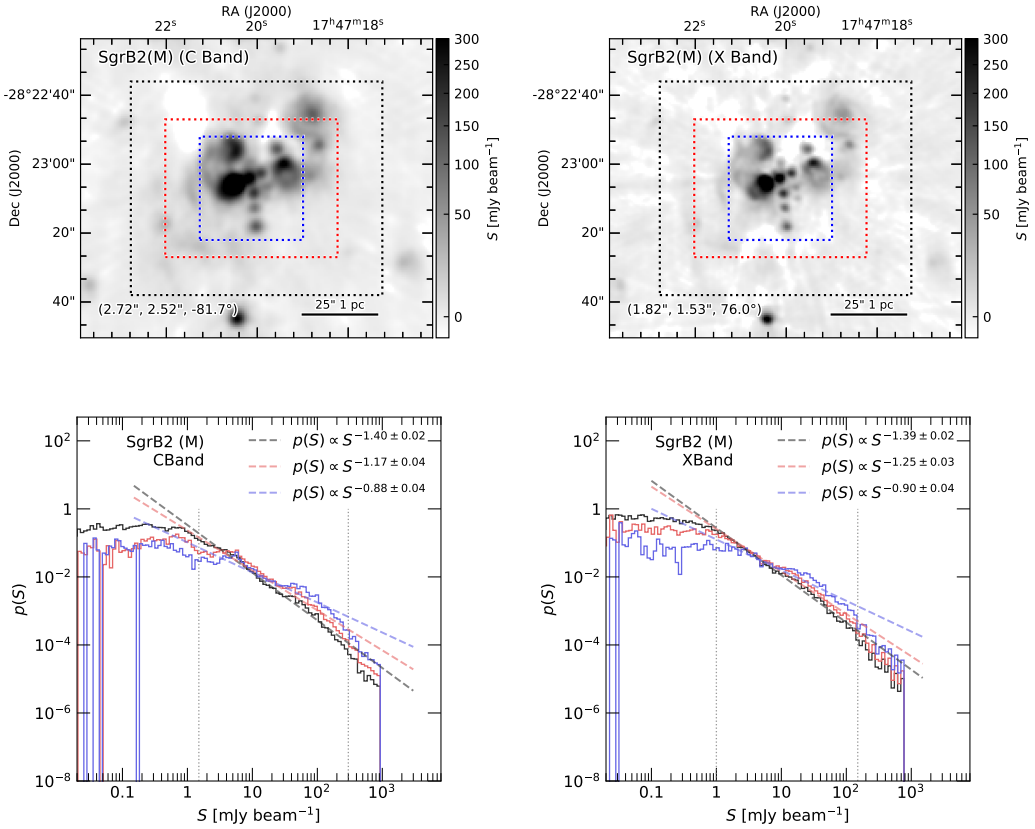

Figure 7.11 PDF of C and X band continuum intensity of SgrB2(M), in panel (a) and (b) respectively. The plower-law fitting are marked as blue dashed lines. The intensity ranges that are taken into account in the power-law fitting are marked with gray dotted lines. The fitting results are written on the upper right corner of each panel.

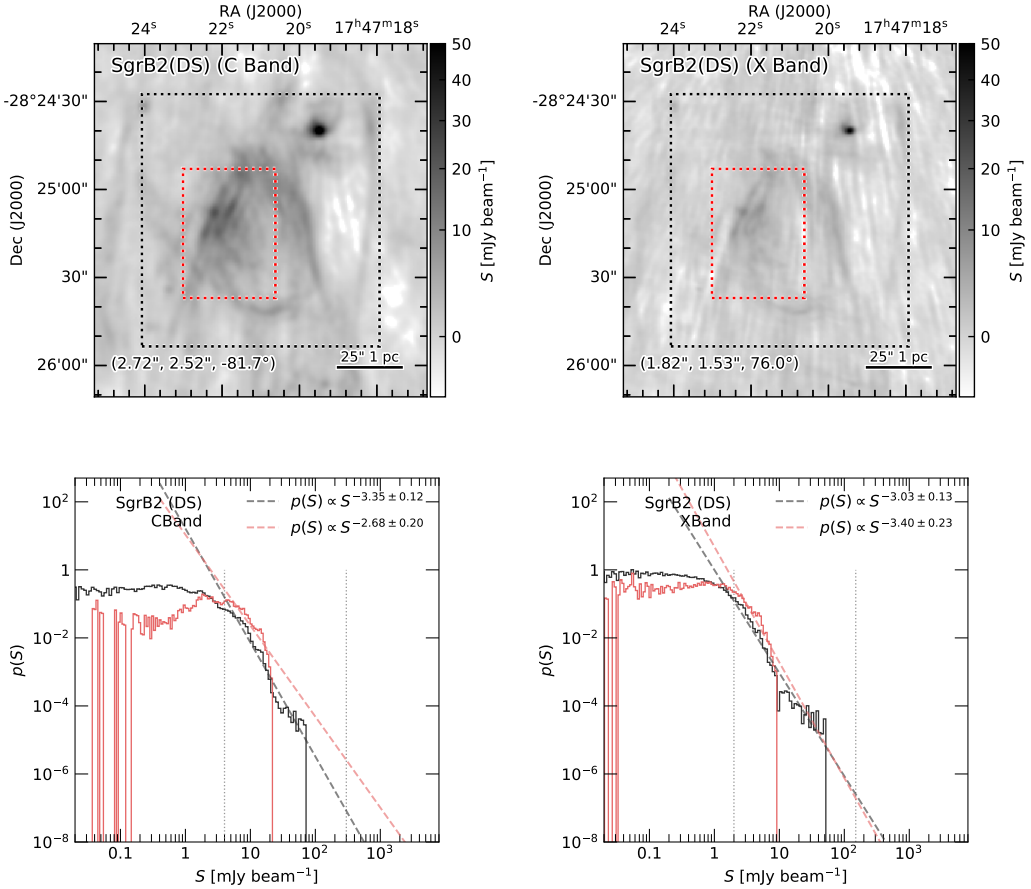

Figure 7.12 PDF of C and X band continuum intensity of SgrB2(DS), in panel (a) and (b) respectively. The plower-law fitting are marked as blue dashed lines. The intensity ranges that are taken into account in the power-law fitting are marked with gray dotted lines. The fitting results are written on the upper right corner of each panel.

7.2.2 Dense gas

HC_3N, which is the first cyanoacetylene molecule detected in space (by Turner, 1971, in SgrB2), traces dense molecular gas. The critical density of HC_3N (10-9), which is the transition observed in this study, is $\gtrsim 10^5\,\mathrm{cm}^{-3}$ (see e.g. Fig. 4 in Costagliola & Aalto, 2010). The peak intensity map of HC_3N (10-9) is shown in Fig. 7.13. Although the data covers the velocity range from -200 km s^{-1} to 200 km s^{-1}, here I use the velocity range 24 km s^{-1} to 96 km s^{-1} to derive the peak intensity.

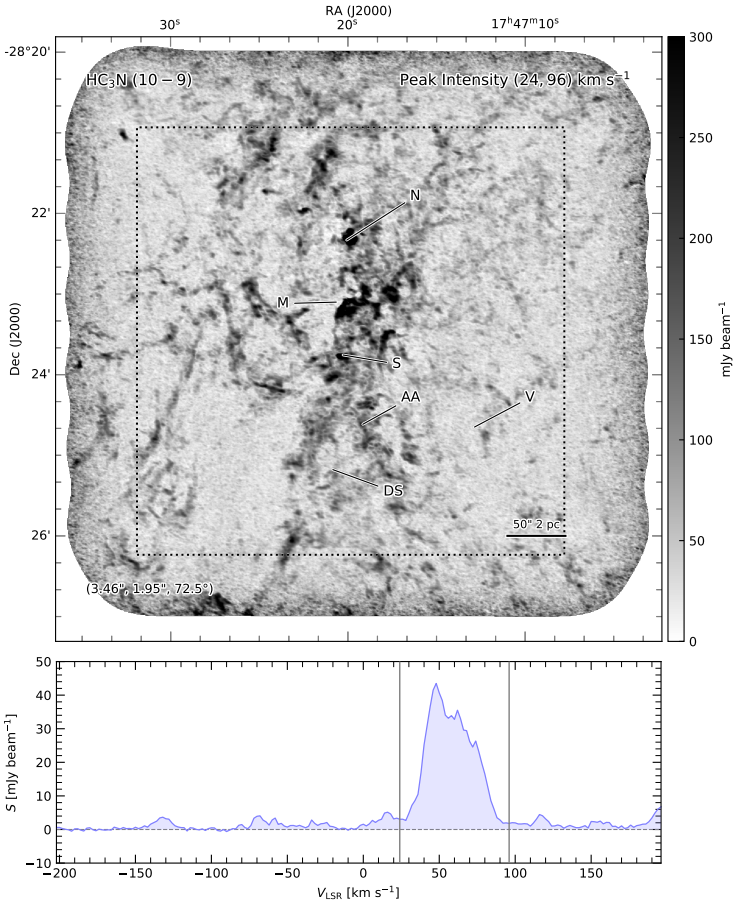

Figure 7.13 Peak intensity map of HC_3N $(10-9)$, from 24 to 96 km s^{-1} . The averaged spectra within the region marked with the box in the upper panel is shown in the lower panel. For the averaging, only spectra that has peak intensity above 150 mJy/beam are taken into account. Some of the important HII regions are marked.

The peak intensity map shows complicated structures, including long ridge, bubble and arcs. These structures appear at different velocities in the datacube. I have taken five velocity cuts, which are sub-cubes of the entire datacube to better display these structures. Using these different velocity ranges I proceed to identify and characterize the different structures. Arcs are described by four parameters, location, radius, angles, velocity. Since an arc is part of a circle, the location is the spatial location of the center of the circle. The radius is the radius of the circle. If the thickness of the arc is not too small compared to the circle size, then the circle should follow the middle curve along the arc. The angles describe

the starting and ending angle of the arc on the circle. The angle is defined with 0 degrees westwards and increasing anti-clockwise. Bubbles are identified as special arcs that have the two angles equal to each other. The velocity is the velocity range of the pixels that belong to the arc or bubble. In the following paragraphs, I describe the structures identified in the HC_3N datacube.

Table 7.2 Table of HC_3N arcs

Arc	RA	Dec	Radius arcsec	(θ_1, θ_2) (deg, deg)	Velocity $km\,s^{-1}$
49A	17:47:23.18	-28:22:48.0	12.0	(180, 330)	48–52
49B	17:47:19.44	-28:21:40.5	17.2	(70, 150)	46–52
55A	17:47:18.20	-28:22:23.5	12.5	(0, 360)	50–58
62A	17:47:24.13	-28:23:42.3	11.0	(120, 330)	52–70
62B	17:47:21.51	-28:23:36.8	7.0	(135, 360)	55–70
63A	17:47:19.46	-28:24:03.1	4.5	(0, 360)	58–60
63B	17:47:20.18	-28:24:48.3	6.5	(0, 180)	60–64
63C	17:47:18.43	-28:24:48.3	21.3	(135, 270)	58–68

26–44 km s^{-1} **:** The peak intensity map and the velocity map are shown in Fig. 7.14. The most prominent structure in this velocity cut is the 'ridge', which extend from $\sim 2'$ to the east of SgrB2(DS) to $\sim 1.5'$ to the east of SgrB2(M), with a length of $\sim 2.5'$ (~ 6 pc) and a width of $\sim 5''$ (~ 0.2 pc). A zoom-in velocity map of the ridge and its position-velocity (P-V) diagrams are shown in Fig. 7.15. The P-V diagram along the ridge (the path is 'Path 0' in Fig. 7.15) shows that its systemic velocity is 30–40 km s^{-1} with a typical line width of 10 km s^{-1} . The P-V diagram of three cuts perpendicular to the ridge (Paths 1 to 3 in Fig. 7.15) display velocity gradients of around $37\,km\,s^{-1}\,pc^{-1}$. The velocity jump between two sides of the ridge is approximately 20 km s^{-1} .

44–54 km s^{-1} **:** The peak intensity map and the velocity map are shown in Fig. 7.16. Two arcs are identified. The arc 49A is to the east of SgrB2(M) and has a radius of $12.0''$ and a velocity in the range48 to 52 km s^{-1} . The arc 49B is to the north of SgrB2(N) and has a radius of $17.2''$ with velocities from 46 to 52 km s^{-1} .

50–60 km s^{-1} **:** The peak intensity map and the velocity map are shown in Fig. 7.17. One bubble is identified. The bubble 55A is to the west of SgrB2(N) and has a radius of $12.5''$ with velocities from 50 to 58 km s^{-1} .

52–72 km s^{-1} **:** The peak intensity map and the velocity map are shown in Fig. 7.18. Two arcs are identified. The arc 62A is to the east of SgrB2(S) and has a radius of $11.0''$ with velocities from 52 to 70 km s^{-1} . The arc 62B is between SgrB2(M) and SgrB2(S) and has a radius of $7.0''$ with velocities from 55 to 70 km s^{-1} .

58–68 km s^{-1} **:** The peak intensity map and the velocity map are shown in Fig. 7.19. Three arcs are identified. The arc 63A is to the south of SgrB2(S) and has a radius of $4.5''$ with velocities from 58 to 60 km s^{-1} . The arc 63B is to the south of 63A and has a radius of $6.5''$ with velocities from 60 to 64 km s^{-1} . Finally, the arc 63C is surrounding 63B and has a radius of $21.3''$ with velocities from 58 to 68 km s^{-1} .

The parameters of these eight arcs are listed in Table 7.2, and they are marked in the corresponding velocity maps as solid curves on top of dashed circles.

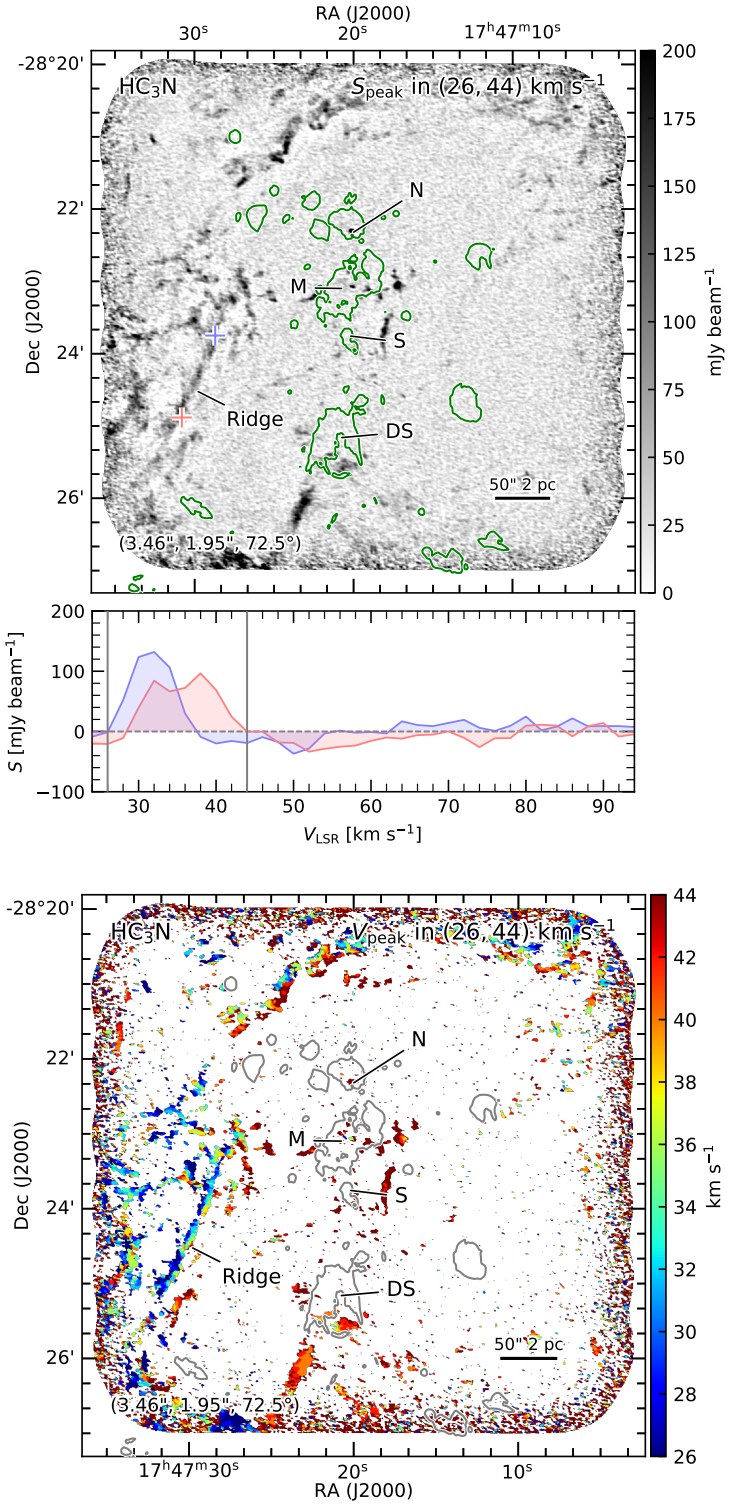

Figure 7.14 Peak intensity map (upper panel) and peak velocity map (lower panel) of HC_3N $(10-9)$ line. The peaks are searched in velocity range 26–44 km s^{-1} . For the peak velocity, spectra with peak intensity below 50 mJy/beam are masked out. Spectra at the spots marked with red and blue '+' in the upper panel are shown in the middle panel. Beam sizes are marked on the lower left corner of the maps, in format $(\theta_{\rm maj}, \theta_{\rm min}, {\rm PA})$. The ridge and some of the important HII regions are marked.

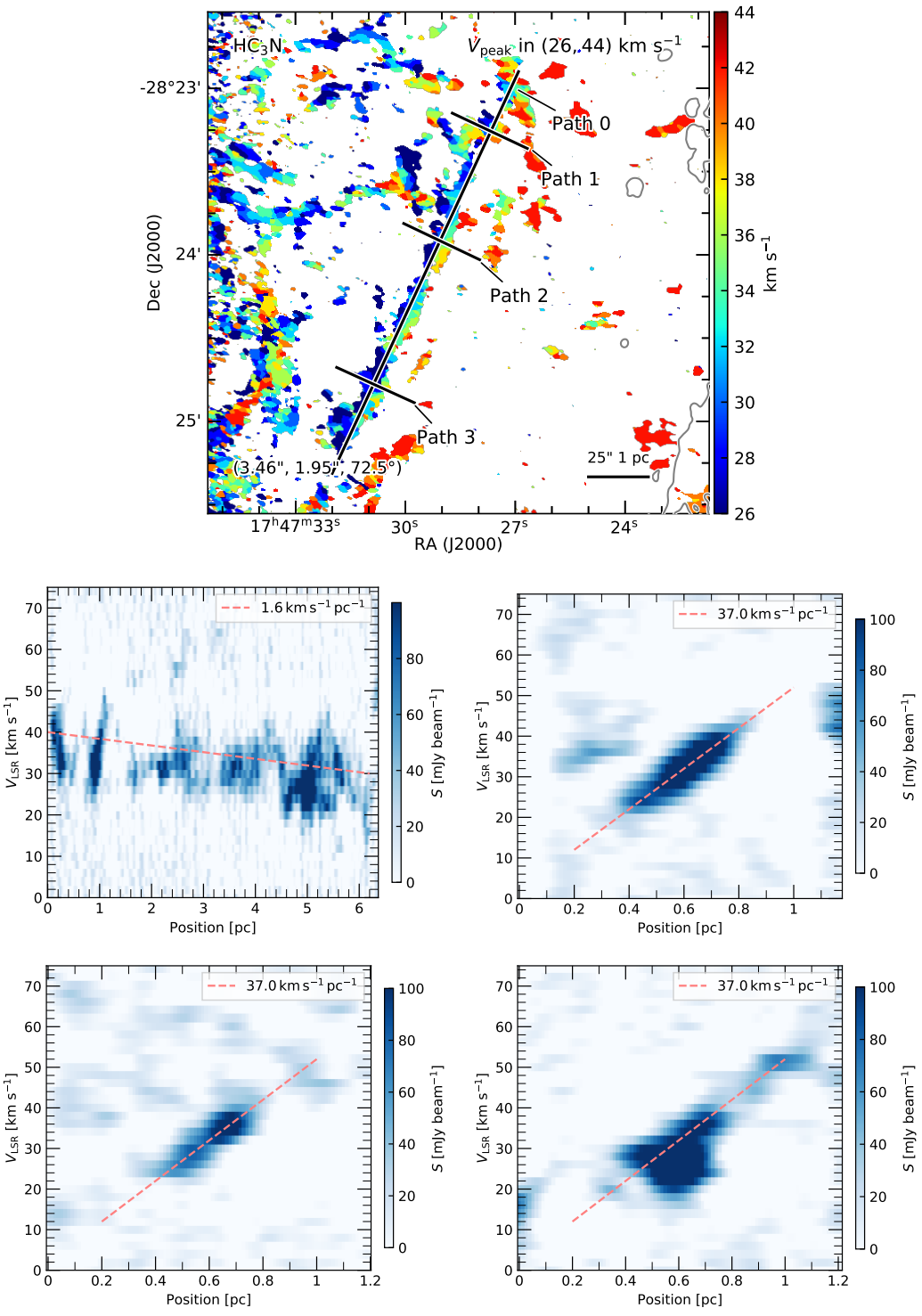

Figure 7.15 PV diagram of the ridge. Four paths are marked on the map. Velocity gradients are marked on the upper right corner of each panel.

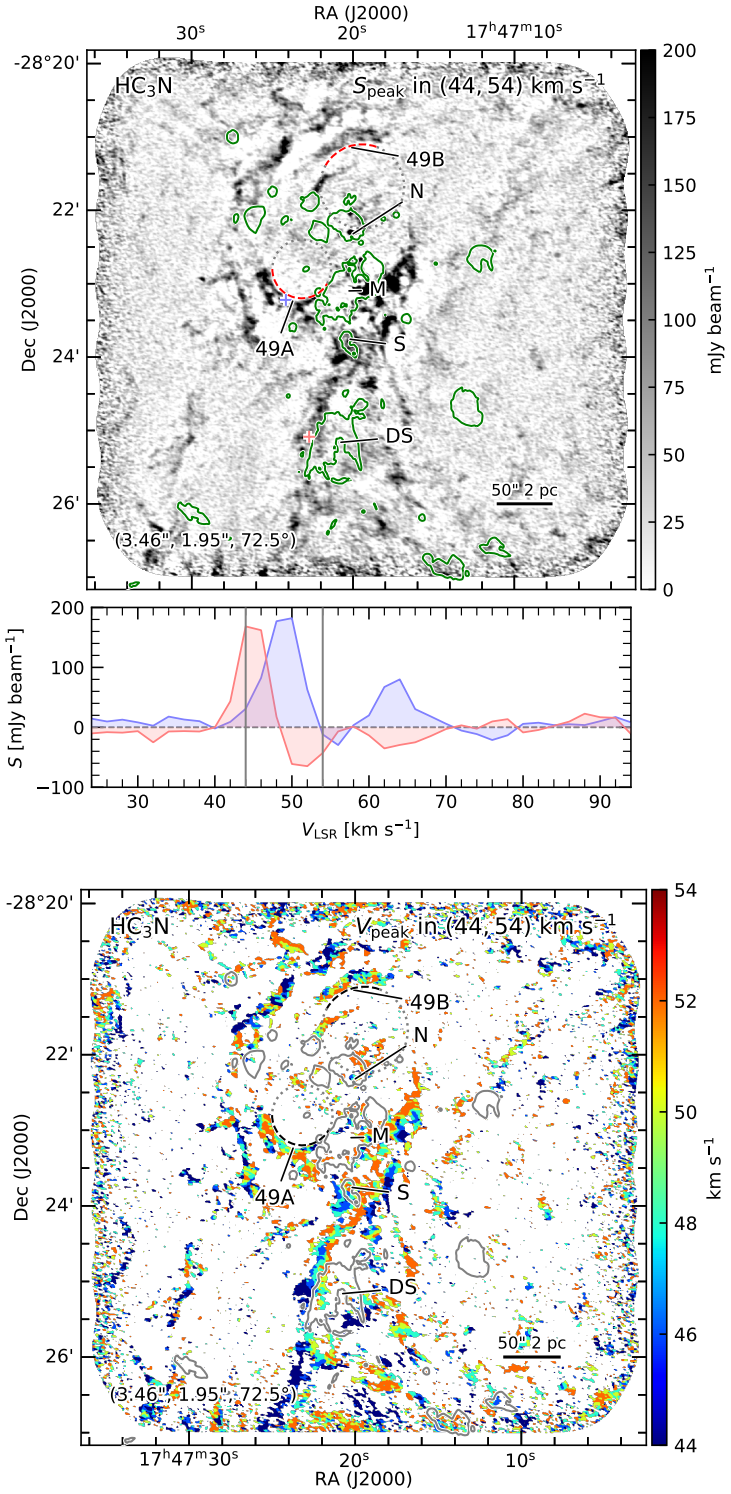

Figure 7.16 Peak intensity map (upper panel) and peak velocity map (lower panel) of HC_3N $(10-9)$ line. The peaks are searched in velocity range 44–54 km s^{-1} . For the peak velocity, spectra with peak intensity below 50 mJy/beam are masked out. Spectra at the spots marked with red and blue '+' in the upper panel are shown in the middle panel. Beam sizes are marked on the lower left corner of the maps, in format $(\theta_{\rm maj}, \theta_{\rm min}, {\rm PA})$. The ridge and some of the important HII regions are marked.

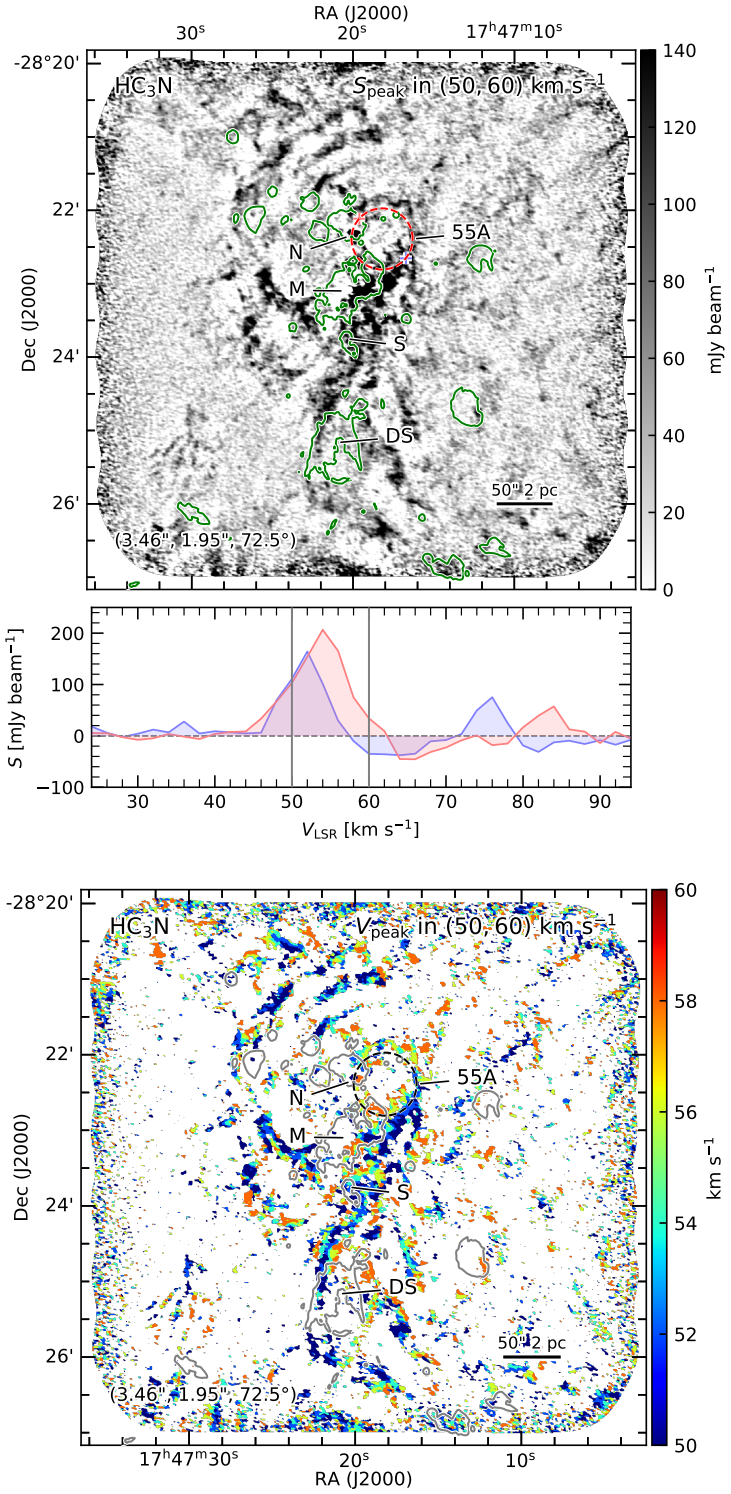

Figure 7.17 Peak intensity map (upper panel) and peak velocity map (lower panel) of HC_3N $(10-9)$ line. The peaks are searched in velocity range 50–60 km s^{-1} . For the peak velocity, spectra with peak intensity below 50 mJy/beam are masked out. Spectra at the spots marked with red and blue '+' in the upper panel are shown in the middle panel. Beam sizes are marked on the lower left corner of the maps, in format $(\theta_{\rm maj}, \theta_{\rm min}, {\rm PA})$. The ridge and some of the important HII regions are marked.

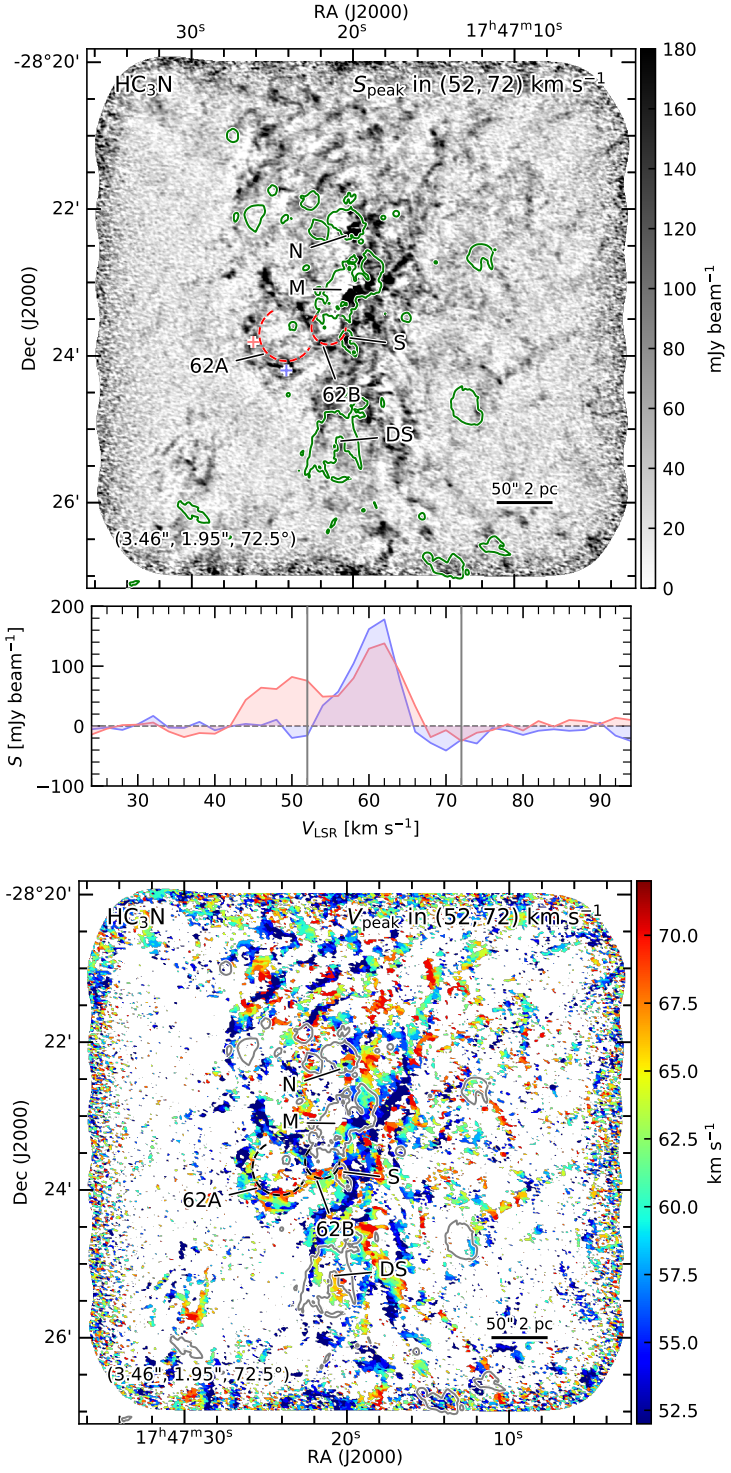

Figure 7.18 Peak intensity map (upper panel) and peak velocity map (lower panel) of HC_3N $(10-9)$ line. The peaks are searched in velocity range 52–72 km s^{-1} . For the peak velocity, spectra with peak intensity below 50 mJy/beam are masked out. Spectra at the spots marked with red and blue '+' in the upper panel are shown in the middle panel. Beam sizes are marked on the lower left corner of the maps, in format $(\theta_{\rm maj}, \theta_{\rm min}, {\rm PA})$. The ridge and some of the important HII regions are marked.

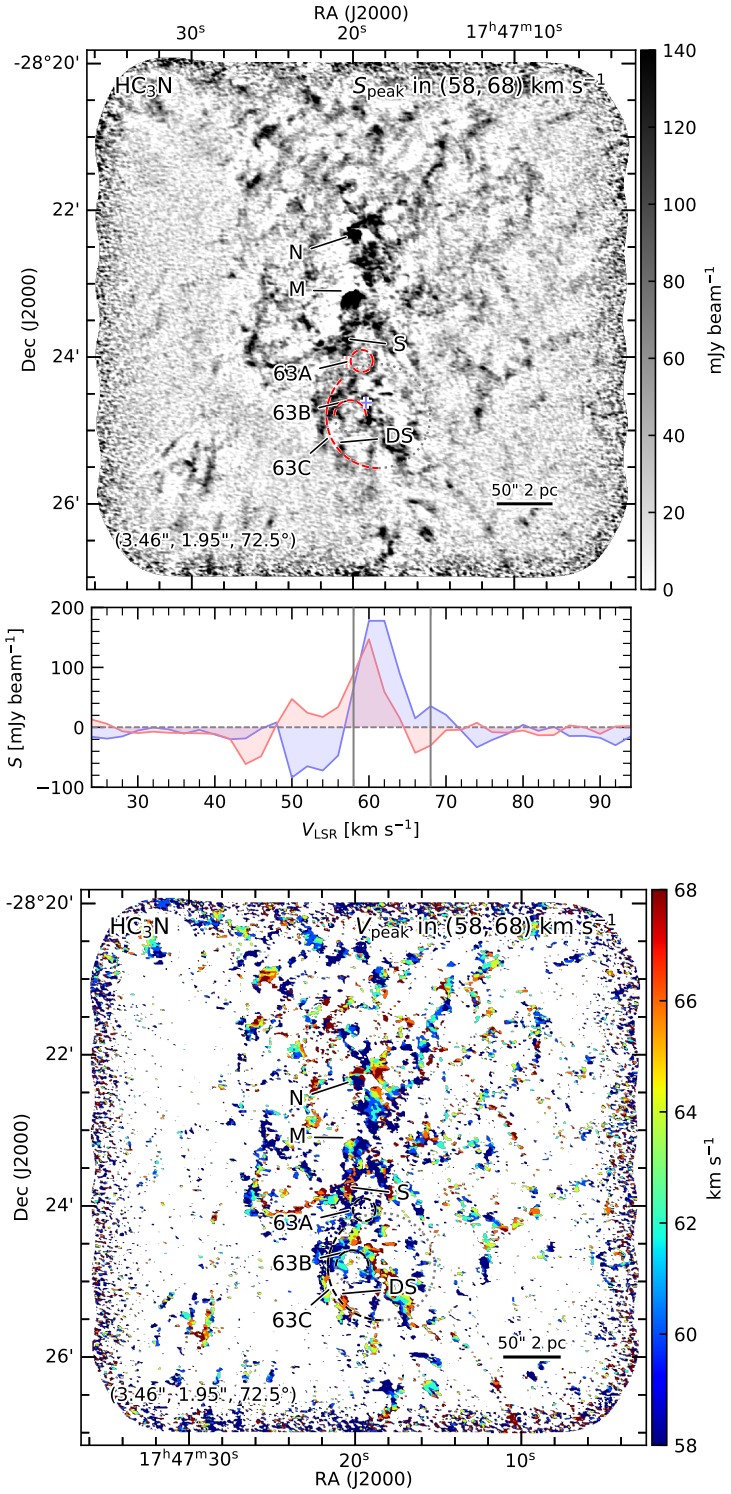

Figure 7.19 Peak intensity map (upper panel) and peak velocity map (lower panel) of HC_3N $(10-9)$ line. The peaks are searched in velocity range 58–68 km s^{-1} . For the peak velocity, spectra with peak intensity below 50 mJy/beam are masked out. Spectra at the spots marked with red and blue '+' in the upper panel are shown in the middle panel. Beam sizes are marked on the lower left corner of the maps, in format $(\theta_{\rm maj}, \theta_{\rm min}, {\rm PA})$. The ridge and some of the important HII regions are marked.

7.3 Discussion

In this section I analyze and discuss the results presented in the previous section. In particular, I discuss the physical meaning of the PDFs that I calculate, the filling factor of the ionized gas, the physical properties of the HII regions in the envelope, and the dense gas in the envelope.

7.3.1 PDFs

The PDFs of the whole SgrB2 region as well as SgrB2(N), (M), and (DS) all partially follow power laws that can be expressed as:

$$p(S) = p_0 S^{\beta}, \tag{7.2}$$

where β is the index of the power-law. I consider a simple, circularly-symmetric HII region with a power-law radial intensity profile:

$$S(R) = S_0 R^{\gamma} \quad (R > R_{\rm C}), \tag{7.3}$$

where R is the projected distance to the center. To avoid singularity, I assume that the power-law profile is only valid outside of a circle in the vicinity of the center, with radius $R_{\rm C}$. The region $R \leq R_{\rm C}$ is considered to be small enough and, therefore, is negligible in the PDF analysis. Here, S is simply the observed flux density. In this model, I do not assume any density profile within the HII region, as long as the observed flux density profile fits Eq. 7.3. If I calculate the PDF of such an HII region, the relationship between β and γ is:

$$\beta = \frac{2}{\gamma} - 1. \tag{7.4}$$

Under the assumption of Eq. 7.3 together with Eq. 7.4, and using β, I derive γ of the flux density profiles of SgrB2 and its subregions. The entire SgrB2 has $\gamma \sim -2.5$, (M) and (N) have γ between -5 and -10 (for the $\beta < -1$ cases, for the mostly zoomed-in cases, where $\beta > -1$, see the discussion in the next paragraph) and (DS) has $\gamma \sim -1.3$. The values of γ close to 0 for the entire SgrB2 and (DS) regions indicate that they have a more extended component compared to (M) and (N), for which the values of $\gamma \ll 0$ suggest the presence of centrally-peaked structures.

It is worth notice that Eq. 7.4 has a singularity at $\gamma = 0$. When $\gamma > 0$, $-1 < \beta < 0$, which means that the intensity distribution is not center-heavy but shows a bright circle around a dim center (bubble-like). The central parts of (N) and (M) both have $\beta > -1$ (see Fig. 7.10 and 7.11), corresponding to $\gamma > 0$, which means that the central parts of (N) and (M) possibly have bubble-like components.

7.3.2 Filling factor

One of the major goals of this study is to estimate the *volume filling factor*, $f_{\rm V}$, of the ionized gas in the entire SgrB2 region. The conventional method is to derive $f_{\rm V}$ from the electron volume density $n_{\rm e}$ (Berkhuijsen, 1998; Berkhuijsen et al., 2006), as

$$f_{\rm V} = \frac{\langle n_{\rm e}^2 \rangle}{n_{\rm e}^2}. \tag{7.5}$$

Although $\langle n_e^2 \rangle$ can be derived from the emission measure, the local electron density, n_e, which is the ratio between emission measure and *dispersion measure* [2], is unknown. Therefore, here we firstly estimate the *area filling factor*, f_A, and then derive f_V from f_A with certain assumptions in the geometry of the SgrB2 envelope.

I define f_A as

$$f_A = \frac{N(S > S_0)}{N}, \tag{7.6}$$

where $N(S > S_0)$ stands for the number of pixels that have intensity larger than the threshold S_0. Different to Eq. 7.1, N is the number of pixels with intensity larger than 0. Hence, f_A can be treated as a function of the threshold S_0. In Fig. 7.20, the $f_A(S_0)$ curves for the C band and X band images are shown. If I set S_0 between σ and 2σ, f_A is between 0.05 and 2. I take 0.1 as the approximated value of f_A. If I assume that the geometry of SgrB2 is spherical, then $f_V = f_A^{3/2} \approx 0.03$. If SgrB2 is cylindrical (with generatrix perpendicular to the line of sight), $f_V = f_A^2 \approx 0.01$. Berkhuijsen (1998) summarized f_V for various n_e in the Galaxy, which shows that $f_V \approx 10^{-4}$ for $n_e \sim 10^3 - 10^4\,\mathrm{cm}^{-3}$. For both geometry assumptions, the f_V estimated for SgrB2 is higher than the typical values in the Galaxy where n_e is similar to that of SgrB2 ($n_e \sim 10^3 - 10^4\,\mathrm{cm}^{-3}$, see Table 7.1).

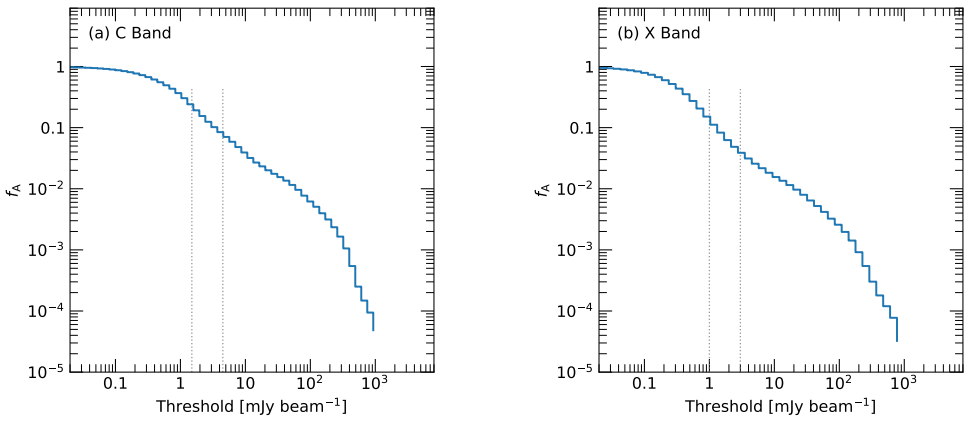

Figure 7.20 The area filling factor curves derived from the C and X band images. The gray dashed lines marks σ and 3σ thresholds.

7.3.3 Properties of HII regions

The physical properties of the HII regions can be derived from their observed parameters, listed in Table 7.3. Assuming that the emission of both the RRLX and the X band continuum are optically thin, the electron temperature T_e can be derived from the ratio between the integrated intensity of RRLX and S_X, according to Eq. A.28. The map of T_e is shown in Fig. 7.21. Most of the HII regions have $T_e \sim 5000\,\mathrm{K}$. The two exceptions are IG2608 ($T_e = 2700\,\mathrm{K}$) and IG2715 ($T_e = 1100\,\mathrm{K}$). These abnormally low T_e might not be physical. A possible reason is that the RRLX emission for these two regions is not under conditions, but it is stimulated. In this scenario, the intensity of the RRLX would be higher than for

[2] Dispersion measure is defined as $\int n_e\, dl$, the integral is along the line of sight.

LTE (see Sect. 6.3.2). The higher intensity of RRLX may underestimate the value derived for T_e.

Table 7.3 Physical parameters of HII regions in the envelope of SgrB2

Region	T_e 10^3 K	EM 10^6 cm^{-6} pc	$\langle n_e \rangle$ 10^3cm^{-3}	log $\dot{N}_{Ly}$ [a]	SP [b]
IG2207	6.0 ± 3.0	2.5 ± 1.3	4.0 ± 0.5	$47.04^{+0.14}_{-0.08}$	B0.5–B0
IG2210	7.3 ± 1.4	2.4 ± 0.9	2.2 ± 0.2	$47.48^{+0.04}_{-0.03}$	O9.5–B0
IG2243	7.3 ± 1.3	2.4 ± 0.5	3.1 ± 0.2	$47.11^{+0.04}_{-0.03}$	B0.5–B0
IG2431	2.9 ± 0.6	0.6 ± 0.3	1.5 ± 0.2	$47.34^{+0.05}_{-0.04}$	O9.5–B0
IG2432	3.4 ± 0.7	0.5 ± 0.2	1.7 ± 0.2	$46.83^{+0.05}_{-0.04}$	B0.5–B0
IG2608	2.7 ± 0.8	0.6 ± 0.4	0.68 ± 0.10	$48.18^{+0.07}_{-0.05}$	O9–O8.5
IG2611	10.6 ± 1.8	3.8 ± 0.9	3.1 ± 0.2	$47.15^{+0.04}_{-0.03}$	B0.5–B0
IG2715	1.1 ± 0.7	0.05 ± 0.06	0.14 ± 0.03	$47.28^{+0.20}_{-0.10}$	B0.5–B0
M92A	5.0 ± 1.2	6.9 ± 6.0	4.2 ± 0.8	$48.25^{+0.05}_{-0.04}$	O8.5–O8
M92B	5.7 ± 1.0	15 ± 12	6.1 ± 1.0	$48.52^{+0.04}_{-0.03}$	O7.5–O7
M92C	7.3 ± 1.3	44 ± 27	10.5 ± 1.4	$48.86^{+0.04}_{-0.03}$	O6.5–O6
M92D	5.6 ± 1.2	6.0 ± 4.0	3.9 ± 0.6	$48.10^{+0.05}_{-0.04}$	O9–O8.5
M93BB	5.0 ± 1.0	4.0 ± 1.9	2.8 ± 0.3	$48.30^{+0.04}_{-0.04}$	O8–O7.5
M93L	6.0 ± 1.1	43 ± 30	9.9 ± 1.5	$49.05^{+0.04}_{-0.03}$	O6.5–O6
M93O	3.8 ± 0.9	1.1 ± 0.4	2.4 ± 0.2	$47.13^{+0.05}_{-0.04}$	B0.5–B0
M93P	7.8 ± 1.3	6.2 ± 1.7	5.7 ± 0.4	$47.28^{+0.04}_{-0.03}$	B0.5–B0
M93Q	5.1 ± 1.0	3.2 ± 0.6	4.7 ± 0.2	$47.07^{+0.04}_{-0.03}$	B0.5–B0
M93R	6.5 ± 0.7	23.2 ± 8.6	6.5 ± 0.6	$48.89^{+0.02}_{-0.02}$	O6.5–O6
M93T	5.0 ± 0.6	3.9 ± 1.3	3.4 ± 0.3	$47.93^{+0.02}_{-0.02}$	O9.5–O9
M93U	5.0 ± 0.6	5.4 ± 3.6	3.3 ± 0.5	$48.35^{+0.02}_{-0.02}$	O8–O7.5
M93W	7.3 ± 1.5	4.1 ± 2.1	3.2 ± 0.4	$47.69^{+0.04}_{-0.04}$	O9.5–B0
M93X	5.6 ± 0.9	4.1 ± 1.3	4.7 ± 0.3	$47.49^{+0.03}_{-0.03}$	O9.5–B0

[a] $\log_{10}\left(\frac{\dot{N}_{Ly}}{s^{-1}}\right)$

[b] Spectral type of star according to Panagia (1973), assuming that the Lyman continuum photons of each HII region are emitted by one star.

When LTE applies and the RRL emission is optically thin, the emission measure (EM) of the HII region can be derived, see Eq. A.27. The map of EM is shown in Fig. 7.21. Most of the HII regions have EM between 10^6 cm^{-6} pc and 5×10^7 cm^{-6} pc. However, IG2715 has EM smaller than 10^5 cm^{-6} pc, which may due to the underestimation of the T_e. When EM is obtained, the averaged number density of electrons, $\langle n_e \rangle$, can be derived, by assuming the geometry of the HII regions to the spherical. Most of the HII regions have $\langle n_e \rangle$ between 10^3 cm^{-3} and 10^4 cm^{-3}. IG2715, due to the underestimated T_e and EM, has $\langle n_e \rangle \sim 10^2$ cm^{-3}, which is probably also underestimated. It is worth to mention that the size used for deriving $\langle n_e \rangle$ is R (listed in Table. 7.1), which might be larger than the actual projected size of the HII regions, especially when the HII region's morphology deviates significantly from a sphere. Thus, $\langle n_e \rangle$ might be slightly underestimated for all the HII regions.

Based on Eq. A.29, the flux of Lyman continuum photons $\dot{N}_{Ly}$ can be derived from S_C. Here I use S_C due to its better image quality. The 22 HII regions have log $\dot{N}_{Ly}$ between 46.83 and 49.05. From $\dot{N}_{Ly}$, I derive the spectral types of the ionizing stars in each HII region. If I assume the mass distribution of the stars that ionize each HII region obeys the IMF as

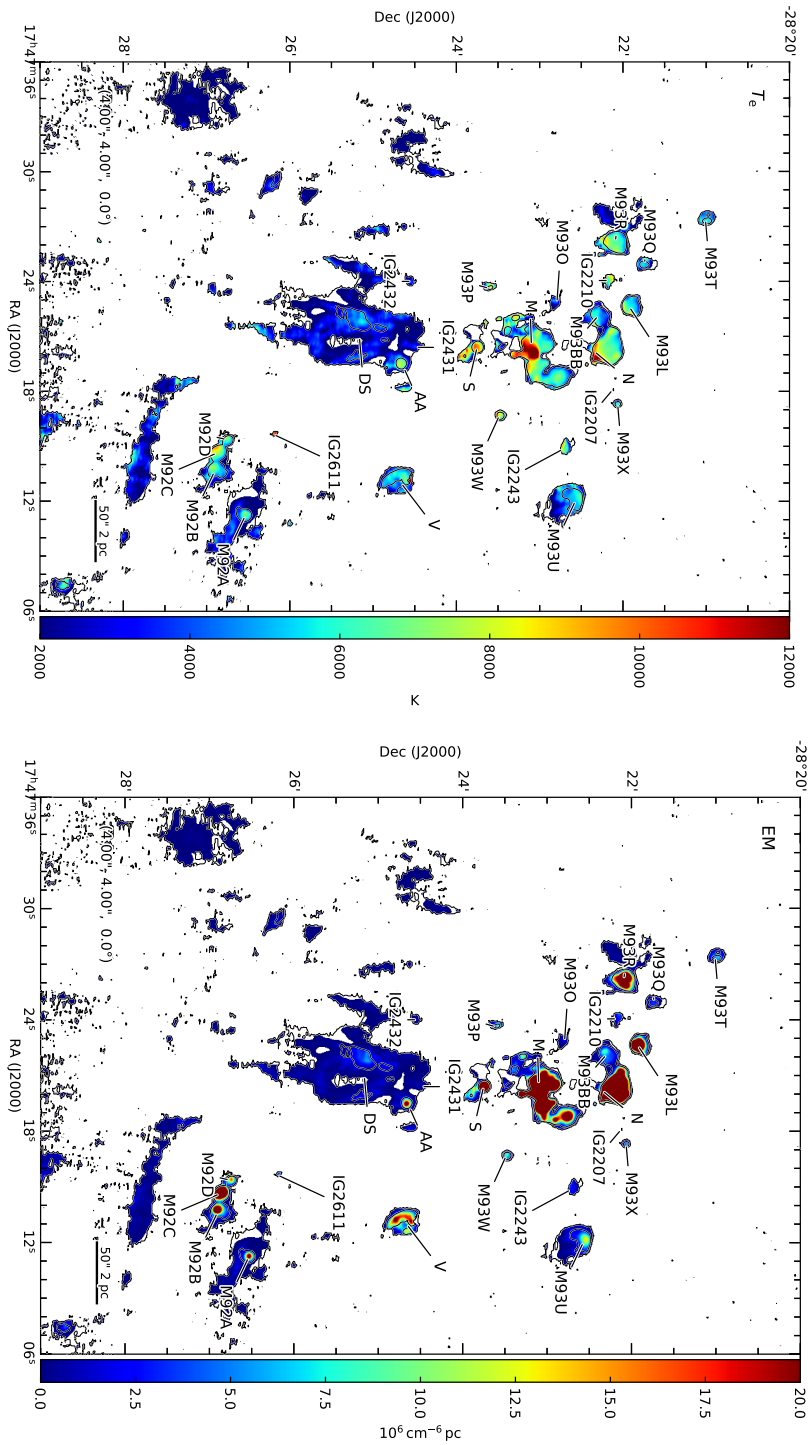

Figure 7.21 Map of T_e (*left panel*) and emission measure (*right panel*) in SgrB2

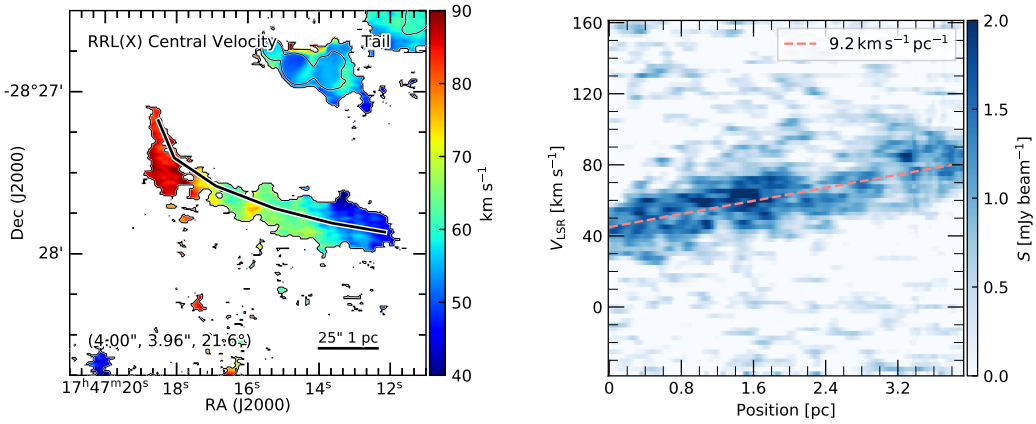

Figure 7.22 PV diagram of the tail. The path that the PV diagram is taken is marked on the map. Velocity gradient is marked on the upper right corner of the panel.

presented in Kroupa (2001), $\xi(m) \propto m^{-\alpha_{\rm K}}$. $\xi(m)$ is the probability of finding a star that has mass between m and $m + \Delta m$. For high-mass stars, $\alpha_{\rm K} = 2.3$. On the other hand, I express $\dot{N}_{\rm Ly}$ as a power-law of the stellar mass, within a small range of $\dot{N}_{\rm Ly}$, as $\dot{N}_{\rm Ly} \propto m^{\beta_L}$. The power index β_L is between 5 and 8 for $\log \dot{N}_{\rm Ly}$ between 46 and 49 (see e.g. Davies et al., 2011), see Fig 7.23 for the plot. Since $\alpha_{\rm K}$ is much smaller than β_L, more lower mass stars cannot compensate the gigantic difference of $\dot{N}_{\rm Ly}$ caused by mass difference. Therefore, it is reasonable to make the assumption that the Lyman continuum photons are mainly from one star, the most massive one. Based on Panagia (1973), the spectral type of the ionizing star of each HII region can be estimated (assuming that the stars are at the Zero-Age Main Sequence, ZAMS). The derived spectral types range from B0.5 to O6.

Apart from the physical properties, the kinematic structures of the HII regions are also characterized. Among all the regions, the curved filament to the south-west of SgrB2(DS) shows a significant velocity gradient. In this study, I call this structure 'tail'. The position-velocity (hereafter PV) diagram of the tail is shown in Fig. 7.22. The velocity gradient along the tail is approximately $9.2\,{\rm km\,s^{-1}\,pc^{-1}}$.

7.3.4 Dense gas in the envelope

The presence of arcs and bubbles suggests that the molecular envelope of SgrB2 is not homogeneous. The arcs 63A, 63B and 63C are spatially correlated with SgrB2(DS), and also have a similar velocity to SgrB2(DS). Thus, they are probably driven by the expansion of SgrB2(DS). The other arcs and bubbles are mostly located in the eastern part of the envelope, to the east of SgrB2(N), SgrB2(M) and SgrB2(S). The origin of these arcs and bubbles is not clear. One possibility is that, as proposed by Martín-Pintado et al. (1999) for the ammonia bubbles in SgrB2, they are driven by expanding HII regions. However, there is no clear spatial correlation between most of the HII regions and the arcs and bubbles detected in this study, which might be due to weak emission from largely-expanded and optically thin HII regions not detectable in our dataset.

Also in the eastern part of the envelope, the ionized gas emission, especially RRLX,

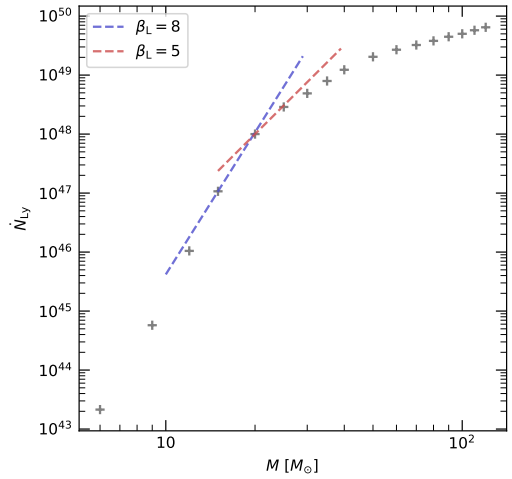

Figure 7.23 $\dot{N}_{\rm Ly}$ against stellar mass. Data points are from Davies et al. (2011), the dashed lines are interpolates between neighboring data points.

displays a straight elongated morphology. One example is the ridge, which is the only elongated structure that has good enough SNR to be analyzed in detail. The ridge has a velocity difference of $\sim 20\,{\rm km\,s^{-1}}$ between the two sides. Such a velocity gradient is consistent with that of C-type shocks (see e.g. Schilke et al., 1997; Gusdorf et al., 2008), when assuming a projection angle of 45°.

7.4 Summary

In this chapter, the results of large scale ionized gas emission, both continuum and RRL, as well as the molecular dense gas emission (traced by the HC_3N species) presented. The following properties of the large scale envelope of SgrB2 are revealed:

- The PDF of the C and X band continuum images in the whole envelope has a power index of −1.7. The PDF of SgrB2(N) and SgrB2(M) tend to have shallower power index, while SgrB2(DS) has a power index of ~ -3.
- The area filling factor of ionized gas in the whole SgrB2 is 0.1. Depending on 3-D geometry, the volume filling factor of ionized gas in SgrB2 may range from 0.03 to 0.01.
- 22 HII regions in the envelope are studied. The electron temperature, emission measure, and spectral type ionized stars are derived.
- Eight arcs and bubbles are identified form HC_3N data cube. Their morphologies and velocity structures are presented. The origin of the bubbles and arcs in the eastern part of the envelope is not clear.

The HII regions in the envelope are more extended than those in SgrB2(M) and SgrB2(N), suggesting that the HII regions in the envelope may be older than those in the central regions SgrB2(M) and SgrB2(N), and therefore, indicating that high-mass star formation might have started throughout the envelope before than in the central regions.

Part IV

Summary and Outlook

Chapter 8

Summary

In this thesis, I studied the high-mass star forming region, SgrB2, with multi-frequency observational data that cover spatial scales from $0.1''$(0.004 pc or 1000 au) up to 20 pc (the size of the envelope) and frequencies from 4 GHz to 346 GHz. The ionized gas content in SgrB2 is mainly traced by the VLA data in the C and X bands (4–12 GHz), observed with configurations A, BnC and D. These datasets cover spatial scales from $0.2''$ to $\sim 15'$ and contains continuum and spectral line (RRLs) data. The high angular resolution observations of VLA in K, Ka, and Q bands with configuration A provides observations of the continuum emission at a resolution of $\sim 0.1''$and covering the frequency range $20-50$ GHz, which traces a mixture of dust and ionized gas continuum emission. Additionally, high angular resolution (resolution$\lesssim 0.5''$) data from ALMA and SMA at mm wavelengths have been used to trace the dust continuum emission at frequencies ranging from 100 to 300 GHz. Complementary to the continuum and RRLs data, I have used HC_3N (10-9) spectral line data observed with ALMA in order to trace and characterize the dense gas in SgrB2. With these datasets, I have studied the properties of SgrB2 at different spatial scales:

Small Scale: I studied the physical properties of 308 dense cores distributed throughout the entire SgrB2 cloud. Out of the 308 cores, 58 are found associated with HII regions (Type I cores). The SEDs of Type I cores have been modeled. Type I cores have a mean m_{H_2} of 150–2500 $M_\odot$, by assuming various dust properties and gas temperatures. Most of the 58 HII regions have a Lyman continuum photon flux $10^{46} - 10^{48}\,s^{-1}$, which corresponds to spectral types of B0 and O9. Evolutionary stages of the cores in SgrB2(N), SgrB2(M), SgrB2(S), and SgrB2(DS) are analyzed. Among the cores in SgrB2(N) and SgrB2(M), 33% and 55% are associated with HII regions, respectively. While for the 46 cores in SgrB2(S) and the 46 cores in SgrB2(DS), this percentage is 4% and 7%, respectively. Out of the 46 cores in SgrB2(DS), 31 are associated with outflows, which are traced by SiO emission. Therefore, I conclude that the cores in SgrB2(M) are most evolved, followed by the cores in SgrB2(N). The cores in SgrB2(S) and SgrB2(DS) are less evolved and are at their very early stages.

Medium Scale: I studied the SgrB2(DS) HII region, which is located in the southern part of the envelope. Sgr B2(DS) is bright at radio wavelengths, with intensities in the range 10–50 mJy/beam, within the observed 4 to 12 GHz frequency range. At $4''$ resolution, DS appears as bubble-like HII region with a diameter of about 1.5 pc, powered by an O7 star, and surrounded by dense gas and a series of dense cores distributed in

an arc structure around it. I find that the total flux of DS decreases from 1.9 Jy at 4 GHz down to 0.5 Jy at 12 GHz. Spectral analysis shows that the spectral index of DS varies from -0.4 to -1.2, suggesting the presence of non-thermal emission, in addition to the thermal emission of the HII region. The RRLs in Sgr B2(DS) are possibly stimulated by synchrotron emission. In collaboration with Padovani et al. (2019), we modeled the observed synchrotron emission, and found that relativistic electrons can be produced via first-order Fermi acceleration, which is triggered by the interaction between the expanding HII region and the denser surrounding material. From the model, we derive maps of the flow velocity in the shock reference frame, magnetic field strength and density in the Sgr B2(DS) region. Velocities are found to be between 35 and 50 km s^{-1} as found in simulations of cometary HII regions of O and B stars driving strong stellar winds. The magnetic field strength is found to be in the range 0.3–4 mG as reported by Crutcher et al. (1996) and the density in the range of $1 - 9 \times 10^4$ cm^{-3}.

Large Scale: I characterized the physical properties of all the HII regions in the envelope as well as the kinematic structure of the envelope. The PDF of the C and X band continuum images in the whole envelope of SgrB2 has a power index of -1.7. The PDF of SgrB2(N) and SgrB2(M) tend to have shallower power index, while SgrB2(DS) has a power index of ~ -3. The area filling factor of the ionized gas in the whole SgrB2 is ~ 0.1. Depending on the assumed 3-D geometry, the volume filling factor of ionized gas in SgrB2 may range from 0.03 to 0.01. I studied 22 HII regions in the nvelope for which I derived electron temperature, emission measure, and flux of Lyman continuum photons consistent with ultracompact HII regions. Eight arcs and bubbles are identified form the HC_3N data cube. Their morphologies and velocity structures have been presented. The HII regions in the envelope appear to be more extended (therefore, probably older) than those in SgrB2(M) and SgrB2(N). This may indicate that high-mass star formation might have started throughout the envelope before than in the central regions of SgrB2.

With these results, I qualitatively depict a *possible* star formation history of SgrB2:

- High-mass stars firstly formed in the envelope. Among the newly formed stars, the one at the center of SgrB2(DS) was one of the brightest (O7). Numerous UCHII regions were ionized and embedded in the dense gas in the envelope. In SgrB2(N) and SgrB2(M), the dense dust cores had just formed but were starless.

- In the envelope, the HII regions were expanding due to pressure, while pushing the surrounding molecular gas. In SgrB2(DS), shock waves appeared. In SgrB2(M), high-mass stars started to form. Later on, high-mass star formation started in SgrB2(N).

- Bubbles and arcs of dense molecular gas were shaped in the envelope by the expanding HII regions. Triggered by the feedback of the older generation of high-mass stars, a new generation of high-mass dense cores formed in the envelope. In SgrB2(DS), the ionized content emit synchrotron emission due to the shocks in it. Surrounding SgrB2(DS), the newly-born high-mass dust cores entered the earliest stages of star formation and had outflows associated with them. However, most of the dust cores in the envelope

are too young to have associated HII regions. While in SgrB2(M) and SgrB2(N), the high-mass star formation goes on, the newly formed stars have already ionized quite a few HII regions. This is SgrB2 today.

Chapter 9

Outlook

This work can be supplemented or extrapolated in the following aspects:

- Quantitatively determination of the ages of the cores and HII regions: Chemical clocks such as carbon chain molecules (e.g. Sakai & Yamamoto, 2013) can be applied to determine the ages of molecular cores. While the age of UCHII regions can be determined by, e.g. the chemical status of its associated photon-dominated regions (see e.g. Stéphan et al., 2018). The age of the large HII regions in the envelope can be determined by dynamical models. Additionally, the outflows traced by SiO can be studied in more detail to better constrain the evolutionary stages of the starless cores surrounding SgrB2(DS). By doing these, we may get a clearer history of star formation in SgrB2.

- SgrB2(DS) is probably not the only HII region in the Universe that has cosmic rays accelerated in an HII region. More observations towards HII regions that fulfills the conditions of our model (Padovani et al., 2019; Meng et al., 2019) are needed to confirm (or falsify) and possibly refine the model.

- Observations on the polarized cm wavelengths emission will confirm the presence of synchrotron emission discovered in this thesis. By doing this we can characterize the orientation of the magnetic field in the envelope of SgrB2. Additionally, this will be a powerful tool to confirm our first-order Fermi acceleration model.

Bibliography

Ando, R., Kohno, K., Umehata, H., et al. 2019, ApJ, 871, 256

Anglada, G., Villuendas, E., Estalella, R., et al. 1998, AJ, 116, 2953

Argon, A. L., Reid, M. J., & Menten, K. M. 2000, ApJS, 129, 159

Bally, J., Aguirre, J., Battersby, C., et al. 2010, ApJ, 721, 137

Belloche, A., Müller, H. S. P., Menten, K. M., Schilke, P., & Comito, C. 2013, A&A, 559, A47

Bergin, E. A., & Tafalla, M. 2007, ARA&A, 45, 339

Berkhuijsen, E. M. 1998, The Volume Filling Factor of the WIM, ed. D. Breitschwerdt, M. J. Freyberg, & J. Truemper, Vol. 506, 301–304

Berkhuijsen, E. M., Mitra, D., & Mueller, P. 2006, Astronomische Nachrichten, 327, 82

Beuther, H., Schilke, P., Sridharan, T. K., et al. 2002, A&A, 383, 892

Bolatto, A. D., Warren, S. R., Leroy, A. K., et al. 2013, Nature, 499, 450

Bonnell, I. A., Bate, M. R., Clarke, C. J., & Pringle, J. E. 2001, MNRAS, 323, 785

Braz, M. A., & Epchtein, N. 1983, A&AS, 54, 167

Breen, S. L., Ellingsen, S. P., Caswell, J. L., & Lewis, B. E. 2010, MNRAS, 401, 2219

Bressan, A., Fagotto, F., Bertelli, G., & Chiosi, C. 1993, A&AS, 100, 647

Caswell, J. L. 2004, MNRAS, 349, 99

Caswell, J. L., Fuller, G. A., Green, J. A., et al. 2010, MNRAS, 404, 1029

Clark, B. G. 1980, A&A, 89, 377

Condon, J. J., Cotton, W. D., Greisen, E. W., et al. 1998, AJ, 115, 1693

Condon, J. J., & Ransom, S. M. 2016, Essential Radio Astronomy

Cornwell, T. J. 2008, IEEE Journal of Selected Topics in Signal Processing, 2, 793

Costagliola, F., & Aalto, S. 2010, A&A, 515, A71

Crutcher, R. M., Roberts, D. A., Mehringer, D. M., & Troland, T. H. 1996, ApJ, 462, L79

Davies, B., Hoare, M. G., Lumsden, S. L., et al. 2011, MNRAS, 416, 972

de Pree, C. G., Gaume, R. A., Claussen, M. J., & Goss, W. M. 1993, in American Astronomical Society Meeting Abstracts, Vol. 183, American Astronomical Society Meeting Abstracts, 13.02

de Pree, C. G., Gaume, R. A., Goss, W. M., & Claussen, M. J. 1995, ApJ, 451, 284

—. 1996, ApJ, 464, 788

De Pree, C. G., Goss, W. M., & Gaume, R. A. 1998, ApJ, 500, 847

De Pree, C. G., Peters, T., Mac Low, M. M., et al. 2014, ApJ, 781, L36

de Vicente, P., Martín-Pintado, J., Neri, R., & Colom, P. 2000, A&A, 361, 1058

de Vicente, P., Martin-Pintado, J., & Wilson, T. L. 1997, A&A, 320, 957

Draine, B. T. 2011, Physics of the Interstellar and Intergalactic Medium

Eker, Z., Bakış, V., Bilir, S., et al. 2018, MNRAS, 479, 5491

Garay, G., Ramirez, S., Rodriguez, L. F., Curiel, S., & Torrelles, J. M. 1996, ApJ, 459, 193

Gaume, R. A., Claussen, M. J., de Pree, C. G., Goss, W. M., & Mehringer, D. M. 1995, ApJ, 449, 663

Ginsburg, A., Henkel, C., Ao, Y., et al. 2016, A&A, 586, A50

Ginsburg, A., Bally, J., Barnes, A., et al. 2018, ApJ, 853, 171

Goicoechea, J. R., Rodríguez-Fernández, N. J., & Cernicharo, J. 2004, ApJ, 600, 214

Goldsmith, P. F., Lis, D. C., Hills, R., & Lasenby, J. 1990, ApJ, 350, 186

Gravity Collaboration, Abuter, R., Amorim, A., et al. 2018, A&A, 615, L15

Gusdorf, A., Cabrit, S., Flower, D. R., & Pineau Des Forêts, G. 2008, A&A, 482, 809

Henshaw, J. D., Longmore, S. N., Kruijssen, J. M. D., et al. 2016, MNRAS, 457, 2675

Högbom, J. A. 1974, A&AS, 15, 417

Hollis, J. M., Jewell, P. R., Remijan, A. J., & Lovas, F. J. 2007, ApJ, 660, L125

Hollis, J. M., Pedelty, J. A., Boboltz, D. A., et al. 2003, ApJ, 596, L235

Jones, D. I., Crocker, R. M., Ott, J., Protheroe, R. J., & Ekers, R. D. 2011, AJ, 141, 82

Jones, D. I., Protheroe, R. J., & Crocker, R. M. 2008, PASA, 25, 161

Jones, P. A., Burton, M. G., Cunningham, M. R., et al. 2012, MNRAS, 419, 2961

Kalberla, P. M. W., Dedes, L., Kerp, J., & Haud, U. 2007, A&A, 469, 511

Kalberla, P. M. W., & Kerp, J. 2009, ARA&A, 47, 27

Kanekar, N., Subrahmanyan, R., Chengalur, J. N., & Safouris, V. 2003, MNRAS, 346, L57

Karzas, W. J., & Latter, R. 1961, ApJS, 6, 167

Kauffmann, J. 2007, PhD thesis, Max-Planck-Institut fuer Radioastronomie

Kauffmann, J., Pillai, T., Zhang, Q., et al. 2017a, A&A, 603, A89

—. 2017b, A&A, 603, A90

Kiminki, M. M., Smith, N., Reiter, M., & Bally, J. 2017, MNRAS, 468, 2469

Klessen, R. S. 2000, ApJ, 535, 869

Kroupa, P. 2001, MNRAS, 322, 231

Kruijssen, J. M. D., Dale, J. E., & Longmore, S. N. 2015, MNRAS, 447, 1059

Kruijssen, J. M. D., & Longmore, S. N. 2013, MNRAS, 435, 2598

Kruijssen, J. M. D., Longmore, S. N., Elmegreen, B. G., et al. 2014, MNRAS, 440, 3370

Kurtz, S. 2002, in Astronomical Society of the Pacific Conference Series, Vol. 267, Hot Star Workshop III: The Earliest Phases of Massive Star Birth, ed. P. Crowther, 81

Kurtz, S. 2005, in IAU Symposium, Vol. 227, Massive Star Birth: A Crossroads of Astrophysics, ed. R. Cesaroni, M. Felli, E. Churchwell, & M. Walmsley, 111–119

LaRosa, T. N., Brogan, C. L., Shore, S. N., et al. 2005, ApJ, 626, L23

LaRosa, T. N., Kassim, N. E., Lazio, T. J. W., & Hyman, S. D. 2000, AJ, 119, 207

Law, C. J., Yusef-Zadeh, F., & Cotton, W. D. 2008a, ApJS, 177, 515

Law, C. J., Yusef-Zadeh, F., Cotton, W. D., & Maddalena, R. J. 2008b, ApJS, 177, 255

Li, A., & Draine, B. T. 2001, ApJ, 554, 778

Lindqvist, M., Winnberg, A., Habing, H. J., & Matthews, H. E. 1992, A&AS, 92, 43

Longmore, S. N., Bally, J., Testi, L., et al. 2013, MNRAS, 429, 987

Madsen, G. J., Reynolds, R. J., & Haffner, L. M. 2006, ApJ, 652, 401

Martín-Pintado, J., Gaume, R. A., Rodríguez-Fernández, N., de Vicente, P., & Wilson, T. L. 1999, ApJ, 519, 667

McKee, C. F., & Tan, J. C. 2003, ApJ, 585, 850

McMullin, J. P., Waters, B., Schiebel, D., Young, W., & Golap, K. 2007, in Astronomical Society of the Pacific Conference Series, Vol. 376, Astronomical Data Analysis Software and Systems XVI, ed. R. A. Shaw, F. Hill, & D. J. Bell, 127

Mehringer, D. M., Goss, W. M., & Palmer, P. 1994, ApJ, 434, 237

Mehringer, D. M., Palmer, P., Goss, W. M., & Yusef-Zadeh, F. 1993, ApJ, 412, 684

Meng, F., Sánchez-Monge, Á., Schilke, P., et al. 2019, A&A, 630, A73

Molinari, S., Bally, J., Noriega-Crespo, A., et al. 2011, ApJ, 735, L33

Morris, M., & Serabyn, E. 1996, ARA&A, 34, 645

Mücke, A., Koribalski, B. S., Moffat, A. F. J., Corcoran, M. F., & Stevens, I. R. 2002, ApJ, 571, 366

Müller, H. S. P., Thorwirth, S., Roth, D. A., & Winnewisser, G. 2001, A&A, 370, L49

Muno, M. P., Bauer, F. E., Bandyopadhyay, R. M., & Wang, Q. D. 2006, ApJS, 165, 173

Ossenkopf, V., & Henning, T. 1994, A&A, 291, 943

Ossenkopf-Okada, V., Csengeri, T., Schneider, N., Federrath, C., & Klessen, R. S. 2016, A&A, 590, A104

Padovani, M., Galli, D., & Glassgold, A. E. 2009, A&A, 501, 619

Padovani, M., Hennebelle, P., & Galli, D. 2013, A&A, 560, A114

Padovani, M., Hennebelle, P., Marcowith, A., & Ferrière, K. 2015, A&A, 582, L13

Padovani, M., Marcowith, A., Hennebelle, P., & Ferrière, K. 2016, A&A, 590, A8

Padovani, M., Marcowith, A., Sánchez-Monge, Á., Meng, F., & Schilke, P. 2019, A&A, 630, A72

Panagia, N. 1973, AJ, 78, 929

Pereira, V., López-Santiago, J., Miceli, M., Bonito, R., & de Castro, E. 2016, A&A, 588, A36

Perley, R. A., & Butler, B. J. 2013, ApJS, 204, 19

Platania, P., Bensadoun, M., Bersanelli, M., et al. 1998, ApJ, 505, 473

Ponti, G., Morris, M. R., Terrier, R., et al. 2015, MNRAS, 453, 172

Protheroe, R. J., Ott, J., Ekers, R. D., Jones, D. I., & Crocker, R. M. 2008, MNRAS, 390, 683

Qin, S.-L., Schilke, P., Rolffs, R., et al. 2011, A&A, 530, L9

Qin, S.-L., Zhao, J.-H., Moran, J. M., et al. 2008, ApJ, 677, 353

Ramírez, S. V., Arendt, R. G., Sellgren, K., et al. 2008, ApJS, 175, 147

Reid, M. J., Menten, K. M., Brunthaler, A., et al. 2014, ApJ, 783, 130

Rosolowsky, E. W., Pineda, J. E., Kauffmann, J., & Goodman, A. A. 2008, ApJ, 679, 1338

Sakai, N., & Yamamoto, S. 2013, Chemical Reviews, 113, 8981

Sánchez-Monge, Á., Kurtz, S., Palau, A., et al. 2013, ApJ, 766, 114

Sánchez-Monge, Á., Schilke, P., Schmiedeke, A., et al. 2017, A&A, 604, A6

Schilke, P. 2015, in EAS Publications Series, Vol. 75-76, EAS Publications Series, 227–235

Schilke, P., Walmsley, C. M., Pineau des Forets, G., & Flower, D. R. 1997, A&A, 321, 293

Schmiedeke, A., Schilke, P., Möller, T., et al. 2016, A&A, 588, A143

Schneider, N., Ossenkopf, V., Csengeri, T., et al. 2015, A&A, 575, A79

Schwörer, A., Sánchez-Monge, Á., Schilke, P., et al. 2019, A&A, 628, A6

Shaver, P. A. 1978, A&A, 68, 97

Shu, F. H., Adams, F. C., & Lizano, S. 1987, ARA&A, 25, 23

Steggles, H. G., Hoare, M. G., & Pittard, J. M. 2017, MNRAS, 466, 4573

Stéphan, G., Schilke, P., Le Bourlot, J., et al. 2018, A&A, 617, A60

Takagi, S.-i., Murakami, H., & Koyama, K. 2002, ApJ, 573, 275

Tan, J. C., Beltrán, M. T., Caselli, P., et al. 2014, Protostars and Planets VI, 149

Thompson, A. R., Moran, J. M., & Swenson, George W., J. 2017, Interferometry and Synthesis in Radio Astronomy, 3rd Edition, doi:10.1007/978-3-319-44431-4

Turner, B. E. 1971, ApJ, 163, L35

van Hoof, P. A. M., Williams, R. J. R., Volk, K., et al. 2014, MNRAS, 444, 420

Veena, V. S., Vig, S., Sebastian, B., et al. 2019, MNRAS, 482, 4630

Veena, V. S., Vig, S., Tej, A., et al. 2016, MNRAS, 456, 2425

Whiteoak, J. B., & Gardner, F. F. 1983, MNRAS, 205, 27P

Wilson, T. L., Rohlfs, K., & Hüttemeister, S. 2009, Tools of Radio Astronomy (Springer-Verlag), doi:10.1007/978-3-540-85122-6

Wolfire, M. G., McKee, C. F., Hollenbach, D., & Tielens, A. G. G. M. 2003, ApJ, 587, 278

Yorke, H. W. 2004, in IAU Symposium, Vol. 221, Star Formation at High Angular Resolution, ed. M. G. Burton, R. Jayawardhana, & T. L. Bourke, 141

Yusef-Zadeh, F., Cotton, W., Wardle, M., & Intema, H. 2016, ApJ, 819, L35

Yusef-Zadeh, F., Muno, M., Wardle, M., & Lis, D. C. 2007a, ApJ, 656, 847

Yusef-Zadeh, F., Wardle, M., Lis, D., et al. 2013, Journal of Physical Chemistry A, 117, 9404

Yusef-Zadeh, F., Wardle, M., & Roy, S. 2007b, ApJ, 665, L123

Yusef-Zadeh, F., Hewitt, J. W., Arendt, R. G., et al. 2009, ApJ, 702, 178

Zinnecker, H., & Yorke, H. W. 2007, ARA&A, 45, 481

Zuckerman, B., Palmer, P., Penfield, H., & Lilley, A. E. 1967, ApJ, 149, L61

Appendix A

Radiative Processes

A.1 Planck law and radiative transfer

The SED of a black body is described by the *Planck law*:

$$B_\nu(T) = \frac{2h\nu^3}{c^2}\frac{1}{e^{h\nu/k_\mathrm{B}T} - 1}, \tag{A.1}$$

where h is the Planck constant, nu is the frequency, c is the speed of light, k_B is the Boltzmann constant, and T is the temperature of the black body.

In the radio regime, we have $h\nu \ll k_B T$, thus,

$$e^{h\nu/k_B T} - 1 \approx h\nu/k_\mathrm{B}T, \tag{A.2}$$

and therefore,

$$B_\mathrm{RJ}(\nu, T) = \frac{2\nu^2}{c^2}k_\mathrm{B}T, \tag{A.3}$$

which is the *Rayleigh-Jeans Law*. A convenient numerical criterion of the validation of Eq. A.3 is $\nu/\mathrm{GHz} \ll 21(T/\mathrm{K})$ (Wilson et al., 2009).

The Planck function $B_\nu(T)$ has the dimension of *specific intensity*, which is generally denoted as I_ν, and defined as:

$$I_\nu = \frac{dP}{d\vec{\Omega}\cdot\vec{d\sigma}\,d\nu}, \tag{A.4}$$

where P is power, $d\vec{\Omega}$ is infinitesimal solid angle, $\vec{d\sigma}$ is the infinitesimal area of surface that is emitting or receiving P, and $d\nu$ is the band width. Although that $B_\nu(T)$ is an instance of specific intensity, I_ν can generally be utilized to describe any signal that a radio telescope receives, not just the thermal emission from a black body. The integral of I_ν over a certain solid angle Ω_0 gives the *flux density*:

$$S_\nu = \int_{\Omega_0} I_\nu \, d\Omega. \tag{A.5}$$

The conventional unit of S_ν is *Jansky* (Jy), defined as $\mathrm{Jy} = 10^{-26}\,\mathrm{Wm^{-2}Hz^{-1}}$. Whereas I_ν usually has the unit of $\mathrm{Jy\,sr^{-1}}$, where sr is steradian. Steradian can be also replaced by beam or square arcsecond etc.. An alternative manner of expressing the specific intensity

and flux density is using *brightness temperature*, denoted as $T_{\rm B}$. The conversion between $T_{\rm B}$ and I_ν and S_ν is:

$$T_{\rm B} = \frac{c^2}{2k_B\nu^2} I_\nu \tag{A.6}$$

$$= \frac{c^2}{2k_B\nu^2\Omega_0} S_\nu. \tag{A.7}$$

The definition of $T_{\rm B}$ might have been inspired by Rayleigh-Jeans Law, but it is valid unconditionally, regardless if Rayleigh-Jeans Law can be applied.

The measuring of S_ν or $T_{\rm B}$ is called *photometry*. In practice, we usually need to do a photometry of S_ν of a source with a spatial extension Ω_0, and sampled by pixels. In radio astronomy, the resolution of a image is expressed as *beam*, $(\theta_{\rm maj}, \theta_{\rm min}, PA)$, where $\theta_{...}$ is defined as FWHM on major and minor axes, and PA is position angle. Usually, the beam pattern is a 2-D Gaussian function:

$$\mathrm{Gau}_{\rm 2D}(x, y) = \exp\left[-\left(\frac{x^2}{2\sigma_X^2} + \frac{y^2}{2\sigma_Y^2}\right)\right]. \tag{A.8}$$

The peak value of a beam is 1. For such a 2-D Gaussian beam:

$$\mathrm{FWHM} = 2\sqrt{2\ln 2}\sigma = 2.355\sigma. \tag{A.9}$$

Then the 2-D integral of the beam pattern is:

$$\int_{-\infty}^{\infty}\int_{-\infty}^{\infty} \mathrm{Gau}_{\rm 2D}(x, y)\,\mathrm{d}x\,\mathrm{d}y. = 2\pi A\sigma_X\sigma_Y \tag{A.10}$$

$$= \frac{\pi\,\theta_{\rm maj}\theta_{\rm min}}{4\ln 2}. \tag{A.11}$$

If I sum up all the I_ν, which is in unit of Jy/beam, of all the pixels of the source, denoted as ΣI_ν. Then I can get S_ν of the source:

$$S_\nu = \frac{4\ln 2\,\delta x\delta y}{\pi\,\theta_{\rm maj}\theta_{\rm min}}\Sigma I_\nu, \tag{A.12}$$

where $(\delta x, \delta y)$ is the pixel size.

The unit of specific intensity that is mostly used in this research is mJy/beam. The conversion of mJy/beam to $T_{\rm B}$ is:

$$\frac{T_{\rm B}}{\rm K} = 1.36\frac{\lambda^2}{\theta_{\rm maj}\theta_{\rm min}}\,\frac{I_\nu}{\rm mJy} \tag{A.13}$$

$$= 1.222\times 10^3\frac{1}{\nu^2\,\theta_{\rm maj}\theta_{\rm min}}\,\frac{I_\nu}{\rm mJy}, \tag{A.14}$$

where λ is in unit of cm, $\theta_{\rm maj}$ and $\theta_{\rm min}$ are in unit of arcsecond, and ν is in unit of GHz.

Usually, the propagation of I_ν involves emission and absorption simultaneously, which can be described by the *equation of transfer*:

$$\frac{dI_\nu}{ds} = -\kappa_\nu I_\nu + j_\nu, \tag{A.15}$$

where κ_ν is the *absorption coefficient* and j_ν is the *emissivity*. We can define a *source function*,

$$S_\nu \equiv \frac{j_\nu}{\kappa_\nu}. \tag{A.16}$$

Following conventions, I denote the source function as S_ν, but it has the same dimension[1] as I_ν and is different from the flux density S_ν. The difference is by a factor of Ω_0. Hence, the equation of transfer can be written as

$$\frac{dI_\nu}{\kappa_\nu\, ds} = -I_\nu + S_\nu. \tag{A.17}$$

We define *optical depth* τ_ν as

$$\tau_\nu(s) = \int_{s_0}^{s} \kappa_\nu(s')\, ds', \tag{A.18}$$

where s can be regarded as the length of path of the propagation of I_ν. Thus, Eq. A.17 is reduced to

$$\frac{dI_\nu}{d\tau_\nu} = -I_\nu + S_\nu, \tag{A.19}$$

which has a solution

$$I_\nu(\tau_\nu) = I_\nu(0)e^{-\tau_\nu} + \int_0^{\tau_\nu} e^{-(\tau_\nu - \tau'_\nu)} S_\nu(\tau'_\nu)\, d\tau'_\nu, \tag{A.20}$$

in which $I_\nu(0)$, the initial specific intensity, can be considered as the background. If we assume that the source function is constant, $\partial S_\nu / \partial \tau'_\nu \equiv 0$, then the solution above can be reduced to

$$I_\nu(\tau_\nu) = I_\nu(0)e^{-\tau_\nu} + S_\nu(1 - e^{\tau_\nu}). \tag{A.21}$$

The term $I_\nu(0)e^{-\tau_\nu}$ can be eliminated by calibration, background subtraction etc.. It is obvious that when $\tau_\nu \ll 1$, $I_\nu(\tau_\nu) \approx S_\nu \tau_\nu$, which is called the scenario of *optically thin*. While if $\tau_\nu \gg 1$, $I_\nu \approx S_\nu$, which is called the scenario of *optically thick*. If the emission obeys the Planck Law, the source function S_ν is $B_\nu(T)$. When Rayleigh-Jeans Law applies, according to Eq. A.6

$$T_\mathrm{B} = \begin{cases} T\tau_\nu & \text{(optically thin)} \\ T & \text{(optically thick)} \end{cases}. \tag{A.22}$$

A.2 Free-free Emission and Radio Recombination Lines

In this section I introduce the emission mechanisms of ionized gas. The region that ionized gas occupies is called HII region. In HII regions, both of continuum and line emission can be detected.

The thermal continuum emission from HII region is *free-free* emission (alternatively called *bremsstrahlung*). The physical origin of free-free emission in HII region is the acceleration of the free charges (mostly free electrons) in the Coulomb field of other charges (e.g. protons). The optical depth of free-free emission is

$$\tau_\mathrm{C} = 3.014 \times 10^{-2} \left(\frac{T_\mathrm{e}}{\mathrm{K}}\right)^{-3/2} \left(\frac{\mathrm{EM}}{\mathrm{cm^{-6}\,pc}}\right) \left(\frac{\nu}{\mathrm{GHz}}\right)^{-2} \langle g_\mathrm{ff} \rangle, \tag{A.23}$$

[1] Although that steradian is physically dimensionless, here we treat it as a 'dimension'. So specific intensity and flux density should have different dimensions, which might helps to avoid possible confusions.

where T_e is the *electron temperature*, and EM is the *emission measure*, which is defined as

$$\mathrm{EM} = \int_{s_1}^{s_2} n_\mathrm{e}^2 \, ds, \tag{A.24}$$

where n_e is the volume density of the electrons, while s is the length of path of emission. The *velocity averaged Gaunt factor* $\langle g_\mathrm{ff} \rangle$ is a correction term for quantum effect, and is a function of electron temperature and frequency. The values of $\langle g_\mathrm{ff} \rangle$ varies under different conditions (see e.g. Karzas & Latter, 1961; van Hoof et al., 2014). Here we use an approximation $\langle g_\mathrm{ff} \rangle \approx 2.732\, T_\mathrm{e}^{0.15} \nu^{-0.1}$ which is valid for $\nu \leq 20\,\mathrm{GHz}$ and $T_\mathrm{e} > 5 \times 10^3\,\mathrm{K}$ (Wilson et al., 2009). Thus Eq. A.23 is approximately

$$\tau_\mathrm{C} = 8.235 \times 10^{-2} \left(\frac{T_\mathrm{e}}{\mathrm{K}}\right)^{-1.35} \left(\frac{\mathrm{EM}}{\mathrm{cm^{-6}pc}}\right) \left(\frac{\nu}{\mathrm{GHz}}\right)^{-2.1}. \tag{A.25}$$

The electrons are not only accelerated but also captured by protons. When a electron is re-combined with a proton to form an atom, the newly formed atom can decay from excited electron states and emit *radio recombination lines* (abbreviated as *RRL*). The frequency of RRL that emitted from a transition from main quantum number n_2 to n_1 is

$$\nu_{n_2 \to n_1} = Rc \left(\frac{1}{n_1} - \frac{1}{n_2}\right), \tag{A.26}$$

where R is the *Rydberg constant*. The nomenclature of RRL is X$n_1\alpha$, where X is the element notion, n_1 is the lower quantum number in the transition, and the α can be replaces by the $(n_2 - n_1)$-th Greek letter. For example, the RRL from the transition from $n2 = 100$ to $n2 = 99$ of a hydrogen atom is denoted as H99α.

The opacity of a RRL is

$$\tau_\mathrm{L} = 1.92 \times 10^3 \left(\frac{T_\mathrm{e}}{\mathrm{K}}\right)^{-5/2} \left(\frac{\mathrm{EM}}{\mathrm{cm^{-6}pc}}\right) \left(\frac{\Delta\nu}{\mathrm{kHz}}\right)^{-1}, \tag{A.27}$$

where $\Delta\nu$ is FWHM of the RRL. When both of the RRL and the free-free emission are optically thin, their intensity ratio is

$$\frac{I_\mathrm{L}}{I_\mathrm{C}} \left(\frac{\Delta v}{\mathrm{km\ s^{-1}}}\right) = 6.985 \times 10^3 \left(\frac{T_\mathrm{e}}{\mathrm{K}}\right)^{-1.15} \left(\frac{\nu}{\mathrm{GHz}}\right)^{1.1}, \tag{A.28}$$

where Δv is the FWHM of the RRL in unit of velocity.

The flux of Lyman continuum photons, $\dot{N}_\mathrm{Ly}$, needed to ionized an HII region can be derived as following (Schmiedeke et al., 2016):

$$\frac{\dot{N}_\mathrm{Ly}}{\mathrm{s^{-1}}} = 8.9 \times 10^{40} \frac{S_\nu}{\mathrm{Jy}} \left(\frac{\nu}{\mathrm{GHz}}\right)^{0.1} \left(\frac{T_\mathrm{e}}{10^4\ \mathrm{K}}\right)^{-0.45} \left(\frac{D}{\mathrm{pc}}\right)^2, \tag{A.29}$$

where S_ν is the flux at frequency ν, T_e is the electron temperature, and D is the distance to the source.

A.3 Dust Emission

Dust cores can be assumed as gray bodies. The gray bodies are emitting in continuum following the solution of the radiative transfer equation,

$$S_\nu = B_\nu(T_\mathrm{d})(1 - e^{-\tau_\nu})\Omega_\mathrm{source}. \tag{A.30}$$

The optical depth, τ_ν, is defined as:

$$\tau_\nu = \int \kappa_\nu \rho \, \mathrm{d}l \approx \kappa_\nu N_\mathrm{d}, \tag{A.31}$$

where l is the depth into the dust core along the line of sight. The absorption coefficient, κ, is usually modeled as a power law function of ν:

$$\kappa_\nu = \kappa_0 \left(\frac{\nu}{\nu_0}\right)^\beta. \tag{A.32}$$

Obviously, a finite β makes S_ν deviate from black body emission but become gray body emission. Ossenkopf & Henning (1994) give the κ_ν values as functions of ν from 1 to 1300 μm (300 THz to 230 GHz), for various dust densities and various nature of dust grains. For simplicity, I consider the case for compact grain with ice mantles 4.5 times the volume (see Fig. 5 in Ossenkopf & Henning, 1994). The extrapolation of κ_ν based on the 100 to 1300 μm part of the model gives $\kappa_0 \approx 1$ cm^2 g^{-1} at 300 GHz (1 mm), with $\beta = 2$. Such extrapolation can be used to estimate the κ_ν for wavelength > mm. For the extrapolated parameters of κ_0 and β, see Table A.1. The nomenclature of different cases is that: "mrn" for grains with no ice mantle, "thin" stands for grains with thin ice mantle, and "thick" stands for grains with thick ice mantle. the number # following the case name stands for that the dust grains in density of $10^\#$ cm^{-3}.

Table A.1 Extrapolation of dust opacity (Ossenkopf & Henning, 1994)

Case	$\kappa_{100\mathrm{GHz}}$ cm^2/g	β	Case	$\kappa_{100\mathrm{GHz}}$ cm^2/g	β	Case	$\kappa_{100\mathrm{GHz}}$ cm^2/g	β
mrn0	0.091(0.007)	1.75(0.02)	thin0	0.138(0.007)	1.77(0.02)	thick0	0.025(0.004)	2.51(0.05)
mrn5	0.236(0.007)	1.54(0.01)	thin5	0.207(0.010)	1.71(0.02)	thick5	0.042(0.006)	2.41(0.04)
mrn6	0.610(0.025)	1.34(0.01)	thin6	0.279(0.015)	1.69(0.02)	thick6	0.045(0.006)	2.42(0.04)
mrn7	1.669(0.093)	1.14(0.02)	thin7	0.321(0.017)	1.70(0.02)	thick7	0.044(0.006)	2.43(0.04)
mrn8	2.631(0.159)	1.05(0.02)	thin8	0.339(0.017)	1.69(0.02)	thick8	0.042(0.006)	2.48(0.05)

Since κ is assumed to be unchanged along the line of sight (not in reality, just an approximation), then the integral of volume density along the light of sight through the core gives the column density N_d. The source angular size Ω_source in radian is A/D^2 where A is the area of the source and D is the distance of the source. Then Eq. A.30 can be written as:

$$S_\nu = \frac{2h\nu^3}{c^2} \frac{1}{e^{\frac{h\nu}{k_\mathrm{B}T_\mathrm{d}}} - 1} \left[1 - e^{-\kappa_0 \left(\frac{\nu}{\nu_0}\right)^\beta N_\mathrm{d}}\right] \frac{A}{D^2}. \tag{A.33}$$

Appendix B

Full list of compact cores in SgrB2

Table B.1 List of compact cores in SgrB2

ID	RA[a]	Dec.[b]	T	$S_{3\sigma,96GHz}$	$S_{p,96GHz}$	δS_{96GHz}	ID_{G18}	$S_{96,G18}$	Cluster	Outflow	Assoc.[a]
1	17:47:23.1669	-28:21:49.75	I	5.79	2.07	0.08	–	–	–	–	–
2	17:47:23.0684	-28:21:55.55	I	26.3	11.8	0.2	–	–	–	–	–
3	17:47:17.3558	-28:22:03.70	I	22.3	12.3	0.2	101	9.78	–	–	–
4	17:47:19.9924	-28:22:04.85	I	226.7	95.6	1.5	264	64.74	N	–	–
5	17:47:20.7539	-28:22:06.45	I	51.9	16.0	1.1	–	–	N	–	–
6	17:47:18.1059	-28:22:06.95	I	10.79	9.37	0.06	102	8.58	–	–	–
7	17:47:19.4659	-28:22:11.80	I	21.1	7.0	0.5	–	–	N	–	–
8	17:47:19.9053	-28:22:17.20	I	619	237	23	171	185.30	N	–	[ARM00]78-27
9	17:47:19.8712	-28:22:18.50	I	1189	501	16	172	372.39	N	–	–
10	17:47:19.4166	-28:22:19.90	I	9.2	4.2	0.2	156	3.12	N	–	–
11	17:47:19.7765	-28:22:20.85	I	223.3	116.4	5.8	173	92.21	N	–	–
12	17:47:19.5037	-28:22:26.80	I	12.3	5.0	0.1	250	3.55	N	–	–
13	17:47:20.0455	-28:22:41.20	I	96.8	68.4	0.5	96	63.55	–	–	[CFG10]G72-31, [MGP94]B
14	17:47:18.6968	-28:22:45.00	I	28.9	9.2	0.7	–	–	–	–	–

Table B.1 List of compact cores in SgrB2 (*continued*)

ID	RA[a]	Dec.[b]	T	$S_{3\sigma,96GHz}$	$S_{p,96GHz}$	δS_{96GHz}	ID_{G18}	$S_{96,G18}$	Cluster	Outflow	Assoc.
15	17:47:19.9015	-28:22:47.25	I	7.0	4.0	0.2	229	3.32	M	–	–
16	17:47:20.0001	-28:22:47.45	I	7.0	3.5	0.2	230	2.70	M	–	–
17	17:47:22.8908	-28:22:48.00	I	8.7	2.6	0.1	–	–	–	–	–
18	17:47:18.6096	-28:22:55.15	I	55.3	17.8	0.7	182	11.44	–	–	[C04]29
19	17:47:19.5606	-28:22:55.35	I	91.2	39.3	1.0	245	24.52	M	–	–
20	17:47:20.1895	-28:22:56.35	I	10.0	4.3	0.2	–	–	M	–	–
21	17:47:20.1289	-28:23:00.25	I	47.2	20.8	1.2	152	16.23	M	–	–
22	17:47:19.3863	-28:23:00.50	I	247.3	90.9	3.9	–	–	M	–	–
23	17:47:19.8561	-28:23:01.60	I	57.8	24.6	5.8	151	20.54	M	–	[CFG10]G67-34
24	17:47:19.5795	-28:23:01.55	I	71.9	23.9	2.0	–	–	M	–	–
25	17:47:20.1668	-28:23:01.80	I	141	48	24	242	32.08	M	–	–
26	17:47:19.9205	-28:23:02.90	I	340.2	189.4	2.0	177	147.28	M	–	–
27	17:47:20.1516	-28:23:03.15	I	1629	906	76	241	138.92	M	–	–
28	17:47:20.2842	-28:23:03.15	I	488	369	19	237	275.08	M	–	–
29	17:47:20.2009	-28:23:03.30	I	2154	898	74	235	824.64	M	–	[BE83]67-35, [MGP94]C
30	17:47:18.7308	-28:23:04.05	I	35.7	15.6	0.7	132	12.12	–	–	–
31	17:47:20.1251	-28:23:04.20	I	3055	1159	60	176	923.55	M	–	[BE83]67-35, [MGP94]C
32	17:47:20.1365	-28:23:04.05	I	3055	1159	60	236	885.12	M	–	[BE83]67-35
33	17:47:19.0870	-28:23:04.35	I	43.4	15.7	0.9	–	–	M	–	–
34	17:47:19.2461	-28:23:04.65	I	32.5	10.0	0.8	–	–	M	–	–
35	17:47:20.1630	-28:23:04.90	I	3637	2006	41	174	1641.99	M	–	[MGP94]C
36	17:47:20.1706	-28:23:04.80	I	3637	2006	41	234	1091.73	M	–	[MGP94]C
37	17:47:20.0569	-28:23:06.00	I	439	99	82	233	49.94	M	–	–
38	17:47:19.6894	-28:23:05.90	I	25.7	15.0	0.9	90	12.69	M	–	–
39	17:47:20.1706	-28:23:06.10	I	710	227	75	178	199.25	M	–	[ARM00]SgrB2M, X305
40	17:47:20.0834	-28:23:06.85	I	289	92	43	225	68.82	M	–	[ARM00]SgrB2M, X305
41	17:47:20.2767	-28:23:05.90	I	232	78	36	240	56.79	M	–	[C04]35
42	17:47:19.7917	-28:23:07.00	I	52.6	29.0	0.7	87	23.14	M	–	–
43	17:47:20.1062	-28:23:08.85	I	266.3	157.0	2.1	180	126.02	M	–	–

Table B.1 List of compact cores in SgrB2 (*continued*)

ID	RA[a]	Dec.[b]	T	$S_{3\sigma,96GHz}$	$S_{p,96GHz}$	δS_{96GHz}	ID_{G18}	$S_{96,G18}$	Cluster	Outflow	Assoc.
44	17:47:20.6707	-28:23:09.80	I	85.5	28.6	2.2	–	–	M	–	–
45	17:47:19.7652	-28:23:10.15	I	39.0	19.8	0.7	86	15.88	M	–	–
46	17:47:20.0493	-28:23:12.90	I	122.9	75.3	0.5	181	59.06	M	–	[CFG10]G65-36
47	17:47:21.9211	-28:23:17.95	I	8.8	3.0	0.2	–	–	–	–	–
48	17:47:19.9887	-28:23:18.40	I	106.2	49.9	0.8	244	35.47	M	–	–
49	17:47:16.7074	-28:23:29.45	I	7.1	2.1	0.2	–	–	–	–	–
50	17:47:23.6642	-28:23:35.05	I	8.2	2.6	0.1	–	–	–	–	–
51	17:47:20.2199	-28:23:45.25	I	10.9	5.3	1.0	80	4.35	S	N	–
52	17:47:20.4472	-28:23:45.55	I	840.5	449.0	4.6	265	356.55	S	N	[LWH92]58-42, [ARM00]58-43
53	17:47:18.6548	-28:24:24.70	I	24.3	14.4	0.2	43	11.91	–	–	[CFG10]G45-42, [MGP94]E
54	17:47:19.4620	-28:24:40.40	I	42.6	17.3	0.4	–	–	–	–	–
55	17:47:23.3432	-28:25:34.35	I	0.39	0.51	0.02	10	0.53	DS	N	X340
56	17:47:20.4740	-28:25:40.55	I	2.63	0.92	0.06	254	0.70	DS	N	–
57	17:47:20.8568	-28:25:48.90	I	0.76	0.69	0.02	54	0.60	DS	Y	–
58	17:47:07.5132	-28:26:24.22	I	2.67	1.41	0.04	55	1.14	–	–	–
59	17:47:26.3325	-28:20:39.49	II	3.10	1.89	0.04	28	1.71	–	–	–
60	17:47:27.2532	-28:20:56.89	II	7.3	3.5	0.2	243	2.95	–	–	–
61	17:47:19.4924	-28:20:58.10	II	2.66	1.12	0.07	33	0.98	–	–	–
62	17:47:20.7954	-28:21:06.95	II	1.31	1.07	0.02	57	1.05	–	–	–
63	17:47:20.6969	-28:21:09.45	II	2.27	1.41	0.02	58	1.19	–	–	–
64	17:47:17.2501	-28:21:11.20	II	1.22	0.77	0.03	60	0.70	–	–	–
65	17:47:22.2007	-28:21:18.25	II	3.99	2.02	0.04	59	1.57	–	–	–
66	17:47:23.6136	-28:21:26.55	II	4.58	2.67	0.05	29	2.29	–	–	–
67	17:47:16.6590	-28:21:32.55	II	1.24	0.83	0.02	61	0.79	–	–	–
68	17:47:22.7084	-28:21:35.10	II	1.36	1.87	0.04	30	1.81	–	–	–
69	17:47:24.0001	-28:21:40.45	II	1.50	0.96	0.03	223	0.87	–	–	–
70	17:47:23.8183	-28:21:41.65	II	3.35	1.72	0.07	31	1.54	–	–	–
71	17:47:24.7237	-28:21:43.59	II	5.4	2.7	0.2	115	2.41	–	–	[CFG10]G95-38, [MGP94]I
72	17:47:24.4813	-28:21:43.74	II	5.06	2.16	0.07	157	1.70	–	–	–

Table B.1 List of compact cores in SgrB2 (*continued*)

ID	RA[a]	Dec.[b]	T	$S_{3\sigma,96GHz}$	$S_{p,96GHz}$	δS_{96GHz}	ID_{G18}	$S_{96,G18}$	Cluster	Outflow	Assoc.
73	17:47:24.0040	-28:21:45.25	II	4.36	2.33	0.07	32	1.89	–	–	–
74	17:47:22.2388	-28:21:49.60	II	4.76	2.24	0.09	224	1.79	–	–	–
75	17:47:17.9658	-28:21:53.15	II	4.33	1.80	0.09	133	1.47	–	–	–
76	17:47:18.0491	-28:21:55.35	II	2.18	1.24	0.06	–	–	–	–	–
77	17:47:16.8747	-28:22:05.80	II	5.98	3.85	0.09	99	3.37	–	–	–
78	17:47:16.9505	-28:22:06.95	II	4.4	2.7	0.1	100	2.21	–	–	–
79	17:47:18.2536	-28:22:10.10	II	4.14	2.25	0.10	105	1.81	–	–	–
80	17:47:19.0037	-28:22:10.40	II	11.8	5.8	0.2	155	4.71	N	–	–
81	17:47:18.3900	-28:22:11.00	II	15.2	6.6	0.5	104	5.07	–	–	–
82	17:47:18.4999	-28:22:11.45	II	27.7	12.1	0.4	103	9.07	N	–	–
83	17:47:19.5682	-28:22:12.05	II	25.7	7.7	0.8	112	5.59	N	–	–
84	17:47:18.1816	-28:22:12.50	II	4.8	2.3	0.1	136	1.77	–	–	–
85	17:47:19.2196	-28:22:11.95	II	23.7	11.9	0.3	107	9.33	N	–	–
86	17:47:18.0793	-28:22:12.55	II	5.6	2.4	0.1	–	–	–	–	–
87	17:47:19.8826	-28:22:13.65	II	337.6	122.0	5.2	252	82.41	N	–	[MGP94]A
88	17:47:17.9808	-28:22:13.15	II	6.9	3.1	0.1	–	–	–	–	–
89	17:47:18.9544	-28:22:13.70	II	22.7	13.4	0.3	106	11.34	N	–	–
90	17:47:19.8788	-28:22:13.70	II	337.6	122.0	5.2	170	92.00	N	–	[MGP94]A
91	17:47:19.2575	-28:22:14.85	II	28.2	14.8	0.4	108	12.33	N	–	[MGP94]F, [CFG10]G77-25
92	17:47:19.6629	-28:22:15.15	II	43.3	14.1	2.2	110	10.59	N	–	–
93	17:47:19.5189	-28:22:14.40	II	30.4	10.3	0.7	111	7.53	N	–	–
94	17:47:19.9015	-28:22:15.55	II	91.9	30.6	7.3	109	24.19	N	–	[ARM00]78-27
95	17:47:19.2992	-28:22:18.20	II	8.0	3.6	0.1	251	2.74	N	–	–
96	17:47:17.2421	-28:22:18.35	II	3.95	1.66	0.05	134	1.36	–	–	–
97	17:47:17.9354	-28:22:19.75	II	3.98	1.99	0.08	137	1.70	–	–	–
98	17:47:18.0225	-28:22:19.95	II	3.73	1.51	0.09	138	1.20	–	–	–
99	17:47:19.8750	-28:22:22.45	II	34.1	14.4	1.8	114	10.65	N	–	–
100	17:47:19.6401	-28:22:24.50	II	21.8	10.4	0.3	113	8.49	N	–	–
101	17:47:14.0635	-28:22:30.59	II	1.29	0.89	0.02	62	0.80	–	–	–

Table B.1 List of compact cores in SgrB2 (*continued*)

ID	RA[a]	Dec.[b]	T	$S_{3\sigma,96GHz}$	$S_{p,96GHz}$	δS_{96GHz}	ID_{G18}	$S_{96,G18}$	Cluster	Outflow	Assoc.
102	17:47:19.5227	-28:22:32.65	II	41.5	22.5	0.2	98	18.05	N	–	[CFG10]G73-29
103	17:47:19.5492	-28:22:35.10	II	6.3	3.5	0.1	231	2.92	N	–	–
104	17:47:19.5265	-28:22:36.75	II	5.1	3.0	0.1	232	2.56	–	–	–
105	17:47:17.8330	-28:22:37.50	II	2.94	1.62	0.06	135	1.45	–	–	–
106	17:47:19.8371	-28:22:40.05	II	34.8	16.1	0.4	97	12.98	–	–	–
107	17:47:17.6701	-28:22:40.70	II	2.46	1.57	0.06	–	–	–	–	–
108	17:47:18.0641	-28:22:44.65	II	7.2	2.8	0.1	–	–	–	–	–
109	17:47:18.4619	-28:22:45.00	II	4.7	1.9	0.1	–	–	–	–	–
110	17:47:14.7868	-28:22:47.99	II	1.42	0.95	0.04	64	0.86	–	–	–
111	17:47:20.8639	-28:22:50.25	II	1.97	1.21	0.05	–	–	M	–	–
112	17:47:20.7578	-28:22:52.25	II	6.9	3.0	0.5	–	–	M	–	–
113	17:47:18.0754	-28:22:52.60	II	14.7	6.1	0.2	94	4.88	–	–	–
114	17:47:19.8030	-28:22:52.45	II	2.86	1.58	0.06	–	–	M	–	–
115	17:47:17.9807	-28:22:53.90	II	6.1	2.3	0.2	–	–	–	–	–
116	17:47:18.0185	-28:22:55.15	II	5.2	2.4	0.1	214	1.94	–	–	–
117	17:47:19.9432	-28:22:55.70	II	3.54	3.07	0.06	247	2.97	M	–	–
118	17:47:14.4495	-28:22:56.34	II	2.51	1.36	0.04	63	1.19	–	–	–
119	17:47:18.7308	-28:22:56.45	II	33.2	12.6	0.5	246	9.09	–	–	–
120	17:47:18.4391	-28:22:56.65	II	10.3	5.8	0.1	95	4.98	–	–	–
121	17:47:20.0683	-28:22:57.40	II	8.3	4.7	0.4	169	3.85	M	–	–
122	17:47:18.1322	-28:23:00.25	II	5.53	3.70	0.06	84	3.50	–	–	–
123	17:47:20.1289	-28:23:00.25	II	47.2	20.8	1.2	–	–	M	–	–
124	17:47:19.5530	-28:23:02.95	II	61.8	20.3	1.5	–	–	M	–	–
125	17:47:19.3825	-28:23:03.15	II	28.1	8.7	1.1	93	6.24	M	–	–
126	17:47:18.0223	-28:23:03.70	II	18.0	13.6	0.1	85	12.74	–	–	–
127	17:47:17.9389	-28:23:04.85	II	7.5	3.1	0.3	215	2.54	–	–	–
128	17:47:18.4428	-28:23:05.60	II	7.2	2.6	0.2	222	1.92	–	–	–
129	17:47:14.5858	-28:23:06.04	II	1.37	1.10	0.03	65	1.16	–	–	–
130	17:47:18.3633	-28:23:06.20	II	7.1	3.3	0.1	153	2.50	–	–	–

Table B.1 List of compact cores in SgrB2 (*continued*)

ID	RA[a]	Dec.[b]	T	$S_{3\sigma,96GHz}$	$S_{p,96GHz}$	δS_{96GHz}	ID_{G18}	$S_{96,G18}$	Cluster	Outflow	Assoc.
131	17:47:20.1478	-28:23:06.75	II	490	227	62	179	126.58	M	–	–
132	17:47:19.1627	-28:23:06.60	II	21.4	6.1	0.7	167	4.11	M	–	–
133	17:47:17.7684	-28:23:06.65	II	0.55	1.15	0.05	154	1.25	–	–	–
134	17:47:19.4772	-28:23:06.80	II	28.2	8.9	0.9	166	6.89	M	–	–
135	17:47:18.5830	-28:23:07.30	II	5.3	2.0	0.1	219	1.47	–	–	–
136	17:47:20.2122	-28:23:06.75	II	295	143	17	239	45.32	M	–	[C04]35
137	17:47:19.6136	-28:23:08.25	II	56.4	27.6	0.9	88	22.60	M	–	–
138	17:47:19.6932	-28:23:07.15	II	21.9	7.8	1.7	150	6.23	M	–	–
139	17:47:18.2648	-28:23:07.10	II	5.21	2.50	0.09	221	1.89	–	–	–
140	17:47:18.1663	-28:23:07.95	II	3.63	1.74	0.09	220	1.33	–	–	–
141	17:47:19.4204	-28:23:07.85	II	28.0	10.1	0.7	165	7.51	M	–	–
142	17:47:20.3108	-28:23:08.35	II	100.2	36.7	6.6	92	31.68	M	–	–
143	17:47:19.5947	-28:23:07.10	II	35.7	14.1	1.3	226	10.73	M	–	–
144	17:47:19.3484	-28:23:09.00	II	17.7	7.7	0.5	91	6.03	M	–	–
145	17:47:19.6894	-28:23:09.30	II	34.4	13.1	1.3	89	9.99	M	–	–
146	17:47:19.9243	-28:23:10.00	II	29.3	9.4	1.4	168	6.62	M	–	–
147	17:47:18.1246	-28:23:10.30	II	0.90	1.10	0.04	216	1.14	–	–	–
148	17:47:15.0063	-28:23:11.59	II	4.28	2.16	0.06	66	1.81	–	–	–
149	17:47:14.8850	-28:23:11.74	II	3.93	1.50	0.07	68	1.19	–	–	–
150	17:47:14.7979	-28:23:12.39	II	3.66	1.75	0.05	67	1.53	–	–	–
151	17:47:17.3819	-28:23:11.95	II	2.44	1.34	0.04	217	1.11	–	–	–
152	17:47:19.4734	-28:23:13.15	II	5.29	3.56	0.05	131	3.20	M	–	–
153	17:47:18.5565	-28:23:13.95	II	5.97	3.69	0.05	149	2.98	–	–	–
154	17:47:20.0834	-28:23:13.50	II	69.9	36.3	2.0	227	2.07	M	–	–
155	17:47:20.0380	-28:23:14.90	II	6.5	2.0	2.2	228	1.32	M	–	–
156	17:47:19.2726	-28:23:14.60	II	1.70	0.91	0.06	218	0.86	M	–	–
157	17:47:18.1473	-28:23:16.70	II	4.72	2.29	0.07	238	1.69	–	–	–
158	17:47:19.4961	-28:23:17.05	II	3.57	2.55	0.09	148	2.09	M	–	–
159	17:47:18.0828	-28:23:21.65	II	4.97	2.68	0.06	164	2.19	–	–	–

Table B.1 List of compact cores in SgrB2 (*continued*)

ID	RA[a]	Dec.[b]	T	$S_{3\sigma,96GHz}$	$S_{p,96GHz}$	δS_{96GHz}	ID_{G18}	$S_{96,G18}$	Cluster	Outflow	Assoc.
160	17:47:19.2461	-28:23:23.65	II	5.1	3.0	0.1	130	2.75	–	–	–
161	17:47:19.0377	-28:23:23.65	II	4.37	1.97	0.04	–	–	–	–	–
162	17:47:19.8523	-28:23:29.25	II	8.7	3.0	0.2	–	–	–	–	–
163	17:47:19.9849	-28:23:30.75	II	10.8	4.8	0.2	270	3.49	–	N	–
164	17:47:20.0001	-28:23:30.55	II	10.8	4.8	0.2	139	3.49	–	–	–
165	17:47:19.7386	-28:23:32.10	II	5.2	2.1	0.2	269	1.82	–	N	–
166	17:47:18.6815	-28:23:32.00	II	7.92	6.14	0.07	83	5.54	–	N	–
167	17:47:20.0797	-28:23:33.90	II	10.3	3.7	0.2	268	2.81	–	N	–
168	17:47:18.4844	-28:23:34.10	II	1.35	1.30	0.05	147	1.28	–	N	–
169	17:47:18.2343	-28:23:39.15	II	3.37	1.76	0.09	124	1.65	–	N	–
170	17:47:18.1434	-28:23:40.10	II	2.55	1.98	0.06	123	1.98	–	N	–
171	17:47:20.1365	-28:23:43.80	II	5.5	3.1	0.2	81	2.92	S	N	–
172	17:47:19.7614	-28:23:43.80	II	19.6	10.8	0.1	82	9.19	S	N	–
173	17:47:18.2911	-28:23:44.15	II	12.9	4.3	0.1	266	3.01	–	N	–
174	17:47:18.3366	-28:23:43.70	II	12.9	4.3	0.2	267	2.78	–	N	–
175	17:47:19.9887	-28:23:44.80	II	8.5	2.9	0.2	–	–	S	N	–
176	17:47:19.5719	-28:23:47.05	II	11.04	5.97	0.09	75	4.86	S	N	–
177	17:47:19.8675	-28:23:47.60	II	14.5	5.1	0.5	248	3.86	S	N	–
178	17:47:19.9281	-28:23:49.20	II	33.5	17.9	0.3	249	7.71	S	N	–
179	17:47:19.7765	-28:23:48.30	II	12.5	4.7	0.3	125	3.87	S	N	–
180	17:47:19.9849	-28:23:48.85	II	32.5	17.9	0.4	76	15.14	S	N	–
181	17:47:20.2994	-28:23:48.60	II	17.5	7.2	0.3	–	–	S	N	–
182	17:47:18.5450	-28:23:49.40	II	4.77	3.60	0.06	73	3.37	–	N	–
183	17:47:19.5833	-28:23:49.85	II	10.4	6.2	0.1	74	5.53	S	N	–
184	17:47:19.6894	-28:23:51.80	II	8.76	4.37	0.09	126	3.31	S	N	–
185	17:47:18.9050	-28:23:52.50	II	16.1	11.5	0.1	72	10.32	S	N	–
186	17:47:18.9921	-28:23:53.70	II	7.7	2.8	0.3	187	1.94	S	N	–
187	17:47:19.5492	-28:23:53.35	II	1.73	1.46	0.08	127	1.49	S	N	–
188	17:47:18.9921	-28:23:53.70	II	7.7	2.8	0.3	186	1.94	S	N	–

Table B.1 List of compact cores in SgrB2 (*continued*)

ID	RA[a]	Dec.[b]	T	$S_{3\sigma,96GHz}$	$S_{p,96GHz}$	δS_{96GHz}	ID_{G18}	$S_{96,G18}$	Cluster	Outflow	Assoc.
189	17:47:21.4704	-28:23:53.20	II	9.8	4.6	0.1	79	3.69	–	N	–
190	17:47:21.3794	-28:23:54.75	II	4.5	2.3	0.2	188	1.99	S	N	–
191	17:47:20.7807	-28:23:53.70	II	4.2	2.1	0.1	144	1.76	S	N	–
192	17:47:19.7007	-28:23:54.20	II	4.4	1.9	0.2	–	–	S	N	–
193	17:47:19.8409	-28:23:54.65	II	8.2	3.5	0.2	78	2.77	S	N	–
194	17:47:19.9205	-28:23:53.65	II	8.1	3.5	0.2	–	–	S	N	–
195	17:47:21.3794	-28:23:54.75	II	4.5	2.3	0.2	–	–	S	N	–
196	17:47:19.7993	-28:23:56.00	II	9.3	4.8	0.2	77	4.02	S	N	–
197	17:47:15.7788	-28:23:55.30	II	2.32	1.19	0.04	69	0.95	–	–	–
198	17:47:19.8068	-28:23:55.90	II	9.3	4.8	0.2	–	–	S	N	–
199	17:47:21.5121	-28:23:56.40	II	2.34	1.30	0.04	263	1.09	–	N	–
200	17:47:19.2043	-28:23:56.75	II	3.17	1.66	0.05	122	1.40	S	N	–
201	17:47:19.9319	-28:23:57.00	II	11.4	7.6	0.1	71	6.91	S	N	–
202	17:47:19.6704	-28:23:58.25	II	4.1	1.5	0.1	184	1.13	S	N	–
203	17:47:19.6136	-28:23:58.25	II	4.95	1.98	0.09	183	1.52	S	N	–
204	17:47:20.9778	-28:23:58.90	II	4.6	2.0	0.1	189	1.75	S	N	–
205	17:47:20.1630	-28:23:58.95	II	3.13	1.72	0.08	185	1.37	S	N	–
206	17:47:20.6898	-28:23:59.30	II	0.29	0.82	0.03	262	0.81	S	N	–
207	17:47:19.9357	-28:23:59.15	II	4.2	2.2	0.1	128	1.91	S	N	–
208	17:47:21.0573	-28:23:59.40	II	3.7	1.6	0.1	261	1.32	S	N	–
209	17:47:20.2578	-28:24:01.05	II	3.9	1.9	0.1	143	1.56	S	N	–
210	17:47:20.7883	-28:24:01.35	II	3.4	2.3	0.1	116	2.12	S	N	–
211	17:47:20.7125	-28:24:01.95	II	7.9	3.9	0.1	117	3.19	S	N	–
212	17:47:20.3374	-28:24:02.35	II	5.71	3.62	0.08	70	3.21	S	N	–
213	17:47:20.0342	-28:24:02.65	II	1.86	1.52	0.05	129	1.50	S	N	–
214	17:47:20.5230	-28:24:02.65	II	2.65	1.16	0.08	–	–	S	N	–
215	17:47:23.0051	-28:24:02.65	II	2.46	1.74	0.02	52	1.44	–	–	–
216	17:47:20.7352	-28:24:02.90	II	6.0	2.4	0.1	190	1.90	S	N	–
217	17:47:20.9285	-28:24:03.15	II	15.5	6.3	0.2	118	4.36	S	N	–

Table B.1 List of compact cores in SgrB2 (*continued*)

ID	RA[a]	Dec.[b]	T	$S_{3\sigma,96GHz}$	$S_{p,96GHz}$	δS_{96GHz}	ID_{G18}	$S_{96,G18}$	Cluster	Outflow	Assoc.
218	17:47:21.0384	-28:24:04.30	II	7.0	2.4	0.2	191	1.85	S	N	–
219	17:47:21.1748	-28:24:05.20	II	3.9	1.5	0.1	192	1.25	S	N	–
220	17:47:21.2771	-28:24:05.65	II	3.28	1.42	0.08	193	1.16	S	N	–
221	17:47:20.8110	-28:24:06.35	II	2.23	1.37	0.03	194	1.12	S	N	–
222	17:47:20.6178	-28:24:10.10	II	2.12	1.09	0.05	140	0.94	–	Y	–
223	17:47:20.7391	-28:24:12.60	II	3.17	1.47	0.05	195	1.14	–	Y	–
224	17:47:20.5799	-28:24:15.30	II	1.70	1.17	0.04	37	1.16	–	N	–
225	17:47:23.0393	-28:24:17.50	II	3.30	1.17	0.06	200	0.94	–	–	–
226	17:47:18.7874	-28:24:17.75	II	14.1	8.1	0.1	39	7.04	–	–	–
227	17:47:21.1067	-28:24:18.50	II	28.9	14.9	0.3	38	12.29	–	Y	[CFG10]G51-49
228	17:47:21.7206	-28:24:18.55	II	2.60	1.00	0.07	196	0.86	–	Y	–
229	17:47:22.9598	-28:24:18.70	II	2.50	1.05	0.06	199	0.90	–	–	–
230	17:47:18.7533	-28:24:18.40	II	14.5	8.1	0.1	40	5.57	–	–	–
231	17:47:21.4553	-28:24:18.95	II	4.3	1.3	0.1	197	1.04	–	Y	–
232	17:47:21.3265	-28:24:19.35	II	4.8	2.6	0.1	36	2.38	–	Y	–
233	17:47:19.2763	-28:24:20.55	II	3.93	1.65	0.06	41	1.28	–	–	–
234	17:47:21.3719	-28:24:21.15	II	4.5	1.6	0.1	198	1.27	–	Y	–
235	17:47:19.1853	-28:24:21.75	II	4.27	1.86	0.06	42	1.44	–	–	–
236	17:47:18.7685	-28:24:24.65	II	10.5	6.4	0.5	44	5.74	–	–	–
237	17:47:18.8822	-28:24:24.80	II	2.9	1.3	0.2	145	1.05	–	–	–
238	17:47:19.1853	-28:24:25.45	II	2.05	0.97	0.03	146	0.82	–	–	–
239	17:47:21.0044	-28:24:26.15	II	4.64	3.75	0.05	35	3.54	–	Y	–
240	17:47:21.6486	-28:24:28.00	II	3.73	1.39	0.09	34	1.07	–	Y	–
241	17:47:21.5956	-28:24:30.70	II	5.69	3.18	0.08	24	2.61	–	Y	–
242	17:47:16.7561	-28:24:31.15	II	4.00	2.18	0.03	27	1.81	–	–	–
243	17:47:16.7410	-28:24:31.35	II	4.00	2.18	0.03	204	1.65	–	–	–
244	17:47:18.7760	-28:24:33.25	II	1.46	1.49	0.02	26	1.47	–	–	–
245	17:47:21.7396	-28:24:33.80	II	3.0	1.2	0.1	260	0.95	–	Y	–
246	17:47:22.2209	-28:24:33.95	II	11.52	7.13	0.08	23	6.24	–	Y	–

Table B.1 List of compact cores in SgrB2 (*continued*)

ID	RA[a]	Dec.[b]	T	$S_{3\sigma,96GHz}$	$S_{p,96GHz}$	δS_{96GHz}	ID_{G18}	$S_{96,G18}$	Cluster	Outflow	Assoc.
247	17:47:16.9418	-28:24:34.00	II	3.90	1.49	0.08	201	1.05	–	–	–
248	17:47:21.7813	-28:24:34.75	II	5.17	2.08	0.09	25	1.61	–	Y	–
249	17:47:21.8381	-28:24:34.10	II	5.32	2.08	0.09	259	1.61	–	Y	–
250	17:47:17.0062	-28:24:34.55	II	2.31	0.97	0.09	203	0.76	–	–	–
251	17:47:16.9570	-28:24:35.95	II	2.44	1.27	0.08	202	1.07	–	–	–
252	17:47:19.6136	-28:24:39.00	II	8.3	2.6	0.3	–	–	–	–	–
253	17:47:21.9215	-28:24:40.10	II	2.00	1.58	0.02	22	1.38	–	Y	–
254	17:47:18.8063	-28:24:41.60	II	4.71	2.13	0.04	56	1.58	–	–	–
255	17:47:22.0315	-28:24:42.75	II	4.68	2.68	0.05	19	2.45	–	Y	[CFG10]G47-55
256	17:47:19.6174	-28:24:44.90	II	1.48	0.79	0.02	142	0.64	–	–	–
257	17:47:22.6265	-28:24:45.20	II	0.48	0.59	0.03	120	0.51	–	Y	–
258	17:47:22.4446	-28:24:46.45	II	-0.77	0.30	0.04	121	0.46	–	N	–
259	17:47:22.0732	-28:24:46.35	II	2.57	1.65	0.02	20	1.41	–	Y	–
260	17:47:18.6926	-28:24:48.50	II	1.07	0.68	0.03	206	0.61	DS	–	–
261	17:47:19.4582	-28:24:48.65	II	2.14	1.09	0.03	205	0.82	DS	–	–
262	17:47:22.0164	-28:24:53.40	II	1.36	0.90	0.02	21	0.83	DS	N	–
263	17:47:22.4674	-28:25:01.55	II	0.63	0.72	0.02	45	0.70	DS	Y	–
264	17:47:22.6683	-28:25:04.60	II	0.96	0.66	0.02	207	0.57	DS	Y	–
265	17:47:23.0056	-28:25:04.95	II	1.71	1.07	0.07	46	0.90	DS	Y	–
266	17:47:22.9829	-28:25:06.35	II	4.07	1.81	0.07	159	1.43	DS	Y	–
267	17:47:21.9104	-28:25:12.80	II	5.1	1.5	0.1	208	1.15	DS	N	–
268	17:47:21.9066	-28:25:14.40	II	4.7	1.4	0.1	209	1.04	DS	N	–
269	17:47:23.1801	-28:25:14.65	II	7.32	5.46	0.04	5	4.75	DS	Y	–
270	17:47:17.6919	-28:25:16.25	II	0.39	0.47	0.02	47	0.46	–	–	–
271	17:47:23.1953	-28:25:17.80	II	2.19	1.13	0.08	6	0.92	DS	N	–
272	17:47:23.2066	-28:25:18.85	II	3.36	2.16	0.05	7	2.02	DS	Y	–
273	17:47:23.1915	-28:25:19.05	II	3.36	2.16	0.05	–	–	DS	N	–
274	17:47:21.8346	-28:25:21.35	II	4.18	2.43	0.06	11	2.21	DS	N	–
275	17:47:23.3545	-28:25:23.55	II	1.56	1.01	0.02	8	0.91	DS	Y	–

Table B.1 List of compact cores in SgrB2 (*continued*)

ID	RA[a]	Dec.[b]	T	$S_{3\sigma,96GHz}$	$S_{p,96GHz}$	δS_{96GHz}	ID_{G18}	$S_{96,G18}$	Cluster	Outflow	Assoc.
276	17:47:15.7172	-28:25:26.80	II	1.00	0.60	0.01	119	0.56	–	–	–
277	17:47:23.4531	-28:25:26.70	II	1.65	1.39	0.02	9	1.38	DS	N	–
278	17:47:19.7273	-28:25:32.05	II	2.04	1.08	0.02	48	0.91	DS	–	–
279	17:47:17.7222	-28:25:38.30	II	1.80	0.84	0.04	253	0.62	–	–	–
280	17:47:17.6084	-28:25:38.85	II	2.09	1.11	0.04	15	0.95	–	–	–
281	17:47:20.8341	-28:25:40.00	II	1.91	0.86	0.04	255	0.69	DS	N	–
282	17:47:22.8922	-28:25:41.45	II	6.0	2.0	0.1	163	1.40	DS	Y	–
283	17:47:20.7128	-28:25:42.75	II	6.5	2.5	0.1	16	1.93	DS	Y	–
284	17:47:22.8127	-28:25:42.35	II	6.8	2.9	0.1	3	2.27	DS	Y	–
285	17:47:20.6445	-28:25:42.05	II	6.1	2.2	0.1	17	1.71	DS	Y	–
286	17:47:22.6307	-28:25:43.00	II	1.50	0.76	0.06	160	0.72	DS	Y	–
287	17:47:21.6907	-28:25:43.25	II	5.28	3.64	0.05	4	3.42	DS	Y	–
288	17:47:21.4860	-28:25:44.30	II	4.42	2.58	0.08	12	2.24	DS	Y	–
289	17:47:20.9857	-28:25:44.55	II	1.89	0.78	0.05	256	0.57	DS	Y	–
290	17:47:21.5542	-28:25:45.10	II	4.0	1.5	0.1	161	1.19	DS	Y	–
291	17:47:22.7786	-28:25:44.55	II	2.10	0.93	0.05	210	0.75	DS	Y	–
292	17:47:21.4367	-28:25:45.50	II	2.7	1.0	0.1	211	0.74	DS	Y	–
293	17:47:21.0880	-28:25:45.50	II	1.78	0.72	0.05	257	0.60	DS	Y	–
294	17:47:22.4071	-28:25:48.90	II	2.06	1.01	0.04	51	0.82	DS	Y	–
295	17:47:19.1890	-28:25:49.00	II	1.13	0.96	0.01	14	0.96	DS	N	–
296	17:47:23.4912	-28:25:49.60	II	2.73	1.35	0.05	141	1.06	DS	Y	–
297	17:47:29.2186	-28:25:50.08	II	1.39	1.16	0.01	53	1.17	–	–	–
298	17:47:23.4533	-28:25:52.05	II	4.44	2.22	0.06	2	1.82	DS	Y	–
299	17:47:21.1828	-28:25:51.75	II	1.73	0.93	0.04	212	0.78	DS	Y	–
300	17:47:23.5064	-28:25:51.00	II	3.88	1.85	0.07	162	1.24	DS	Y	–
301	17:47:21.2473	-28:25:53.50	II	3.27	1.75	0.05	18	1.58	DS	Y	–
302	17:47:23.3965	-28:25:53.45	II	2.29	0.88	0.09	258	0.73	DS	Y	–
303	17:47:21.4899	-28:25:53.75	II	1.97	0.96	0.03	49	0.80	DS	Y	–
304	17:47:21.5278	-28:25:54.20	II	1.76	0.81	0.04	50	0.74	DS	Y	–

Table B.1 List of compact cores in SgrB2 (*continued*)

ID	RA[a]	Dec.[b]	T	$S_{3\sigma,96GHz}$	$S_{p,96GHz}$	δS_{96GHz}	ID_{G18}	$S_{96,G18}$	Cluster	Outflow	Assoc.
305	17:47:18.6811	-28:25:54.50	II	3.71	1.70	0.05	13	1.34	DS	–	–
306	17:47:21.5050	-28:25:55.20	II	1.60	0.70	0.05	158	0.66	DS	Y	–
307	17:47:23.3851	-28:25:55.20	II	3.00	1.54	0.04	1	1.25	DS	Y	–
308	17:47:18.9995	-28:26:02.65	II	1.42	0.70	0.04	213	0.61	–	–	–

[a] Types, references, and aliases of the associated objects are as follows:

[**ARM00**] OH maser (Argon et al., 2000). G000.6MN-00.0XY is abbreviated as MN-XY.

[**CFG10**] 6 GHz CH_3OH maser (Caswell et al., 2010). G000.6MN-00.0XY is abbreviated as MN-XY.

[**MGP94**] 4.8 GHz H_2CO maser (Mehringer et al., 1994). Sgr B2 Maser X is abbreviated as X.

[**C04**] 1720 MHz OH maser (Caswell, 2004). OH 000.666-00.0MN is abbreviated as MN.

[**BE83**] 134.825 μm and 135.945 μm OH maser (Braz & Epchtein, 1983). OH 0.6MN -0.0XY is abbreviated as MN-XY.

[**LWH92**] 1612 MHz OH maser (Lindqvist et al., 1992). OH 0.6MN -0.0XY is abbreviated as MN-XY.

X305 X-ray source (Takagi et al., 2002). CXOU J174720.2-282305 is abbreviated as X305.

X340 X-ray source (Muno et al., 2006). 2MASS J17472335-2825340 is abbreviated as X340.

Appendix C

Maps and SEDs of Type I cores

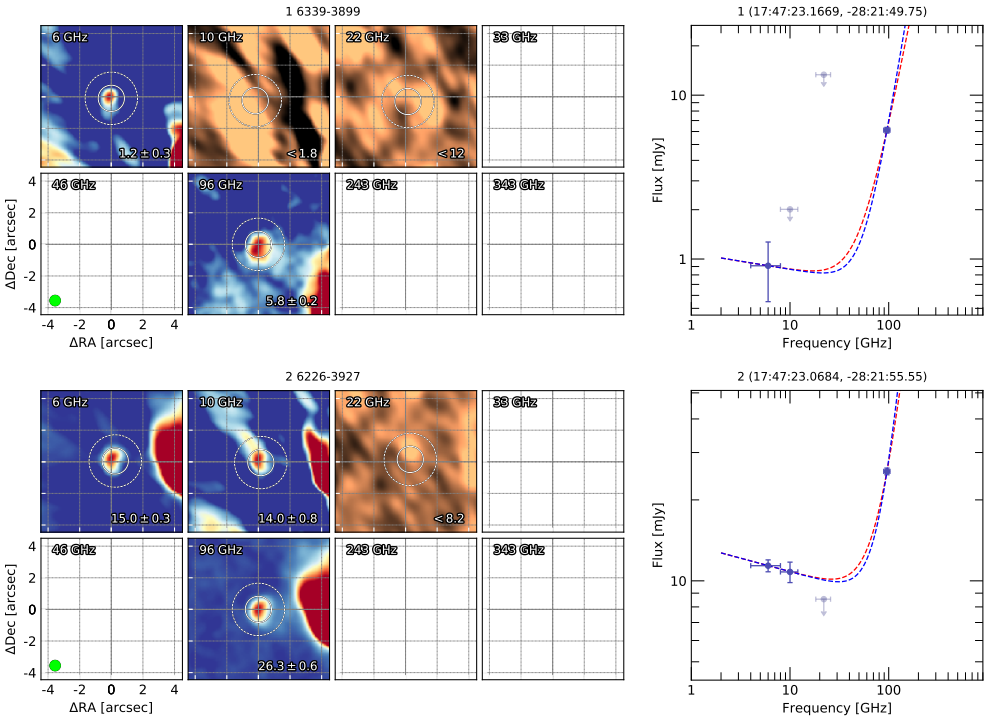

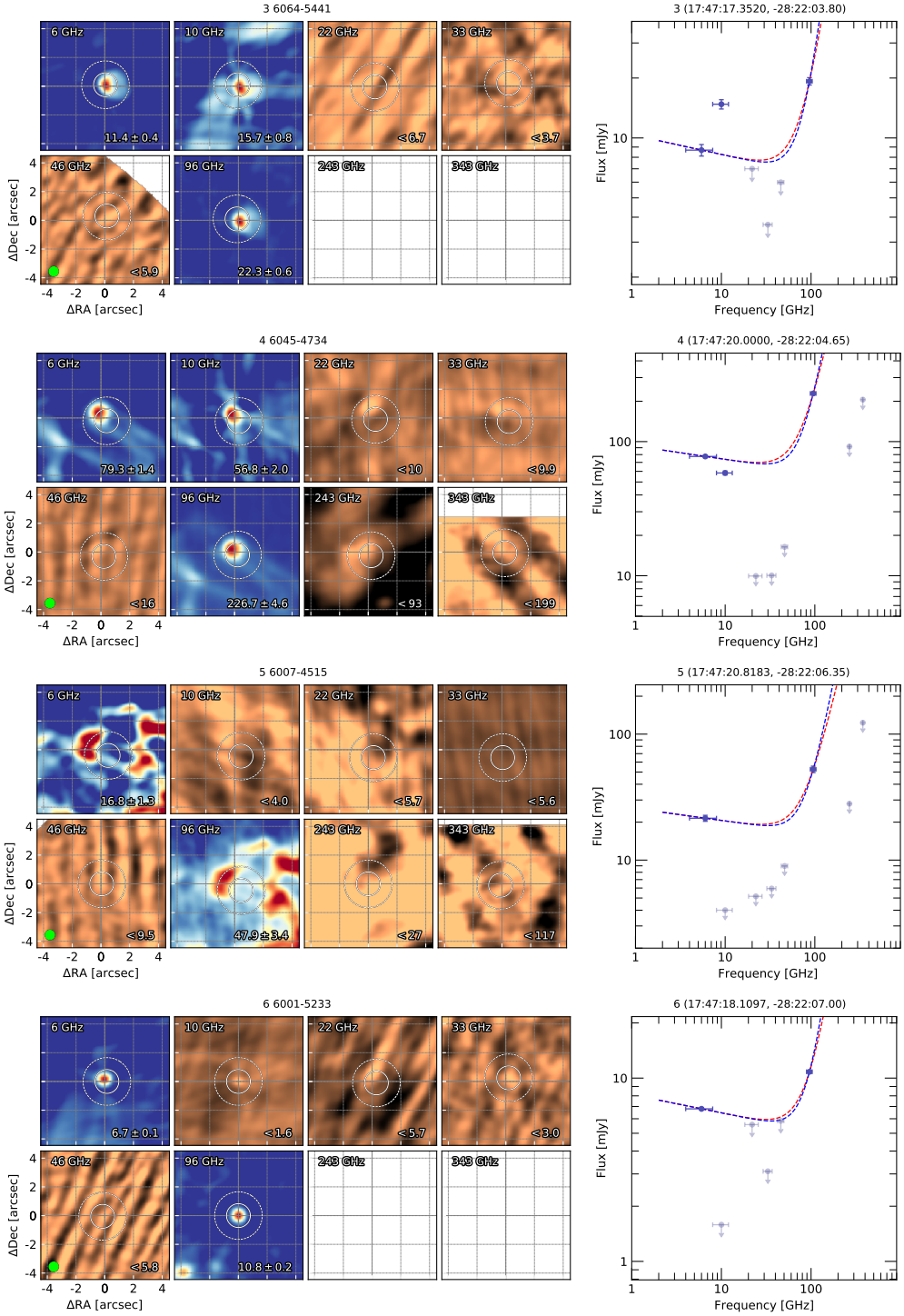
3 6064-5441
6 GHz
11.4 ± 0.4
10 GHz
15.7 ± 0.8
22 GHz
< 6.7
33 GHz
< 8.7
46 GHz
< 5.9
96 GHz
22.3 ± 0.6
243 GHz
343 GHz
ΔDec [arcsec]
ΔRA [arcsec]
3 (17:47:17.3520, -28:22:03.80)
Flux [mJy]
Frequency [GHz]
4 6045-4734
6 GHz
79.3 ± 1.4
10 GHz
56.8 ± 2.0
22 GHz
< 10
33 GHz
< 9.9
46 GHz
< 16
96 GHz
226.7 ± 4.6
243 GHz
< 93
349 GHz
< 199
4 (17:47:20.0000, -28:22:04.65)
5 6007-4515
6 GHz
16.8 ± 1.3
10 GHz
< 4.0
22 GHz
< 5.7
33 GHz
< 5.6
46 GHz
< 9.5
96 GHz
47.9 ± 3.4
243 GHz
< 27
343 GHz
< 117
5 (17:47:20.8183, -28:22:06.35)
6 6001-5233
6 GHz
6.7 ± 0.1
10 GHz
< 1.6
22 GHz
< 5.7
33 GHz
< 3.0
46 GHz
< 5.8
96 GHz
10.8 ± 0.2
243 GHz
343 GHz
6 (17:47:18.1097, -28:22:07.00)

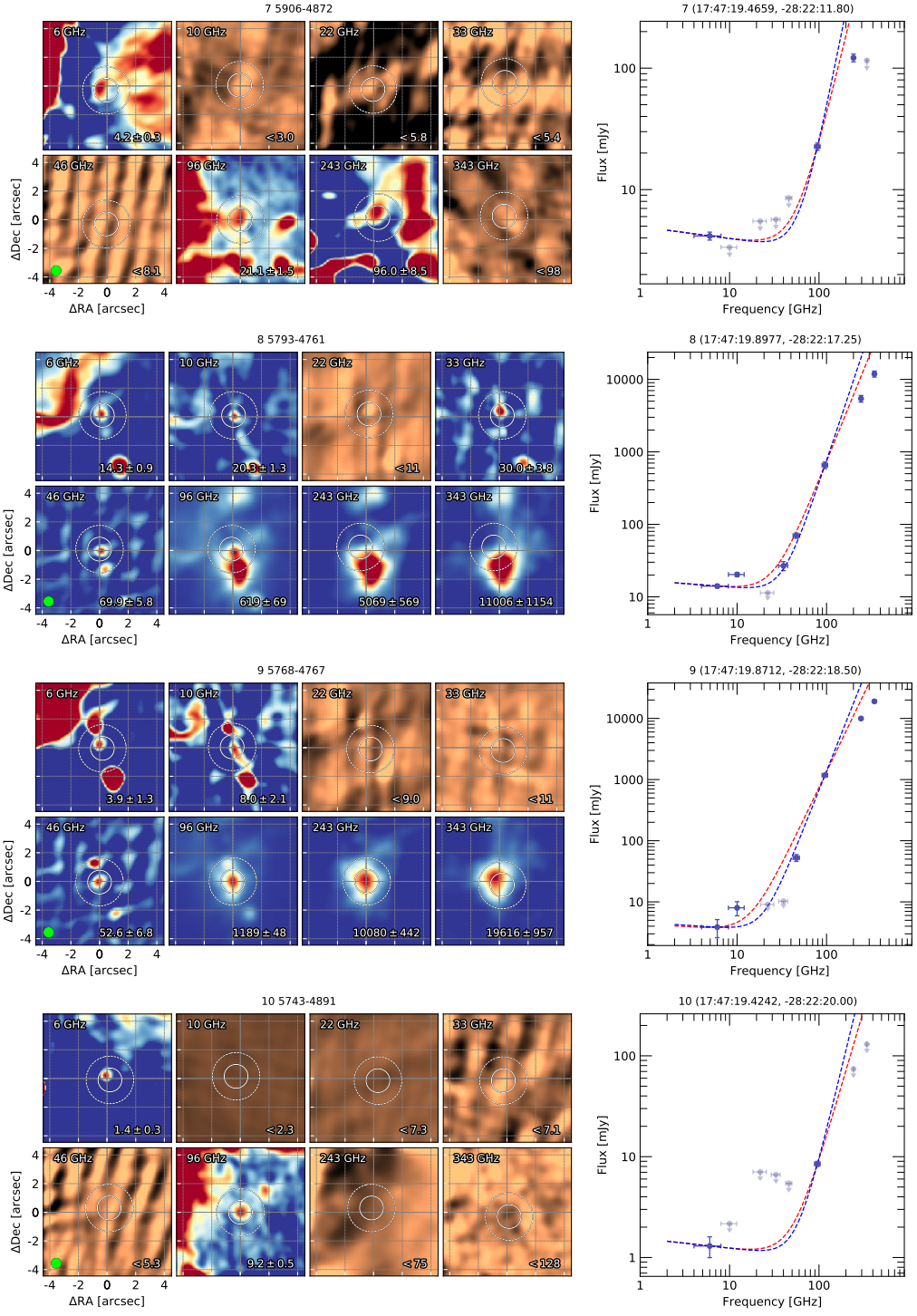
7 5906-4872
6 GHz
4.2 ± 0.3
10 GHz
< 3.0
22 GHz
< 5.8
33 GHz
< 5.4
46 GHz
< 8.1
96 GHz
21.1 ± 1.5
243 GHz
96.0 ± 8.5
343 GHz
< 98
ΔDec [arcsec]
ΔRA [arcsec]
7 (17:47:19.4659, -28:22:11.80)
Flux [mJy]
Frequency [GHz]
8 5793-4761
6 GHz
14.3 ± 0.9
10 GHz
20.3 ± 1.3
22 GHz
< 11
33 GHz
30.0 ± 3.8
46 GHz
69.9 ± 5.8
96 GHz
619 ± 69
243 GHz
5069 ± 569
343 GHz
11006 ± 1154
ΔDec [arcsec]
ΔRA [arcsec]
8 (17:47:19.8977, -28:22:17.25)
Flux [mJy]
Frequency [GHz]
9 5768-4767
6 GHz
3.9 ± 1.3
10 GHz
8.0 ± 2.1
22 GHz
< 9.0
33 GHz
< 11
46 GHz
52.6 ± 6.8
96 GHz
1189 ± 48
243 GHz
10080 ± 442
343 GHz
19616 ± 957
ΔDec [arcsec]
ΔRA [arcsec]
9 (17:47:19.8712, -28:22:18.50)
Flux [mJy]
Frequency [GHz]
10 5743-4891
6 GHz
1.4 ± 0.3
10 GHz
< 2.3
22 GHz
< 7.3
33 GHz
< 7.1
46 GHz
< 5.3
96 GHz
9.2 ± 0.5
243 GHz
< 75
343 GHz
< 128
ΔDec [arcsec]
ΔRA [arcsec]
10 (17:47:19.4242, -28:22:20.00)
Flux [mJy]
Frequency [GHz]

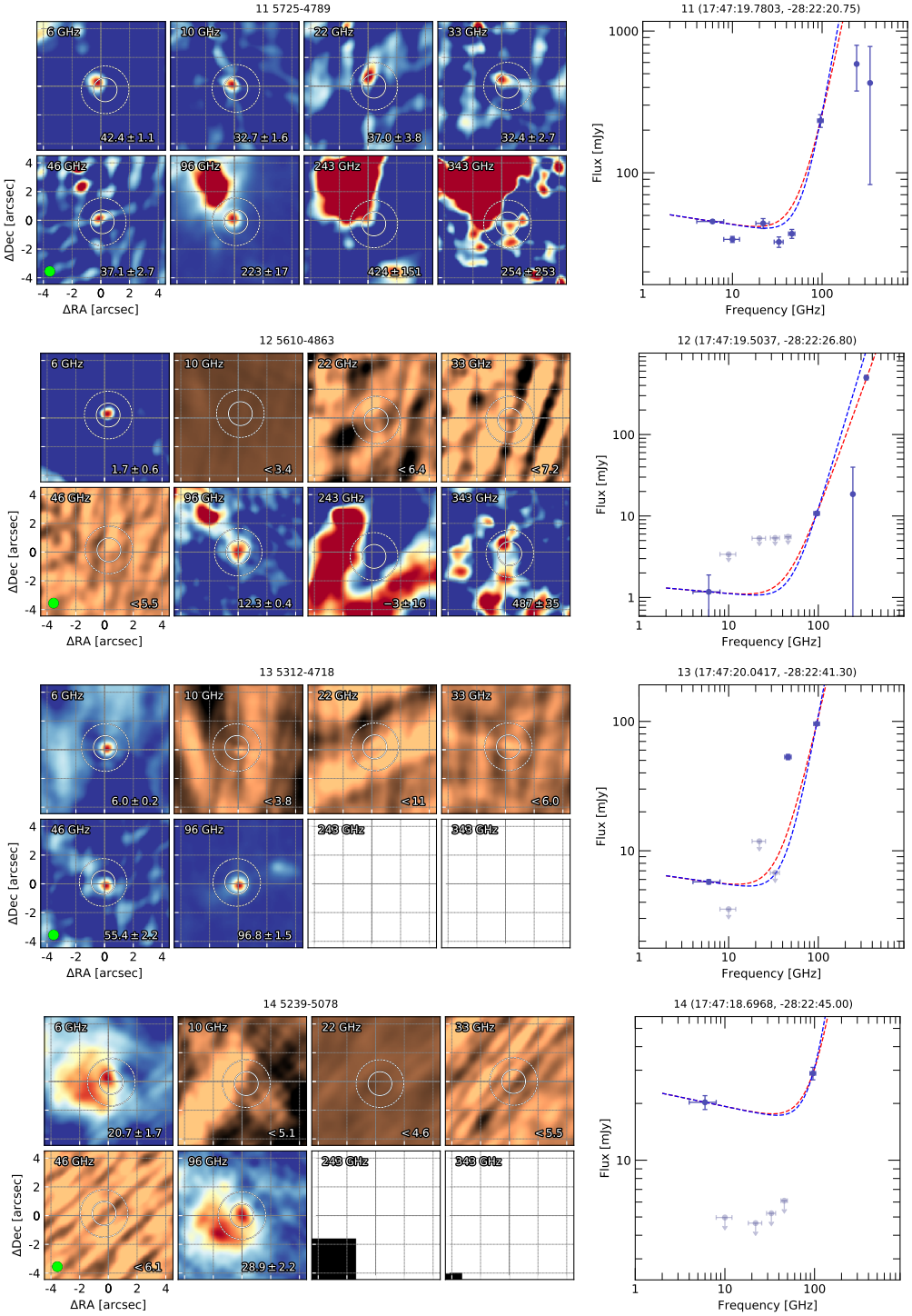
11 5725-4789
6 GHz
42.4 ± 1.1
10 GHz
32.7 ± 1.6
22 GHz
37.0 ± 3.8
33 GHz
32.4 ± 2.7
46 GHz
37.1 ± 2.7
96 GHz
223 ± 17
243 GHz
424 ± 151
343 GHz
254 ± 253
ΔDec [arcsec]
ΔRA [arcsec]
11 (17:47:19.7803, -28:22:20.75)
Flux [mJy]
Frequency [GHz]
12 5610-4863
6 GHz
1.7 ± 0.6
10 GHz
< 3.4
22 GHz
< 6.4
33 GHz
< 7.2
46 GHz
< 5.5
96 GHz
12.3 ± 0.4
243 GHz
−3 ± 16
343 GHz
487 ± 85
12 (17:47:19.5037, -28:22:26.80)
13 5312-4718
6 GHz
6.0 ± 0.2
10 GHz
< 3.8
22 GHz
< 11
33 GHz
< 6.0
46 GHz
55.4 ± 2.2
96 GHz
96.8 ± 1.5
243 GHz
343 GHz
13 (17:47:20.0417, -28:22:41.30)
14 5239-5078
6 GHz
20.7 ± 1.7
10 GHz
< 5.1
22 GHz
< 4.6
33 GHz
< 5.5
46 GHz
< 6.1
96 GHz
28.9 ± 2.2
243 GHz
343 GHz
14 (17:47:18.6968, -28:22:45.00)

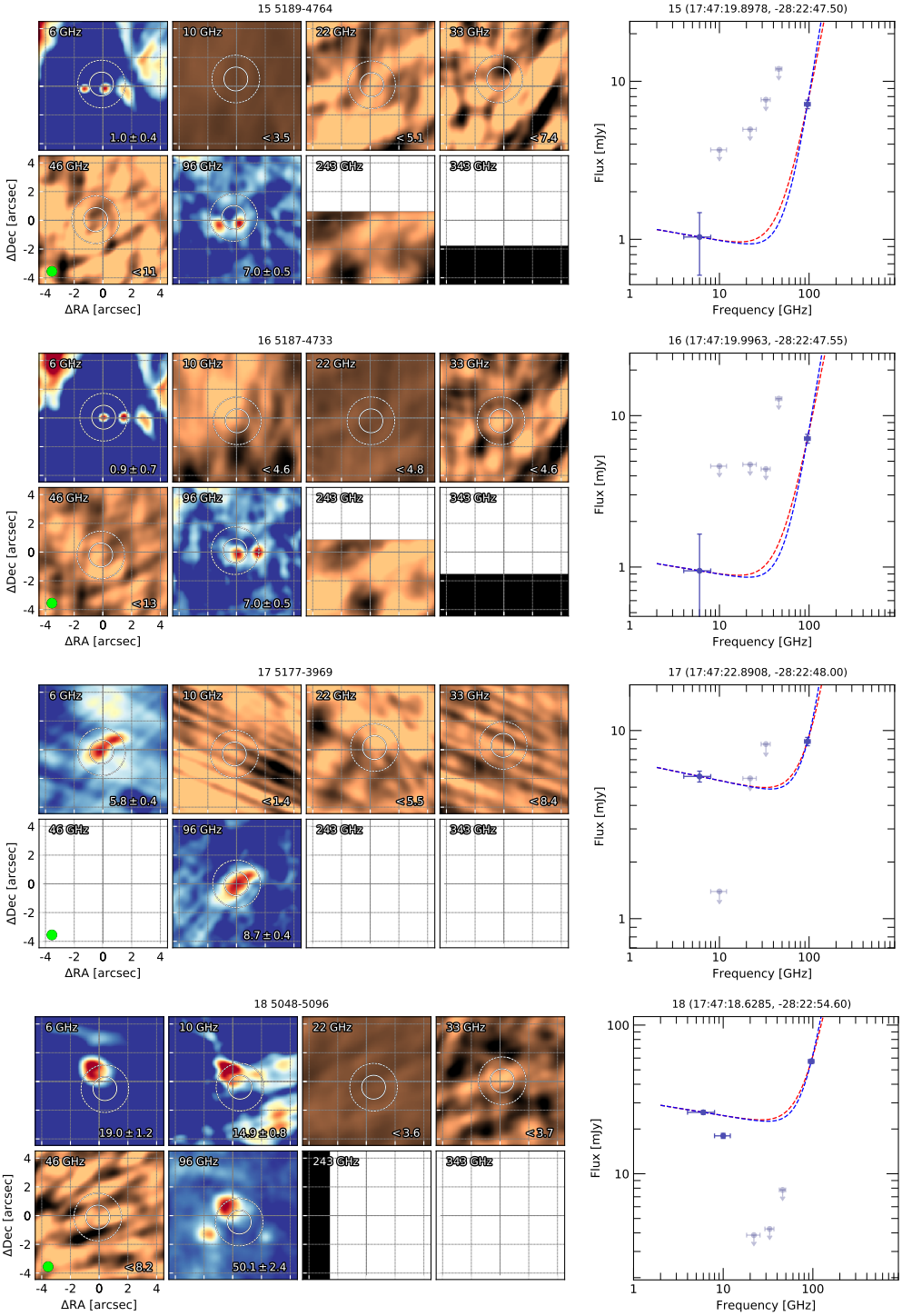
15 5189-4764
6 GHz
1.0 ± 0.4
10 GHz
< 3.5
22 GHz
< 5.1
33 GHz
< 7.4
46 GHz
< 11
96 GHz
7.0 ± 0.5
243 GHz
343 GHz
ΔDec [arcsec]
ΔRA [arcsec]
15 (17:47:19.8978, -28:22:47.50)
Flux [mJy]
Frequency [GHz]
16 5187-4733
6 GHz
0.9 ± 0.7
10 GHz
< 4.6
22 GHz
< 4.8
33 GHz
< 4.6
46 GHz
< 13
96 GHz
7.0 ± 0.5
243 GHz
343 GHz
ΔDec [arcsec]
ΔRA [arcsec]
16 (17:47:19.9963, -28:22:47.55)
Flux [mJy]
Frequency [GHz]
17 5177-3969
6 GHz
5.8 ± 0.4
10 GHz
< 1.4
22 GHz
< 5.5
33 GHz
< 8.4
46 GHz
96 GHz
8.7 ± 0.4
243 GHz
343 GHz
ΔDec [arcsec]
ΔRA [arcsec]
17 (17:47:22.8908, -28:22:48.00)
Flux [mJy]
Frequency [GHz]
18 5048-5096
6 GHz
19.0 ± 1.2
10 GHz
14.9 ± 0.8
22 GHz
< 3.6
33 GHz
< 3.7
46 GHz
< 8.2
96 GHz
50.1 ± 2.4
243 GHz
343 GHz
ΔDec [arcsec]
ΔRA [arcsec]
18 (17:47:18.6285, -28:22:54.60)
Flux [mJy]
Frequency [GHz]

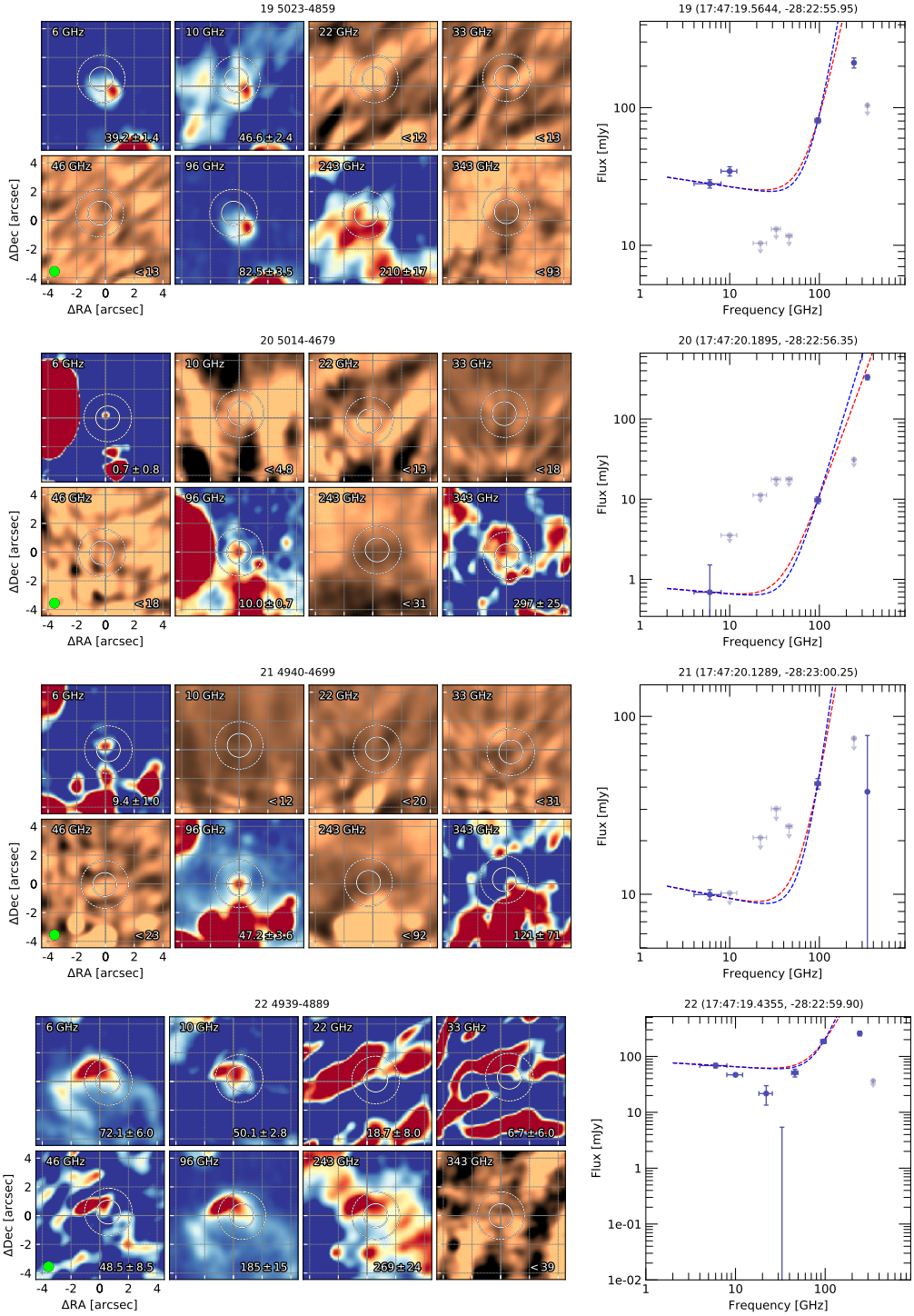
19 5023-4859
6 GHz
39.2 ± 1.4
10 GHz
46.6 ± 2.4
22 GHz
< 12
33 GHz
< 13
46 GHz
< 13
96 GHz
82.5 ± 3.5
243 GHz
210 ± 17
343 GHz
< 93
ΔDec [arcsec]
ΔRA [arcsec]
19 (17:47:19.5644, -28:22:55.95)
Flux [mJy]
Frequency [GHz]
20 5014-4679
6 GHz
0.7 ± 0.8
10 GHz
< 4.8
22 GHz
< 13
33 GHz
< 18
46 GHz
< 18
96 GHz
10.0 ± 0.7
243 GHz
< 31
343 GHz
297 ± 25
ΔDec [arcsec]
ΔRA [arcsec]
20 (17:47:20.1895, -28:22:56.35)
Flux [mJy]
Frequency [GHz]
21 4940-4699
6 GHz
9.4 ± 1.0
10 GHz
< 12
22 GHz
< 20
33 GHz
< 31
46 GHz
< 28
96 GHz
47.2 ± 3.6
243 GHz
< 92
343 GHz
121 ± 71
ΔDec [arcsec]
ΔRA [arcsec]
21 (17:47:20.1289, -28:23:00.25)
Flux [mJy]
Frequency [GHz]
22 4939-4889
6 GHz
72.1 ± 6.0
10 GHz
50.1 ± 2.8
22 GHz
18.7 ± 8.0
33 GHz
67 ± 6.0
46 GHz
48.5 ± 8.5
96 GHz
185 ± 15
243 GHz
269 ± 24
343 GHz
< 39
ΔDec [arcsec]
ΔRA [arcsec]
22 (17:47:19.4355, -28:22:59.90)
Flux [mJy]
Frequency [GHz]

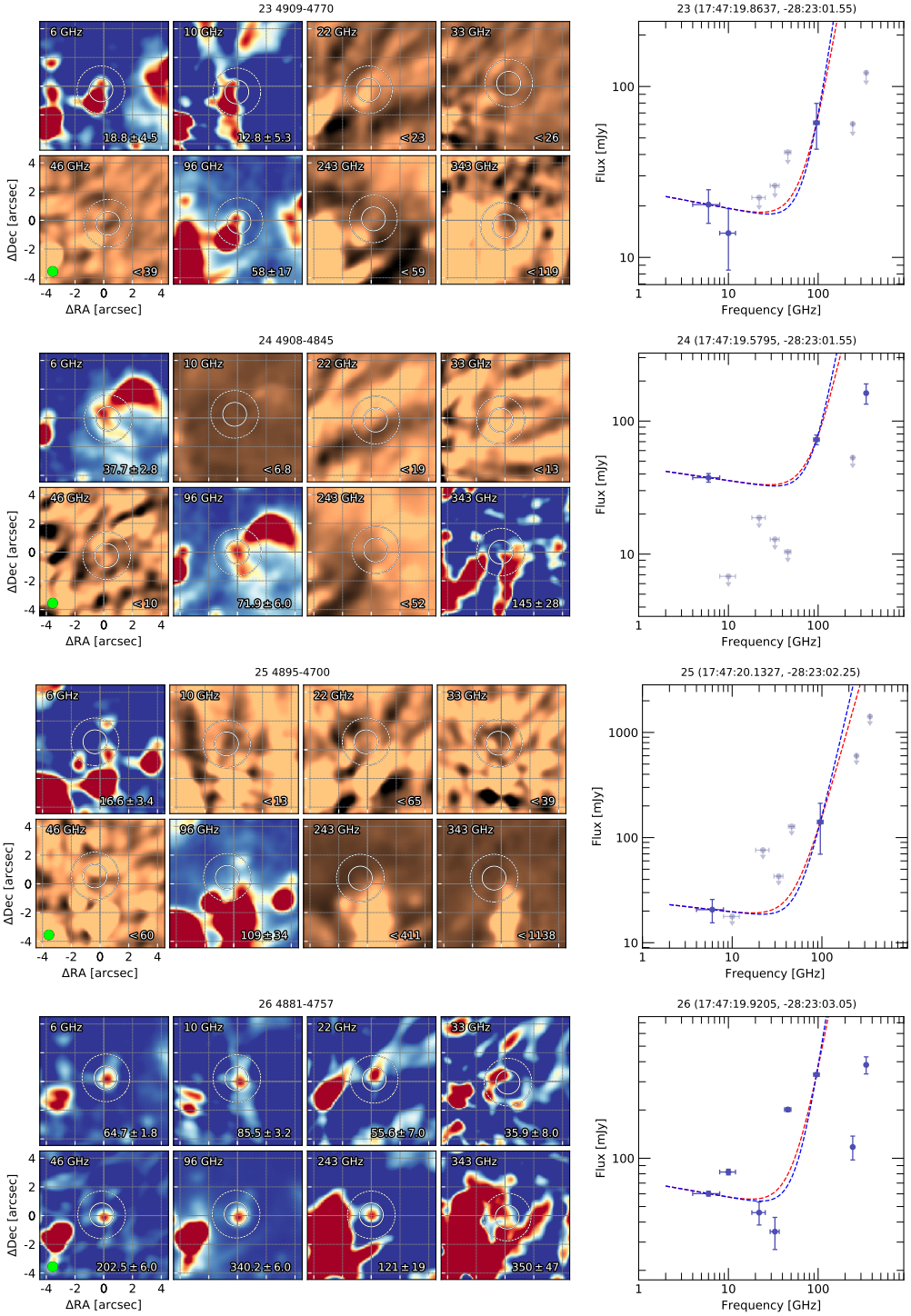
23 4909-4770
6 GHz
18.8 ± 4.5
10 GHz
12.8 ± 5.3
22 GHz
< 23
33 GHz
< 26
46 GHz
< 39
96 GHz
58 ± 17
243 GHz
< 59
349 GHz
< 119
ΔDec [arcsec]
ΔRA [arcsec]
23 (17:47:19.8637, -28:23:01.55)
Flux [mJy]
Frequency [GHz]
24 4908-4845
6 GHz
37.7 ± 2.8
10 GHz
< 6.8
22 GHz
< 19
33 GHz
< 13
46 GHz
< 10
96 GHz
71.9 ± 6.0
243 GHz
< 52
343 GHz
145 ± 28
ΔDec [arcsec]
ΔRA [arcsec]
24 (17:47:19.5795, -28:23:01.55)
Flux [mJy]
Frequency [GHz]
25 4895-4700
6 GHz
16.6 ± 3.4
10 GHz
< 13
22 GHz
< 65
33 GHz
< 39
46 GHz
< 60
96 GHz
109 ± 34
243 GHz
< 411
343 GHz
< 1138
ΔDec [arcsec]
ΔRA [arcsec]
25 (17:47:20.1327, -28:23:02.25)
Flux [mJy]
Frequency [GHz]
26 4881-4757
6 GHz
64.7 ± 1.8
10 GHz
85.5 ± 3.2
22 GHz
55.6 ± 7.0
33 GHz
35.9 ± 8.0
46 GHz
202.5 ± 6.0
96 GHz
340.2 ± 6.0
243 GHz
121 ± 19
343 GHz
350 ± 47
ΔDec [arcsec]
ΔRA [arcsec]
26 (17:47:19.9205, -28:23:03.05)
Flux [mJy]
Frequency [GHz]

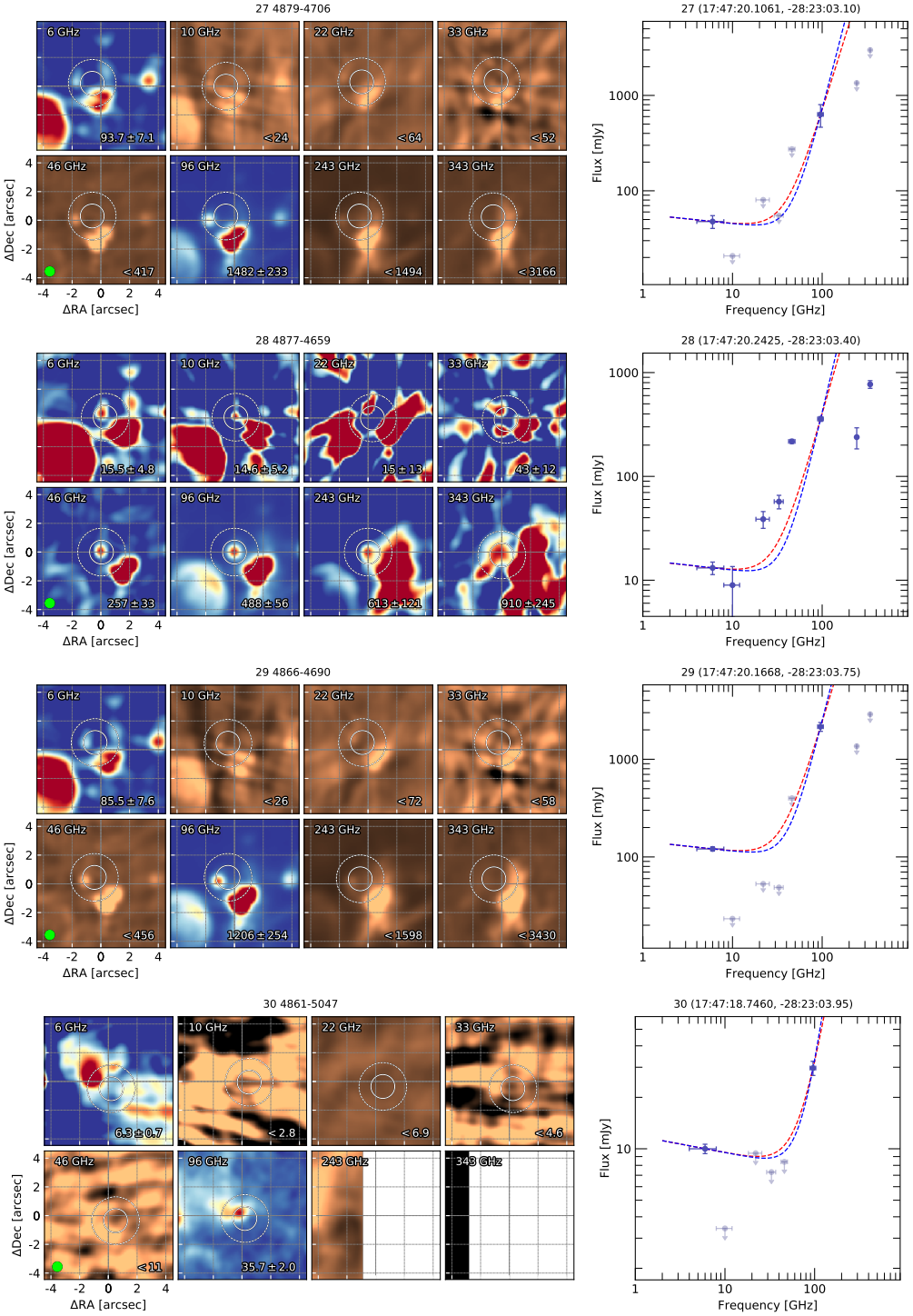
27 4879-4706
6 GHz
93.7 ± 7.1
10 GHz
< 24
22 GHz
< 64
33 GHz
< 52
46 GHz
< 417
96 GHz
1482 ± 233
243 GHz
< 1494
343 GHz
< 3166
ΔDec [arcsec]
ΔRA [arcsec]
27 (17:47:20.1061, -28:23:03.10)
Flux [mJy]
Frequency [GHz]
28 4877-4659
6 GHz
15.5 ± 4.8
10 GHz
14.6 ± 5.2
22 GHz
15 ± 13
33 GHz
43 ± 12
46 GHz
257 ± 33
96 GHz
488 ± 56
243 GHz
613 ± 121
343 GHz
910 ± 245
ΔDec [arcsec]
ΔRA [arcsec]
28 (17:47:20.2425, -28:23:03.40)
Flux [mJy]
Frequency [GHz]
29 4866-4690
6 GHz
85.5 ± 7.6
10 GHz
< 26
22 GHz
< 72
33 GHz
< 58
46 GHz
< 456
96 GHz
1206 ± 254
243 GHz
< 1598
343 GHz
< 3430
ΔDec [arcsec]
ΔRA [arcsec]
29 (17:47:20.1668, -28:23:03.75)
Flux [mJy]
Frequency [GHz]
30 4861-5047
6 GHz
6.3 ± 0.7
10 GHz
< 2.8
22 GHz
< 6.9
33 GHz
< 4.6
46 GHz
< 11
96 GHz
35.7 ± 2.0
243 GHz
343 GHz
ΔDec [arcsec]
ΔRA [arcsec]
30 (17:47:18.7460, -28:23:03.95)
Flux [mJy]
Frequency [GHz]

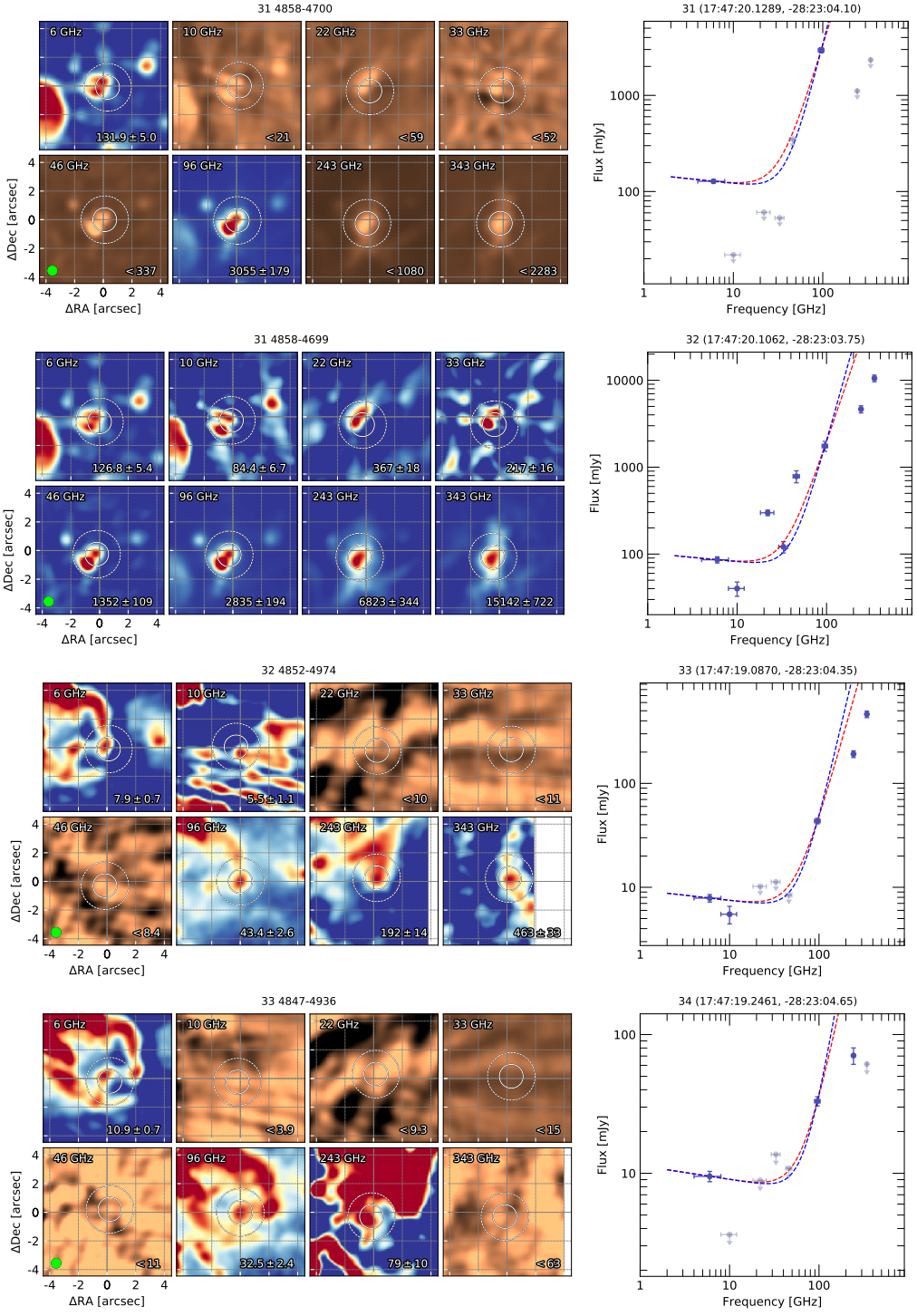
31 4858-4700
6 GHz
131.9 ± 5.0
10 GHz
< 21
22 GHz
< 59
33 GHz
< 52
46 GHz
< 337
96 GHz
3055 ± 179
243 GHz
< 1080
343 GHz
< 2283
ΔDec [arcsec]
ΔRA [arcsec]
31 (17:47:20.1289, -28:23:04.10)
Flux [mJy]
Frequency [GHz]
31 4858-4699
6 GHz
126.8 ± 5.4
10 GHz
84.4 ± 6.7
22 GHz
367 ± 18
33 GHz
217 ± 16
46 GHz
1352 ± 109
96 GHz
2835 ± 194
243 GHz
6823 ± 344
343 GHz
15142 ± 722
ΔDec [arcsec]
ΔRA [arcsec]
32 (17:47:20.1062, -28:23:03.75)
Flux [mJy]
Frequency [GHz]
32 4852-4974
6 GHz
7.9 ± 0.7
10 GHz
5.5 ± 1.1
22 GHz
< 10
33 GHz
< 11
46 GHz
< 8.4
96 GHz
43.4 ± 2.6
243 GHz
192 ± 14
343 GHz
463 ± 39
ΔDec [arcsec]
ΔRA [arcsec]
33 (17:47:19.0870, -28:23:04.35)
Flux [mJy]
Frequency [GHz]
33 4847-4936
6 GHz
10.9 ± 0.7
10 GHz
< 3.9
22 GHz
< 9.3
33 GHz
< 15
46 GHz
< 11
96 GHz
32.5 ± 2.4
243 GHz
79 ± 10
343 GHz
< 63
ΔDec [arcsec]
ΔRA [arcsec]
34 (17:47:19.2461, -28:23:04.65)
Flux [mJy]
Frequency [GHz]

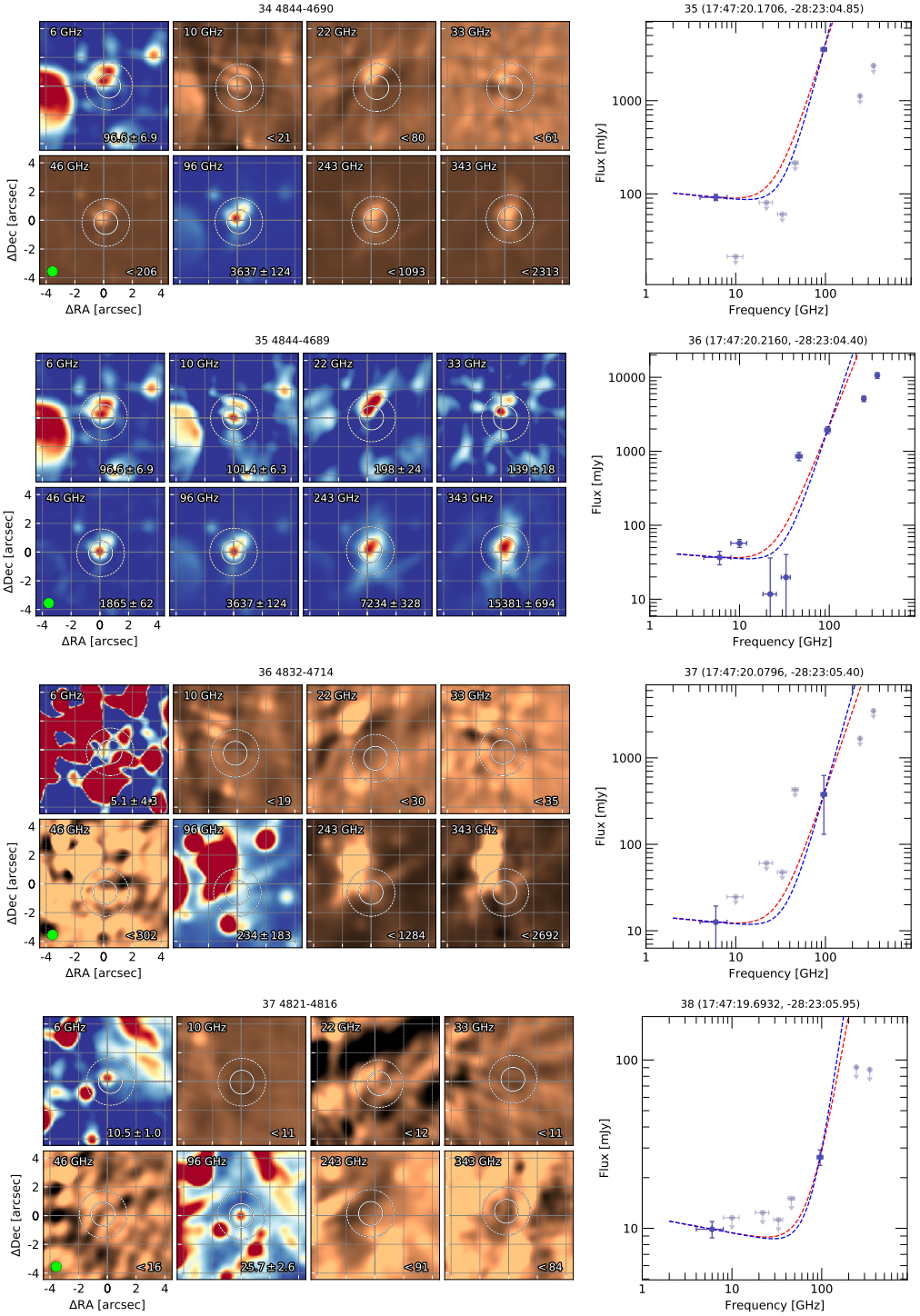
34 4844-4690
6 GHz
96.6 ± 6.9
10 GHz
< 21
22 GHz
< 80
33 GHz
< 61
46 GHz
< 206
96 GHz
3637 ± 124
243 GHz
< 1093
343 GHz
< 2313
ΔDec [arcsec]
ΔRA [arcsec]
35 (17:47:20.1706, -28:23:04.85)
Flux [mJy]
Frequency [GHz]
35 4844-4689
6 GHz
96.6 ± 6.9
10 GHz
101.4 ± 6.3
22 GHz
198 ± 24
33 GHz
139 ± 18
46 GHz
1865 ± 62
96 GHz
3637 ± 124
243 GHz
7234 ± 328
343 GHz
15381 ± 694
ΔDec [arcsec]
ΔRA [arcsec]
36 (17:47:20.2160, -28:23:04.40)
Flux [mJy]
Frequency [GHz]
36 4832-4714
6 GHz
5.1 ± 4.3
10 GHz
< 19
22 GHz
< 30
33 GHz
< 35
46 GHz
< 302
96 GHz
234 ± 183
243 GHz
< 1284
343 GHz
< 2692
ΔDec [arcsec]
ΔRA [arcsec]
37 (17:47:20.0796, -28:23:05.40)
Flux [mJy]
Frequency [GHz]
37 4821-4816
6 GHz
10.5 ± 1.0
10 GHz
< 11
22 GHz
< 12
33 GHz
< 11
46 GHz
< 16
96 GHz
25.7 ± 2.6
243 GHz
< 91
343 GHz
< 84
ΔDec [arcsec]
ΔRA [arcsec]
38 (17:47:19.6932, -28:23:05.95)
Flux [mJy]
Frequency [GHz]

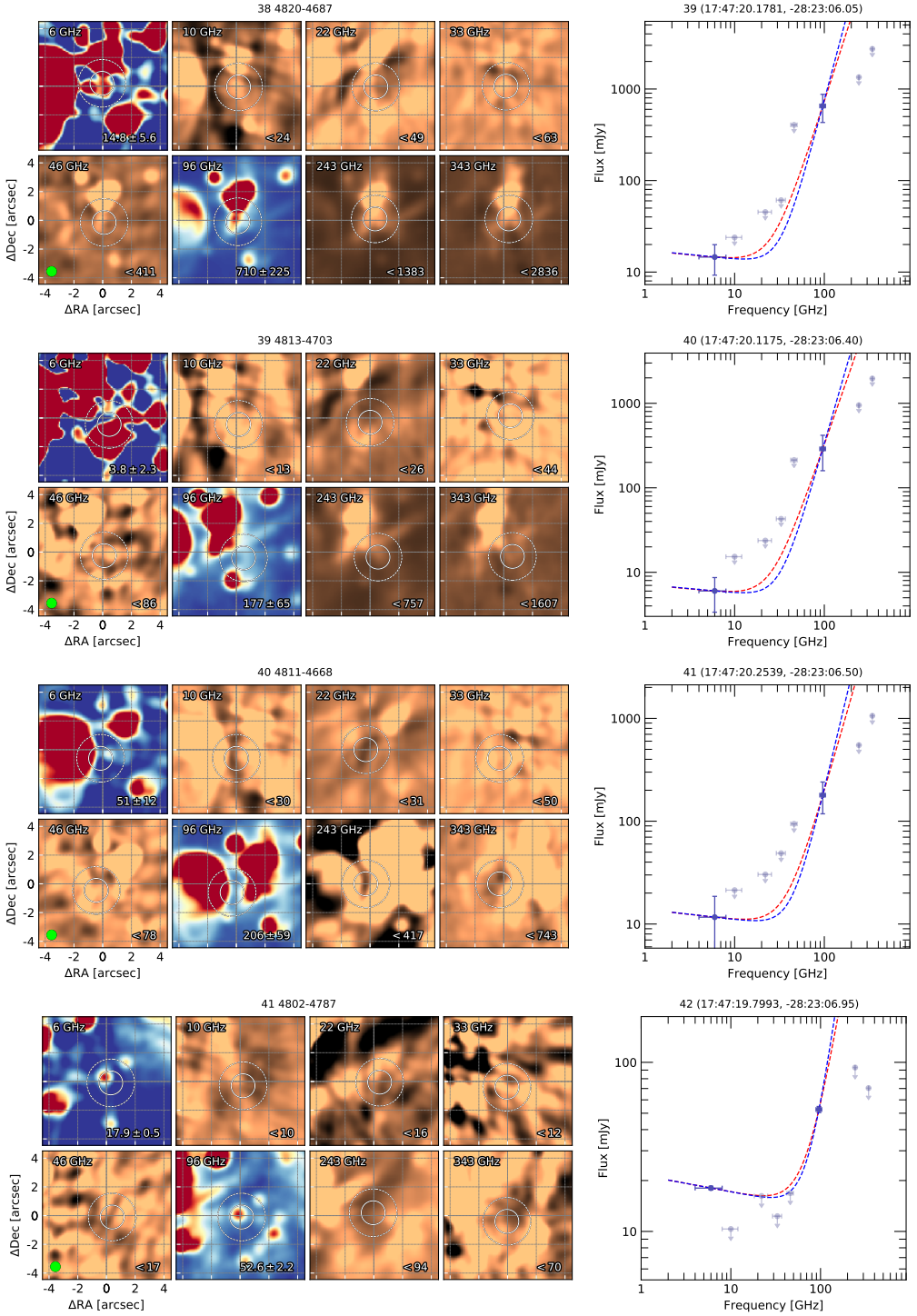
38 4820-4687
6 GHz
14.8 ± 5.6
10 GHz
< 24
22 GHz
< 49
33 GHz
< 63
46 GHz
< 411
96 GHz
710 ± 225
243 GHz
< 1383
343 GHz
< 2836
ΔDec [arcsec]
ΔRA [arcsec]
39 (17:47:20.1781, -28:23:06.05)
Flux [mJy]
Frequency [GHz]
39 4813-4703
6 GHz
3.8 ± 2.3
10 GHz
< 13
22 GHz
< 26
33 GHz
< 44
46 GHz
< 86
96 GHz
177 ± 65
243 GHz
< 757
343 GHz
< 1607
ΔDec [arcsec]
ΔRA [arcsec]
40 (17:47:20.1175, -28:23:06.40)
Flux [mJy]
Frequency [GHz]
40 4811-4668
6 GHz
51 ± 12
10 GHz
< 30
22 GHz
< 31
33 GHz
< 50
46 GHz
< 78
96 GHz
206 ± 59
243 GHz
< 417
343 GHz
< 743
ΔDec [arcsec]
ΔRA [arcsec]
41 (17:47:20.2539, -28:23:06.50)
Flux [mJy]
Frequency [GHz]
41 4802-4787
6 GHz
17.9 ± 0.5
10 GHz
< 10
22 GHz
< 16
33 GHz
< 12
46 GHz
< 17
96 GHz
52.6 ± 2.2
243 GHz
< 94
343 GHz
< 70
ΔDec [arcsec]
ΔRA [arcsec]
42 (17:47:19.7993, -28:23:06.95)
Flux [mJy]
Frequency [GHz]

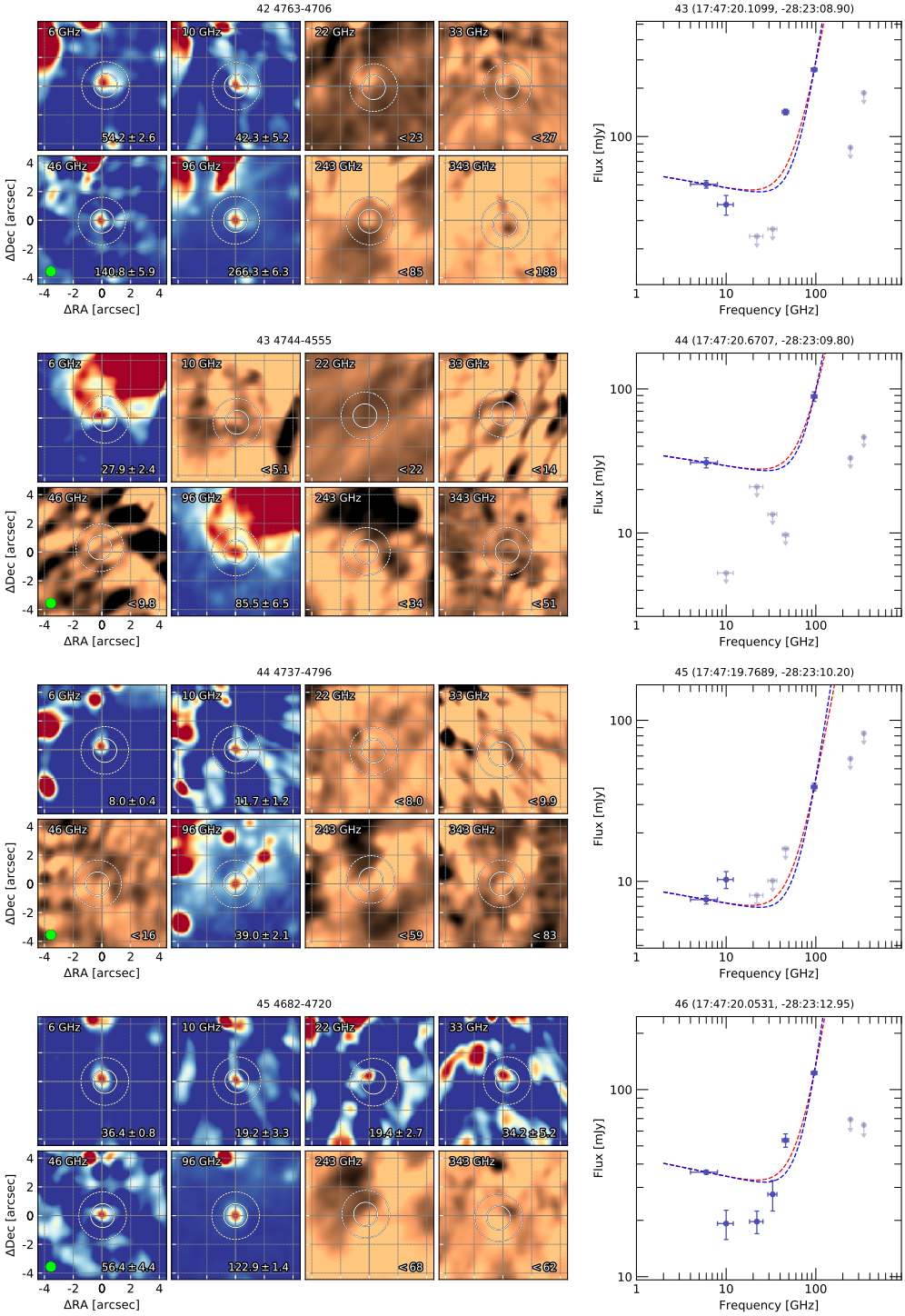
42 4763-4706
6 GHz
54.2 ± 2.6
10 GHz
42.3 ± 5.2
22 GHz
< 23
33 GHz
< 27
46 GHz
140.8 ± 5.9
96 GHz
266.3 ± 6.3
243 GHz
< 85
343 GHz
< 188
ΔDec [arcsec]
ΔRA [arcsec]
43 (17:47:20.1099, -28:23:08.90)
Flux [mJy]
Frequency [GHz]
43 4744-4555
6 GHz
27.9 ± 2.4
10 GHz
< 5.1
22 GHz
< 22
33 GHz
< 14
46 GHz
< 9.8
96 GHz
85.5 ± 6.5
243 GHz
< 34
343 GHz
< 51
ΔDec [arcsec]
ΔRA [arcsec]
44 (17:47:20.6707, -28:23:09.80)
Flux [mJy]
Frequency [GHz]
44 4737-4796
6 GHz
8.0 ± 0.4
10 GHz
11.7 ± 1.2
22 GHz
< 8.0
33 GHz
< 9.9
46 GHz
< 16
96 GHz
39.0 ± 2.1
243 GHz
< 59
343 GHz
< 83
ΔDec [arcsec]
ΔRA [arcsec]
45 (17:47:19.7689, -28:23:10.20)
Flux [mJy]
Frequency [GHz]
45 4682-4720
6 GHz
36.4 ± 0.8
10 GHz
19.2 ± 3.3
22 GHz
19.4 ± 2.7
33 GHz
34.2 ± 5.2
46 GHz
56.4 ± 4.4
96 GHz
122.9 ± 1.4
243 GHz
< 68
343 GHz
< 62
ΔDec [arcsec]
ΔRA [arcsec]
46 (17:47:20.0531, -28:23:12.95)
Flux [mJy]
Frequency [GHz]

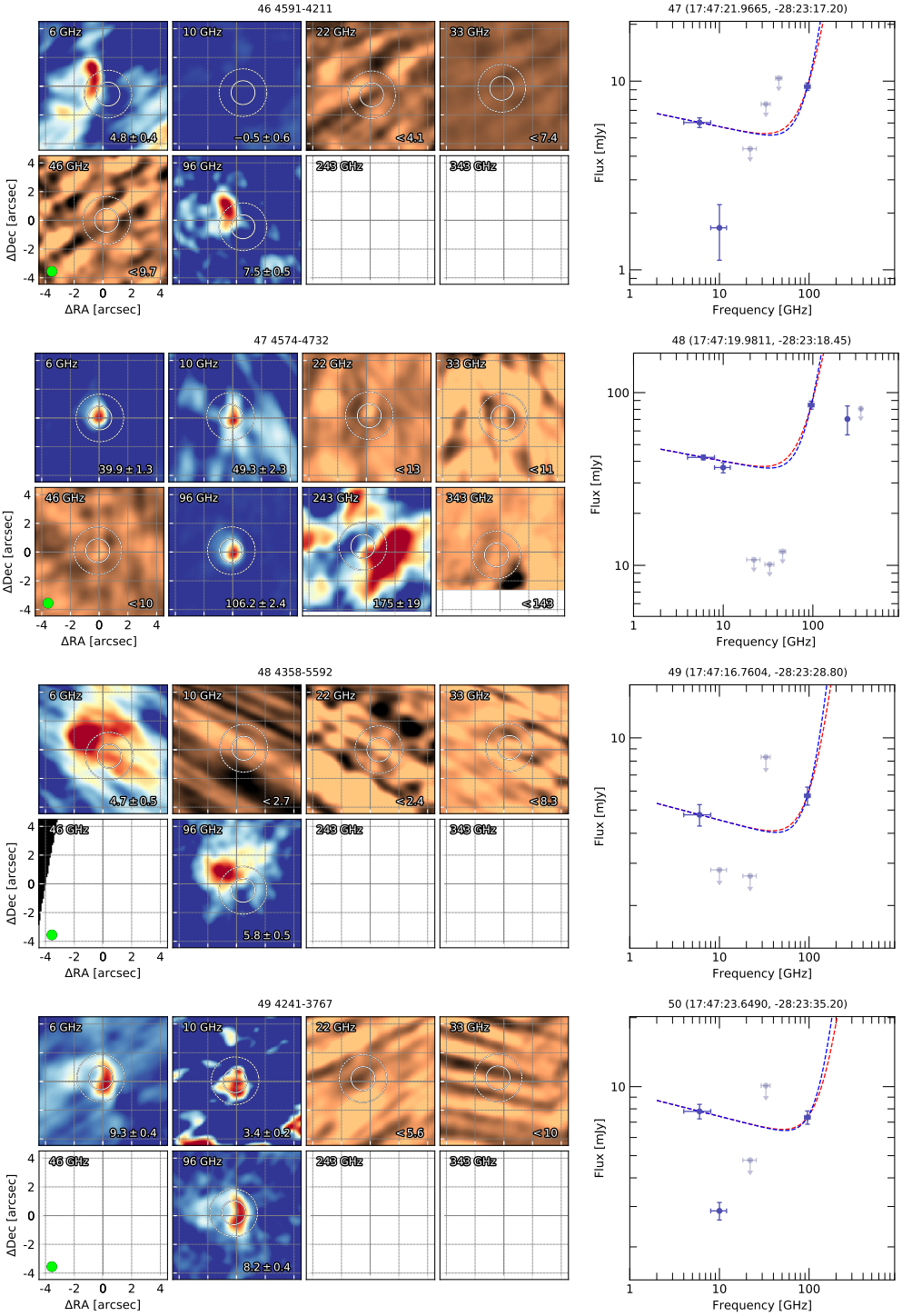
46 4591-4211
6 GHz
4.8 ± 0.4
10 GHz
−0.5 ± 0.6
22 GHz
< 4.1
33 GHz
< 7.4
46 GHz
< 9.7
96 GHz
7.5 ± 0.5
243 GHz
343 GHz
ΔDec [arcsec]
ΔRA [arcsec]
47 (17:47:21.9665, -28:23:17.20)
Flux [mJy]
Frequency [GHz]
47 4574-4732
6 GHz
39.9 ± 1.3
10 GHz
49.3 ± 2.3
22 GHz
< 13
33 GHz
< 11
46 GHz
< 10
96 GHz
106.2 ± 2.4
243 GHz
175 ± 19
343 GHz
< 143
48 (17:47:19.9811, -28:23:18.45)
48 4358-5592
6 GHz
4.7 ± 0.5
10 GHz
< 2.7
22 GHz
< 2.4
33 GHz
< 8.3
46 GHz
96 GHz
5.8 ± 0.5
243 GHz
343 GHz
49 (17:47:16.7604, -28:23:28.80)
49 4241-3767
6 GHz
9.3 ± 0.4
10 GHz
3.4 ± 0.2
22 GHz
< 5.6
33 GHz
< 10
46 GHz
96 GHz
8.2 ± 0.4
243 GHz
343 GHz
50 (17:47:23.6490, -28:23:35.20)

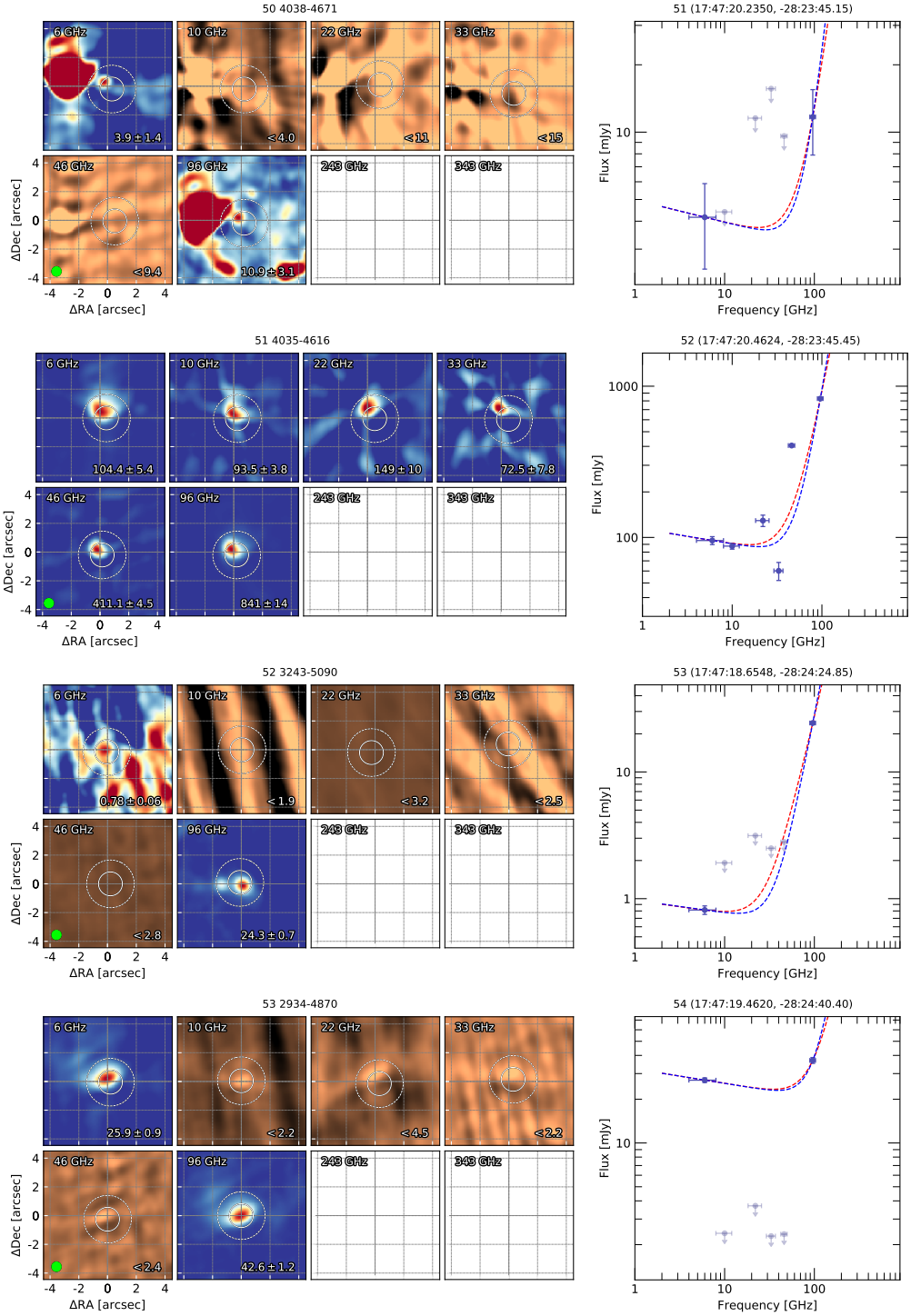
50 4038-4671
6 GHz
10 GHz
22 GHz
33 GHz
46 GHz
96 GHz
243 GHz
343 GHz
3.9 ± 1.4
< 4.0
< 11
< 15
< 9.4
10.9 ± 3.1
ΔDec [arcsec]
ΔRA [arcsec]
51 (17:47:20.2350, -28:23:45.15)
Flux [mJy]
Frequency [GHz]
51 4035-4616
104.4 ± 5.4
93.5 ± 3.8
149 ± 10
72.5 ± 7.8
411.1 ± 4.5
841 ± 14
52 (17:47:20.4624, -28:23:45.45)
52 3243-5090
0.78 ± 0.06
< 1.9
< 3.2
< 2.5
< 2.8
24.3 ± 0.7
53 (17:47:18.6548, -28:24:24.85)
53 2934-4870
25.9 ± 0.9
< 2.2
< 4.5
< 2.2
< 2.4
42.6 ± 1.2
54 (17:47:19.4620, -28:24:40.40)

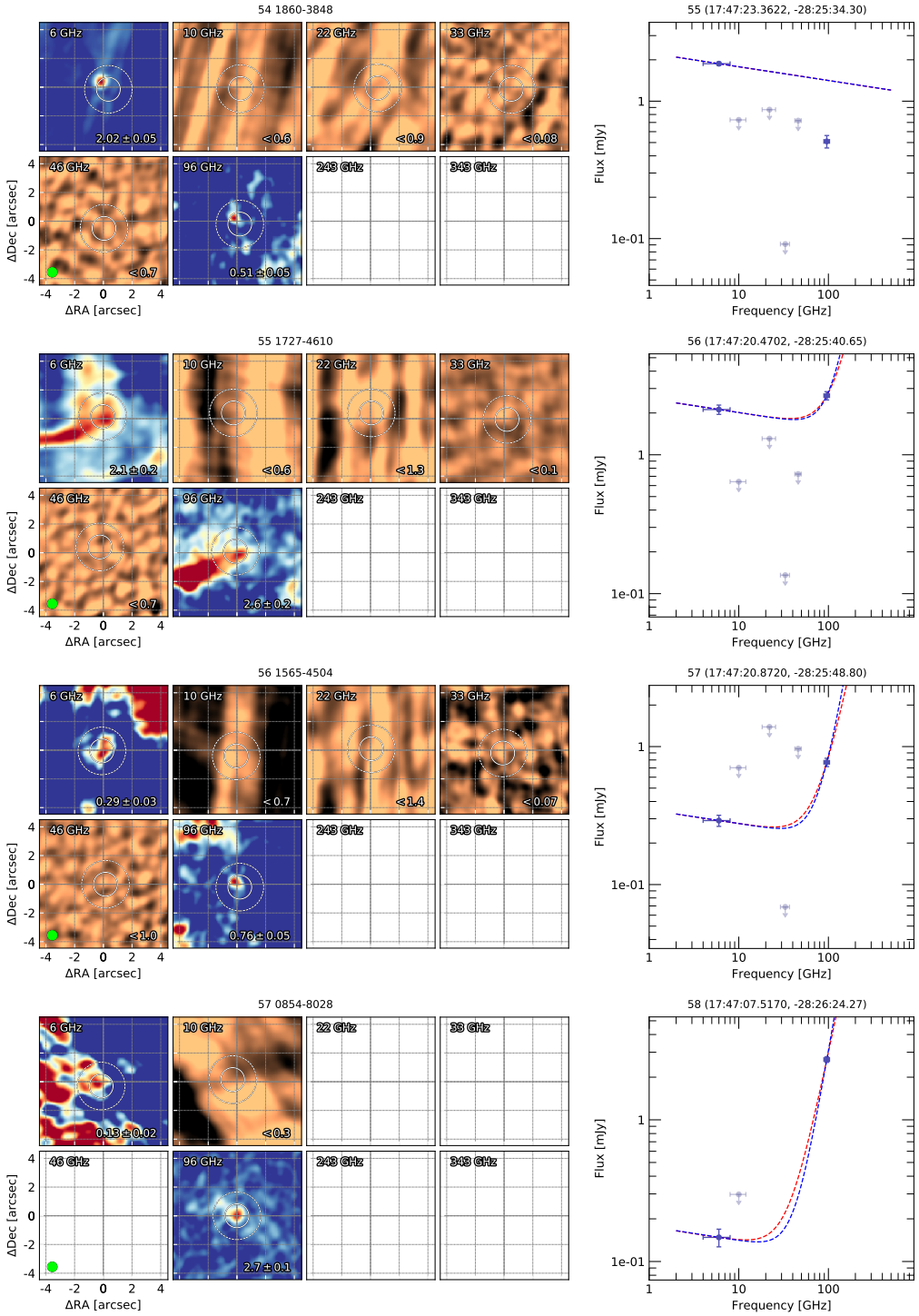

Figure C.1 *Left panels:* Maps of the 58 Type I cores. *Right Panels:* SED plots of the 58 Type I cores. Red dashed curves are the solution for the 'mrn8' case while the blue dashed line for the 'thin8' case.

Acknowledgement

This work was supported by the Collaborative Research Centre 956, sub-projects A6, funded by the Deutsche Forschungsgemeinschaft (DFG) - project ID 184018867.

First of all, I would like to thank my mentor and advisor Prof. Dr. Peter Schilke, your support is the biggest motivation for me to move forward. Your insight in physics and passion for science has always inspired me. From you, I learned not only about astrophysics, but also how to be an intellectual. I would like to thank Dr. Á. Sánchez-Monge for your constant encouragement, help, and the most detailed instructions. During the most difficult phases of my studies and research, it was your enlightenment that helped me to overcome one difficulty after another. Your generosity and selflessness have made you a lifelong role model for me. I would like to thank Andreas Schwörer, I am so lucky to have a friend like you. We had coffee together, traveled together, complained together and laughed together. These are some of the best memories I have in Germany. We were like comrades in arms, going through thick and thin together. Long live our friendship!

I would also like to thank my colleagues: Veena, Anika, Claudia, Dirk, Flavia, Gwendoline, Kai, Liem, Mahya, Mitra, Nassim, Niraj, Roja, Stefan, Sümeyye, Thomas, and Tiwanwei. You have given me immense help and joy! I would like to thank Adam, you have selflessly shared your data and taught me a lot about how to solve problems. You have helped me to make great progress in this study during my two-month visit to Socorro. I would also like to thank Bill for mentoring me during my visit to Charlottesville. I want to thank my friends, Jiaqi Cai and Dr. Zhongyi Zhang. Many years from now, I'll miss the smell of hotpot, the bubbles of the beer, and the laughter that lasts forever.

My parents, thank you! Since I was a child, you have always been my strong support. I still remember that when I was six years old, you took me to the Beijing Planetarium. I still remember the night sky in 1997 when you accompanied me to watch the Comet Hale-Bopp. I especially want to thank my wife, Dr. Wendan Li, for your unwavering love and tolerance for me. Loving you is like loving life. Finally, I want to thank my newborn daughter, Xiangxu Meng, who has brought me so much joy. You are a forming star.

Erklärung zur Dissertation
gemäß der Promotionsordnung vom 12. März 2020

Diese Erklärung muss in der Dissertation enthalten sein.
(*This version must be included in the doctoral thesis*)

„Hiermit versichere ich an Eides statt, dass ich die vorliegende Dissertation selbstständig und ohne die Benutzung anderer als der angegebenen Hilfsmittel und Literatur angefertigt habe. Alle Stellen, die wörtlich oder sinngemäß aus veröffentlichten und nicht veröffentlichten Werken dem Wortlaut oder dem Sinn nach entnommen wurden, sind als solche kenntlich gemacht. Ich versichere an Eides statt, dass diese Dissertation noch keiner anderen Fakultät oder Universität zur Prüfung vorgelegen hat; dass sie - abgesehen von unten angegebenen Teilpublikationen und eingebundenen Artikeln und Manuskripten - noch nicht veröffentlicht worden ist sowie, dass ich eine Veröffentlichung der Dissertation vor Abschluss der Promotion nicht ohne Genehmigung des Promotionsausschusses vornehmen werde. Die Bestimmungen dieser Ordnung sind mir bekannt. Darüber hinaus erkläre ich hiermit, dass ich die Ordnung zur Sicherung guter wissenschaftlicher Praxis und zum Umgang mit wissenschaftlichem Fehlverhalten der Universität zu Köln gelesen und sie bei der Durchführung der Dissertation zugrundeliegenden Arbeiten und der schriftlich verfassten Dissertation beachtet habe und verpflichte mich hiermit, die dort genannten Vorgaben bei allen wissenschaftlichen Tätigkeiten zu beachten und umzusetzen. Ich versichere, dass die eingereichte elektronische Fassung der eingereichten Druckfassung vollständig entspricht."

Teilpublikationen:

The physical and chemical structure of Sagittarius B2. V. Non-thermal emission in the envelope of Sgr B2
F. Meng, Á. Sánchez-Monge, P. Schilke, M. Padovani, A. Marcowith, A. Ginsburg, A. Schmiedeke, A. Schwörer, C. DePree, V. S. Veena, and Th. Möller
Astronomy and Astrophysics, 630, A73 (2019)
https://doi.org/10.1051/0004-6361/201935920

Datum, Name und Unterschrift 13.07.2020, Fanyi Meng, Fanyi Meng